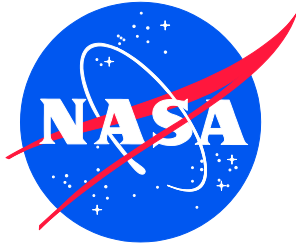# Nondestructive Evaluation (NDE) Methods and Capabilities Handbook

Patricia A. Howell, Editor
Langley Research Center, Hampton, Virginia

February 2020

NASA STI Program . . . in Profile

Since its founding, NASA has been dedicated to the advancement of aeronautics and space science. The NASA scientific and technical information (STI) program plays a key part in helping NASA maintain this important role.

The NASA STI program operates under the auspices of the Agency Chief Information Officer. It collects, organizes, provides for archiving, and disseminates NASA's STI. The NASA STI program provides access to the NTRS Registered and its public interface, the NASA Technical Reports Server, thus providing one of the largest collections of aeronautical and space science STI in the world. Results are published in both non-NASA channels and by NASA in the NASA STI Report Series, which includes the following report types:

- TECHNICAL PUBLICATION. Reports of completed research or a major significant phase of research that present the results of NASA Programs and include extensive data or theoretical analysis. Includes compilations of significant scientific and technical data and information deemed to be of continuing reference value. NASA counter-part of peer-reviewed formal professional papers but has less stringent limitations on manuscript length and extent of graphic presentations.

- TECHNICAL MEMORANDUM. Scientific and technical findings that are preliminary or of specialized interest, e.g., quick release reports, working papers, and bibliographies that contain minimal annotation. Does not contain extensive analysis.

- CONTRACTOR REPORT. Scientific and technical findings by NASA-sponsored contractors and grantees.

- CONFERENCE PUBLICATION. Collected papers from scientific and technical conferences, symposia, seminars, or other meetings sponsored or co-sponsored by NASA.

- SPECIAL PUBLICATION. Scientific, technical, or historical information from NASA programs, projects, and missions, often concerned with subjects having substantial public interest.

- TECHNICAL TRANSLATION. English-language translations of foreign scientific and technical material pertinent to NASA's mission.
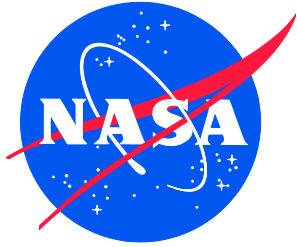
Specialized services also include organizing and publishing research results, distributing specialized research announcements and feeds, providing information desk and personal search support, and enabling data exchange services.

For more information about the NASA STI program, see the following:

- Access the NASA STI program home page at *http://www.sti.nasa.gov*

- E-mail your question to help@sti.nasa.gov

- Phone the NASA STI Information Desk at 757-864-9658

- Write to:
NASA STI Information Desk
Mail Stop 148
NASA Langley Research Center
Hampton, VA 23681-2199

Nondestructive Evaluation (NDE) Methods and Capabilities Handbook

Patricia A. Howell, Editor
Langley Research Center, Hampton, Virginia

APPROVED FOR PUBLIC RELEASE

Statement of Intent

This Handbook is a product of the Advanced Composites Project (ACP), a multiyear collaboration between National Aeronautics and Space Administration (NASA), the aerospace industry, universities, and other government agencies with the goal of reducing the timeline to develop and certify composite structures for commercial and military aeronautic vehicles.

This Handbook is a guidance document that facilitates the selection of appropriate Nondestructive Evaluation (NDE) techniques and provides recommended protocols for detecting and characterizing common flaw types in complex composite structures. It seeks to reduce the time required to develop qualified inspection processes for composite aircraft structures during the development, certification, and manufacturing phases by providing a reference that helps minimize trial and error. The handbook provides guidance on best practices, techniques, and settings, for specific flaw types and geometries. The intent is to give an unbiased assessment of the technologies for different inspection needs—not to recommend any particular technology for a particular inspection requirement.

Development of this handbook was guided by a survey of industry that directed the scope and intent of the handbook. This survey revealed that inspection of manufacturing defects in Carbon Fiber Reinforced Polymer (CFRP) composites was the most significant area of interest. The survey further revealed that industry was united in expressing the need for a set of realistic NDE standards for composites. Therefore, the first step in developing this handbook was to manufacture a set of realistic NDE standards. A total of 88 NDE standards were manufactured and are detailed in Appendix C. They include flat as well as complex geometry components containing the most common manufacturing defects: porosity, delaminations, fiber defects (laps, gaps, folds, missing tows, wrinkles, etc.), and low-velocity impact damage. These standards were tested by the consortium members in a round-robin fashion, and are used in the handbook to illustrate the complexity and expected results of various NDE methods for the detection of the different defect types.

This Handbook is meant to be a reference document, and consequently there is significant redundancy in information. The intent is to keep all relevant information in one place rather than sending the reader to multiple sections of the document. The handbook contains the major sections delineated as follows:

Section 1. Contributing Authors: The ACP handbook team members as well as additional contributors from industry, government and universities.

Section 2. Introduction: Description of the ACP, where this handbook fits in the project, and details of the industry survey that resulted in the development of this handbook.

Section 3. NDE Guidance Matrix: A table that provides an applicability rating for NDE techniques as they apply to given flaw types.

Section 4. Inspection Guidance by Flaw Type: Guidance on inspection of typical composite defect types is discussed in this section. Effective, marginally effective, and ineffective inspection technologies for each defect type are reviewed in detail, with advantages and disadvantages for each inspection technique tabulated for easy reference. An emphasis is placed on traditional, widely applied NDE techniques. This section begins with working definitions of each of the defect types examined, followed by inspection guidance for each flaw type.

Section 5. Inspection Technology Summaries and Capabilities: This section of the handbook is organized by inspection technology. Each NDE technique includes a brief technical explanation of the physics of the technique. It also covers some of the specifics important to the inspection of solid laminate CFRP composites. The intent of this section is to facilitate determining which NDE technique might work for a specific inspection application and which will not, where to start and what to consider (from the perspective of the physics of the technique), and how the energy interacts with the composite material. Predominately discussed are the techniques used to inspect each of the NDE standards developed for the ACP. However, also included are well known NDE techniques that are not typically used for inspection of CFRP composites, why they are not used, and the kind of composites for which that technique might be more suitable.

Section 6: Further Reading: This section contains other documents of interest regarding inspection of composites.

Appendix A: **Survey**: NASA Advanced Composites Project NDE – State of the Practice Report

Appendix B: **Overview of Standards: Photos and Descriptions:** Consortium members fabricated 88 composite laminate standards with representative defect types typical in a manufacturing environment based on the results of the survey discussed in Appendix A. These defects are positioned within both flat panels and geometrically complicated locations and include defects ranging from delaminations and porosity to Automated Fiber Placement (AFP) tow defects and impact damage. Descriptions and photographs are detailed in this appendix, organized by defect type.

Appendix C: **Round-robin test matrix**: Details of the standards each consortium member tested and the NDE technologies applied by each are included in this appendix.

Appendix D: **Manufacturing and Design Documents and Validation Reports**: Each consortium company chose or was assigned standards to fabricate based on manufacturing capabilities. Appendix D details the manufacturing information for each type of standard as fabricated and organized by partner.

Appendix E: **Individual Test Reports**: Results of each inspection by each consortium member for each standard tested are contained in Appendix E. Included are the equipment used, settings, parameters, and examples of results.

Table of Contents

List of Figures

List of Tables

Nomenclature

μA	Microampere
μm	Micrometer/Micron
μs	Microseconds
1D	One-Dimensional
2D	Two-Dimensional
3D	Three-Dimensional
ABS	Acrylonitrile Butadiene Styrene
ACAD	Air Coupled Acoustic Drive
ACC	Advanced Composites Consortium
ACP	Advanced Composites Project
ACT	Air Coupled Transducer
ADR	Assisted Defect Recognition
AFP	Automated fiber placement
AISI	American Iron and Steel Institution
AMT	Active Microwave Thermography
ANSI	American National Standards Institute
APF	Automated Fiber Placement
ARC	Ames Research Center
ASME	American Society of Mechanical Engineers
ASNT	American Society of Nondestructive Testing
ASTM	American Society for Testing and Materials
ATL	Automated Tape Lay-Up
AWG	Arbitrary Waveform Generator
AWS	American Welding Society
BMS	Boeing Material Specification
BSI	British Standards Institution
BVID	Barely Visible Impact Damage
BW	Back Wall
C	Celsius
CAD	Computer-Aided Design
CAFA	Combined Analytical Finite Element Approach
CCD	Charge-coupled Device
CDRH	Center for Devices and Radiological Health
CFRP	Carbon Fiber Reinforced Polymer
CMOS	complementary metal oxide semiconductor
CNN	Convolutional Neural Network
CO_2	Carbon Dioxide
COPV	Composite Over-Wrap Pressure Vessel
CPV	Composite Pressure Vessel
CR	Computed Radiography
CST	Charge Simulation Technique
CT	Computed Tomography
CTE	Coefficient of Thermal Expansion
DAQ	Data Acquisition
dB	Decibel
dB/in	Decibels Per Inch
DDA	Digital Detector Array
DOF	Degree of Freedom
DR	Digital Radiography
DRC	Digital Radiography Center
ECT	Eddy Current Thermography
EFIT	Elastodynamic Finite Integration Technique

FBH	Flat-bottom holes
FD	Finite Difference
FDA	Food and Drug Administration
FEA	Finite Element Analysis
FEM	Finite Element Method
FEP	Fluorinated Ethylene Propylene
FLIR	Forward-looking Infrared
FMC	Full Matrix Capture
FOD	Foreign Object Debris
FOV	Field of View
ft-lbs	Foot Pounds
GE	General Electric
GHz	Gigahertz
GN_2	Gaseous Nitrogen
gsm	Grams per square meter
GWUT	Guided Wave Ultrasound
Hz	Hertz
ID	Inner Diameter
IDIQ	Indefinite Delivery/Indefinite Quantity
IEC	International Electrotechnical Commission
IML	Inner Mold Line
in	Inch
in/min	Inches per Minute
InSb	Indium Antimonide
ipm	Images per Minute
IR	Infrared
IRT	Infrared Thermography
ISTIS	*In Situ* Thermal Inspection System
J/cm^2	Joules Per Square Centimeter
K	Kelvin
KeV	Kiloelectron Volt
kg	Kilograms
kg/cm^2	kilogram per square centimeter
kHz	Kilohertz
kV	Kilovolts
kW	kilowatt
LaRC	Langley Research Center
LBI	Laser Bond Inspection
LMCO	Lockheed-Martin Company
LPS	Local Positioning System
LST	Line Scanning Thermography
LT	Lock-In Thermography
m^2	Square Meter
m^2/hr	Meters Square per Hour
mA	Miliampere
MECAD	Mechanically Coupled Acoustic Drive
MGBM	Multi-Gaussian Beam Model
MHz	Megahertz
mHz	Millihertz
mK	Millikelvin
mm	Millimeter
MPa	Megapascals
ms	Meter per Second
MS/s	Megasamples/second

msec	Millisecond
MSFC	Marshall Space Flight Center
NAS	National Aerospace Standard
NASA	National Aeronautics and Space Administration
Nd:Glass	Neodymium Glass Laser
NDE	Nondestructive Evaluation
NDI	Nondestructive Inspection
NDT	Nondestructive Test
NEDT	Noise Equivalent Differential Temperature
NGIS	Northrop Grumman Innovation Systems
nm	Nanometer
ns	Nanosecond
OEM	Original Equipment Manufacturer
OML	Outer Mold Line
ONR	Office of Naval Research
OSHA	Occupational Safety and Health Administration
PA	Phased Array
PCA	Principal Component Analysis
PEUT	Pulse Echo Ultrasound
PMC	Polymer Matrix Composite
PML	Perfectly Matched Layer
POC	Point of Contact
PoD	Probability of Detection
PPT	Pulsed-Phase Thermography
psi	Pounds Per Square Inch
PT	Pressure-Sensitive Tape
PTFE	Polytetraflouroethylene (Teflon™)
PVDF	polyvinylidene fluoride
PWI	Plane Wave Imaging
PW-UTC	Pratt Whitney – United Technology Corporation
PZT	Piezoelectric Sensors/Transducer
R&D	Research and Development
RAH	Refresh After Heat
RBH	Refresh Before Heat
RGB	Red, Green, and Blue
RMS	Root Mean Squared
ROI	Region of Interest
RPF	Release Ply Fabric
RSG	Rotated-Staggered Grid
RVE	Representative Volume Element
s	Seconds
SAE	Society of Automotive Engineers
SAFE	Semi-Analytical Finite Element
SAR	Synthetic Aperture Radar
sec	Seconds
SHM	Structural Health Monitoring
SLDV	Scanning Laser Doppler Vibrometer
SMAAART	Structures, Materials, Aerodynamics, Aerothermodynamics, and Acoustics Research and Technology
SME	Subject Matter Expert
SNR	Signal to Noise Ratio
SOFI	Spray on Foam Insulation
SoP	State-of-Practice
sq. ft/hr	square foot per hour

SSFT	Single-Side Flash Thermography
SSIR	Single-Sided Infrared Thermography
SVD	Singular Value Decomposition
TC2	Technical Challenge 2
TDRS	Time Domain Reflectometry Systems
TFM	Total Focus Method
Tg	Glass Transition Temperature
THz	Terahertz
TPS	Thermal Protection System
TSR	Thermographic Signal Reconstruction
TT	Through Transmission
TTIR	Through-Transmission Infrared Thermography
TTUT	Through-Transmission Ultrasound
TWI	Thermal Wave Imaging System
USC	University of South Carolina
UT	Ultrasound
VaRTM	Variation Resin Transfer Molding
VSHM	Visualized Structural Health Monitoring
XCT	X-ray Computed Tomography

1.0 Contributing authors

Name	Role	Organization
Core Team		
Daniel Perey	Rapid Inspection & Characterization ACP Subproject Manager	NASA
Patricia Howell	Technical Lead NDE Handbook, X-ray CT, Thermography	NASA
Dr. Gary Georgeson	ACC CRT Lead	Boeing
Morteza Safai	Shearography, X-ray, Ultrasound, Thermography	Boeing
Dr. Jill Bingham	Ultrasound	Boeing
Shannon Adams	Ultrasound	Northrop Grumman
Dr. Christopher Deemer	LBID, Thermography	Northrop Grumman
Dr. Clint Thomson	Ultrasound	Northrop Grumman
Dr. Lingyu Yu	Guided Wave Ultrasound	USC
Rusty Jones	NDE Inspection Consultant, CMH-17 Rep	NIAR
Richard Klaassen	Ultrasound	GE Aviation
K. Elliott Cramer	Branch Head, Nondestructive Evaluation Sciences Branch (NESB)	NASA
Contributors		
Dr. Erik Frankfurter	NDE Simulations	NASA
Dr. William P. Winfree	Chief Engineer for Measurement Science X-ray CT NDE	NASA
Dr. Elizabeth Gregory	In-situ Thermography	NASA
Peter Juarez	In-situ Thermography	NASA
John Newman	Shearography	Laser Technology Inc
Joseph Zalameda	Thermography	NASA
Dr. Ramy Harik	Profilometry	USC
Christopher Sacco	Profilometry	USC
Dr. Cara Campbell-Leckey	Assistant Branch Head, NESB	NASA
Dr. Jim Troy	Motion Controller	Boeing
Bill Motzer	Laser Ultrasound	Boeing
Scott Lee	Automation	Boeing
Barry Fetzer	Robotics, Ultrasound	Boeing
Alan Stewart	LBID/Bond Strength	Boeing
Nathan Chapdelaine	MP&P Engineer BR&T, Digital Radiography Center (DRC)	Boeing
Danny Gill	Ultrasound	Northrop Grumman
Robert Anderson	Ultrasound	Northrop Grumman
Jacob Ketcham	Thermography	Northrop Grumman
Jeffrey P. Seebo	Ultrasound	Analytical Mechanics Associates (AMA), Inc
William Sommer	X-ray CT	Analytical Services & Materials (AS&M)
James Bly	Thermography	AS&M
John Magradey	X-ray CT, Ultrasound	NASA Internships, Fellowships & Scholarships (NIFS)
Sean Balduc	Thermography	NIFS

Michael Wrona	Ultrasound, Laser Vibrometry	NIFS
Desalegn Delelegn	Data Analytics, X-ray CT	NIFS
Dr. Steven Shepard	Thermography	Thermal Wave Imaging
Jake Thams	Thermography	Thermal Wave Imaging
Tasdiq Ahmed	Thermography	Thermal Wave Imaging
Dr. Reza Zoughi	Microwave NDE	Missouri S&T
Dr. Eric Madaras	Terahertz NDE	NASA
Dr. Patrick Johnston	Polar Backscatter UT	NASA
Joshua Brown	Robotics	AMA
Dr. Russell Wincheski	Eddy Current NDE	NASA
Nathan Smith	Penetrant Testing NDE	NASA
Sourav Banerjee	Ultrasound	USC
David G. Shutty	Database & Thermography	NASA
Darren Pifer	Database & IT	Science Systems and Applications Inc (SSAI)
Kelvin G. Boston	Composites fabrication	NASA
Assessment Support		
Amy Tarnowski	Project Coordinator/Technical Editor	AMA, Inc
Laura Bass	Technical Editor	AMA, Inc
Erin Moran	Technical Editor	AMA, Inc
Dee Bullock	Technical Editor	AMA, Inc

2.0   Introduction

Under the Advanced Composites Project (ACP), the National Aeronautics and Space Administration (NASA) has collaborated with members of the aerospace industry to reduce the timeline to develop and certify composite structures for commercial and military aeronautic vehicles[1]. NASA and industry have identified three focus areas, or technical challenges, as having major impact on the current certification timeline. One focus area, Technical Challenge #2 (TC2) – Rapid Inspection, addressed the need to increase the inspection throughput (i.e., number of parts or total area on a component inspected per unit time) by the development of more efficient quantitative and practical inspection methods, data management methods, models, and modeling tools. One of the objectives in TC2 was to develop tools for rapid quantitative characterization of defects. Traditional methods of nondestructive evaluation (NDE) used for isotropic materials, such as metals, are not always adequate for composite applications. This is a contributing factor to the cost and complexity of developing new structural composites. Additionally, the defects of interest in composite materials are significantly different from metals.

Therefore, under the ACP TC2, NASA initiated an assessment of the current state-of-practice (SoP) in the aerospace industry for the NDE of composite structural components. This assessment attempted to determine what factors most influence the NDE process for composites. This effort spanned the fixed-wing, rotary-wing, and propulsion segments of the aircraft industry and solicited input from a corresponding cross-section of the aviation industry. Critical defect types, current inspection methods, NDE data exchange methods, processes and methods suitable for automation or improvement, and other issues associated with the inspection and certification of composite

---

[1] Techport, "Advanced Composites Project, Advanced Air Vehicles Program, Aeronautics Research Mission Directorate (ARMD)," NASA Langley Research Center, Project Status Report, URL: https://techport.nasa.gov/view/13280, 2016, p. 9.

aerospace structures were identified. Based on the results of this assessment, NASA procured from the ACP industry partners a set of composite specimens (standards) that contain a range of controlled defects representing those typically found in aerospace composite structures. Defect types included those created in the manufacturing process, such as varying amounts of porosity, varying degrees of fiber waviness, and inserts representing delaminations. In addition to the composite specimens, the industry partners also provided details on the fabrication procedures and confirmed the target defects.

NASA then conducted a process of inter-laboratory, round-robin testing of these standards among the members of the NASA Advanced Composites Consortium (ACC)[2]. The ACC is a public-private partnership to advance knowledge about composite materials, reduce the certification timeline, and improve the performance of future aircraft. The NDE techniques used in the round-robin testing include, but are not limited to: ultrasound (UT), laser-based UT, thermography, and X-ray Computed Tomography (XCT). This NDE Methods and Capabilities Handbook documents the SoP review results, the manufacturing and validation of the NDE standards, and the results of the round-robin testing.

2.1   Scope

The intent of this NDE Methods and Capabilities Handbook is to create a publically available guidance document that can facilitate the selection of appropriate NDE techniques for specific types of composite aircraft structures. It provides recommended protocols to quickly establish inspection procedures for these methods for detecting and characterizing common flaw types in complex composite structures. It includes an NDE guidance matrix that provides an applicability rating for NDE techniques as they apply to given flaw types. This Handbook also contains details that lead to the applicability rating including, but not limited to; specimen details, inspection parameters, data analysis techniques, inspection efficiency (speed and cost), and limitations. Additionally, details of the implementation of an online database that will serve as a repository for, and provide industry and academia access to, the NDE data collected during the round-robin testing are included. The data and specimens utilized in the development of the handbook will be available through The National Institute for Aviation Research, Wichita State University, Wichita, Kansas.

This handbook also facilitates the understanding of the limitations of current state-of-the-art NDE methods for the inspection of common defect types in composite materials. It is not a comprehensive guide to NDE, nor is it a complete inspection manual for all types and geometries of composite structures. As such, it serves as a starting point for developing practical inspection methods and protocols that must be tailored to specific applications. While the NDE performance results discussed in this handbook include an array of state-of-the-art and emerging NDE techniques, new inspection techniques arise frequently. Further, the authors recognize that each NDE technique itself has a wide range of inspection parameters. Variations in these parameters can lead to results that vary widely from the results presented here, even on the same specimen. In addition, hardware variations and approaches to data analysis can impact the inspection results. Finally, the authors recognize that, in addition to conventional NDE techniques, the field of Structural Health Monitoring (SHM), sometimes referred to as in-situ NDE, is continuing to

---

[2] Austin, S., 2017, "Advanced Composite Consortium (ACC)," from http://www.nianet.org/advanced-composite-consortium-acc/

advance at a rapid pace. While closely related to NDE, this handbook does not include any SHM techniques.

The data contained in this Handbook are from the eighty-eight NDE standards fabricated by ACC industry partners using one of three material systems. Forty-six of the standards used an IM7/8552 or IM7/8552-1 material system with the fibers being either uni-directional, braided, woven, or slit-tape. Ten standards used BMS 8-276 material system and eight used T-800SC Triaxial Braid [0/+60/-60] with 3M AMD-825. The geometries produced include twenty-one flat panels, 10 S-curved panels, nine wedges, eight radius corner standards, eight rotorcraft blade-spar tubes, four step, and four flange standards. While this is a reasonable cross-section of materials found in the aerospace industry today, it is by no means comprehensive of all the material systems currently in use. The authors recognize that the performance of any particular NDE technique is material system specific; therefore, the results presented in this handbook may not be directly applicable to other composite materials.

Finally, the standards used to create this handbook have only a limited range of real and simulated defect types. The specimens include twenty-two with various types of simulated delaminations, twenty with varying amounts of porosity, nine with automated fiber placement (AFP) tow defects, seven with fiber wrinkling, two with microcracking, and two with bond integrity or weak bond defects. There are also multiple ways of creating any of these defect types in an NDE standard. For example, delamination/disbond NDE standards can be fabricated using a number of different well-known methods[3,4]. For this handbook, a majority of the delamination specimens were fabricated by hand layup, with Polytetrafluoroethylene (PTFE or Teflon™) inserts added at various locations throughout the thickness to represent delamination damage. Most of the circular co-cured inserts are 0.25-inch-diameter (0.635 cm) PTFE film. A few inserts are 0.1- to 1-inch-diameter (0.254 cm to 2.54 cm) PTFE film. In some geometries, the manufacturer used rectangular and square PTFE strips in place of circular film. In addition, a number of specimens had 0.25-inch-diameter (0.635 cm) flat-bottom holes (FBHs) added after cure. To simulate internal disbonds more accurately, some of the FBHs were subsequently back-filled with cured epoxy. Standards made using different techniques to represent delamination damage will produce results that differ from those discussed in this handbook requires noting.

2.1.1 Relationship to Technical Standards Documents

A technical standard is an established norm or requirement regarding a technical system. Usually, such a document establishes uniform engineering or technical criteria, methods, processes and practices. For NDE in general and the NDE of composites in particular, a number of technical standards exist. In the United States, a number of professional and industrial organizations, as well as federal government agencies, lead the development and maintenance of technical standards in the field of NDE. These include:
- The American Society for Testing and Materials (ASTM) International
- The Society of Automotive Engineers (SAE)
- The American Iron and Steel Institution (AISI)

---

[3] DiMondi, V., 1980, Interlaminar Flaw Propagation Mode II (No. CCM-80-18), DELAWARE UNIV NEWARK CENTER FOR COMPOSITE MATERIALS.
[4] Waddell, M.C., 2013, Comparison of Artificial Delamination Methods for use with Nondestructive Testing, Summary Report 2013, UNSW@ADFA.

- The American Welding Society (AWS)
- The American Society of Mechanical Engineers (ASME) International

A few examples of technical standards related to NDE in general and NDE of composite materials are:
- ASTM E1495, Standard Guide for Acousto-Ultrasonic Assessment of Composites, Laminates, and Bonded Joints.
- E2191, Standard Test Method for Examination of Gas-Filled Filament-Wound Composite Pressure Vessels Using Acoustic Emission
- SAE ARP5606, Solid Composite Laminate nondestructive inspection (NDI) Reference Standards
- SAE ARP5606, Composite Honeycomb NDI Reference Standards
- National Aerospace Standard (NAS) 410, Certification & Qualification of Nondestructive Test Personnel
- NAS 999, Nondestructive Inspection of Advanced Composite Structure

The website for the Nondestructive Testing (NDT) Resource Center, a National Science Foundation-funded NDT education organization, contains an extensive list of these technical standards and a discussion of their purpose, history, advantages, and disadvantages[5]. It is not the intention of the authors that this document become a technical standard. This handbook has not been written with the rigor of a technical standard, but rather it is a guide for understanding the application, as well as limitations, of current state-of-the-art NDE methods for the inspection of certain defects in composite materials. It is intended to be used as an aid in the development of practical inspection methods and protocols for these types of defects in similar types of composite materials and structures.

2.2 State of The Practice Assessment

The goal of the SoP survey was to assess the current practice for NDE/NDT of composite structures, drawing from as large a cross-section of aerospace and other composites industries as practical. The survey sought to identify critical defect types, inspection methods, and NDE data-exchange methods. It also attempted to determine processes and methods suitable for automation or improvement of composite NDE inspections, as well as other issues associated with the inspection and certification of composite aerospace structures. The results represent the responses from relevant points of contact involved in composite design, testing, fabrication, inspection, NDT equipment sales, NDT research and development (R&D), and NDT management. One hundred fifty-three individuals, representing about one-tenth of those invited to participate, took the survey. Nearly half (46%) currently work in the aerospace industry with the remainder working in other related industries that utilize composites such as the automotive industry.

The SoP survey revealed that the most widely used composite structure type of interest is the solid graphite epoxy laminate structure, followed by sandwich structure, particularly comprised of honeycomb core. Figure 2.2-1 shows a pie graph of the answer to the SoP survey question: "With which type of composite structure do you primarily work?" The type of NDT methods that are

---

[5] https://www.nde-ed.org/GeneralResources/Standards/standards.htm, accessed 9/13/17.

most common (when both fabrication and in-service inspection are combined) are Visual and Tap Testing, followed by Through-Transmission Ultrasound (TTUT), Pulse Echo Ultrasound (PEUT), X-ray methods (Digital, Computed Tomography (CT), and Film—in that order), Infrared Thermography (IRT), and Low-Frequency UT/Bond Testing. The relative use of the methods by the SoP survey respondents is shown in Figure 2.2-2.
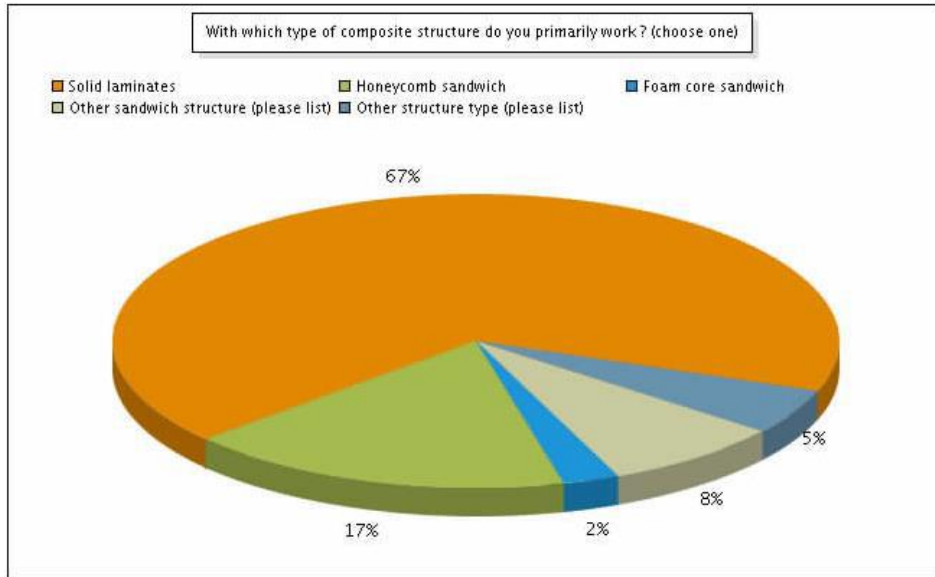
Figure 2.2-1. Pie Graph of respondents by composite structure, indicating the type with which they primarily work.
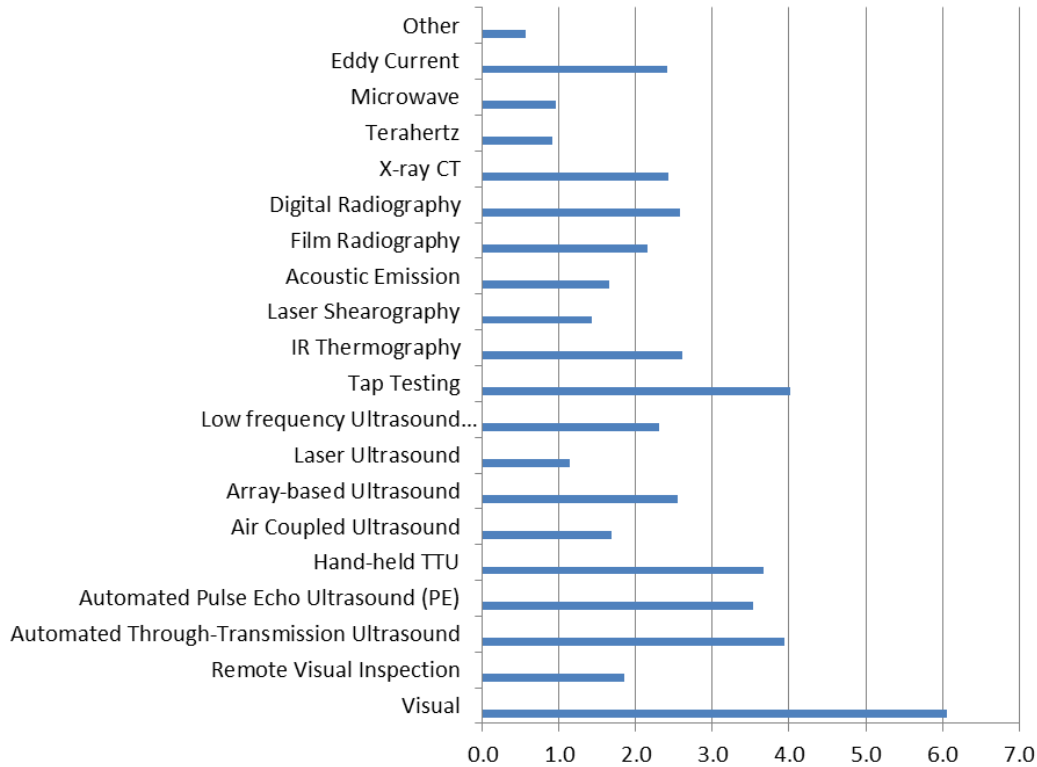
Figure 2.2-2. Combined response (fabrication and in-service NDE) to the question "What inspection techniques are currently used?" Zero indicates least used and 7 indicates most used.

Table 2.2-1 summarizes the top SoP survey answers to question topics (listed in column headers) about composite defects. The most common composite defects addressed by industry survey respondents are delaminations, disbonds, and weak bonds (bond integrity/strength). These three defects are also of most concern, and according to survey respondents receive the largest amount of research in the industry. The type of defects viewed as most challenging to address are microcracking, bond integrity/strength, and moisture ingress. It is important to note when separated as a group, fabricators listed porosity, foreign material, and fiber waviness, along with delaminations/disbonds, at the top of their list of defects they encounter.

Most respondents (64%) agreed that they deal with flaws that need better physical reference standards. Therefore, based on the results from the survey, ACP chose to fabricate NDE standards to represent the top four defects listed in Table 2.2-1 under the column "Better Standards Needed." For simplicity of fabrication, and because this was the primary composite material of interest in the SoP survey, the team chose to make NDE standards only from solid laminate composite material. Additionally, some variations in part geometry were also included in the standards fabricated. It was also decided not to fabricate bond integrity/strength standards at this time, due in part to the additional difficulty of creating reference standards for this defect type—although these standards may be included in the future. In addition to the defect types identified by the SoP survey, we fabricated several standards that contained defects commonly occurring during the manufacture of composites using AFP equipment, such as ply laps, gaps and twisted or folded tows.

7

Table 2.2-1. Summary of top SoP survey answers to a series of questions about composite defects, with 1 being highest priority and 5 being lowest priority.

Question Topic / Rank	Most Challenging Defect	Frequency of Defect	Better Standards Needed	Defects of Concern	Effect to Structure
1	Microcracking	Delaminations	Porosity	Disbonds	Disbonds
2	Bond Integrity/ Strength	Disbonds	Disbonds	Delaminations	Delaminations
3	Moisture Ingress	Bond Integrity/ Strength	Wrinkles/Fiber Waviness	Foreign Material	Bond Integrity/ Strength
4	Heat Damage	Porosity of Laminates	Delaminations	Microcracking	Wrinkles/Fiber Waviness
5	Wrinkles/Fiber Waviness	Moisture Ingress	Bond Integrity/ Strength	Bond Integrity/ Strength	Porosity

3.0   NDE Guidance Matrix

This section presents a quick reference table (Table 3.0-1) for all methods tested on all defect types. It delineates the overall performance of the method, the detectability of the specific defect type, and compares the inspection time, cost, advantages, and disadvantages for NDE techniques as they apply to given flaw types. Details are available in subsequent sections. Blank columns in the table mean that the method was not tested for that defect type.

Table 3.0-1. Methods tested on all defect types.

		Porosity	Delaminations	FOD/Inclusions	Fiber Defects	Impact Damage
Ultrasound						
Pulse-echo	Overall Performance	Effective	Effective	Effective	Effective	Effective
	Detection	Quantitative with size and depth information	Strong signals from surface-parallel delaminations	Effective for most types of common FOD	shown to detect twists, folds, missing tows, fiber wrinkles	Quantitative with size and depth information
	Inspection time	Manual scanning can be prohibitively time consuming, Improved with robotic scanning systems 6"x6" at 1/100" resolution immersion scanning ~10 min 8'x9' 1/10" resolution captured water column scanning system ~1 hour				
	Equipment cost	Affordable; Automated systems and software for C-scan, B-scan imaging can be expensive Immersion scan setup from $50k (pieced) to $250k(commercially available full system)				
	Advantages	Portable, safe, mature				
	Disadvantages	Requires contact and surface coupling fluid, complex contours require significant effort				
Through Transmission	Overall Performance	Effective	Marginally effective	Marginally effective	Marginally effective	Marginally effective
	Detection	Quantitative with size and depth information	can find location and size of a delamination, but not the depth	can find location and size of a FOD, but not the depth	can find location and size of a fiber defects, but not the depth	can find location and size of impact damage, but not the depth
	Inspection time	Manual scanning can be prohibitively time consuming, Improved with automated scanning systems				
	Equipment cost	Affordable; Automated systems and software for C-scan, B-scan imaging can be expensive				
	Advantages	Portable, safe, mature				
	Disadvantages	Requires contact and surface coupling fluid, complex contours require significant effort				
Guided Wave /Laser Vibrometry	Overall Performance	Ineffective			Marginally effective	
	Detection	Cannot detect bulk porosity			Shown to detect fiber wrinkles	
	Inspection time	Moderate LDV 5"x5" region with moderate resolution 6-7 hours SLDV 5"x5" region with moderate resolution 3-4 hours				

		Porosity	Delaminations	FOD/Inclusions	Fiber Defects	Impact Damage
	Equipment cost	Moderate LDV $35k-$40k; SLDV ~$55k-$60k				
	Advantages	large area, sensitive to small defects; waves propagate long distances without much energy loss				
	Disadvantages	primarily a laboratory technique				
Thermography						
Single-Sided Flash	Overall Performance	Marginally Effective	Effective	Effective	Effective	Effective
	Detection:	Can detect concentrations of porosity	Easily detects subsurface delaminations	Detects many common types of FOD	shown to detect AFP fiber defects, wrinkles	Detects subsurface BVID impact damage in composites
	Inspection time:	Fast 1'x1' flash system 1-2 seconds depending on target depth of defect; Robotically scanning large acreage regions (fuselage sections) 2x as fast as manual scanning				
	Equipment cost:	Moderate $10k for microbolometer camera setup up to $250k for commercially available system with research grade infrared camera				
	Advantages:	Fast, large area inspection; non-contact;				
	Disadvantages:	Thickness limitations (defects generally > 2x as wide as depth for detectability); More difficult to interpret than TT thermography for porosity detection		FOD not detectable if material is of similar thermal diffusivity as composite unless the FOD causes a disbond	Difficult to detect twisted tow fiber defects due to resolution	deeper damage masked by damage closer to surface
Through-Transmission Flash	Overall Performance	Effective	Marginally Effective	Marginally Effective	Marginally Effective	Marginally Effective
	Detection:	Quantitative for variations in bulk porosity by calculating diffusivity	TT thermography not normally performed for detection of these types of defects. For deeper defects when access to both sides of part accessible, single-sided thermography usually performed on both sides for best results			
	Inspection time:	Fast				

		Porosity	Delaminations	FOD/Inclusions	Fiber Defects	Impact Damage
	Equipment cost:	Moderate				
	Advantages:	Fast, large area inspection; non-contact				
	Disadvantages:	Requires access to both sides of part				
Radiography						
Computed Radiography	Overall Performance	Marginally Effective	Ineffective	Marginally Effective	No Standards Tested	Ineffective
	Detection:	porosity can be detected by CR from multiple directions	Sensitive to orientation	Detects many common types of FOD		
	Inspection time:	Faster than X-ray film				
	Equipment cost:	Moderate				
	Advantages:	suitable for complex parts				
	Disadvantages:	Two dimensional (2D) image, sensitive to defect orientation, radiation safety concerns		FOD not detectable if material is of similar density as composite unless the FOD causes a disbond		
Digital Radiography	Overall Performance	Marginally Effective	Ineffective	Marginally Effective	No Standards Tested	Ineffective
	Detection:	Sensitive to density variations caused by voids; porosity can be detected by DR from multiple directions	Sensitive to orientation	Detects some common types of FOD		
	Inspection time:	Moderate				
	Equipment cost:	Moderate				
	Advantages:	suitable for complex parts				

		Porosity	**Delaminations**	**FOD/Inclusions**	**Fiber Defects**	**Impact Damage**
	Disadvantages:	2D image, sensitive to defect orientation, radiation safety concerns		FOD not detectable if material is of similar density as composite unless the FOD causes a disbond		
Backscatter X-ray	Overall Performance	Marginally Effective	Marginally Effective	Marginally Effective	No Standards tested	Ineffective
	Detection:	Sensitive to density variations that can be correlated to porosity	Sensitive to material density changes that can indicate delaminations	Detects some common types of FOD		
	Inspection time:	Real-time or near real-time				
	Equipment cost:	High				
	Advantages:	can be portable with adequate safety precautions; relatively insensitive to changes in part contours, angles, and thickness, non-contact, single-sided				
	Disadvantages:	radiation safety, no defect depth information, high initial equipment cost				
Computed Tomography	Overall Performance	Effective	Effective	Effective	Effective	Effective
	Detection:	Direct measurement of individual pores possible	Excellent quantitative information of delamination size and depth			
	Inspection time:	High 8 hours for a single scan 1"x1" for high resolution				
	Equipment cost:	High ~ $1 million				
	Advantages:	non-contact; high resolution; Full volume density map with cross-sectional image slices and depth; information, quantifiable, used as 'ground truth' for validation of other NDE techniques; images generally easy to interpret				

		Porosity	Delaminations	FOD/Inclusions	Fiber Defects	Impact Damage
	Disadvantages:	Radiation shielding/safety; typically not portable, requires access to all sides of part; requires large data storage capability; resolution dependent on part size				
Shearography						
	Overall Performance	Ineffective	Marginally Effective	Effective	Marginally Effective	Marginally Effective
	Detection:	Typically cannot directly detect porosity	Sensitive to delaminations sufficiently large to cause surface deformations under load	Shown to detect most common types of FOD	Shown to detect fiber defects large enough to cause surface deformations under load	Sensitive to impact damage sufficiently large to cause surface deformations under load
	Inspection time:	Fast/large area				
	Equipment cost:	Moderate				
	Advantages:	non-contact; single-sided				
	Disadvantages:	subsurface defects must be sufficiently large to cause surface deformations; direct line of sight needed, depth quantification difficult without a priori knowledge; laser safety; can be destructive if applied load too large				
Visual						
	Overall Performance	Marginally Effective		Ineffective	Ineffective	Marginally Effective
	Detection:	Qualitative, Surface only		No surface indication of most FOD		Only if BVID has some surface indentation
	Inspection time:	Fast				
	Equipment cost:	Low				
	Advantages:	non-contact, can be performed without instrumentation or with inexpensive equipment such as cameras, borescopes, and magnifiers; can find imperfections inside radii and complex curvatures				
	Disadvantages:	limited to surface inspections; insensitive to bulk porosity, inspector dependent				
Tap Testing						
	Overall Performance	Ineffective	Marginally effective	Ineffective	Ineffective	Ineffective

		Porosity	Delaminations	FOD/Inclusions	Fiber Defects	Impact Damage
	Detection:	Not detected	Can detect delaminations with skilled technician	Not detected		
	Inspection time:	Fast				
	Equipment cost:	Low				
	Advantages:	Speed, cost, equipment				
	Disadvantages:	no permanent record; qualitative, no depth information, inspector dependent				

4.0   Inspection Guidance by Flaw Type

As discussed in the Section 2.0 Introduction, this Handbook is limited in scope to manufacturing defects in carbon fiber reinforced polymer (CFRP) composites. The Handbook is intended to assist NDE inspectors with experience examining metals to transition to inspecting the more complex composite structures and to provide specific guidance on inspection parameters in the growing use of composites in industry. The intent is to give an unbiased assessment of several NDE technologies for different inspection needs. It is not intended to recommend any particular technology for a particular inspection requirement. Guidance on inspection of typical composite defect types is discussed in this section.

Effective, marginally effective, and ineffective inspection technologies for each defect type are reviewed in detail, with advantages and disadvantages for each inspection technique tabulated for easy reference. An emphasis is placed on common, widely applied NDE techniques. This section begins with working definitions of each of the defect types examined, followed by inspection guidance for each flaw type.

4.1   Descriptions and Characteristics of Defect Types

4.1.1   Porosity Defect Description

Porosity is an accumulation of small-disconnected voids, (e.g., gas, or air bubbles) in a composite layer, volume, or bondline. Porosity in a composite can have a detrimental effect on the strength and mechanical properties of the structure and can substantially degrade the interlaminar shear strength, compressive strength, and the transverse flexural strength of laminated composites[1]. Consequently, it is important to provide inspection method guidance for the detection and quantification of porosity.

Porosity is a manufacturing defect, which occurs during the cure process. An amorphous distribution of vapor and voids can occur in the matrix due to a variety of causes, including internal vapor pressure from contaminants like water, inadequate external pressure being applied (e.g., a broken bag), or residual stress pulling layers apart locally.

Porosity comes in a range of configurations. On one end of the spectrum is bulk porosity, which is characterized by voids distributed through many adjacent plies, where the voids are nearly spherical in shape. At the other end of the spectrum is a single, large planar void, which might be better described as a delamination. Between those two extremes is a range of void shapes and distributions, which can be loosely described as laminar porosity. Laminar porosity can be comprised of voids of various sizes in a single ply layer, or through a variety of plies; they can be circular and small, or elongated and large.

Examples of porosity in composite laminates are given in Figure 4.1-1 and Figure 4.1-2. Specifically, Figure 4.1-1 shows three distinct void types that are present in a sample with high porosity.

15
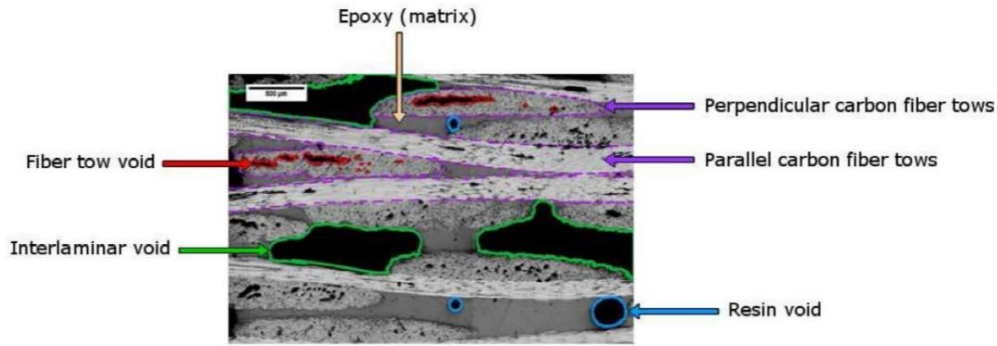
Figure 4.1-1. Cross-section of an un-debulked and uncured MTM 45-1 5HS prepreg laminate showing different types of voids[3] Error! Reference source not found..

| *a) Laminate with localized porosity[4].* | *b) Typical cross-section of a (0/90)₁₆ composite with void volume fraction of 7.06%[5]* |
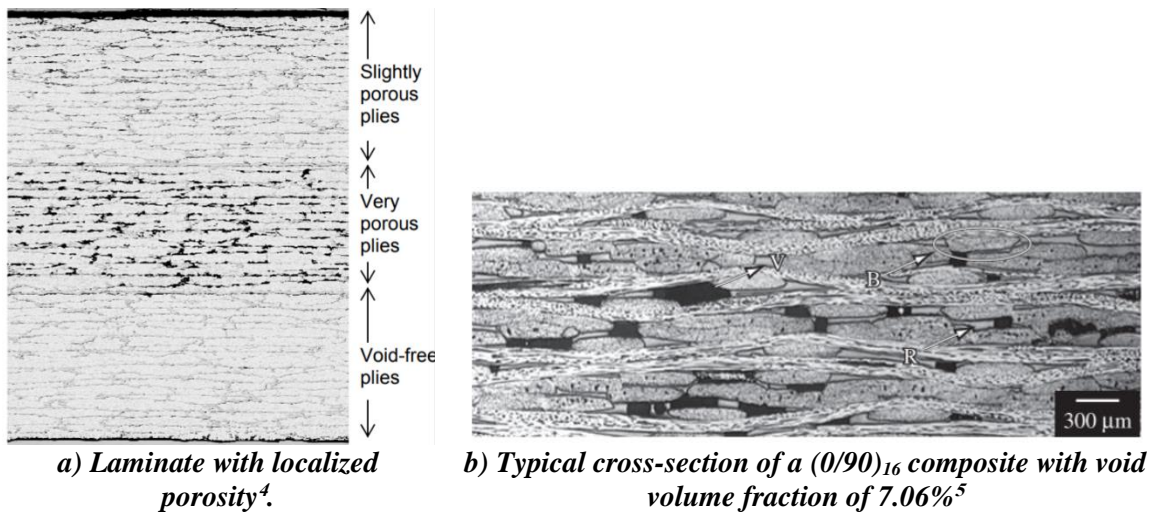
Figure 4.1-2. Pictures of porosity defects.

The severity of porosity is generally graded as a percent of volume affected. For example, a sample deemed to have no porosity might be measured as having void content in the range of 0% to 1% of the sample's volume. Severe porosity might be measured at a level of 10% of the volume fraction.

Porosity limits are commonly included in drawing acceptance criteria for composite components. Porosity is different from most other defect conditions because it does not exhibit a crisp boundary; it typically presents itself as a bulk property (a uniform condition throughout the entire volume of a component), or as a gradient in the bulk property. The nature of the void characteristics determines whether its behavior trends more toward that of a delamination (severe laminar porosity) or bulk porosity (small spherical voids randomly distributed through the component's thickness).

The standards developed for the ACP include 21 specimens containing porosity. These include porosity at radii, in flat or step panels, in wedges, and in flat woven CFRP composites. Effort was made to create specimens with 'small,' 'medium,' and 'large' amounts of porosity as a percent of volume.

4.1.2 Delaminations Defect Description

Delaminations are the separation between plies in a laminate. Common causes in manufacturing are impacts, propagation from foreign material such as tape, and improper machining such as dull cutting tools. They can often accompany, or result from other defects such as, impact damage or wrinkles. Delaminations may have substantial air pockets/gaps between the plies (Figure 4.1-3), or they may be in direct contact with little to no air gap between them. While delaminations can often form in-service as the result of fatigue, impacts, and other stresses, this section will focus on delaminations created as the result of manufacturing conditions and processes.
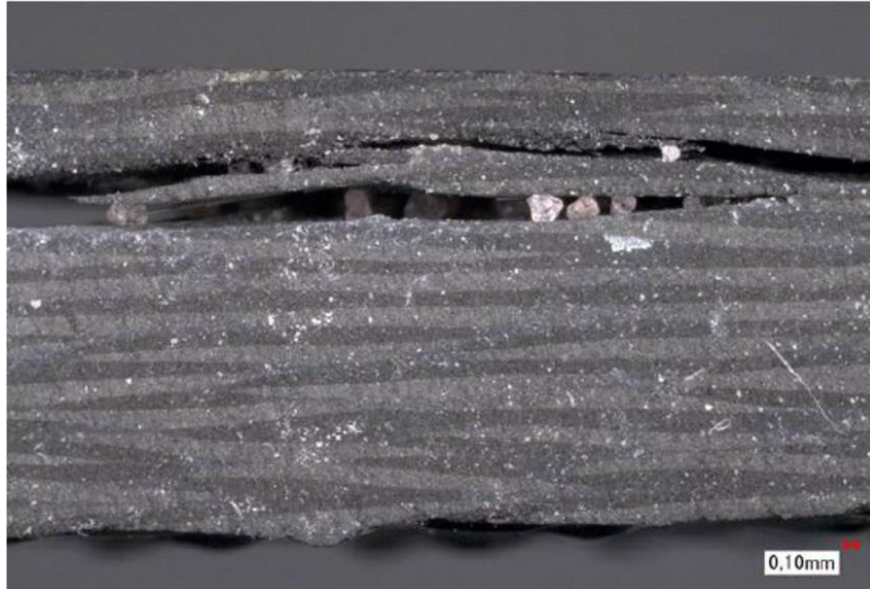
Figure 4.1-3. Delamination from imbedded abrasive cutting particles in CFRP [ref. 1].

The standards developed for the ACP program include 27 specimens containing delaminations. These include delaminations at radii, in flat or step panels, in wedges, flat woven CFRP composites and in woven flanges.

4.1.3 Foreign Object Debris (FOD) and Inclusions Defect Description

During manufacturing, it is possible that loose peel ply, bagging materials, metal, etc. may embed themselves between laminae causing localized weaknesses, effective disbonds in the material, crack initiation locations, and regions of high stress. Some possible FOD materials are shown in Figure 4.1-4, including various vacuum bagging films, adhesive tapes, backing materials, fiber materials, lint, broken cutting blades, metal shavings, etc. Additionally, stray pieces of loose carbon prepreg material can adhere to the bottom of a ply during layup and easily go unnoticed to become entrapped in the laminate stack causing a localized thickness variation, which can skew subsequent plies.
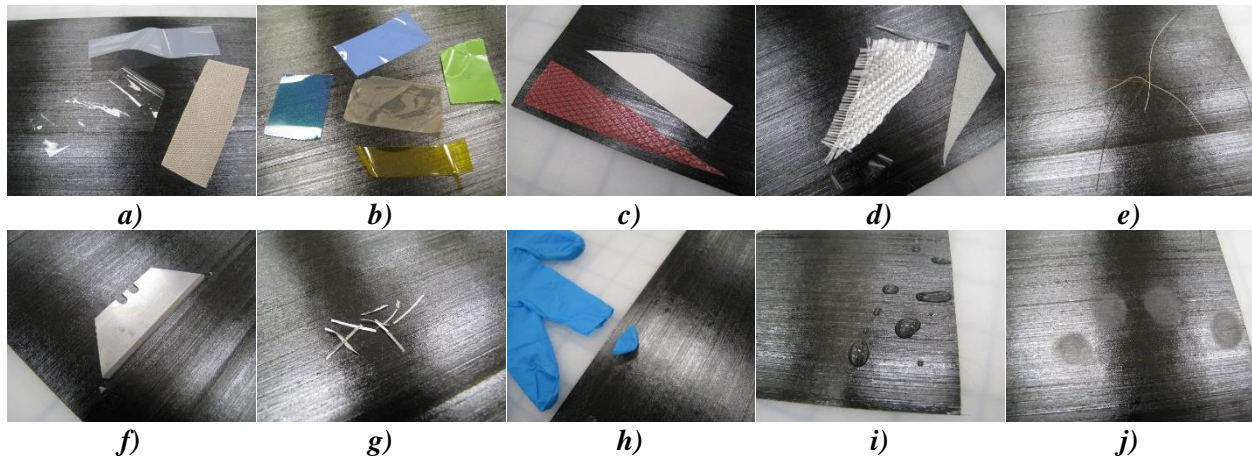
Figure 4.1-4. Some possible FOD materials.
a) Various Vacuum Bagging Films: 0.001-inch clear fluorinated ethylene propylene (FEP) release film, .002-inch Blue release film, and .0025-inch Teflon release peel-ply. b) Various types of adhesive tapes: D. Blue, Lt. Blue, and Green Flashbreaker tapes; Brown Teflon tape, and Yellow Kapton tape. c) Manufacturer's paper and plastic protective backing materials. d) Dry fiberglass and pre-impregnated fiberglass materials causing cross-contamination when carbon and fiberglass layups are pre-formed on the same uncleaned surfaces.
e) Hair, clothes lint, etc. f) Broken pieces of cutting blade can be left in prepreg laminate. g) Tiny metal shavings can enter laminate from misuse and/or poorly prepared caul plates or tooling. h) Torn finger-tip of personal protective equipment (PPE) glove usually due to overuse of gloves. i) Humidity, moisture, release agents, solvents, etc. normally not allowed in the layup area, j) Fingerprint oils contamination due to lack of PPE use.

The NDE standards developed under this project included one flat FOD panel shown in Figure 4.1-5. The material is IM7/8552-1 carbon fiber/epoxy 0.25-inch slit tape. It varies from 8 to 48 plies, with Grafoil inserts placed at the mid-ply for the varying thicknesses. See Appendix D for more information.
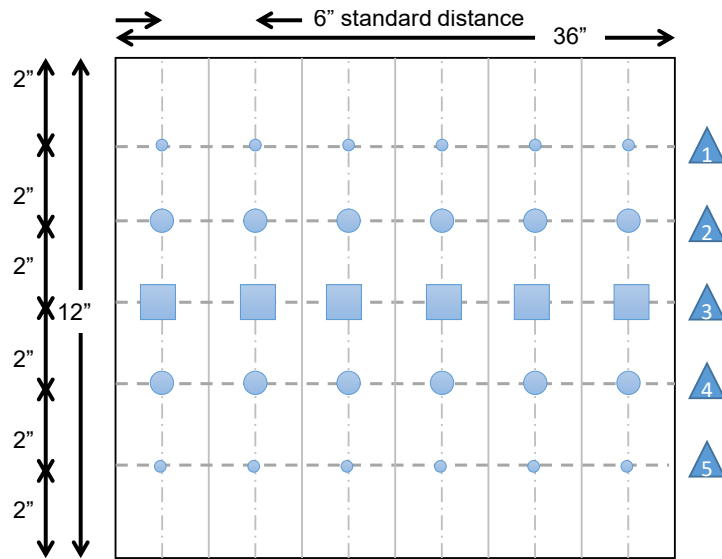
Figure 4.1-5. NDE Standard with Graphoil inserts located at the midply for varying thicknesses (top); defect map within panel (bottom).

Additionally, the ACP developed 10 S-curve panels made of BMS8-276 carbon fabric plies ranging from 8 to 48 plies thick. Shown in an example in Figure 4.1-6, these panels were manufactured containing inserts of brass foil, release ply, and pressure-sensitive tape. For more information, please see Appendix D.

Figure 4.1-6. S-curve panels with various inserts.
Release Film, Bagging Film, Prepreg Cutting Blade, Prepreg Protective Film-BD, Brass sheet,
Tooltech Tape, Flash BreakerPrepreg Protective Film-UD.

4.1.3.1   References

1. Poudel, Anish; Shrestha, Shashi Shekhar; Sandhu, Jaswinder Singh; Chu, Tsuchin Philip; and Pergantis, Charles George: "Comparison and analysis of Acoustography with other NDE techniques for foreign object inclusion detection in graphite epoxy composites," *Composites Part B: Engineering* Volume 78, 1 September 2015, Pages 86-94.
2. Nestleroth, J. B.; Rose, J. L.; Bashyam, M.; and Subramanian, K.: "Physically Based Ultrasonic Feature Mapping for Anomaly Classification in Composite Materials," *Materials Evaluation*, Vol 43, April 1985.
3. Bates, D.; Smith, G.; Lu, D.; and Hewitt, J.: "Rapid thermal non-destructive testing of aircraft components," *Composites Part B: Engineering* Volume 31, Issue 3, April 2000, Pages 175-185.
4. Toscano, C.; Meola, C.; Iorio, M. C.; and Carlomagno, G. M.: "Porosity and Inclusion Detection in CFRP by Infrared Thermography," *Advances in Optical Technologies*, Volume 2012, Article ID 765953, 6 pages.
5. Garnier, Christian; Pastor, Marie Laetitia; Eyma, Florent; and Lorrain, Bernard: "The detection of aeronautical defects insitu on composite structures using Non Destructive Testing," *Composite Structures*, Volume 93, Issue 5, April 2011, Pages 1328-1336.

4.1.4   Fiber Defects Defect Description

Fiber defects can occur during AFP process or during hand layup of composite parts. As it is the fiber that predominantly carries the load in a composite part, inspecting for fiber defects is critical. AFP defects include fiber (or tape) twists, folds, overlaps of tape courses, gaps between tape courses, wrinkles, and bridging defects (see Figure 4.1-7). Eleven defect standards typical of AFP defects were created for the ACP. Fiber defects found in sheet layups include in or out of plane fiber waviness, wrinkles, and snags. Nine of these standards were created for the ACP.
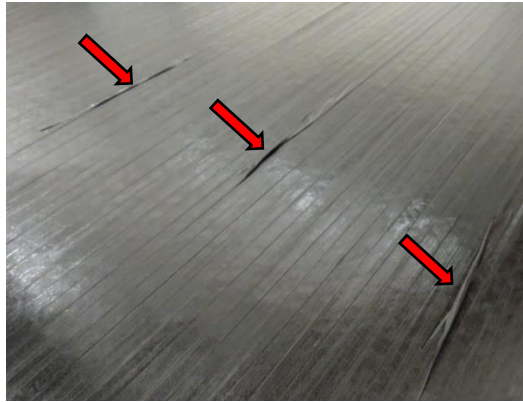
a) Twisted tows.
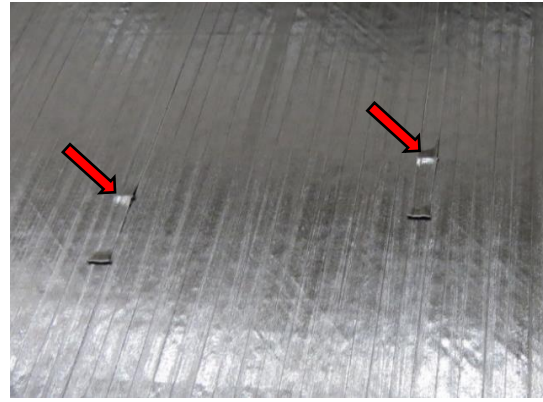
b) Folded tows.
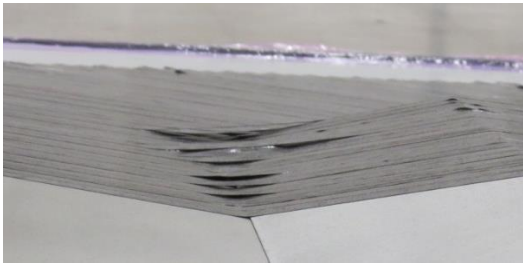
c) Bridging Defects.
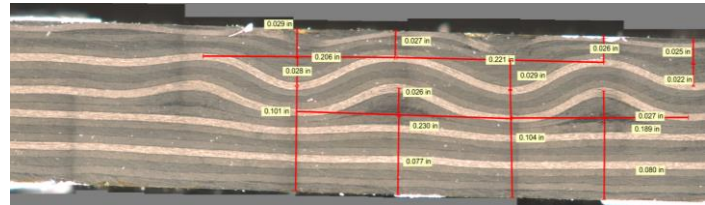
d) Wrinkles.

Figure 4.1-7. Example fiber defects standards.

AFP is an automated method of composite fabrication that drastically reduces the variability of part quality compared to hand layup. The use of robots to place the pre-preg material limits some types of flaws, but can result in other flaws such as tow overlaps and gaps, tow twists or peel-up, and FOD. Fiber wrinkling is often the result of geometry changes such as material conformed to bends and radii, flanges, or ply drop-offs. Detection of AFP defects during the layup process is discussed in detail in Section 5.6.3.

4.1.4.1   References

1. Piascik, Robert S.: *Phase III - MPCV LAS ACM C/C-SiC Parts Performance-Testing Approach for Certification*, NESC-RP-13-00914, 9/2016.
2. Howell, Patricia A.; and Winfree, William P.: *C/C-SiC Pintle and Pintle Guide, NESC Phase III X-ray CT Inspection Analysis Report High Thrust (HT)-9 / ATP / HT-10 Results*, NESC-RP-13-00914, Appendix A, 178 pages, 9/2016.
3. Abdi1, F.; Gurdal, Z.; Huang, D.; and Housner, J. M.: "Certification Modeling Of Composites Fuselage, Considering Effect of Defects From Fiber Placement Manufacturing Processes," *AIAA SciTech 2017, 55th AIAA Aerospace Sciences Meeting*, 9−13 January 2017, Grapevine, Texas.
4. Smith, Robert A.; Mukhopadhyay, Supratik; Lawrie, Andrew; and Hallett, Stephen R.: "Applications of ultrasonic NDT to aerospace composites," *5th International Symposium on NDT in Aerospace*, 13−15th November 2013, Singapore.
5. Xie, Ningbo; Smith, Robert A.; Mukhopadhyay, Supratik; and Hallett, Stephen R.: "Modelling the Mechanical Properties of Wrinkled composites from NDT Data," *20th International Conference on Composite Materials*, Copenhagen, 19−24th July 2015.

6. Nelson, Luke J; and Smith, Robert A.: "Three-dimensional fiber-orientation characterization in monolithic carbon-fiber composites," *11th European Conference on Non-Destructive Testing* (ECNDT 2014), October 6–10, 2014, Prague, Czech Republic.
7. Adams, R. D.; and Cawley, P.: "A review of defect types and nondestructive testing techniques for composites and bonded joints," *NDT International*, Volume 21, Issue 4, August 1988, Pages 208-222.
8. Potter, K. D.: "Understanding the Origins of Defects and Variability in Composites Manufacture," *17th International Conference on Composite Materials*, Edinburgh, UK, 27–31 July 2009.

4.1.5 Impact Damage Defect Description

Impact damage in composites results in a complex layered combination of delaminations, fiber/tow breakage, and matrix cracking. XCT slices in three orthogonal directions showing typical impact damage in a CFRP composite laminate is shown in Figure 4.1-8
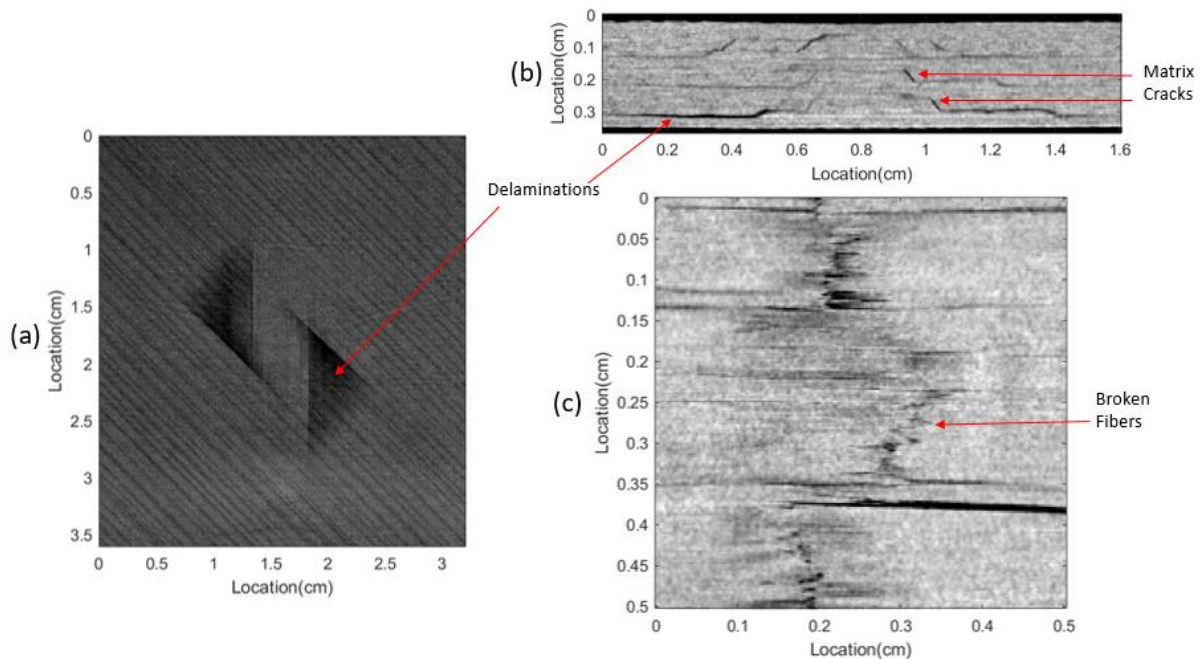
***Figure 4.1-8. XCT slices of typical impact damage in the three orthogonal directions.
a) Normal to the ply at the interface between plies. b) Cross-section through the depth. The impact
occurred at the top edge of the specimen. c) Cross-section through the width.***

For impact damage sites created by point loads (e.g., tool drop impingement), the diameter of the damage typically increases at subsequent laminates within the material, away from the initial impact point at its surface (Figure 4.1-9). Impacts create a characteristic rotating 'butterfly' pattern through the thickness of the composite. The rotation of the characteristic damage is a result of the ply direction in the layup as shown in Figure 4.1-10.

22
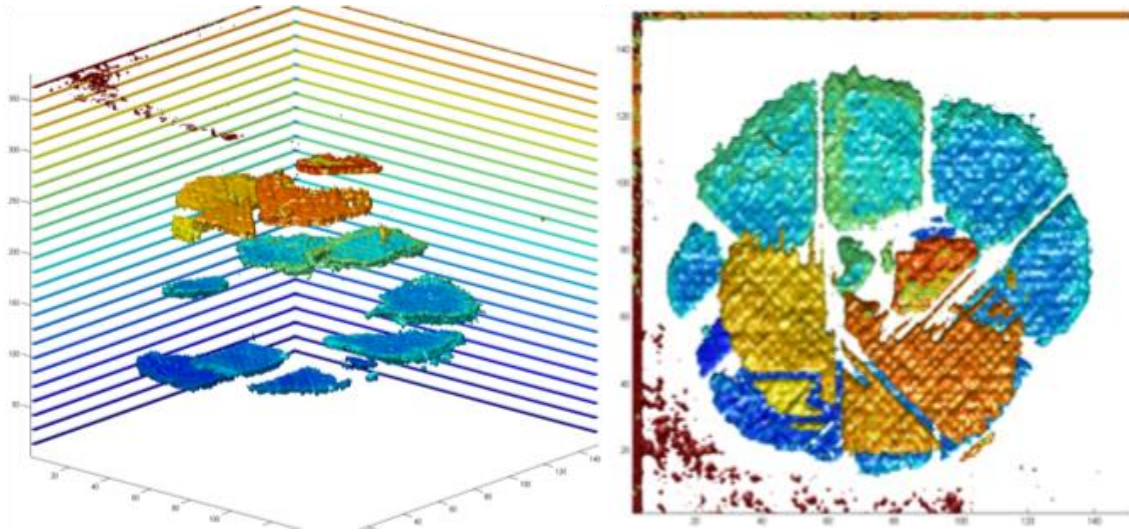
Figure 4.1-9. Ultrasonic three-dimensional (3D) representation (left) of impact damage in composites, showing the multi-layered damage of increasing diameter (right) throughout the thickness of the material.[1]
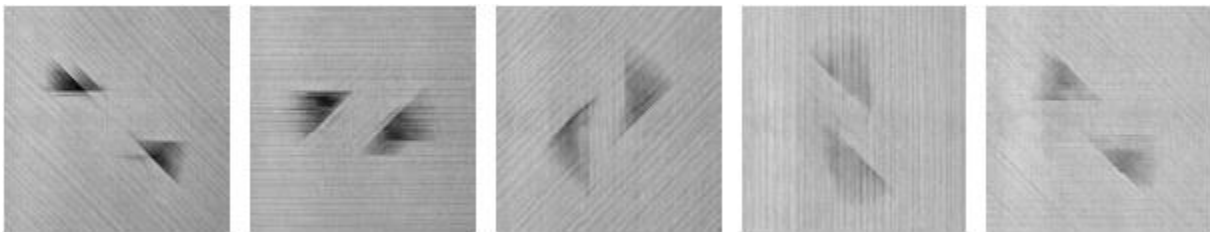
Figure 4.1-10. XCT slices in the plane of subsequent plies showing the characteristic 'butterfly' pattern of damage.

For this Handbook, where the scope is limited to the detection of manufacturing defects in solid laminate carbon fiber composites, the most common impact damage scenario involves tool drops, inadvertent contact with machinery or building structure, or damage from handling. In these cases, Barely Visible Impact Damage (BVID) is often the result. Unlike metals, BVID in composites can result in significant subsurface damage with little surface indentation. The set of NDE standards created for the round-robin testing in this handbook included 17 impacted specimens ranging in size from 3 × 5 inches to 22 × 22 inches and ranging in thickness from 8 plies to 32 plies. All of the impacts are classified as BVID and resulted in subsurface damage.

4.1.5.1   References

1. Juarez, Peter D. and Leckey, Cara A.C., "Multi-frequency local wavenumber analysis and ply correlation of delamination damage," *Ultrasonics*, Vol 62, p 56-65, 2015.
2. Howell, P. A.; Winfree, W. P.; and Cramer, K. E.: "On-orbit Passive Thermography," *Nondestructive Testing and Evaluation*, Vol. 23-3, 195-210 (2008).
3. de Albuquerque, V. H. C.; Tavares, J. M. R.; and Durão, L. M.: "Evaluation of delamination damages on composite plates using techniques of image processing and analysis and a backpropagation artificial neural network," in Eng Opt *2008-International Conference on Engineering Optimization*, 2008.

4. Sammons, D.; Chen, L.; and Milletich, R.: *Summary of results from application of CNN to NASA image data*, white paper, NASA Langley Research Center, Office of the Chief Information Officer, Hampton, Virginia, October 2016.

5. Delelegn, D. T.: *Non-Destructive Evaluation For Composite Material*, Master's thesis, Old Dominion University, 2018.

6. Garnier, Christian; Pastor, Marie Laetitia; Eyma, Florent; Lorrain, Bernard: "The detection of aeronautical defects insitu on composite structures using Non Destructive Testing," *Composite Structures*, Volume 93, Issue 5, April 2011, Pages 1328-1336.

7. Naik, N. K.; Sekher, Y. Chandra; and Meduri, Sailendra: "Damage in woven-fabric composites subjected to low-velocity impact," *Composites Science and Technology*, Volume 60, Issue 5, April 2000, Pages 731-744.

8. Polimeno, U.; and Meo, M.: "Detecting barely visible impact damage detection on aircraft composites structures," *Composite Structures*, Volume 91, Issue 4, December 2009, Pages 398-402.

9. Shen, Qin; Omar, Mohammed; and Dongri, Shan: "Ultrasonic NDE Techniques for Impact Damage Inspection on CFRP Laminates," *Journal of Materials Science Research*, Vol 1, No 1, January 2012, 16 pages.

4.2 Porosity Inspection Guidance

4.2.1 Porosity Detection and Characterization Executive Summary

The evaluation of porosity in composite parts is required by aerospace production procedures, especially for structural components to guarantee mechanical performance and safety standards [ref. 6]. Aerospace composite porosity can be caused during several manufacturing processes and can compromise the mechanical integrity of resulting structures. Bulk porosity can be difficult to detect and quantify using common NDE methods since direct volume fraction measurements are often not feasible. Instead, measurable NDE parameters (e.g., signal intensity) must be correlated to destructive "ground truth" measurements such as cross-section photographs and/or acid digest. The techniques proven to be effective at detecting porosity are TTUT, infrared (IR) thermography, and radiography. When selecting an inspection technique, consideration should be given to the type(s) and severity of porosity needing to be detected and characterized. Porosity, which is comprised of voids larger than roughly 6 mm in size and/or is concentrated in a single ply interface, will not be covered in this section because inspection of that void type has more in common with delaminations.

A brief overview of NDE methods is provided in Table 4.2-1. The porosity standards tested in a round-robin assessment in this project as well as the experience of subject matter experts (SMEs) among the Consortium members resulted in evaluation of NDE methods effective for the detection and evaluation of porosity as follows:

Effective Methods
- PEUT
- TTUT
- XCT
- TT Thermography

Marginally Effective Methods
- Visual Inspection
- Computed Radiography (CR)
- Digital Radiography (DR)
- X-ray Backscatter
- Single-sided Thermography

Ineffective Methods
- Shearography
- Guided Wave Ultasound (GWUT)

Participating Partner(S)
- NASA
- Northrop Grumman
- General Electric (GE)
- University of South Carolina (USC)

Table 4.2-1. Advantages and disadvantages of various methods on detecting porosity in composites.

Effective Detection and Characterization Methods for Porosity		
Detection Method	**Advantages**	**Disadvantages**
Ultrasound	• Manufacturing maturity, widely supported in industry, numerous equipment and supplier options • Inexpensive options • Can be highly portable • Several automated systems available • Both single-sided and transmission configurations • Safety • Defect detection, discrimination, and depth determination techniques	• Typically requires coupling fluid that may contaminate or compromise the structure • Requires surface contact • Requires relatively smooth surface for good surface coupling • Automated systems and software for C-scan, B-scan imaging can be expensive • Manual and automated raster scanning for 100% inspection can be time consuming • May require complex contour following robotics and software for curved geometries

Effective Detection and Characterization Methods for Porosity		
Detection Method	**Advantages**	**Disadvantages**
XCT	- Direct measurement of individual pores possible - Non-contact - Excellent potential for spatial fidelity, sizing, shape definition - Provides permanent visual digital scan record - Full volume density map with cross-sectional image slices and depth information - Relatively insensitive to changes in part contours, angles, and thicknesses—contour following robotics generally not required - Images are relatively easy to interpret	- Radiation/shielding safety concerns - Typically, not portable - Requires access to all sides of the part - High initial equipment cost - Computationally intensive - Scans, software reconstruction, and data evaluation are time consuming - Requires large data storage capabilities - Not typically applicable to scan large parts or assemblies
TT Thermography	- Relatively fast/large area inspection - Non-contact - Quantitative for variations in bulk porosity by calculating diffusivity - No harmful radiation or surface heating - Relatively insensitive to changes in part contours, angles, and thicknesses—contour following robotics generally not required	- Composite thickness limitations; IR camera requires direct line of sight - Sometimes requires high emissivity coatings. - Requires access to both sides of part - Not widely used in industry for porosity quantification

Marginally Effective Detection and Characterization Methods for Porosity		
Detection Method	**Advantages**	**Disadvantages**
Visual Inspection	- Direct and rapid inspection - Non-contact - Low-cost - Can be performed without instrumentation or with inexpensive equipment such as cameras, borescopes, and magnifiers - Can find imperfections inside radii and complex curvatures if accessible - Direct analysis with photographs	- Limited to surface inspections - Insensitive to bulk features - Requires direct line of sight - Observation data can be user-dependent - Porosity quantification often requires digital images and software
Computed Radiography	- Sensitive to density variations, caused by material differences, voids, or other defects effecting the density of material the X-rays pass through. - Suitable for complex parts - Resolution generally better than DR - Faster results than film X-ray	2D image - the results are superimposed images of the defects - Sensitive to defect orientation - Radiation safety concerns

	• Generally spherical, porosity is often detected by CR from multiple directions	
Digital Radiography	• Sensitive to density variations, caused by material differences, voids, or other defects effecting the density of material the X-rays pass through • Generally spherical, porosity is often detected by DR from multiple directions	• 2D image - the results are superimposed images of the defects • Sensitive to defect orientation • Radiation safety concerns
X-ray Backscatter	• Sensitive to material density changes that can be correlated to porosity • Non-contact • Single sided • Method is real-time or near-real-time • Provides permanent visual record (film or digital image) • Can be portable with adequate safety precautions • Relatively insensitive to changes in part contours, angles, and thicknesses—contour following robotics generally not required	• Radiation safety concerns, particularly in portable applications • Single shot does not provide depth of porosity • High initial equipment cost
Single-Sided Thermography	• Relatively fast/large area inspection • Non-contact • No harmful radiation or surface heating • Relatively insensitive to changes in part contours, angles, and thicknesses—contour following robotics generally not required	• Composite thickness limitations; can usually only distinguish near-surface porosity variations when heating and detecting from same side • IR camera requires direct line of sight • Sometimes requires high emissivity coatings.

Ineffective Detection and Characterization Methods for Porosity		
Detection Method	**Advantages**	**Disadvantages**
Shearography	• Relatively fast/large area inspection • Non-contact • Single sided inspection • No harmful radiation or surface heating • Relatively insensitive to changes in part contours, angles, and thicknesses—contour following robotics generally not required	• Typically, cannot directly detect porosity • Subsurface defects must be sufficiently large to cause surface deformations • Requires direct line-of-sight with imager • Defect depth determination is not straight forward without a-priori knowledge of the structure • May require surface coating or modification on glossy surfaces for successful inspection

Guided Wave UT	• Large area inspection • Waves propagate long distances without much energy loss • Sensitivity to small defects	• For composites, still primarily a laboratory technique

4.2.2   Porosity Inspection Technologies

A challenge posed by porosity detection and characterization is the variety of configurations that porosity can exhibit, varying in both size and distribution. Size can range from fine bubbles to large voids, where large voids begin to have characteristics similar to delaminations or foreign material. Distribution can range from uniformly distributed throughout the volume to laminar concentrations, where laminar concentrations also tend towards characteristics of delaminations. While porosity is formed by gases and volatiles in the matrix, delaminations are formed when the laminated material becomes separated due to faulty processing or material damage. Typically, porosity is discriminated from a discrete void, disbond, or delamination by size. In practice, a single "pore" has a dimension less than any defect criteria class and will typically range from 10–1000 µm in size.

Porosity is different from most other defect conditions because it does not exhibit a crisp boundary; it typically presents itself as a bulk property (a uniform condition throughout the entire volume or a region of a component), or as a gradient in the bulk property. "Sizing" for porosity is typically defined as the envelope dimensions for the grouping (for example 'a 1"x2" region of porosity located 5" from the left edge of the part'), not the individual pores or void space.

A number of manufacturing processes can cause unwanted composite porosity including:
1. Absorbed moisture in prepreg;
2. Out-of-date prepreg material (shelf-life exceedance);
3. Resin/adhesive outgassing during the cure process;
4. Trapped air or volatiles;
5. Insufficient vacuum pressure or loss of bag pressure during cure;
6. Improper cure temperature and rates.

Quantifiable parameters for porosity typically include dimensional and/or area measurements of the out-of-tolerance porosity region as well as porosity-volume fraction or percentage. Most inspection methods presented below cannot provide a direct measure of the porosity-volume fraction, but instead require independent visual or chemical measurements (such as cross-section microphotographs or acid digest) that can be correlated to an indirect measurement parameter such as ultrasonic attenuation, change in radiation transmission intensity, or thermal diffusivity.

A listing of inspection methods is provided below along with brief descriptions of common inspection strategies. A more extensive overview of the inspection methods is covered in Section 5 of this Handbook. Individual reports for selected inspection methods for the NDE standards tested are provided in Appendix E, which include inspection method, the ACC partners involved in the round-robin testing, sample descriptions, measurement setups, test results, and technique applicability ranking.

A method-selection summary based on defect type is provided in the ASTM Designation E2533-17 [ref. 7].

Appendix E of the Handbook offers a ranking scheme based on a simple 0–3 star scale, with 0 being the lowest applicability ranking and 3 being the highest. The applicability ranking is based primarily on the success of the method for detecting a defect in that particular standard. However, in practice other parameters such as cost, training, and manufacturing environment constraints should be considered when selecting an inspection method.

A summary of these test methods, results, and rankings for porosity inspection is provided below and is elaborated further in Section 5 and Appendix E.

A brief overview of inspection methodologies used for porosity inspection is provided below and includes a general listing of advantages and disadvantages for each general method.

4.2.2.1   Ultrasonic Testing

Ultrasonic inspection is the most common method used in industry for subsurface porosity detection and quantification. The method is generally inexpensive and highly portable, and can be used during the fabrication process, as a final inspection, and during field inspections. Porosity scatters sound energy, so the indication of the presence of porosity is the detection of reduced sound energy penetrating the component. Higher levels of porosity scatter progressively more sound energy, so characterization of severity is based on quantifying the portion of incident sound that is able to pass through the part.

In addition to reducing the sound energy, the scattering created by porosity results in blurred inspection images for high levels of porosity.

Other features of a component can cause sound absorption and scatter including external geometry, (e.g., surface roughness and ridges), internal complexity, (e.g., ply drops), and fiber architecture (e.g., braided fiber vs. uni-directional plies).

During measurements, ultrasonic waves are transmitted into the composite, typically with a piezoelectric transducer. The ultrasonic wave is typically emitted as a short burst or wave packet pulse in order to more easily provide temporal (or depth) information about the composite structure. The wave transmits into, then reflects, scatters or attenuates as it passes through the material. The resulting waves are received either with the same or a separate transducer. Generally, a coupling medium (such as water) is used to facilitate acoustic wave energy transmission between the transducer and composite. This can be achieved through contact methods, squirter nozzles, or immersion baths.

Several approaches can be used to assess porosity with UT:
1. TT: One probe emits a sound beam which passes through the component, and a second probe receives the sound beam;
2. Pulse-echo back wall: A probe emits a sound beam which passes through the component, reflects off the component back wall and the original probe receives the reflected signal;
3. Pulse-echo reflector plate: A probe emits a sound beam, which passes through the component, reflects off a metal plate placed behind the part, and travels back through the part. The original probe receives the reflected signal.

Each approach can be combined with either of these configurations:
1. Immersion: The component and probe are immersed in water or other liquid couplant;
2. Contact: The probe(s) is placed in direct contact with the component, with a thin layer of couplant between the probe and part.

3. Noncontact nonimmersion: Probe is not in direct contact with the part but not immersed (such as squirter or captured water column).

Using one or more of these combined approaches and configurations allows an inspector to obtain a baseline signal amplitude, and then compare that to the signal strength after passing through the component. Note: some energy is expected to be lost due to reflections at known interfaces and attenuation inherent to the material. Losses greater than those expected can be assigned a cause such as porosity.

During composite inspection, the ultrasonic wavelength (on the order of 1 mm) is usually larger than any individual pore diameter dimension. Consequently, traditional ultrasonic inspection methods cannot be used to directly image or quantify sub-surface pores. Instead, in this Rayleigh scattering regime, the amplitude of the ultrasonic signal decreases exponentially as a function of depth and the level of attenuation (attenuation coefficient) increases with increased porosity. When data are collected as a C-scan, the porosity and its severity are visually evident, as shown in Figure 4.2-1. Correlation with actual porosity levels can be established by destructive evaluation of test coupons. The "ground truth" measurement of porosity is typically accomplished by techniques such as acid digestion and optical imaging. The output of these techniques is in the form of percent porosity; for example, a sample might have 2% porosity, meaning 2% of the volume is air and the remaining 98% is comprised of fiber and matrix. The limitation of these measurements is that both have a 1-sigma accuracy of approximately ±1% (i.e., a sample measuring 2% could actually have 1% or 3% porosity). The consequence of this accuracy is that the ultrasonic estimate of porosity, as grounded in this destructive test, cannot be more accurate than ±1%.
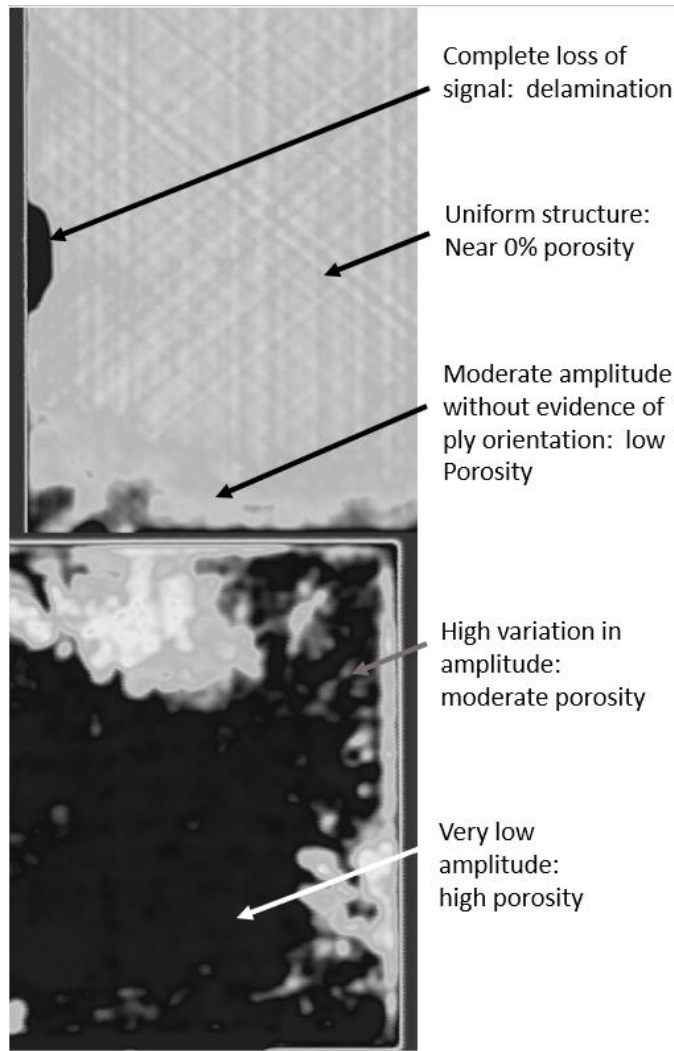
Figure 4.2-1. Qualitative Estimates of porosity based on visual features in TTUT C-scan.

Correlation of measured porosity and ultrasonic attenuation begins with a reference signal. The reference needs to capture the behavior of the entire data collection system, without the component present. As one example, this could be a complete immersion TT setup without the component that is being inspected. Another example is a contact probe placed directly on a metal (highly reflective) plate. Following the reference measurement, a component can be inserted into the inspection, and the resulting ultrasonic attenuation can be measured in decibels (dB). It is known that composite materials without porosity attenuate sound energy, and the thicker the component, the more sound is attenuated. For this reason, thickness needs to be accounted for in the correlation relationship, so the resulting attenuation measurement might take the form of decibels per inch (dB/in). Furthermore, a correction to the attenuation might be included in this value due to reflection coefficients at various interfaces.

Using the correlation method described above for a given composite system, once the attenuation coefficient (often expressed in units of dB/in) is measured over a range of porosity levels, a characteristic correlation curve can be determined for the composite as shown in Figure 4.2-2. It should be noted that a correlation curve is valid only for a specific material system at a given

frequency and that the attenuation-porosity relationship must be re-characterized if either of these parameters is changed.

Figure 4.2-2 shows a sketch of an attenuation versus porosity relationship having several characteristics:

1. At 0% porosity, the line begins above 0 dB/in—this is due to the attenuation expected for a pristine composite material. This includes effects of surface reflections and sound attenuation caused by scattering from fibers in a matrix;
2. The blue data points are used to plot a best-fit relation (dashed line) between porosity and attenuation. Note that points falling above and below the line include errors from the ground truth measure as well as from the ultrasonic technique. It should be expected that outlier data points could fall two percentage points above or below the line;
3. The black data points represent samples with extreme attenuation, but not porosity— these likely represent delaminations;
4. The brown data points falling between the bulk porosity line (blue) and the delaminations (black) represent laminar porosity—a population of samples whose characteristics lie between bulk porosity and delaminations.
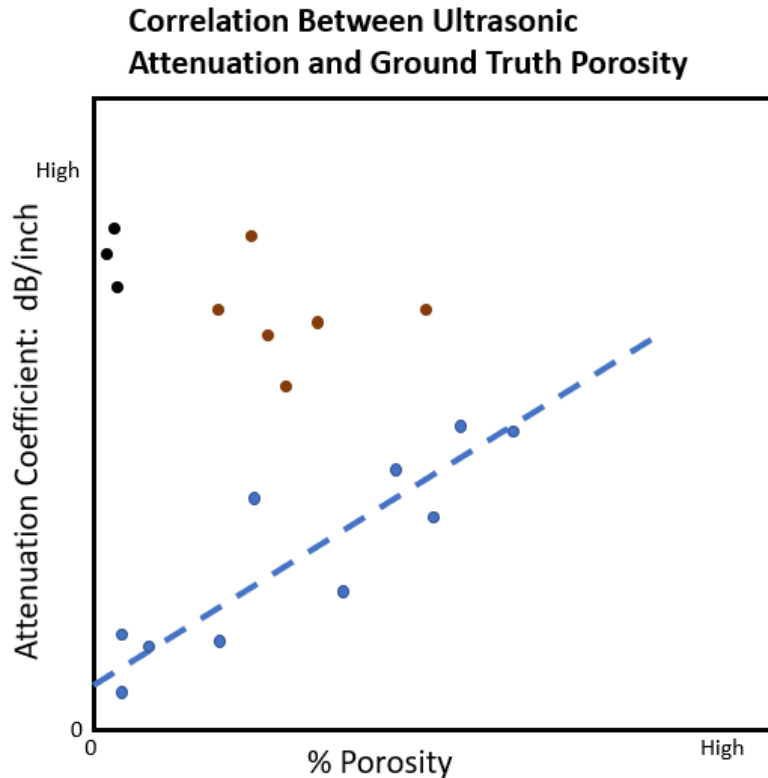
Figure 4.2-2. Correlation between porosity and ultrasonic attenuation.

As mentioned previously, the ground truth measurement typically has an accuracy of ±1% porosity. Ultrasonic measurements also have an accuracy consideration. Typical repeatability of UT measurements is on the order of ±1 dB. This can become a significant source of error, as a 1-dB error on a 0.1-inch-thick component leads to an error in attenuation measurement of 10 dB/in.

Factors that can affect the slope of the porosity relationship of Figure 4.2-2 include those that relate to the wavelength/pore size ratio, such as transducer frequency and bandwidth. Smaller wavelengths, or larger void sizes, lead to higher attenuation and steeper slopes.

The ability of UT to measure porosity can vary with the type of polymer matrix composite (PMC). Compared to uni-ply layups, braided composite can have a higher baseline attenuation coefficient due to increased waviness of fibers. Fiber diameter and matrix absorption characteristics can also affect the baseline attenuation coefficient. While these effects change the y-intercept of the plot in Figure 4.2-2, they typically have little effect on the slope of the porosity relationship. This is because, generally speaking, all fibers have properties of "ceramics," and the matrix is typically a "plastic," resulting in a similar acoustic impedance structure.

The shape of the transmitted sound beam can also be a source of variation, and needs to be considered when comparing attenuation coefficients for different inspections. While uni-ply layups will support beam formation within a component (e.g., sub-surface focusing), the wavy fibers of a braided architecture typically disrupt a sound beam, so that whatever beam shape strikes the component surface, the beam inside the component will only expand, not focus. The consequence of this behavior is that for uni-ply structures, higher resolution can be achieved by pushing the focal point of the beam to the center of the component thickness, but for braided structures, the focal point should be on the incident surface. Similarly, the receiving transducer should be focused at the center of the uni-ply component, but should be designed to match the beam exiting the surface of the braided component.

Finally, consideration should be given to the frequency content of the transmitted signal. It is known that the received signal typically has lower-frequency content than the transmitted signal. In order to maximize sensitivity of signal detection, one inspection strategy is to match the receiving transducer to the frequency profile expected to exit the component. For example, one might transmit at 2 MHz, but receive at 1 MHz. This strategy is good for detecting delaminations and wrinkles; however, the porosity relationship shown in Figure 4.2-2 is based on attenuation at a single frequency. Thus, the receiving transducer should be the same frequency as the transmitting transducer.

Because porosity can generally only be detected by measuring sound attenuation, (rather than reflected energy), depth cannot be measured, nor can porosity be distinguished from other features which attenuate sound. Complementary pulse-echo inspections can identify delaminations and foreign material, but microcracks and wrinkles have similar responses to porosity, so indication identification can be ambiguous.

Some advantages of ultrasonic methods include:
1. Manufacturing maturity, widely supported in industry, numerous equipment and supplier options;
2. Inexpensive equipment options;
3. Can be highly portable;
4. Several automated systems commercially available;
5. Both single-sided and TT configurations can be used;
6. Low safety concerns;
7. Defect detection, discrimination, and depth determination techniques exist.

Some disadvantages include:
1. Typically requires a coupling fluid that may contaminate or compromise the structure;
2. Can require surface contact;
3. Contact methods require relatively smooth surface for good surface coupling;
4. Automated systems and software for C-scan, B-scan imaging can be expensive;
5. Manual and automated raster scanning for 100% inspection can be time consuming;
6. May require complex contour following robotics and software for automated scanning of curved geometries.

4.2.2.1.1 Pulse-Echo Ultrasound (PEUT)

A single ultrasonic transducer, with straight alignment, is used to transmit an ultrasonic wave pulse into one side of the composite. Return signals are received using the same transducer from the same side of the composite. Porosity acts to attenuate the return signals that reflect from underlying features and interfaces. A diagram of a PEUT setup for porosity detection is shown in Figure 4.2-3.
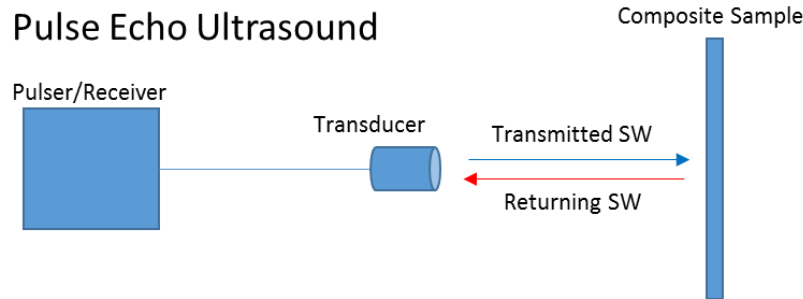
Figure 4.2-3. Diagram showing Northrop Grumman Innovation Systems (NGIS) setup of PEUT for porosity detection used on Appendix E samples.

PEUT was completed on 20 samples by Northrop Grumman, NASA, and GE Aviation. An example of results for PEUT is shown in Figure 4.2-4. Overall, it was determined that PEUT is a good method for determining porosity.
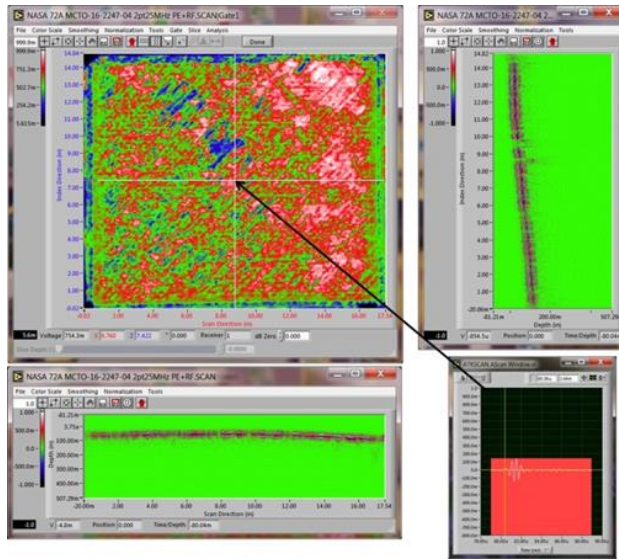
Figure 4.2-4. Example of PEUT data obtained by NGIS.
See specimen #72: NASA-03-Porosity-Panel-004 in Appendix E for more detail.

4.2.2.1.2 Through-Transmission Ultrasound (TTUT)

An ultrasonic transducer is used to transmit an ultrasonic wave pulse into the composite. The wave pulse is transmitted through the composite and is received using a second transducer on the opposing side. Porosity acts to attenuate the transmitted signal. A diagram of a TTUT setup for porosity detection is shown in Figure 4.2-5.
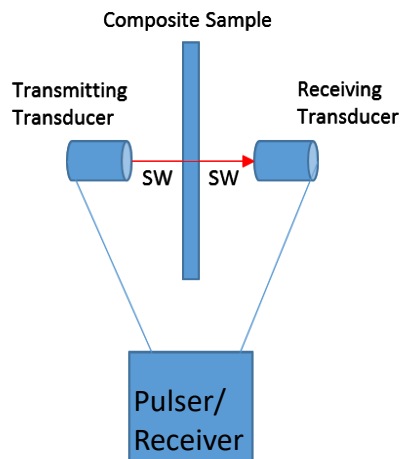
Figure 4.2-5. Diagram showing NGIS setup of TTUT for porosity detection used on
Appendix E samples.

TTUT was completed on 20 samples by Northrop Grumman, NASA, and GE Aviation. An example of results for TTUT is shown in Figure 4.2-6. Overall, it was determined that TTUT is a good method for determining porosity.

35
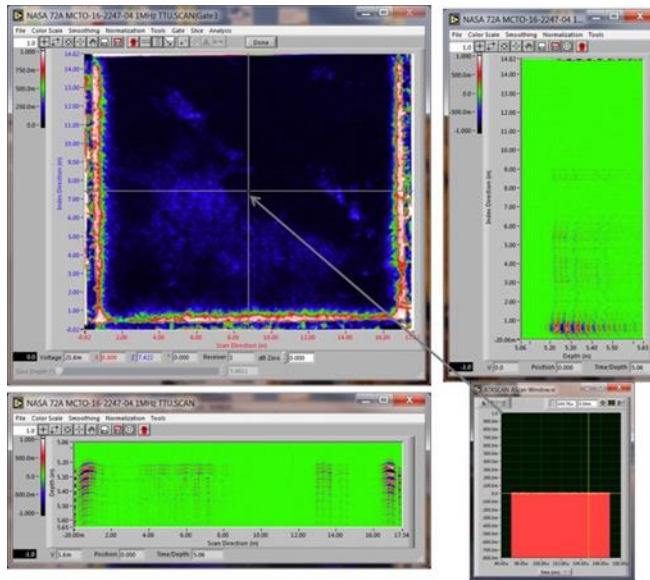
Figure 4.2-6. Example of TTUT data obtained by NGIS.
See specimen #72: NASA-03-Porosity-Panel-004 in Appendix E for more detail.

4.2.2.1.3 Single-Sided Pitch Catch Ultrasound

An ultrasonic transducer with straight or angled alignment is used to transmit an ultrasonic wave pulse into one side of the composite. Return signals are received using a second adjacent transducer. Porosity acts to attenuate the return signals that reflect from underlying features and interfaces.

While used routinely in metals for detection of vertical cracks, inspection of weld joints, etc., it is not often used in composite inspection as the defects typically line up parallel with the surface, between ply layers. Pitch Catch UT was not used to test porosity for this Handbook because porosity increases the attenuation due to scattering, making TTUT or single element PEUT preferable.

4.2.2.1.4 Phased Array Ultrasound (PAUT)

A phased array transducer consists of multiple, single-element transducers that utilize a subset of array elements to transmit an ultrasonic wave pulse into the composite. Return signals are received with the same subset of array elements or different array elements. Porosity acts to attenuate the return signals that reflect from underlying features and interfaces. Variations of PAUT can include synchronized TT configurations involving two arrays.

While phased array is routinely used in metals for detection of vertical cracks, inspection of weld joints, etc., it is not often used in composite inspection as the defects typically line up parallel with the surface between ply layers and are easily found with single probe methods (contact or emersion methods).

4.2.2.1.5 Guided Wave Ultrasound (GWUT)

An ultrasonic transducer or sparsely populated series of transducers are used to excite pulsed guided wave modes into a composite that travel in directions parallel to the composite surface plane. Additional transducer(s) or laser Doppler vibrometer (LDV) are used to receive the emanating wave pulses. Porosity acts to attenuate the transmitted signals. A diagram for a guided

36

wave setup using a piezoelectric transducer (PZT) as the transmitter and a scanning LDV (SLDV) as the receiver to detect porosity is shown in Figure 4.2-7.
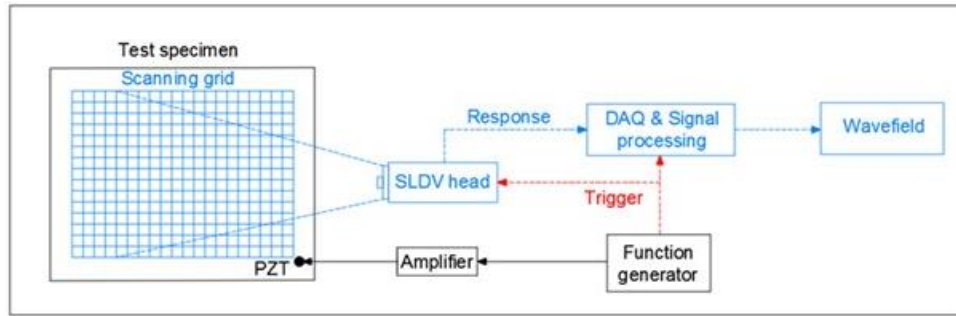
Figure 4.2-7. Diagram showing USC setup for GWUT used on samples in Appendix E.

GWUT was completed on one ACP standard. An example of results for GWUT is shown in Figure 4.2-8. It was determined that while porosity can be detected in the sample, the location cannot be confirmed so it is a poor method for determining porosity.
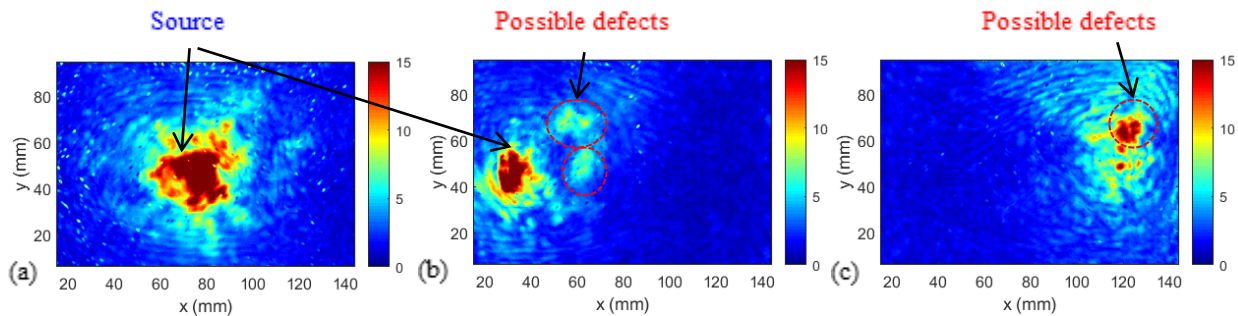
Figure 4.2-8. Example of GWUT data obtained by USC.
See specimen #30: NASA-RP-40MP in Appendix E for more detail.

4.2.2.2   Radiographic Testing

Radiographic methods can be used to detect subsurface porosity during fabrication at the end of the manufacturing cycle, and during in-service inspections. Radiographic inspection measures the density of a component, and the introduction of voids, regardless of void size, reduces that density. Radiography typically offers detection sensitivity on the order of 1% difference in mass (density).

Radiographic testing is typically performed in a transmission setup with a source on one side of the part and detector on the opposing side. Transmitted X-ray radiation is converted to an image by exposing film, an imaging plate, or an electronic digital detector array (DDA). The amount of transmitted radiation that penetrates the part depends on the energy of the incident beam, the material thickness, density, and scattering effects. Porosity generally reduces the density of the composite, increasing the relative transmitted energy[7].

Several approaches can be used to assess porosity with radiography:
1. Direct radiography (digital or film) is done by passing radiation directly through the component to detect variations in total mass. While this is effective at detecting individual pockets of air, it does not detect separations like delaminations, which are void regions, but do not change the amount of through-thickness mass;

2. 3D CT provides a volumetric assessment of porosity. One drawback is that absolute density measurements can be corrupted by artifacts from component geometry, including total thickness and sharp corners.

Some overall advantages of radiographic methods include:
1. Sensitive to material density changes that can be correlated to porosity;
2. Non-contact;
3. Method is real-time or near-real-time;
4. Provides permanent visual record (film or digital image);
5. Can be portable with adequate safety precautions;
6. Relatively insensitive to changes in part contours, angles, and thicknesses—contour following robotics generally not required.

Some overall disadvantages include:
1. Radiation safety concerns, particularly in portable applications;
2. Single shot does not provide depth of porosity;
3. Access to both sides of the part is necessary;
4. High initial equipment cost.

4.2.2.2.1   Backscatter X-ray

Backscatter X-ray is a radiographic method that requires access to only one side of the part. During backscatter X-ray, the composite material is exposed to a narrow-collimated radiation source resulting in Compton-scattering of photons back to a large detector. By translating the collimated source across the part surface, a 2D scattered intensity image is created. Backscatter X-ray is sensitive to changes in atomic number. Hence, similar to other radiographic methods, porosity can change the intensity of the resulting 2D image and this can be correlated to porosity volume fraction. Advantages and disadvantages of Backscatter X-ray are similar to other radiographic methods, but a key advantage is that Backscatter X-ray is single sided and is more sensitive to low atomic number materials.

Backscatter X-ray on the NDE standards developed under the ACP was not a good technique to detect the porosity. Scattering from the composite polymer overwhelmed any small signal due to porosity.

Some advantages of Backscatter X-ray testing include:
1. Sensitive to material density changes that can be correlated to porosity;
2. Non-contact;
3. Single sided;
4. Method is real-time or near-real-time;
5. Provides permanent visual record (film or digital image);
6. Can be portable with adequate safety precautions;
7. Relatively insensitive to changes in part contours, angles, and thicknesses—contour following robotics generally not required.

Some disadvantages of Backscatter X-ray testing include:
1. Radiation safety concerns, particularly in portable applications;
2. Single shot does not provide depth of porosity;
3. High initial equipment cost.

4.2.2.2.2   X-ray Computed Tomography (XCT)

Like other radiographic methods, CT can be used to detect sub-surface porosity during fabrication and at the end of the manufacturing cycle. Since XCT requires scanning of all sides of a structure/component and requires adequate shielding to reduce human X-ray exposure, it is typically not used for in-service field inspections. XCT testing is typically performed in a transmission setup with a source on one side of the part and detector on the opposing side. The part or source/detector are then rotated 360° (some applications of limited angle CT can be performed with a smaller rotational field) and a collection of multiple "views" are processed by software to create a 3D volume reconstruction of the part. The amount of transmitted radiation that penetrates the part depends on the energy of the incident beam, the material thickness, density, and scattering effects. The X-ray attenuation is approximately a function of the integral of the X-ray attenuation path between the X-ray source and a point on the detector array. Porosity generally reduces the density of the composite, increasing the relative transmitted energy[3]. This translates to a change of contrast in the resulting inspection images. XCT systems exist with micron (µm) resolution (micro-focus CT) allowing direct imaging of pore sizes, volume density, and shape. However, such systems typically cannot accommodate large aerospace structures making their use impractical or unfeasible for large-component inspections. A diagram of an XCT setup for porosity detection is shown in Figure 4.2-9. XCT data are often used in porosity detection as a validation of other NDE techniques as they provide a 'ground truth' quantitative evaluation of the porosity within the part.
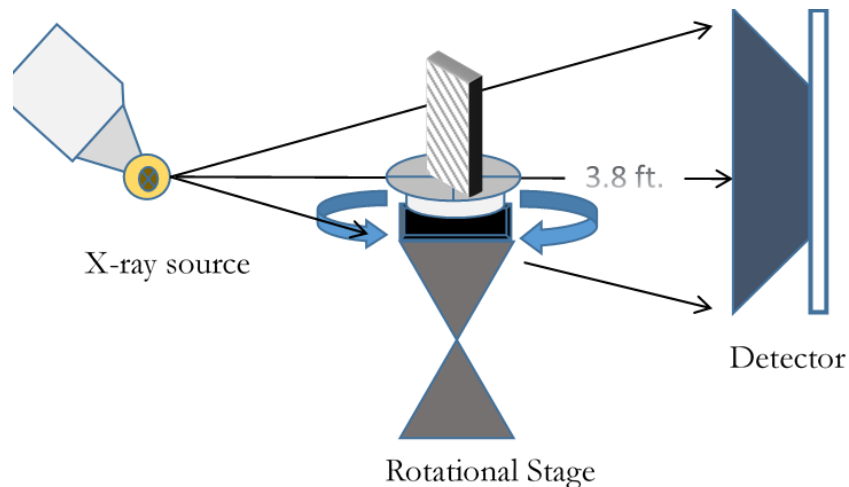
Figure 4.2-9. Diagram showing NASA setup of XCT for porosity detection used on Appendix E samples.

Some advantages of XCT include:
1. Direct measurement of individual pores possible;
2. Non-contact;
3. Excellent potential for spatial fidelity, sizing, shape definition;
4. Provides permanent visual digital scan record;

5. Full volume density map with cross-sectional image slices and depth information;
6. Relatively insensitive to changes in part contours, angles, and thicknesses—contour following robotics generally not required;
7. Images are relatively easy to interpret.

Some disadvantages of XCT include:
1. Radiation/shielding safety concerns;
2. Typically not portable;
3. Requires access to all sides of the part;
4. High initial equipment cost;
5. Computationally intensive;
6. Scans, software reconstruction, and data evaluation are time consuming;
7. Requires large data storage capabilities;
8. Not typically applicable to scan large parts or assemblies.

NASA performed XCT on ten NDE standards; an example of XCT results is shown in Figure 4.2-10 and Figure 4.2-11. Overall, it was determined that XCT is an appropriate method for detecting porosity, albeit with disadvantages.
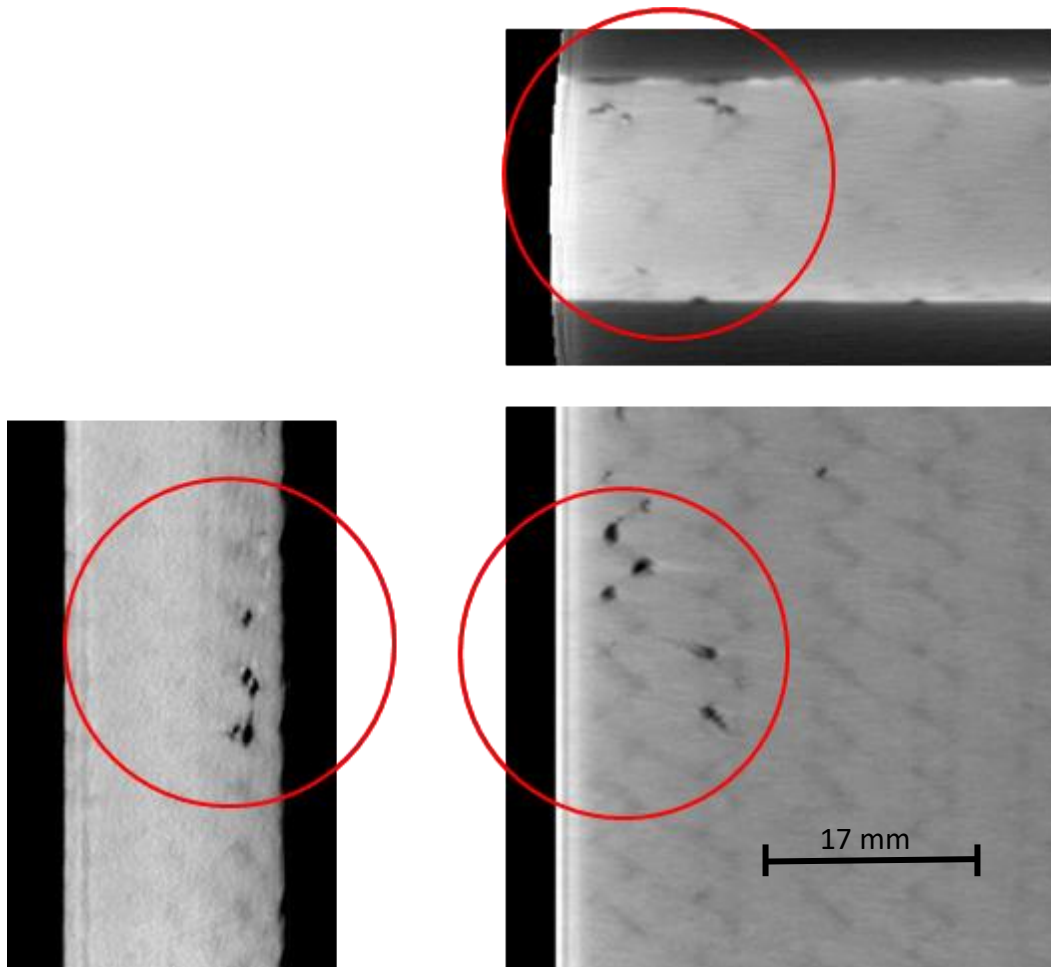
Figure 4.2-10. Example of XCT data obtained by NASA.
See specimen #48: A tri-axial braided woven CFRP. See Appendix E for more detail.

40
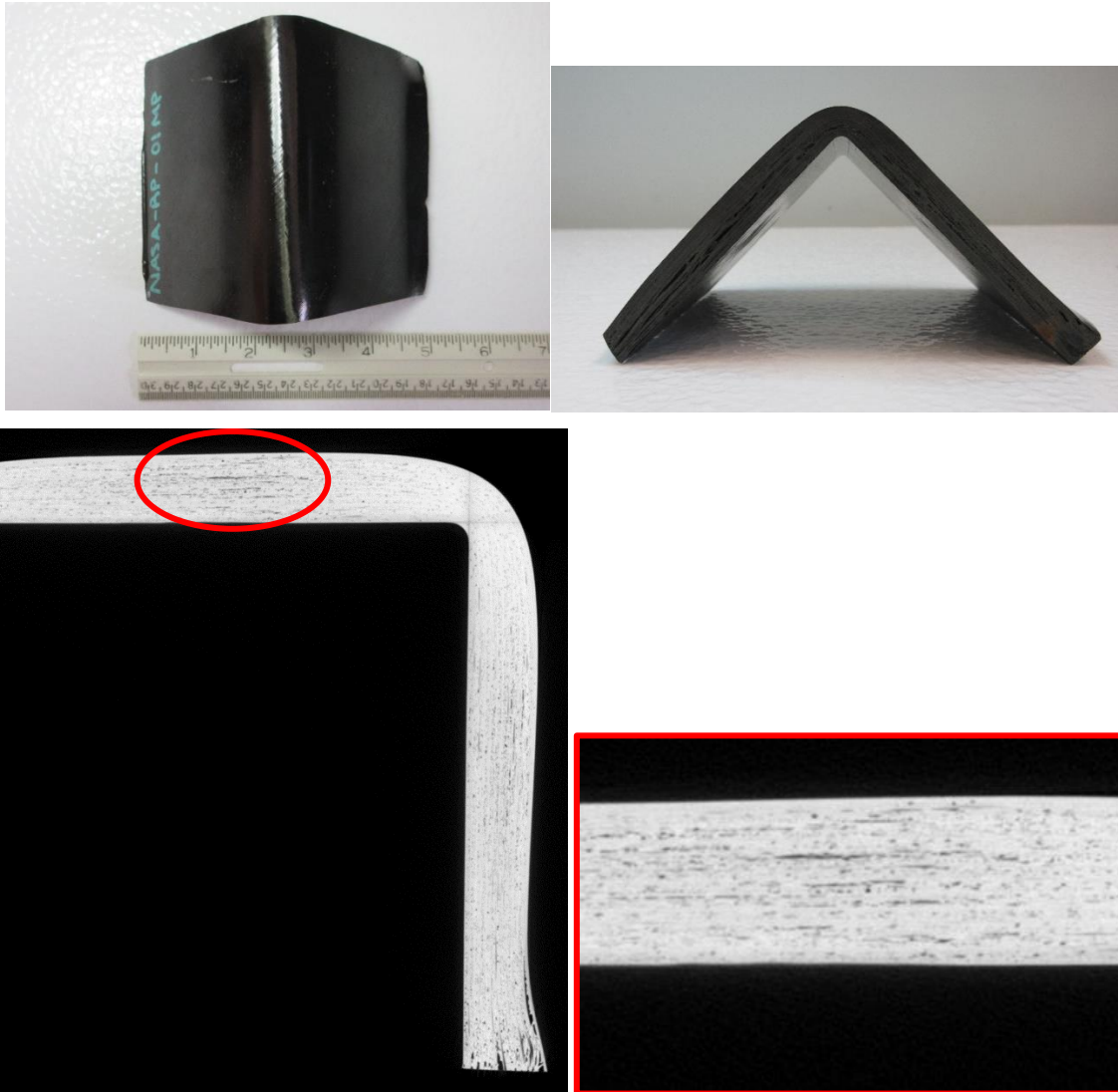
Figure 4.2-11. (Top) Photos of NDE standard #22, NDE standard #22, a thick uniply (0/90/45) with a 0.1-inch inside radius curvature. (Bottom) XCT data show the standard contains significant porosity, with the porosity in some locations being laminar and tending toward disbonds.
Severe delaminations formed at the edges, which can also be seen in thermography
images in Figures 4.2-16.

For detailed analysis of XCT performed on samples, see Appendix E. For a more detailed explanation of Radiography techniques and how they were used to quantify defects such as porosity, see Section 5.3.

4.2.2.3 Infrared Thermographic Testing

Thermographic methods can be used to detect subsurface porosity during fabrication, at the end of the manufacturing cycle, and during in-service inspections. Thermography equipment can be made to be highly portable, and depending on the technique, can be performed in both a single-sided and TT measurement configurations. During thermography measurements, an energy source such as visible/IR radiation, convection, conduction, mechanical vibration, or induction are used to introduce heat into the composite part. Alternately, the part can be locally cooled using convection

or conduction. The rate of heat flow and resulting temperature changes depend on variations in the thermal diffusivity of the material. Defects, such as porosity, will alter the thermal diffusivity and typically restrict heat flow. Resulting changes in surface temperature distributions are then measured using an infrared camera.

Some advantages of thermographic methods include:
1. Relatively fast/large area inspection;
2. Non-contact;
3. Single-sided inspection option;
4. No harmful radiation or significant surface heating;
5. Relatively insensitive to changes in part contours, angles, and thicknesses—contour following robotics generally not required.

Some disadvantages of thermographic methods include:
1. Composite thickness limitations;
2. IR camera requires direct line of sight;
3. Sometimes requires high emissivity coatings;
4. Not widely used in industry for porosity quantification.

Several thermography techniques are used for composites inspection in industry including passive thermography, flash/pulse thermography, pulsed-phase thermography (PPT), lock-in thermography, step-heating thermography, and vibro-thermography[8].

4.2.2.3.1 *Single-Sided Infrared Thermography (SSIR)*

SSIR uses an IR camera with a flash bulb placed between it and the composite part. A short-duration flash bulb is used to introduce heat to the part, and then the infrared camera is used to take a time series of thermal images as the heat conducts through the structure. Composites with a high thermal diffusivity will cool down more quickly, while components with porosity (lower thermal diffusivity) will cool down more slowly. This behavior is proportional to the quantity of porosity in the component. A diagram of a single-sided setup for porosity detection is shown in Figure 4.2-12.
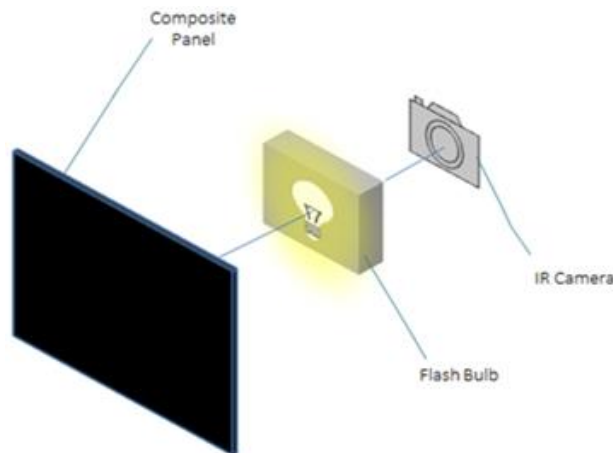
Figure 4.2-12. Diagram showing NGIS setup for SSIR used on samples in Appendix E.

SSIR was completed on nine samples by NASA and Northrop Grumman. An example of results for single-sided thermography performed on NDE standard #22 (Figure 4.2-13) is shown in Figure

4.2-14. Overall, while some features are detectable in the standards, they were not well correlated to porosity, and it was determined that SSIR is a poor technique to determine porosity.
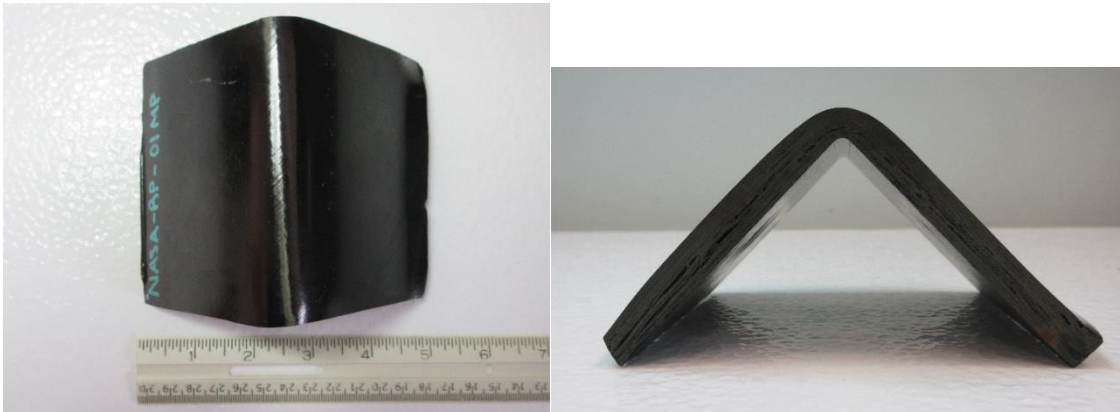
Figure 4.2-13. NASA-RP-01MP NDE Standard.

| *(Left)* | *(Center)* | *(Right)* |
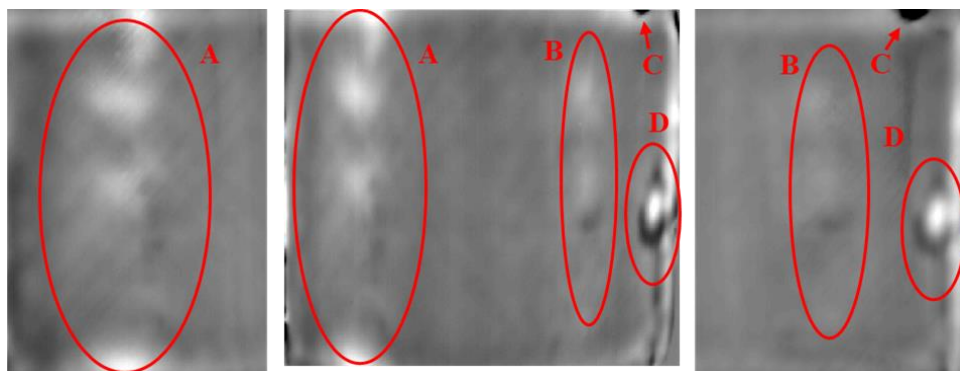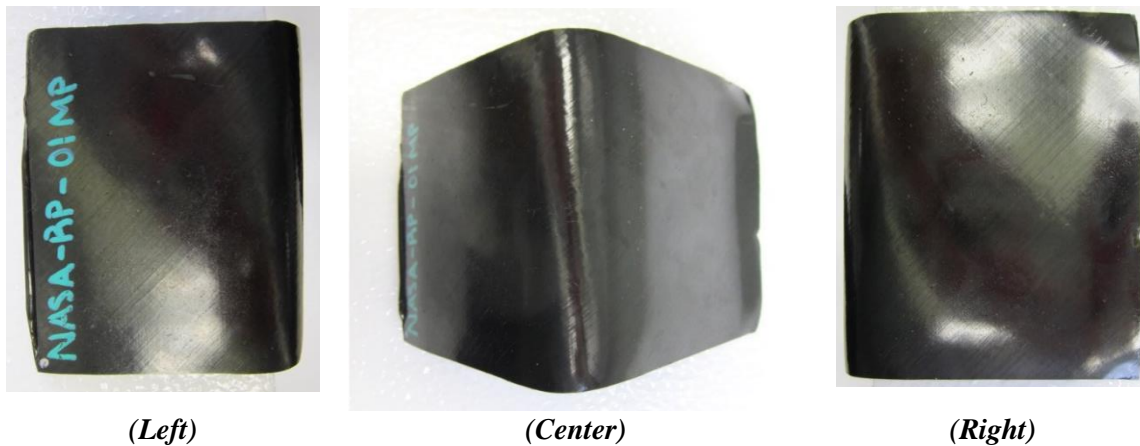
Figure 4.2-14. Example of SSIR for porosity NDE standard #22: NASA-RP-01MP.
Processed (PCA) thermal data. The regions A and B, each located halfway down sides of standard #22, are indicative of porosity but signals are ill-defined.

4.2.2.3.2 *Through-Transmission Infrared Thermography (TTIR)*

TTIR uses an IR camera with a flash bulb placed on the opposite side of the composite part. A short-duration flash bulb is used to introduce heat to the part, and then the IR camera is used to take a time series of thermal images as heat conducts through the part. In a TT measurement, the heat observed by the infrared camera on the opposite side of the flash bulb is shown to be

mathematically proportional to the product of the diffusivity times the thickness. A diagram of a TT setup for porosity detection is shown in Figure 4.2-15.
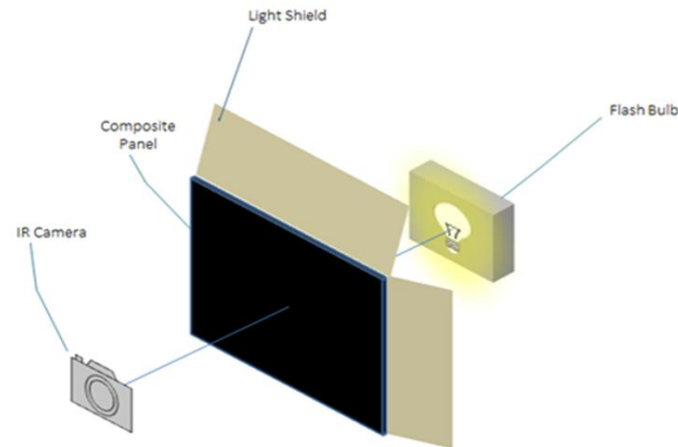
Figure 4.2-15. Diagram showing NGIS setup for TTIR used on samples in Appendix E.

TTIR was completed on nine samples by NASA and Northrop Grumman. An example of results for TTIR is shown in Figure 4.2-16. Comparing this image to the XCT images of the same specimen, the severe delaminations along the edge (G) are clearly visible. By fitting the heat-up portion of the TT data to a linear curve, the diffusivity can be calculated and an overall bulk porosity determined. See Section 5.2.3 for details.

Overall, it was determined that TTIR is capable of detecting porosity in cases where the porosity is locally concentrated. Thermography is a large area, fast, noncontact NDE method that is often used in conjunction with UT methods where inspection is first performed with thermography and smaller areas of interest are inspected in greater detail with UT.
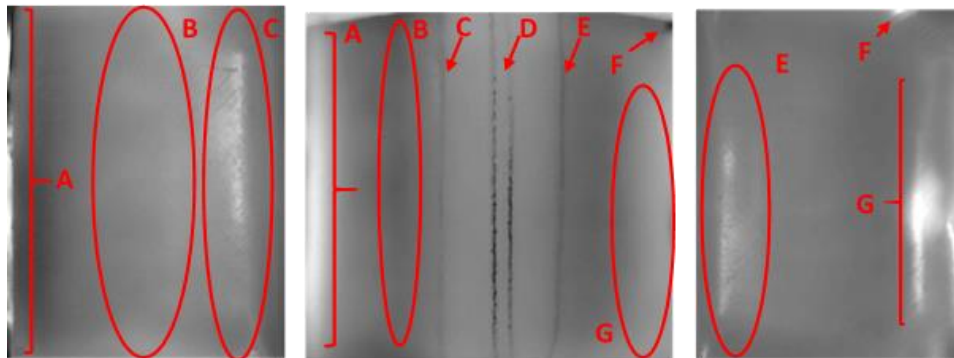
Figure 4.2-16. Example of TTIR data obtained by NASA (See specimen #22: NASA-RP-01MP).
This is the same specimen as shown in Figure 4.2-12, with the data taken in the TT mode as opposed to the single-sided mode. C, E, and G are typical of localized porosity indications.

For detailed analysis of thermography performed on samples, see Appendix E. For a more detailed explanation of Thermographic techniques and how they were used to quantify defects such as porosity see Section 5.

4.2.2.4 Visual Testing

Visual testing is effective for detecting surface porosity during fabrication, at the end of the manufacturing cycle, and during in-service inspections and performed with or without the aid of

instrumentation. For composites, visual inspection is generally limited to the surface porosity, which is not always indicative of bulk or volume porosity. Consequently, although the visual method can be valuable for a quick initial assessment of composite porosity condition, it must be followed up with one of the other inspection methods discussed in this Handbook.

Some advantages of the visual inspection method include:
1. Direct and rapid inspection;
2. Non-contact;
3. Low-cost;
4. Can be performed without instrumentation or with inexpensive equipment such as cameras, borescopes, and magnifiers;
5. Can find imperfections inside radii and complex curvatures;
6. Direct reporting with photographs.

Some disadvantages include:
1. Limited to surface inspections; insensitive to bulk features;
2. Requires direct line of sight;
3. Observation data can be user-dependent;
4. Porosity quantification often requires digital images and software.

4.2.2.5   Shearography

Shearography is typically not used for porosity inspection in industry, but can be a useful method to further diagnose an indication to discriminate between porosity and other flaw types such as delaminations or disbonds. Shearography equipment is portable, single sided, and non-contact. Inspections can be performed relatively quickly since area images can be captured within seconds. During shearography measurements, a stress is applied to a composite structure through various methods including heat, vacuum, pressure, mechanical force, acoustic, or vibration. The article is illuminated with a laser speckle pattern, and an interferometer-based imager is used to measure small out-of-plane displacements. Porosity will typically not lead to direct out-of-plane displacements unless it causes a measureable change in the modulus leading out-of-plane deformation or it initiates a larger delamination or disbond. Another example of when shearography can be useful in discriminating porosity versus a disbond is when looking at skin-to-core bondlines.

Some advantages of shearography inspections include:
1. Relatively fast/large area inspection;
2. Non-contact;
3. Single-sided inspection;
4. No harmful radiation or surface heating;
5. Relatively insensitive to changes in part contours, angles, and thicknesses—contour following robotics generally not required.

Some disadvantages include:
1. Typically, cannot directly detect porosity;
2. Subsurface defects must be sufficiently large to cause surface deformations;
3. Requires direct line-of-sight with imager;

4. Defect depth determination is not straight forward without *a-priori* knowledge of the structure;
5. May require surface coating or modification on glossy surfaces for successful inspection.

4.2.3 Porosity Standards

A summary of porosity standards and test methods is provided in Table 4.2-2. Due to number and breadth of samples and inspection methodologies, not all methods described above were tested for all specimens. Instead, the Handbook along with Appendix E acts as a preliminary guide to porosity inspection.

Table 4.2-2. Summary of porosity specimens tested by consortium.

#	Reference Standard	Structure	Material	Configuration/ Radius	Defects and features	Dimensions (inches)	Partner: Tests
22	NASA-RP-01MP	Uni-ply 0/90/45	IM7/8552	0.1-inch radial inside curve	Radius Panel 0.1 inch Curve Rad with medium porosity	$4.5 \times 2.5 \times 4$	NASA: SSIR, TTIR
26	NASA-RP-10MP	Uni-ply 0/90/45	IM7/8552	1.0-inch radial inside curve	Radius Panel 1.0 inch Curve Rad with medium porosity	$4.5 \times 2.5 \times 4$	NASA: SSIR, TTIR
28	NASA-RP-20MP	Uni-ply 0/90/45	IM7/8552	2.0-inch radial inside curve	Radius Panel 2.0 inch Curve Rad with medium porosity	$4.5 \times 2.0 \times 4$	NASA: SSIR, TTIR
30	NASA-RP-40MP	Uni-ply 0/90/45	IM7/8552	4.0-inch radial inside curve	Radius Panel 4.0 inch Curve Rad with medium porosity	$4.5 \times 1.25 \times 6$	NASA: PEUT, TTUT; USC: GWUT
77	NASA-005-Porosity-001	Quasi-isotropic	IM7/8552 satin weave fabric and unidirectional	Rotorcraft blade spar tube	Porosity	$11.5 \times 8.5 \times 2.8$	GE: PEUT, TTUT
78	NASA-005-Porosity-002	Quasi-isotropic	IM7/8552 satin weave fabric and unidirectional	Rotorcraft blade spar tube	Porosity	$11.5 \times 8.5 \times 2.8$	GE: PEUT, TTUT
79	NASA-005-Porosity-003	Quasi-isotropic	IM7/8552 satin weave fabric and unidirectional	Rotorcraft blade spar tube	Porosity	$11.5 \times 8.5 \times 2.8$	NASA: PEUT GE: PEUT, TTUT
80	NASA-005-Porosity-004	Quasi-isotropic	IM7/8552 satin weave fabric and unidirectional	Rotorcraft blade spar tube	Porosity	$11.5 \times 8.5 \times 2.8$	GE: PEUT, TTUT;
73	NASA-005-STANDARD-001	Quasi-isotropic	IM7/8552 satin weave fabric and unidirectional	Rotorcraft blade spar tube	Pristine	$11.5 \times 8.5 \times 2.8$	GE: PEUT, TTUT
2	NASA-S-MP	Uni-ply 0/90/45	IM7/8552	Step heights: 0.1 inch to 1.0 inch	Step with medium porosity	$14 \times 8 \times 1.5$	GE: PEUT, TTUT; NASA: XCT NGIS: PEUT, SSIR, TTIR
3	NASA-S-HP	Uni-ply 0/90/45	IM7/8552	Step heights: 0.1 inch to 1.0 inch	Step with high porosity	$14 \times 8 \times 1.5$	GE: PEUT, TTUT; NASA: XCT NGIS: PEUT, SSIR, TTIR

69	NASA-03-Porosity-Panel-001	Fiber Placed Panel	IM7/8552-1 Slit Tape w/ IM7/8552 Fabric Outer Mold Line (OML)	Flat panel	Porosity	15 × 17.5 × 0.15	NASA: PEUT GE: PEUT, TTUT NGIS: PEUT, TTUT, TTIR, SSIR
70	NASA-03-Porosity-Panel-002	Fiber Placed Panel	IM7/8552-1 Slit Tape w/ IM7/8552 Fabric OML	Flat panel	Porosity	15 × 17.5 × 0.15	NASA: PEUT GE: PEUT, TTUT NGIS: PEUT, TTUT, TTIR, SSIR
71A&B	NASA-03-Porosity-Panel-003	Fiber Placed Panel	IM7/8552-1 Slit Tape w/ IM7/8552 Fabric OML	Flat panel	Porosity	14 × 16 × 0.15	GE: PEUT, TTUT; NASA: PEUT, XCT NGIS: PEUT, TTUT, SSIR, TTIR USC: GWUT
72A&B	NASA-03-Porosity-Panel-004	Fiber Placed Panel	IM7/8552-1 Slit Tape w/ IM7/8552 Fabric OML	Flat panel	Porosity	15 × 17.5 × 0.15	GE: PEUT, TTUT; NASA: PEUT, XCT NGIS: PEUT, TTUT, SSIR, TTIR USC:GWUT
10	NASA-W-5MP	Uni-ply 0/90/45	IM7/8552	Height: 0.25 inch to 1.0 inch, 5 deg slope	Wedge Interleaved 5 deg with medium porosity	12 × 3 × 1.5	GE: PEUT, TTUT; NASA: XCT
12	NASA-W-20MP	Uni-ply 0/90/45	IM7/8552	Height: 0.25 inch to 1.0 inch, 20 deg slope	Wedge Interleaved 20 deg with medium porosity	12 × 3 × 1	GE: PEUT, TTUT; NASA: XCT
13	NASA-W-IL-20MP	Uni-ply 0/90/45	IM7/8552	Height: 0.25 inch to 1.0 inch, 20 deg slope	Wedge Step 20 deg with medium porosity	12 × 3 × 1.5	GE: PEUT, TTUT; NASA: XCT
48	UTC 6 Porosity 2	Triaxial Braid, 0/+60/-60	T-800SC Triaxial Braid 0/+60/-60 with 3M AMD-825	Flat panel	Porosity	13 × 13 × 0.65	GE: PEUT, TTUT; NASA: XCT
49	UTC 8 Porosity 1	Triaxial Braid, 0/+60/-60	T-800SC Triaxial Braid 0/+60/-60 with 3M AMD-825	Flat panel	Porosity	13 × 13 × 0.65	GE: PEUT, TTUT
50	UTC 11 Baseline 2	Triaxial Braid, 0/+60/-60	T-800SC Triaxial Braid 0/+60/-60 with 3M AMD-825	Flat panel	Baseline	12 × 11 × 0.5	GE: PEUT, TTUT; NASA: PEUT USC:GWUT

4.2.3.1 References

1. Hsu, David K.; and Uhl, Kevin M.: *A morphology study of porosity defects in graphite-epoxy composites*, Center for NDE, Iowa State University, Ames, IA 50011.
2. Fernlund, G.; Wells, J.; Fahrang, L.; Kay, J.; and Poursartip, A: "Causes and remedies for porosity in composite manufacturing," *IOP Conference Series: Materials Science and Engineering*, Vol. 139, No. 1, 012002, 2016.
3. Farhang, J.: "Void evolution during processing of out of autoclave prepreg laminates," Ph.D. Thesis at the University of British Columbia, Canada, 2016.
4. Oliver, P. A.; Mascaro, B.; Margueres, P.; and Collombet, F.: "CFRP with voids: ultrasonic characterization of localized porosity acceptance criteria and mechanical characteristics," *16th International Conference on Composite Materials*, Kyoto, Japan, 2007/
5. Ancelotti, A. C.; Pardini, L. C.; Bezerra, E. M.; and Roach, D.: "Use of the Mar-Lin criteria to determine the influence of porosity on the iosipescu and short beam shear properties in carbon fiber polymer matrix composites," *Materials Research*, Vol. 13, No. 1, pp. 63-69, 2010.
6. Di Landro, L.; Montalto, A.; Bettini, P.; Guerra, S.; Montagnoli, F.; and Rigamonti, M.: "Detection of voids in carbon/epoxy laminates and their influence on mechanical properties," *Polymers and Polymer Composites*, Vol. 25, No. 5, pp. 371-380, 2016.
7. ASTM: *Standard Guide for Nondestructive Testing of Polymer Matrix Composites Used in Aerospace Applications*, ASTM E2533-17.
8. Maldague, Xavier P.V.; and Moore, Patrick O.: *Nondestructive Testing Handbook, 3rd Edition: Volume 3, Infrared and Thermal Testing*, American Society for Nondestructive Testing, 2001.

4.3 Delamination Inspection Guidance

4.3.1 Delamination Detection and Characterization Executive Summary

Delaminations in composites pose several challenges for inspection. They vary in size, and in extreme cases, when very large (occupy a large portion of the region of data collected for example), they can appear as a defect-free part with a lack of discrete defect boundaries. The lack of physical separation in delaminations that contain no air gap also reduces detectability in most NDE methods. They are also planar defects and therefore detectability is highly dependent on orientation, which becomes particularly important in parts with complicated geometries. Because delaminations typically occur between two adjacent plies (i.e., interlaminar), they are well suited for detection with UT if the ultrasonic interrogation remains normal to the air gap created by the interior delamination. The decrease in mechanical properties/strength caused by delaminations also makes them detectable with methods such as shearography, which utilize changes in mechanical deformation caused by defects. While the large planar nature of delaminations is beneficial in detection with UT, this makes methods such as 2D radiography unsuitable. XCT can detect delamination damage using multiple projections from various angles; however, this is often not feasible due to the high aspect ratios and large sizes of composite panels. IRT can detect delaminations but is often limited by the thickness of the specimen.

A brief overview of NDE methods is provided in Table 4.3-1. The delamination standards tested in a round-robin assessment in this project, as well as the experience of SMEs among the

Consortium members resulted in evaluation of NDE methods effective for the detection and evaluation of delaminations as follows:

Effective methods
- PEUT
- TTUT
- IRT
- XCT

Marginally Effective methods
- Visual Inspection
- Backscatter X-ray
- Shearography

Ineffective methods
- CR
- Digital Radiography

Participating partner(s)
- NASA
- Boeing
- GE
- USC

Table 4.3-1. Advantages and disadvantages of various methods on detecting delaminations in composites.

Effective Detection and Characterization Methods for Delaminations		
Detection Method	**Advantages**	**Disadvantages**
Ultrasound	- Achieves strong signals from surface-parallel delaminations - Manufacturing maturity, widely supported in industry, numerous equipment and supplier options - Inexpensive options - Can be highly portable - Several automated systems available - Both single-sided and transmission configurations - Safety - Defect detection, discrimination, and depth determination techniques	- Typically requires coupling fluid that may contaminate or compromise the structure - Requires surface contact - Requires relatively smooth surface for good surface coupling - Automated systems and software for C-scan, B-scan imaging can be expensive - Manual and automated raster scanning for 100% inspection can be time consuming - May require complex contour following robotics and software for curved geometries
Thermography	- Changes in thermal conductivity can indicate delaminations - Relatively fast/large area inspection - Non-contact - Single sided inspection option	- Composite thickness limitations; IR camera requires direct line of sight - Sometimes requires high emissivity coatings

	• No harmful radiation or surface heating • Relatively insensitive to changes in part contours, angles, and thicknesses—contour following robotics generally not required	
XCT	• Non-contact • Excellent potential for spatial fidelity, sizing, shape definition • Provides permanent visual digital scan record • Full volume density map with cross-sectional image slices and depth information • Relatively insensitive to changes in part contours, angles, and thicknesses—contour following robotics generally not required • Images are relatively easy to interpret	• Radiation/shielding safety concerns • Typically not portable • Requires access to all sides of the part • High initial equipment cost • Computationally intensive • Scans, software reconstruction, and data evaluation are time consuming • Requires large data storage capabilities • Not typically applicable to scan large parts or assemblies

Marginally Effective Detection and Characterization Methods for Delaminations		
Detection Method	**Advantages**	**Disadvantages**
Visual Inspection	• Direct and rapid inspection • Non-contact • Low-cost • Can be performed without instrumentation or with inexpensive equipment such as cameras, borescopes, and magnifiers • Can find imperfections inside radii and complex curvatures • Direct reporting with photographs	• Limited to surface inspections • Insensitive to bulk features • Requires direct line of sight • Observation data can be user-dependent
X-ray Backscatter	• Sensitive to material density changes and scatter features that can indicate delaminations • Non-contact • Single sided • Method is real-time or near-real-time • Provides permanent visual record (film or digital image) • Can be portable with adequate safety precautions • Relatively insensitive to changes in part contours, angles, and thicknesses—contour following robotics generally not required	• Radiation safety concerns, particularly in portable applications • Single shot does not provide depth of delamination • High initial equipment cost • Limited resolution compared to other radiography methods

Marginally Effective Detection and Characterization Methods for Delaminations		
Detection Method	**Advantages**	**Disadvantages**
Shearography	• Sensitive to the differences in stress response caused by delaminations • Relatively fast/large area inspection • Non-contact • Single sided inspection • No harmful radiation or surface heating • Relatively insensitive to changes in part contours, angles, and thicknesses—contour following robotics generally not required	• Subsurface defects must be sufficiently large to cause surface deformations • Requires direct line-of-sight with imager • Defect depth determination is not straight forward without a-priori knowledge of the structure • May require surface coating or modification on glossy surfaces for successful inspection

Ineffective Detection and Characterization Methods for Delaminations		
Detection Method	**Advantages**	**Disadvantages**
Computed Radiography	• Sensitive to density variations, caused by material differences, voids, or other defects effecting the density of material the X-rays pass through. • Suitable for complex parts • Resolution generally better than DR • Faster results than film X-ray	• 2D image - the results are superimposed images of the defects • Sensitive to defect orientation • Radiation safety concerns
Digital Radiography	• Sensitive to density variations, caused by material differences, voids, or other defects effecting the density of material the X-rays pass through	• 2D image - the results are superimposed images of the defects • Sensitive to defect orientation • Radiation safety concerns

4.3.2 Delamination Inspection Technologies

Through the testing of multiple specimens with various NDE methods, the participating partners demonstrated the benefits, disadvantages, and limitations of each method for detecting delaminations in the standards. For example, the 8276-200 standard specimens contain simulated delaminations in both flat and radial geometries using various inserts to achieve the effect of delaminations. Creating accurate simulated delaminations for standards is a challenge in the industry. A common method is the use of foreign material inserts such as release-ply tape or coated brass to induce disbonding and air pockets between lamina. This method can accurately represent delaminations for UT methods, for the most part, but can have varying effectiveness with other methods. For instance, the significantly higher density of the brass compared to the composite allows for significantly easier detection with X-ray methods. Using IRT, the high thermal conductivity of the brass also allows for increased detectability that does not represent a true delamination. However, the inserts of material with similar physical properties to composite can more accurately represent delaminations, though often these reflect delaminations with less significant gaps, often worst-case scenarios for detection.

Delaminations can occur in various geometries. For the purpose of this Handbook, they were tested under flat panel, radii, and wedge geometries. The simplicity of the flat panel configuration allows

for improved detection. In UT inspection, the delaminations align with the ultrasonic path for the best reflection and attenuation. Additionally, curved or wedge geometries add a more complicated baseline signal to discern the delamination signal from which is a concern that applies to almost all NDE methods.

A brief overview of inspection methodologies used for porosity inspection is provided below and includes a general listing of advantages and disadvantages for each general method.

4.3.2.1 Ultrasonic Testing

Ultrasonic methods to inspect for delaminations can be viewed broadly as PEUT and TTUT. When inspecting for delaminations, PEUT is often preferred because it only requires one-sided access (a benefit for large panels and structures). Additionally, PEUT can effectively detect delaminations that have filled with water due to being open to the surface in a submersion inspection. TTUT can be beneficial in highly attenuative materials where the signal path would be half the distance traveled for PEUT. UT inspection is most effective in geometries where the plies are aligned perpendicular to the ultrasonic signal, providing the greatest reflection. Curved geometries require curve following or fitted probes for the best results, increasing the time and cost to develop inspection techniques. UT also requires a certain level of surface smoothness; however, composites often meet this criterion. Figure 4.3-1 shows the result of a TTUT scan of the 8276-200-56-48 standard containing various inserts to simulate delaminations. The yellow streak in the upper half of the images is the curvature of the panel, which obscures the indications and reduces the ability to detect. One may also note the brass inserts provide the greatest signal responses followed by the pressure-sensitive tape (PT) and release ply fabric (RPF) inserts, respectively. This is because the brass inserts simulated the greatest degree of disbanding. From these data, one can see the worst-case scenario for detecting delaminations is abnormal shaped small delaminations located in the radius section.

| *a) RPF.* | *b) Brass.* | *c) Inserts.* |
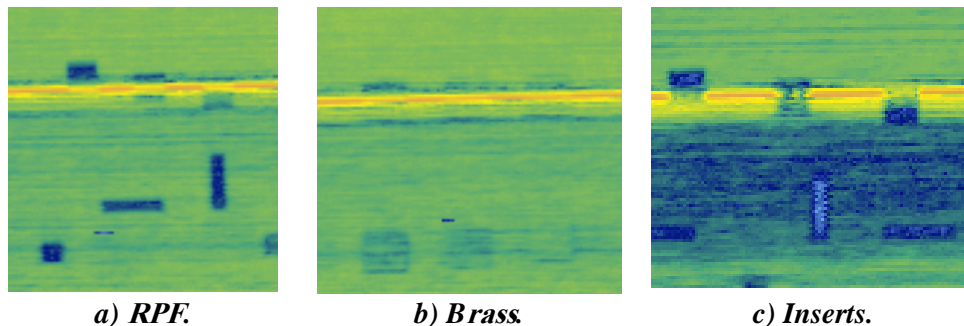
Figure 4.3-1. Standard 8276-200-56-48 A&B TTUT scans showing PT.

4.3.2.2 Thermography

IRT is applied to identifying delaminations in thinner panels. It includes advantages such as speed of data collection for large areas and visual results rather than the waveform results from UT. IRT requires that the delaminations create enough of a change in the thermal gradient of the part, which is not always the case with delaminations that maintain contact between the separated plies as they can still effectively transfer heat. It also has a significant reduction in sensitivity for thicker parts, and surface conditions can notably affect the thermal signature. The Flash IRT images for Standard 8276-200-58-8 are shown in (Figure 4.3-2). The standard was eight plies thick, providing excellent sensitivity. In the lower image, the brass inserts are extremely visible due to their significantly different thermal properties compared to the composite. Another interesting feature of note is the

visibility of the surface writing, made with a simple paint marker, which significantly affects how the surface absorbed the heat from the flash, demonstrating the sensitivity of flash thermography to surface features and coatings.
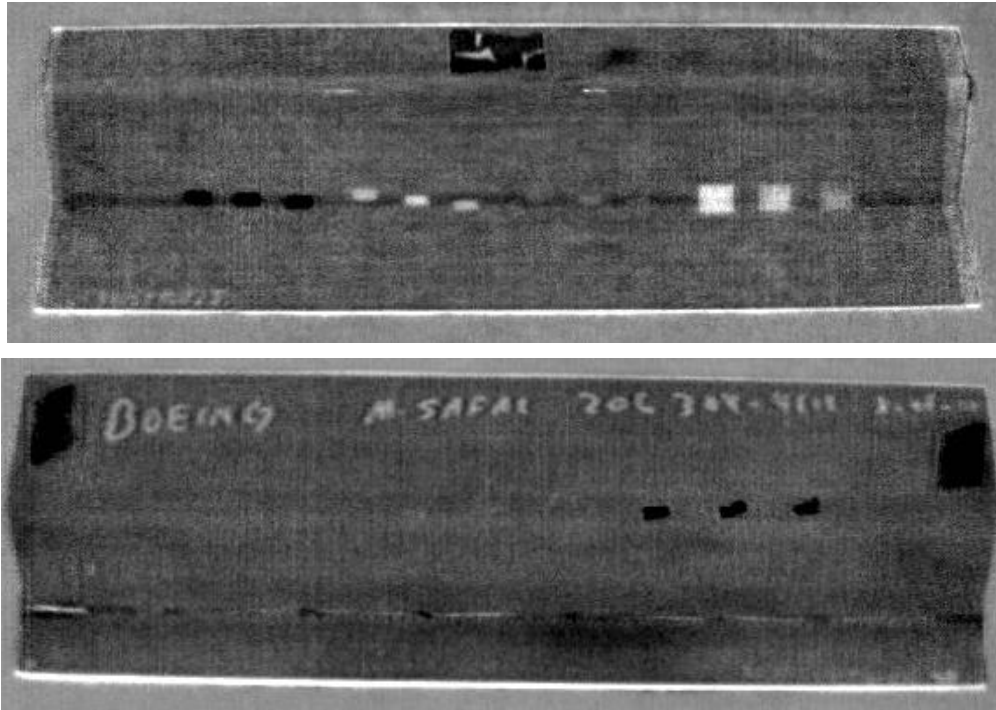
Figure 4.3-2. Standard 8276-200-58-8 A&B greyscale IR image standards with inserts.
(Top: PT and RPF, Bottom: brass).

4.3.2.3   X-ray CT

Unlike 2D X-ray imaging, XCT produces a full 3D volume of data and can display interior slice views of the object. This allows for detailed detection of flaws. Depending on the size of the specimen, which determines the achievable resolution, delamination damage is generally detectable with XCT. Visualization of the delaminations is facilitated by rotating the data volume such that the ply orientation of the composite is aligned with the x-, y- or z-plane. In this orientation, data from an interface between two plies are easily viewed as a 2D slice of the data. For panels with curvature, it is normally possible to map the coordinate system to a coordinate system where the ply interface is contained in a single plane.
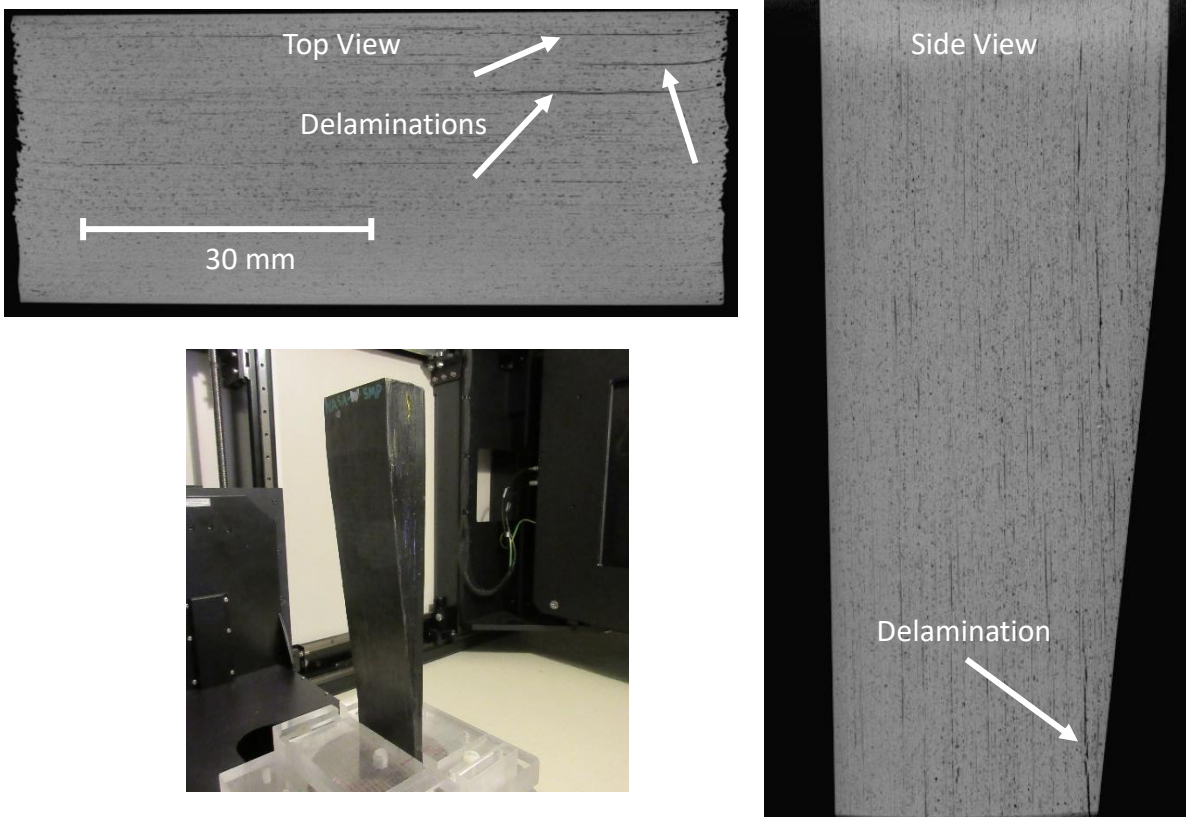
Figure 4.3-3. Standard NASA-W-5MP X-ray CT slices of delaminations within specimen.

4.3.2.4 Shearography

Shearography is a well-suited method for inspecting for delaminations that other methods may miss because it leverages the mechanical deformation effects from delaminations. Vacuum shearography, for instance, can cause the separation of plies in a closed delamination and detect the resulting deformation on the surface. However, shearography is limited by the complexity of the part. It can inspect contours and flat sections, but requires different mechanical excitation for different scenarios.

4.3.2.5 Computed Radiography and Digital Radiography

Standards were inspected using CR and DR, however the nature of delaminations makes inspection with these methods difficult, and radiography is one of the most cost prohibitive methods. This is because delaminations, as simple separation of plies, do not create a large change in density from a 2D perspective. Additionally, delaminations in intimate contact are nearly impossible to identify with these methods. In the case of the delamination standards, the different material types can potential be detected and the brass inserts are certainly visible, however this is not a proper representation of delaminations from a radiography perspective. CR was able to identify the insert

locations (Figure 4.3-4) because of its use of multiple angle projections, but CR is not a practical option in most production settings due to time, cost, and size constraints. For smaller parts with enough time however, it is an effective option that can accommodate many geometries and has excellent resolution. This makes CR a useful tool in development of parts or verifying other NDE techniques.

a) RPF.   *b) Brass.*   *c) Inserts.*
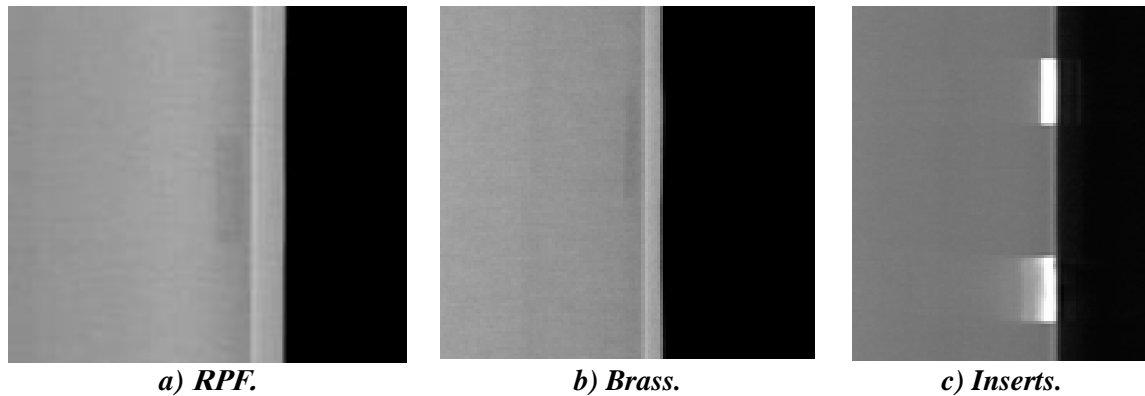
Figure 4.3-4. 8276-200-58-26 A&B CT slice view showing PT.

4.3.3 Delamination Standards

A summary of delamination standards and test methods is provided in Table 4.3-2. Due to number and breadth of samples and inspection methodologies, not all methods described above were tested. Instead, the handbook along with Appendix E acts as a preliminary guide to delamination inspection.

Table 4.3-2. Summary of delamination specimens tested by consortium.

#	Reference Standard	Structure	Material	Configuration/ Radius	Defects and features	Dimensions (inches)	Partner: Tests
16	NASA-RP-01D	Uni-ply 0/90/45	8552/IM7	0.1-inch radial inside curve, delams along curve & flat surfaces	Radius Panel 0.1-inch Curve Rad with defects	$4.5 \times 2.5 \times 4$	USC: GWUT
18	NASA-RP-10D	Uni-ply 0/90/45	8552/IM7	1.0-inch radial inside curve, delams along curve & flat surfaces	Radius Panel 1.0-inch Curve Rad with defects	$4.5 \times 2.5 \times 4$	USC: GWUT
19	NASA-RP-20D	Uni-ply 0/90/45	8552/IM7	2.0-inch radial inside curve, delams along curve & flat surfaces	Radius Panel 2.0-inch Curve Rad with defects	$4.5 \times 1.5 \times 4$	USC: GWUT
20	NASA-RP-40D	Uni-ply 0/90/45	8552/IM7	4.0-inch radial inside curve, delams along curve & flat surfaces	Radius Panel 4.0-inch Curve Rad with defects	$4.5 \times 1.25 \times 6$	USC: GWUT NASA: PEUT
35	8276-200-58-8 A	laminate	8276 Tape	S curve (__╱⌐) **58°** slant with two 0.2° radii	multiple types of delamination simulators (teflon, graton tape, air pillows, mold release wax, brass inserts, etc)	$20 \times 6 \times 2.4$	Boeing: PEUT, SSIR, DR, CR, XCT
36	8276-200-58-26 A	"	8276 Tape	S curve (__╱⌐) **58°** slant with two 0.2° radii	"	$20 \times 6 \times 2.4$	Boeing: PEUT, SSIR, DR, CR, XCT
37	8276-200-58-48 A	"	8276 Tape	S curve (__╱⌐) **58°** slant with two 0.2° radii	"	$20 \times 6 \times 2.4$	Boeing: PEUT, SSIR, DR, CR, XCT NASA: PEUT, XCT
38	8276-200-56-48 A	"	8276 Tape	S curve (__╱⌐) **56°** slant with two 0.2° radii	"	$20 \times 6 \times 2.4$	Boeing: PEUT, SSIR, DR, CR, XCT
39	8276-200-59-48 A	"	8276 Tape	S curve (__╱⌐) **59°** slant with two 0.2° radii	"	$20 \times 6 \times 2.4$	Boeing: PEUT, SSIR, DR, CR, XCT NASA: XCT
41	8276-200-58-26 B	"	8276 Tape	S curve (__╱⌐) **58°** slant with two 0.2° radii	"	$20 \times 6 \times 2.4$	NASA: XCT
43	8276-200-56-48 B	"	8276 Tape	S curve (__╱⌐) **56°** slant with two 0.2° radii	"	$20 \times 6 \times 2.4$	NASA: XCT
44	8276-200-59-48 B	"	8276 Tape	S curve (__╱⌐) **59°** slant with two 0.2° radii	"	$20 \times 6 \times 2.4$	NASA: XCT
1	NASA-S-D	Uni-ply 0/90/45	8552/IM7	Step heights: 0.1-inch to 1.0-inch, Delams: Ply 1, Mid Ply, Last Ply	Step with FBH defects	$1 \times 8 \times 1.5$	GE: PEUT, TTUT NGIS: PEUT

#	Reference Standard	Structure	Material	Configuration/ Radius	Defects and features	Dimensions (inches)	Partner: Tests
8	NASA-W-IL-20D	Uni-ply 0/90/45	8552/IM7	Height: 0.25-inch to 1.0-inch, 20 deg slope, delams start-end of slope	Wedge Interleaved 20 deg with defects	12 × 3 × 1.1	GE: PEUT, TTUT
11	NASA-W-IL-5D	Uni-ply 0/90/45	8552/IM7	Height: 0.25-inch to 1.0-inch, 5 deg slope	Wedge Step 5 deg with defects	12 × 3 × 1.5	GE: PEUT, TTUT; NASA: XCT
45	NASA-TAB-FBH-FLAT	Triaxial Braid, 0/+60/-60	T-800SC Triaxial Braid 0/+60/-60 with 3M AMD-825	Flat panel	Delam/ disbond (FBH)	16 × 10 × 0.75	GE: PEUT, TTUT; NASA: XCT USC: GWUT
47	NASA-TAB-P-FLAT	Triaxial Braid, 0/+60/-60	T-800SC Triaxial Braid 0/+60/-60 with 3M AMD-825	Flat panel	Delamination (Air Pillow)	13 × 13 × 0.5	GE: PEUT, TTUT; NASA: PEUT, XCT USC: GWUT
54	NASA-TAB-05P-FLANGE1	Triaxial Braid, 0/+60/-60	T-800SC Triaxial Braid 0/+60/-60 with 3M AMD-825	Flange	Delamination (Air Pillow)	12 × 4.5 × 2.5	GE: PEUT, TTUT
55	NASA-TAB-05P-FLANGE2	Triaxial Braid, 0/+60/-60	T-800SC Triaxial Braid 0/+60/-60 with 3M AMD-825	Flange	Delamination (Air Pillow)	12 × 4.5 × 2.5	NASA: SSIR, TTIR
52	NASA-TAB-BASE1-FLANGE	Triaxial Braid, 0/+60/-60	T-800SC Triaxial Braid 0/+60/-60 with 3M AMD-825	Flange	Baseline	11 × 4.5 × 2.25	GE: PEUT, TTUT

4.3.4 References

1. SOM/SEM based characterization of internal delaminations of CFRP samples machined by AWJM – Scientific Figure on ResearchGate. Available from: https://www.researchgate.net/figure/Detail-of-embedded-particles-in-fiber-delamination_fig3_288446023 [accessed 17 May, 2019]

4.4   FOD and Inclusions Inspection Guidance

4.4.1   FOD Detection and Characterization Executive Summary

The evaluation of FOD in composite parts is required by aerospace production procedures, especially for structural components to guarantee mechanical performance and safety standards. FOD can compromise the mechanical integrity of resulting structures. The techniques proven to be effective at detecting porosity are TTUT and IR and sometimes radiography. When selecting an inspection technique, consideration should be given to the type(s) of FOD needing to be detected and characterized.

During manufacturing it is possible that loose peel ply, bagging materials, metal etc. may embed themselves between laminae causing localized weaknesses, effective disbonds in the material, crack initiation locations, and regions of high stress. It is therefore critical to prevent and detect FOD in composite materials. Due to the variety of possible materials included in the general term of FOD, ranging from metals to thin layers of adhesive tape, it is more complicated to delineate specific NDE technologies that can effectively detect all FOD. Some techniques might work extremely well for metals while not detecting other FOD materials at all. TTUT is excellent at detecting some types of inclusions; however, it does not quantify the depth of defect, for example.

A brief overview of NDE methods is provided in Table 4.4-1. The FOD standards tested in a round-robin assessment in this project as well as the experience of SMEs among the Consortium members resulted in evaluation of NDE methods effective for the detection and evaluation of FOD as follows:

Effective Methods
- UT
- Thermography
- XCT
- Shearography

Marginally Effective Methods
- CR
- DR
- X-ray Backscatter

Ineffective Methods
- Visual
- GWUT

Participating Partner(S)
- NASA
- Boeing

Table 4.4-1. Advantages and disadvantages of various methods on detecting FOD/inclusions in composites.

Effective Detection and Characterization Methods for FOD/Inclusions		
Detection Method	**Advantages**	**Disadvantages**
Ultrasound	• Manufacturing maturity, widely supported in industry, numerous equipment and supplier options • Inexpensive options • Can be highly portable • Several automated systems available • Both single-sided and transmission configurations • Safety • Defect detection, discrimination, and depth determination techniques • Effective for most types of common FOD	• Typically requires coupling fluid that may contaminate or compromise the structure • Requires surface contact • Requires relatively smooth surface for good surface coupling • Automated systems and software for C-scan, B-scan imaging can be expensive • Manual and automated raster scanning for 100% inspection can be time consuming • May require complex contour following robotics and software for curved geometries
Single-Sided Thermography	• Relatively fast/large area inspection • Non-contact • No harmful radiation or surface heating • Relatively insensitive to changes in part contours, angles, and thicknesses—contour following robotics generally not required	• FOD width must be larger the deeper it is in the specimen. • FOD not detectable if material is of similar thermal diffusivity as composite unless the FOD causes an air gap to form around it (poor consolidation) • IR camera requires direct line of sight
XCT	• 3-dimensional view of complete volume promises detection of most types of FOD • Non-contact • Excellent potential for spatial fidelity, sizing, shape definition • Provides permanent visual digital scan record • Full volume density map with cross-sectional image slices and depth information • Relatively insensitive to changes in part contours, angles, and thicknesses—contour following robotics generally not required	• Radiation/shielding safety concerns • Typically, not portable • Requires access to all sides of the part • High initial equipment cost • Computationally intensive • Scans, software reconstruction, and data evaluation are time consuming • Requires large data storage capabilities • Not typically applicable to scan large parts or assemblies at high enough resolution. • Resolution related to part size.

	Images are relatively easy to interpret	

Shearography	• Relatively fast/large area inspection • Non-contact • Single sided inspection • No harmful radiation or surface heating • Relatively insensitive to changes in part contours, angles, and thicknesses—contour following robotics generally not required • Shown to detect some types of FOD	• Subsurface defects must be sufficiently large to cause surface deformations • Requires direct line-of-sight with imager • Defect depth determination is not straight forward without a-priori knowledge of the structure • May require surface coating or modification on glossy surfaces for successful inspection

Marginally Effective Detection and Characterization Methods for FOD		
Detection Method	**Advantages**	**Disadvantages**
Computed Radiography	• Sensitive to density variations, caused by material differences, voids, or other defects effecting the density of material the X-rays pass through. • Suitable for complex parts • Resolution generally better than DR • Faster results than film X-ray • Results dependant on FOD material (metallic inclusions can be detected while materials close in density to the composite cannot)	• 2D image - the results are superimposed images of the defects • Sensitive to defect orientation • Radiation safety concerns • Detection depends on density of inclusion • Cannot identify many common FOD materials
Digital Radiography	• Sensitive to density variations, caused by material differences, voids, or other defects effecting the density of material the X-rays pass through • Results dependent on FOD material (metallic inclusions can be detected while materials close in density to the composite cannot)	• 2D image - the results are superimposed images of the defects • Sensitive to defect orientation • Radiation safety concerns • Detection depends on density of inclusion • Cannot identify many common FOD materials

Marginally Effective Detection and Characterization Methods for FOD		
Detection Method	**Advantages**	**Disadvantages**
X-ray Backscatter	• Sensitive to material density changes that can be correlated to porosity • Non-contact • Single sided • Method is real-time or near-real-time	• Radiation safety concerns, particularly in portable applications • High initial equipment cost • Dependent on depth and density of inclusion.

	• Provides permanent visual record (film or digital image) • Can be portable with adequate safety precautions • Relatively insensitive to changes in part contours, angles, and thicknesses—contour following robotics generally not required	

Ineffective Detection and Characterization Methods for FOD		
Detection Method	**Advantages**	**Disadvantages**
Visual Inspection	• Direct and rapid inspection • Non-contact • Low-cost • Can be performed without instrumentation or with inexpensive equipment such as cameras, borescopes, and magnifiers • Can find imperfections inside radii and complex curvatures • Direct reporting with photographs	• Limited to surface inspections • Insensitive to bulk features • Requires direct line of sight • Observation data can be user-dependent • Porosity quantification often requires digital images and software
Guided Wave UT	• Large area inspection • Waves propagate long distances without much energy loss • Sensitivity to small defects	• For composites, still primarily a laboratory technique

4.4.2   FOD Inspection Technologies

A challenge posed by FOD/inclusion detection and characterization is the variety of different materials that are common FOD materials as described in Section 4.1.3. These materials range from thin metallic shavings to loose fibers, cloth, or tape. They are varying in both size and distribution. Size can range from fine fiber strands to large pieces of peel ply and may or may not have caused delaminations around the FOD.

A listing of inspection methods is provided in the following sections along with brief descriptions of common inspection strategies. A more extensive overview of the inspection methods is covered in Section 5 of this Handbook. Individual test reports for selected inspection methods for the NDE standards tested are provided in Appendix E, which include method, partners, samples descriptions, measurement setups, test results, and technique applicability ranking.

A brief overview of inspection methodologies used for FOD detection is provided below and includes a general listing of advantages and disadvantages for each general method.

4.4.2.1   Ultrasound

PEUT is generally a highly effective method for FOD detection, as shown in Figures 4.4-1 to 4.4.6. Water-coupled PEUT scans were performed on this standard to demonstrate the feasibility of detecting defects in thick carbon-composite laminates on a stepped-thickness panel with FOD placed throughout and laminate thickness ranging from 0.1 to 1.0 inch. Scans were performed from

the flat tool-side to determine detection dependency on both defect depth and diameter. Different frequencies including 2.25 MHz and 5.0 MHz were sampled to observe frequency dependence.

For higher frequency PEUT, thicker step panels can be too thick and attenuating. For lower frequency PEUT on thinner panels, internal and back wall gated signals could not be individually resolved due to the relatively large wavelength.

Figure 4.4-1. Photograph of NDE Standard #68, flat step panel with inclusions.
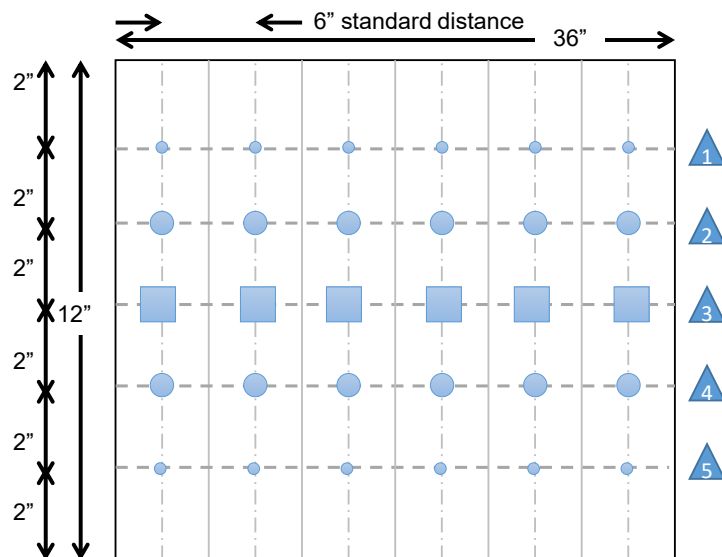
Figure 4.4-2. Defect map within NDE standard #68.

63
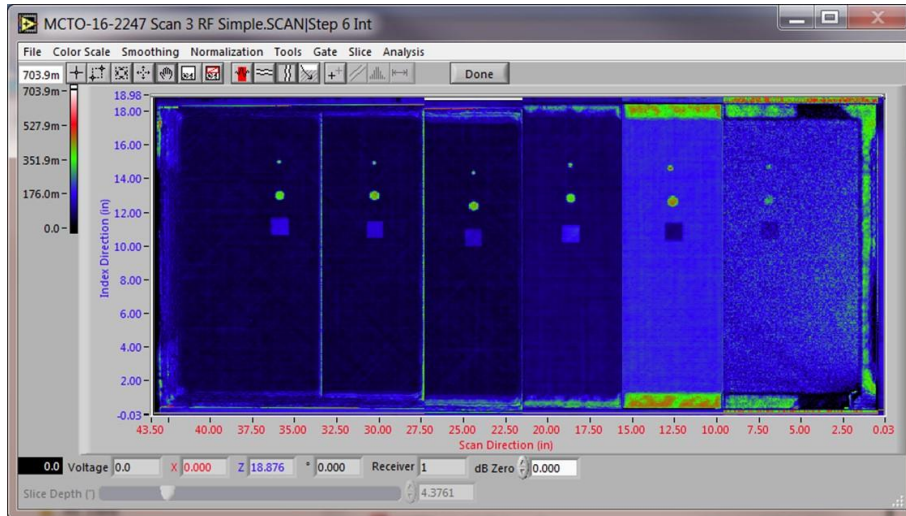
Figure 4.4-3. PEUT C-scans at 2.25 MHz for steps 1-6 (internal gate).
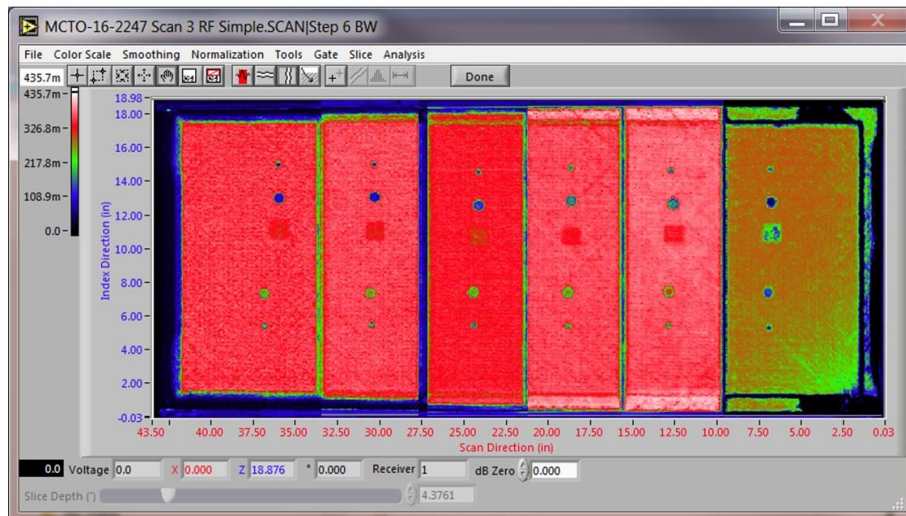
Figure 4.4-4. PEUT C-scans at 2.25 MHz for steps 1-6 (back wall gate).
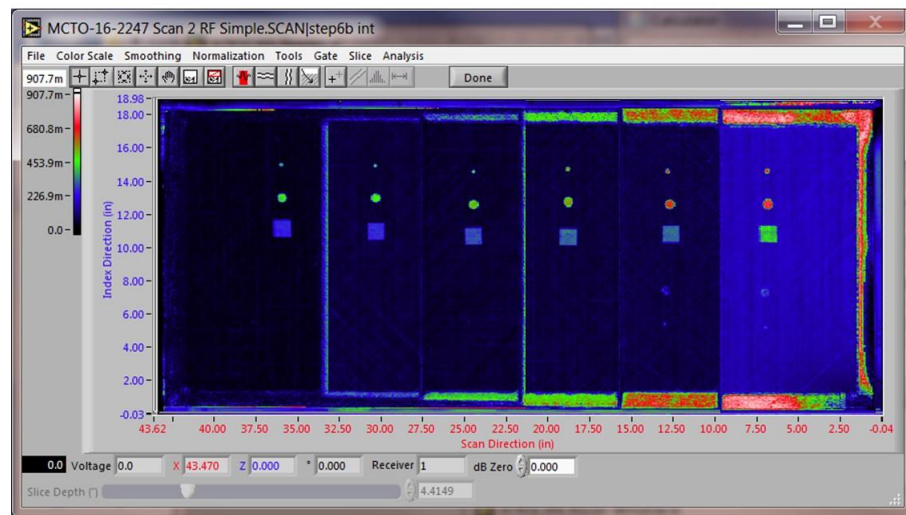
Figure 4.4-5. PEUT C-scans at 5.0 MHz for steps 1-6 (internal gate).

64
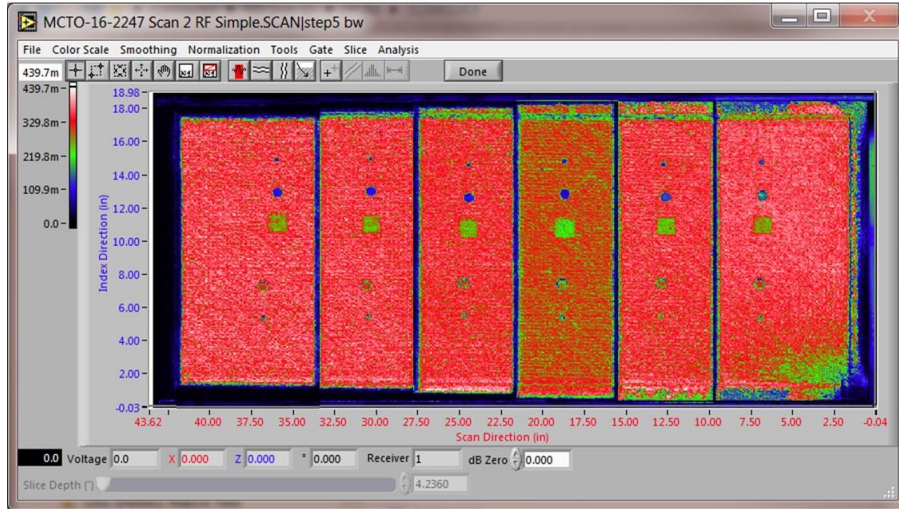
Figure 4.4-6. PEUT C-scans at 5.0 MHz for steps 1-6 (back wall gate).

4.4.2.2 Thermography

Thermography is a very effective method to detect various inclusions in a composite panel. Its large area and fast inspection capabilities make it ideal for use as a first route inspection technique. It also lends itself to robotic automation (see Section 5.6.2). Depending on the FOD material and its location within the thickness of the composite, different inclusions will appear at different times after the heat pulse—the deeper the defect the later in time it will appear. For FOD materials that are on the order of the diffusivity of the CFRP composite itself, the ability of thermography to detect the FOD will depend largely on whether or not the FOD resulted in a small air gap around the FOD. As a general rule of thumb, detection of defects in thermography is limited to defects of width greater than 2 times the depth of the defect.

Examples of thermographic detection of inclusions in the NDE standards developed under the ACP are shown below using the S-curve Standards. The S-curve standards are carbon fiber composite panels with foreign material inserts in various layers to evaluate the detectability. These inserts are largely grouped around the angle in the panel, however not exclusive to this area. The standards vary in thickness, utilizing 8, 26, and 48 plies of carbon fiber fabric with exterior layers of fiberglass. Thermography results on standard #36 (Figure 4.4-7) are shown in Figure 4.4-8.

Because the flash heat diffuses through the thickness of the part, inserts at different layers should appear most clearly at varying times. This can be observed in the lower image of Figure 4.4-8, where one set of inserts gives a significant thermal signature while the others are just starting to show, because the thermal diffusion wave has not interacted with the deeper inserts yet. Similarly, the uppermost sets of inserts show up most clearly in the upper image. As the heat wave progresses through the material, the inserts heat up and cool faster than the surrounding material, leading to initially lighter indications followed by darker indications as time progresses. This is seen in the upper image where the PT inserts close to the surface have begun to cool faster (dark) while the lower inserts are heating up faster (light).
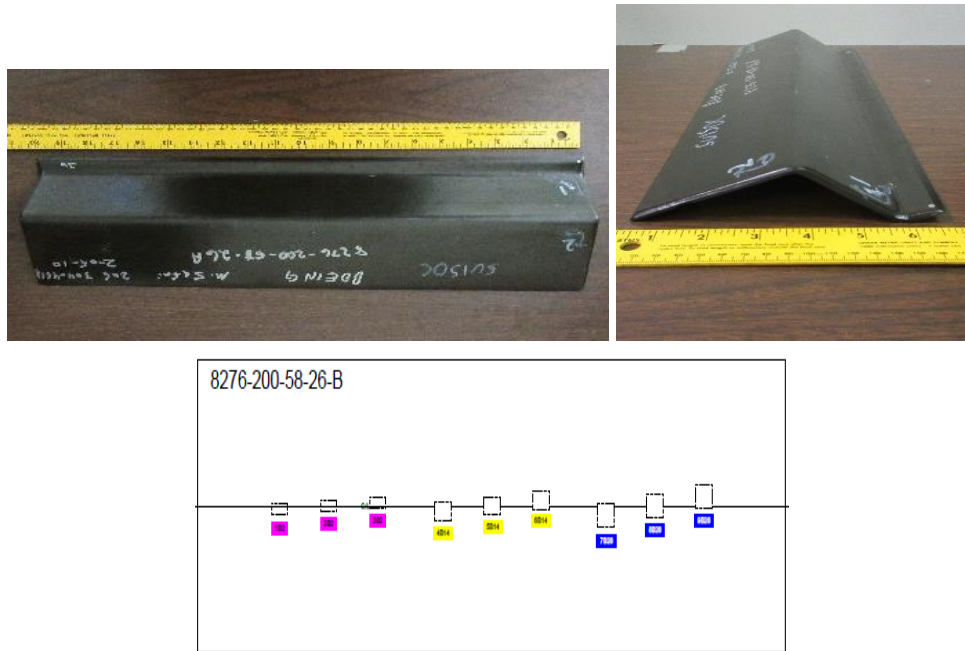
Figure 4.4-7. Photographs and inclusion map of NDE standard #36.
Purple inclusions are brass, yellow inclusions are PT and RPF, Blue are brass inclusions located between deeper plies.
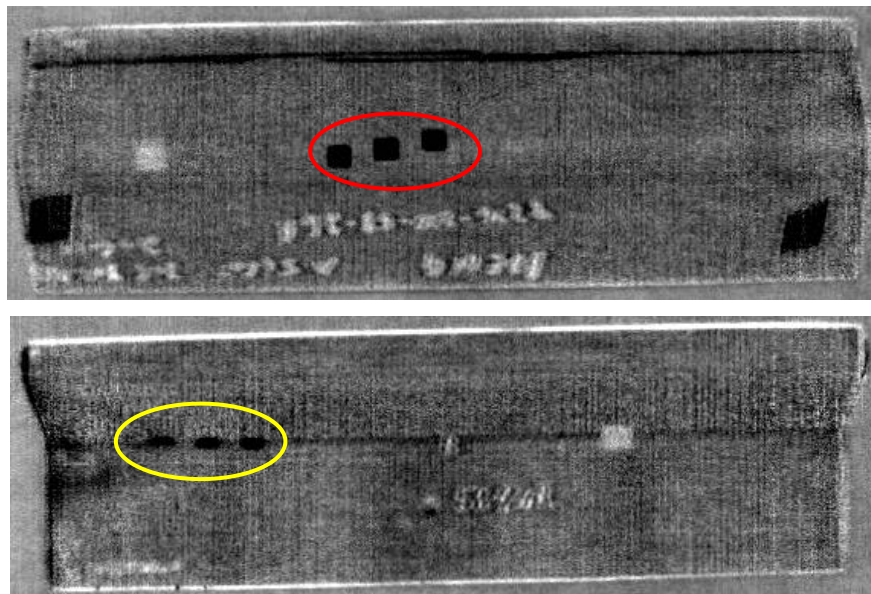
Figure 4.4-8. Greyscale IR image of radii delamination standard inserts.
(Top: PT and RPF, Bottom: brass). The top image is earlier in time after the flash heat was applied, showing near surface PT inclusions (red circle). In the lower image (later in time), the deeper brass inserts (yellow circle) are visible.

4.4.2.3   Radiography

4.4.2.3.1   Computed Radiography (CR) and Digital Radiography (DR)

CR X-ray imaging is sensitive to density variations, caused by material differences, voids, or other defects effecting the density of material the X-rays pass through. Because this imaging is 2D, the

results are superimposed internal images of the specimens. The resulting digital images are 16-bit greyscale images with the greyscale values representing the material density at each location (lighter corresponding to denser regions). Brightness and contrast settings are varied to make defects visible. In addition, multiple filters are used to make defect identification easier for the operator. In the standards, the inserts show as rectangular areas with lighter values (negative image).

Using the same NDE standard #36 described in Figure 4.4-7 illustrates the capability of CR to detect FOD in CRFP composites. The PT and RPF inserts are undetected for this laminate thickness (Figure 4.4-9a and b). Because the densities of the carbon fiber base material and the inserts are similar, a single ply insert does not create a large enough density variation, limiting the detectability. The brass inserts, however, cause a very large density variation and are readily observable in all laminate thicknesses (Figure 4.4-9c). Metal FOD in composite structures often show this degree of detectability due to the relatively high density of the metal compared to the composite.

| *a) RPF.* | *b) Brass.* | *c) Insert locations for 8276-200-58-26 standard (filter applied).* |
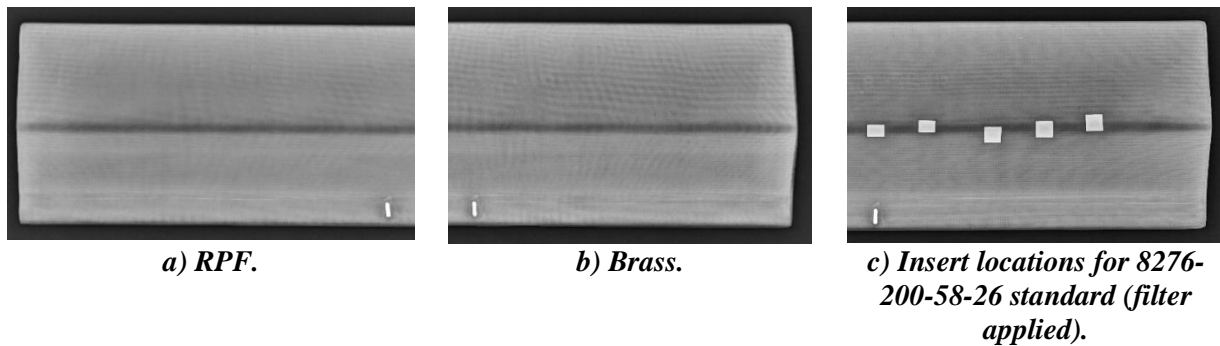
Figure 4.4-9. CR images of PT.
X-ray CR is capable of detecting the brass inserts but is unable to detect the PT and RPF inserts.

Similarly, the same NDE standard #36 was tested using DR with the expected results very comparable to CR. Figure 4.4-10 illustrates the DR results for this specimen.

The PT and RPF inserts are undetectable in this laminate thickness (Figure 4.4-10a and b). Because the densities of the carbon fiber base material and the inserts are similar, a single ply insert does not create a large density variation, thereby limiting the detectability. This detectability also drops as the laminate increases in thickness. The brass inserts, however, cause a very large density variation and are readily observable in all laminate thicknesses (Figure 4.4-10c). Metal FOD in composite structures often show this degree of detectability due to the relatively high density of the metal compared to the composite.

| *a) RPF.* | *b) Brass.* | *c) Insert locations in 8276-200-58-26 standard.* |
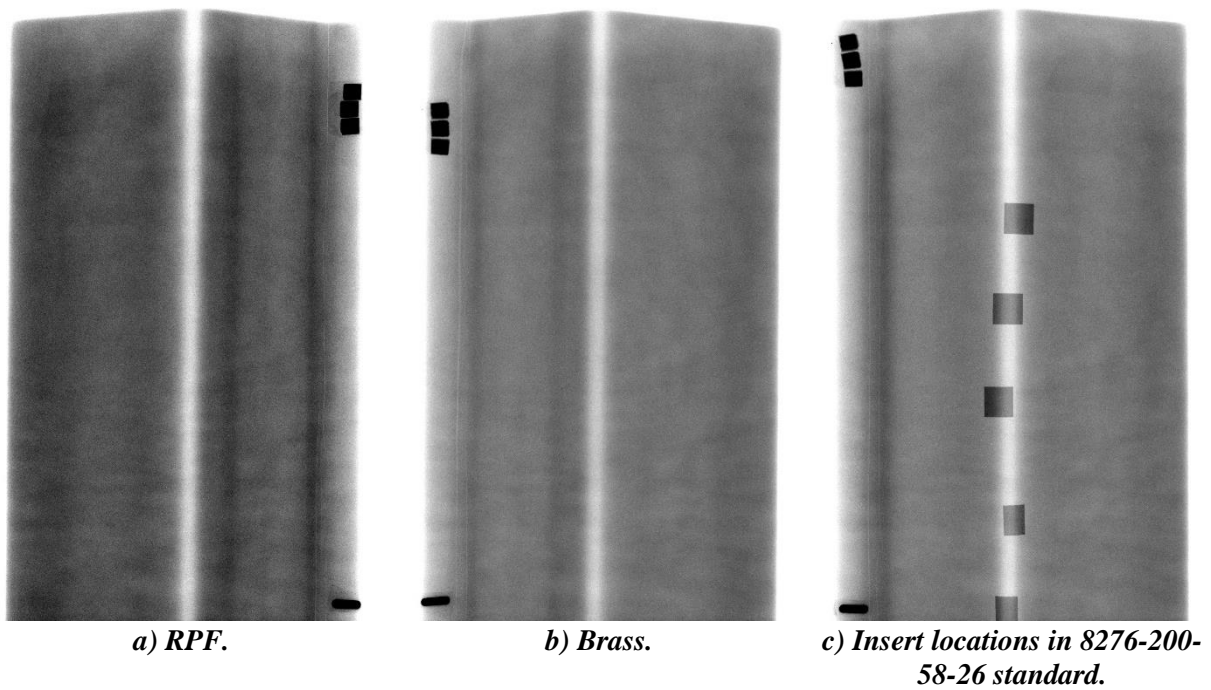
Figure 4.4-10. DR images of PT.
X-ray CR is capable of detecting the brass inserts but is unable to detect the PT and RPF inserts.

4.4.2.3.2   Backscatter X-ray

Backscatter X-ray is particularly sensitive to material differences that cause large variations in scatter. Metallic foreign material or water in honeycomb panels are examples of detectable phenomena. It is not sensitive in thicker parts however, as the scattered X-rays deeper in the part fail to generate a clear image. In this standard, the brass inserts provide a detectable scatter, however this scatter is only resolved in the shallow layers, becoming fainter and undetectable at the back layers. This is seen in Figure 4.4-11 as the shallow inserts on the left side (red circle) are clearly detectable, but the deeper inserts in the middle (white circle) are faint with the back inserts located to the right (yellow circle) not visible at all. The indications on the sides of the panel are the grips used to hold the part for scanning.
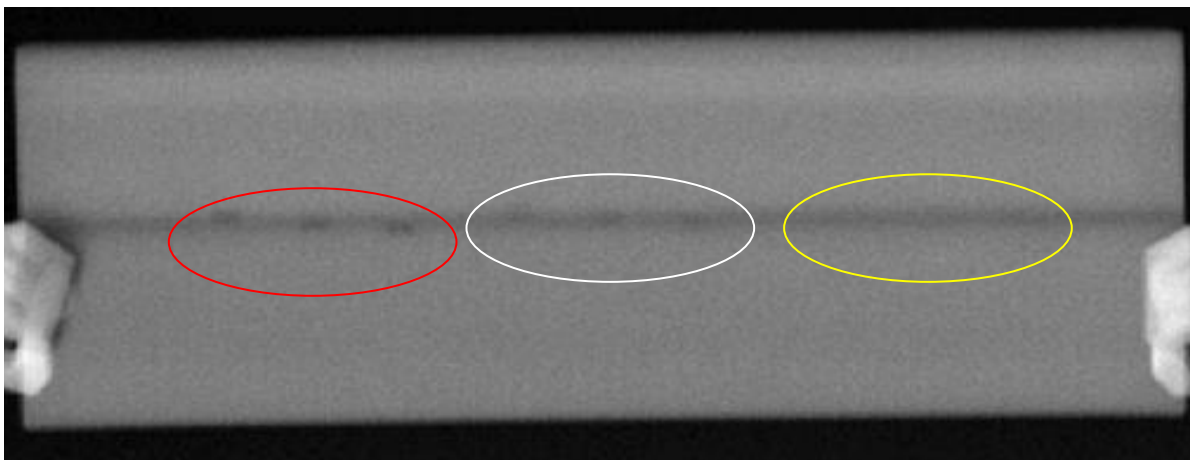
Figure 4.4-11. X-ray backscatter image of 8276-200-58-26 standard with brass inserts.

68

4.4.2.3.3   X-ray Computed Tomography (XCT)

XCT results are shown below to easily detect the brass inserts (Figure 4.4-12) and to be capable of detecting the PT and RPF inserts (Figure 4.4-13), for specimen #39, an S curve 59° slant with two 0.2" radii. There are multiple types of delamination simulators within the sample. X-ray CT was performed on this specimen in NASA Langley's large CT system with the settings defined in E.39.1.6. The scan was done in segments to ensure high resolution. The segments can be stitched together using post processing.

Figure 4.4-12. CT slice of specimen #39 Boeing-8276-200-56-48B view showing detectability of simulated disbonds (inserts).

After aligning the volume coordinate system to correspond with the panel geometry, the slice view can be used to inspect conditions at each lamina. The inserts are clearly visible (Figure 4.4-12), showing with less density for PT and RPF and higher density for brass. The brass is the most readily observable, followed by the PT with the RPF having the lowest detectability. The RPF may show the least response due to similar density to base material or due to a strong interface with little voiding or delamination to be detected.

The CT scanning and reconstruction process is subject to artificial and undesirable artifacts. These are the result of multiple conditions. The direction of rotation leaves an underlying direction to the noise of the data set, aligning with the rotation. This is seen as a light, roughly vertical streaking seen in Figure 4.4-12. The presence of high-density material in an otherwise low-density structure often creates even more intense ray artifacts, seen as shadow-like streaks emanating from the high-density material. If defects are present in these dark artifacts, their detectability is reduced. Lastly, the part may rotate in and out of the cone-beam of the X-rays during the scan, leaving the top and bottom edges of the volume not fully defined.

The detectability of the inserts relies on viewing the slices at the appropriate angle, which aligns with the lamina. This means the inserts within the curve of the panel, while still detectable, are less apparent (Figure 4.4-13), and operators must be careful to attempt to identify them. The inserts are also more visible when they induce delamination with air or if they have a much greater density than the composite material. The delaminations can be seen from all viewing directions. The white

69

regions represent inserts of higher density than the bulk within the specimen to simulate delaminations. The specimen is fabricated in such a way that the delaminations are present in the curved radius as well as the flat regions at varying depths. No matter the depth or region of the specimen, all simulated defects are easily viewed.
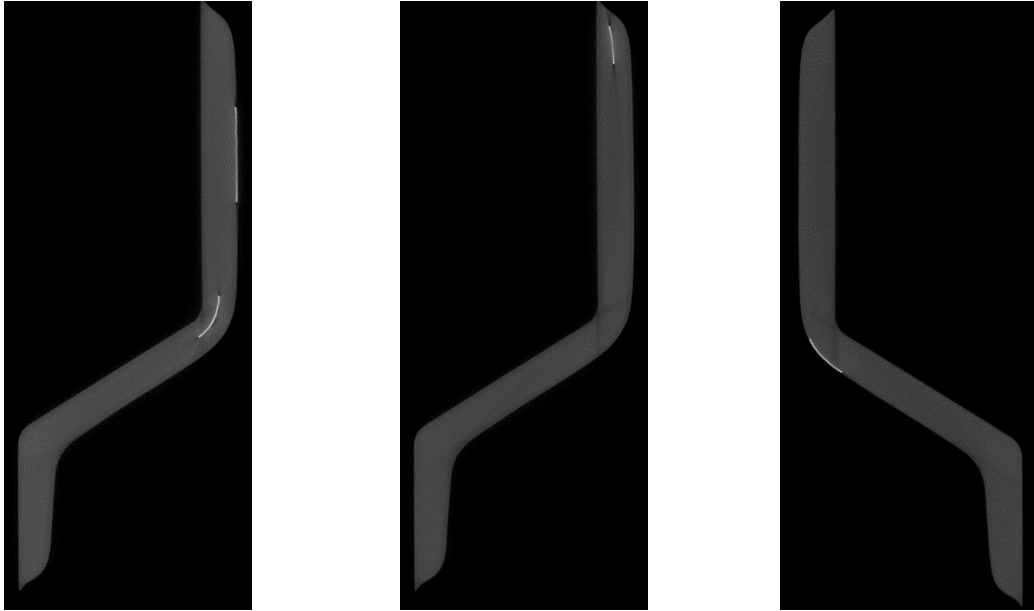
Figure 4.4-13. CT slice view showing PT and RPF inserts.

4.4.2.4   Shearography

Shearography is capable of detecting FOD in CFRP composites as shown in Figure 4.4-14. None of the NDE standards developed under the ACP containing FOD were tested with shearography. However, detection of FOD in composites has been shown in composite inspections.

4.4.2.5   Visual

Visual inspection of FOD and inclusions is applicable only to the extent that the FOD produces a bump in the laminate surface, typically only at the top or bottom layer of the composite panel depending on the thickness of the FOD. Therefore, visual inspection is not typically constructive for detection of inclusions.

4.4.3   FOD Standards

A summary of FOD standards and test methods is provided in Table 4.4-2. Due to number and breadth of samples and inspection methodologies, not all methods described above were tested. Instead, the Handbook along with Appendix E acts as a preliminary guide to FOD inspection.

Table 4.4-2. Summary of FOD specimens tested by consortium.

#	Reference Standard	Structure	Material	Configuration / Radius	Defects and features	Dimensions (inches)	Partner: Tests
68	NASA-03-FOD-Panel-001	Fiber Placed Panel	IM7/8552-1 Slit Tape w/ IM7/8552 Fabric OML	Flat panel	FOD	19 × 43 × 0.3	GE: PEUT, TTUT; NASA: XCT NGIS: PEUT, TTUT
35	8276-200-58-8 A	laminate	8276 Tape	S curve (__/⎺) **58°** slant with two 0.2° radii	multiple types of delamination simulators (teflon, graton tape, air pillows, mold release wax, brass inserts, etc)	20 × 6 × 2.4	Boeing: TTUT, SSIR, DR, CR, Backscatter, XCT
36	8276-200-58-26 A	"	8276 Tape	S curve (__/⎺) **58°** slant with two 0.2° radii	"	20 × 6 × 2.4	Boeing: TTUT, SSIR, DR, CR, XCT
37	8276-200-58-48 A	"	8276 Tape	S curve (__/⎺) **58°** slant with two 0.2° radii	"	20 × 6 × 2.4	Boeing: PEUT, SSIR, DR, CR, XCT NASA: PEUT
38	8276-200-56-48 A	"	8276 Tape	S curve (__/⎺) **56°** slant with two 0.2° radii	"	20 × 6 × 2.4	Boeing: TTUT, DR, CR, XCT
39	8276-200-59-48 A	"	8276 Tape	S curve (__/⎺) **59°** slant with two 0.2° radii	"	20 × 6 × 2.4	Boeing: TTUT, DR, CR, XCT NASA: XCT
43	8276-200-56-48 B	"	8276 Tape	S curve (__/⎺) **56°** slant with two 0.2° radii	"	20 × 6 × 2.4	NASA: XCT
44	8276-200-59-48 B	"	8276 Tape	S curve (__/⎺) **59°** slant with two 0.2° radii	"	20 × 6 × 2.4	NASA: XCT

4.5 Fiber Defects Inspection Guidance

4.5.1 Fiber Defect Detection and Characterization Executive Summary

Detection of fiber defects includes methods suitable for both *in situ* detection during AFP tape layup process, as well as methods suitable for detection in cured AFP or sheet layup parts. *In situ* inspection of AFP fiber defects is covered in detail in Section 5.6.3.2. The 20 Fiber Defect NDE standards developed under the ACP are cured sheet layup parts. Detection of fiber defects in these standards that is discussed in this section.

The techniques proven to be effective at detecting fiber defects (for AFP and non AFP, such as hand layup parts) are PEUT, IRT, and XCT. GWUT has shown promise in the detection of fiber wrinkles but is still primarily a laboratory technique.

A brief overview of NDE methods is provided in Table 4.5-1. The fiber defect standards tested in a round-robin assessment in this project as well as the experience of SMEs among the Consortium members resulted in evaluation of NDE methods effective for the detection and evaluation of fiber defects as follows:

Effective Methods
- UT
- Thermography
- XCT

Marginally Effective Methods
- GWUT
- Shearography

Ineffective Methods
- Visual

Participating Partner(S)
- NASA

Table 4.5-1. Advantages and disadvantages of various methods on detecting fiber defects in composites.

Effective Detection and Characterization Methods for Fiber Defects		
Detection Method	**Advantages**	**Disadvantages**
Ultrasound	• Manufacturing maturity, widely supported in industry, numerous equipment and supplier options • Inexpensive options • Can be highly portable • Several automated systems available • Detected all types of fiber defects tested: twists, folds, laps, gaps, wrinkles • Both single-sided and transmission configurations	• Typically requires coupling fluid that may contaminate or compromise the structure • Requires surface contact or water based coupling for noncontact • Requires relatively smooth surface for good surface coupling • Automated systems and software for C-scan, B-scan imaging can be expensive

Effective Detection and Characterization Methods for Fiber Defects		
Detection Method	**Advantages**	**Disadvantages**
	• Safety • Defect detection, discrimination, and depth determination techniques • Effective for all most types of common fiber defects	• Manual and automated raster scanning for 100% inspection can be time consuming • May require complex contour following robotics and software for curved geometries
Single-Sided Thermography	• Relatively fast/large area inspection • Non-contact • No harmful radiation or surface heating • Relatively insensitive to changes in part contours, angles, and thicknesses—contour following robotics generally not required • Suitable for detection of AFP fiber defects of folds and missing tows • Suitable for detection of fiber wrinkles in ply layup composite	• Difficult to detect twisted tow fiber defects. • IR camera requires direct line of sight
XCT	• 3-dimensional view of complete volume promises detection of most types of fiber defects • Non-contact • Excellent potential for spatial fidelity, sizing, shape definition • Provides permanent visual digital scan record • Full volume density map with cross-sectional image slices and depth information – extremely detailed damage information • Provides validation of defect detection for other NDE technique development • Images are relatively easy to interpret	• Radiation/shielding safety concerns • Typically, not portable • Requires access to all sides of the part • High initial equipment cost • Computationally intensive • Scans, software reconstruction, and data evaluation are time consuming • Requires large data storage capabilities • Not typically applicable to scan large parts or assemblies at high enough resolution. • Resolution related to part size

Marginally Effective Detection and Characterization Methods for Fiber Defects		
Detection Method	**Advantages**	**Disadvantages**
Shearography	• Relatively fast/large area inspection • Non-contact • Single sided inspection • No harmful radiation or surface heating • Relatively insensitive to changes in part contours, angles, and thicknesses—contour following robotics generally not required	• Subsurface defects must be sufficiently large to cause surface deformations • Requires direct line-of-sight with imager • Defect depth determination is not straight forward without a-priori knowledge of the structure

	• Capable of detecting fiber defects such as wrinkled fibers and fiber bridging	• May require surface coating or modification on glossy surfaces for successful inspection
Guided Wave UT	• Large area inspection • Waves propagate long distances without much energy loss • Sensitivity to small defects • Detected fiber wrinkle defects	• For composites, still primarily a laboratory technique

Ineffective Detection and Characterization Methods for Fiber Defects		
Detection Method	**Advantages**	**Disadvantages**
Visual Inspection	• Direct and rapid inspection • Non-contact • Low-cost • Can be performed without instrumentation or with inexpensive equipment such as cameras, borescopes, and magnifiers • Can find imperfections inside radii and complex curvatures • Direct reporting with photographs	• Limited to surface inspections • Insensitive to bulk features • Requires direct line of sight • Observation data can be user-dependent • Fiber defect quantification often requires digital images and software • Requires defect to alter surface for detection

4.5.2 Fiber Defects Inspection Technologies

Detection of AFP defects including twists, folds, overlaps of tape courses, gaps between tape courses, wrinkles, and bridging defect standards after composite part completion. Eleven defect standards typical of AFP defects were created for the ACP. Fiber defects found in sheet layups include in or out of plane fiber waviness, wrinkles, and snags. Nine of these standards were created for the ACP.

A brief overview of inspection methodologies used for fiber defect detection is provided below and includes examples for each NDE technique.

4.5.2.1 Ultrasound

UT is an effective method to detect both AFP fiber defects such as twists and folds as well as ply layup fiber defects such as wrinkles.

Specimen #57 (photographs shown in Figure 4.5-1), is a fiber placed flat panel fabricated from IM7/8552-1 Slit Tape with the objective of achieving twisted tows beneath the first ply of the sample. PEUT testing was performed on this specimen with results shown in Figure 4.5-2. Evidence of three twisted tows in the material appears in the middle of the specimen. The fiber twists reflect and cause perturbations in the ultrasonic waves that differ from the pattern representing the bulk of the material. This difference, while small, makes detection of the twisted tows possible. These defects were detected at a depth of .02 inch.
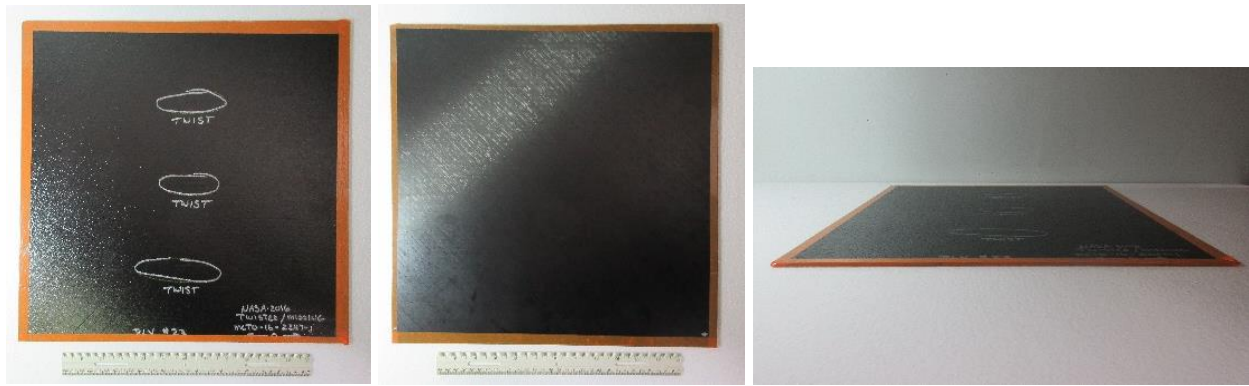
Figure 4.5-1. Photographs of specimen #57: NASA 03 Twisted Tow 001.
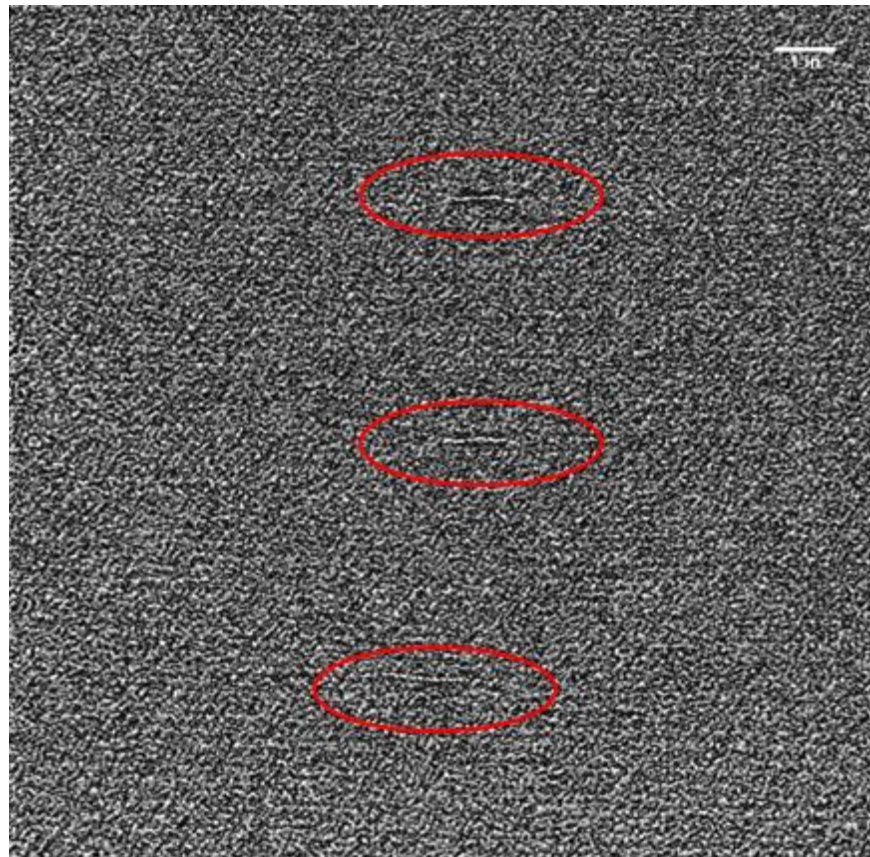
Figure 4.5-2. UT image showing surface flaws on a near-surface twisted tows.

Specimen #60 (photographs shown in Figure 4.5-3), is a fiber placed flat panel fabricated from IM7/8552-1 Slit Tape with the objective of achieving folded tows beneath the first ply of the sample. PEUT testing was performed on this specimen with results shown in Figure 4.5-4. Evidence of three folded tows in the material appears in the middle of the specimen. The fiber folds reflect and cause perturbations in the ultrasonic waves that differ from the pattern representing the bulk of the material. This difference, while small, makes visual detection of the folded tows possible. These defects were detected at a depth of 0.006 inch just below the first ply of the composite.
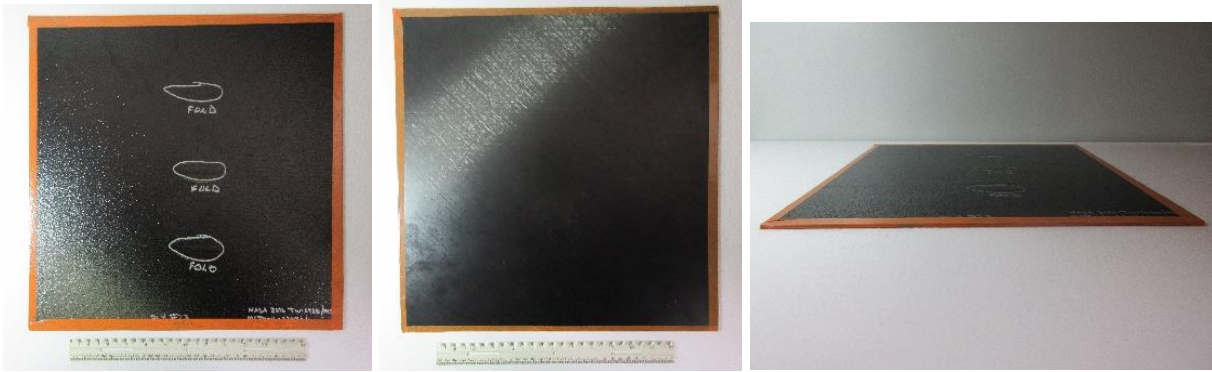
Figure 4.5-3. Photographs of NDE standard #60: NASA-03-Folded Tow 001.
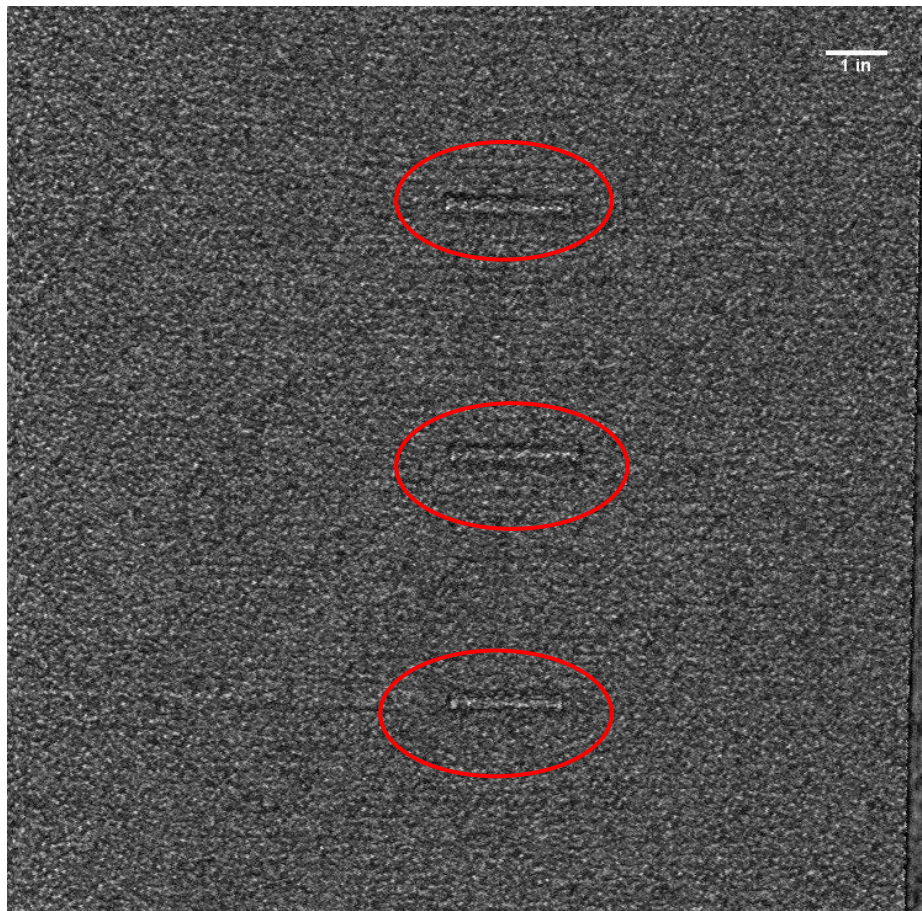
Figure 4.5-4. UT image showing folded tows near surface of the specimen.

A photograph of NDE standard #31 is shown in Figure 4.5-5 (left). Fiber wrinkles in this standard are easily detected and characterized by PEUT. PEUT images taken at an early time step show the indications of fiber wrinkling near the surface of the material. The wrinkles cause severe perturbations in the ultrasonic waves that are easily seen throughout the sample as shown in Figure 4.5-5 (right).
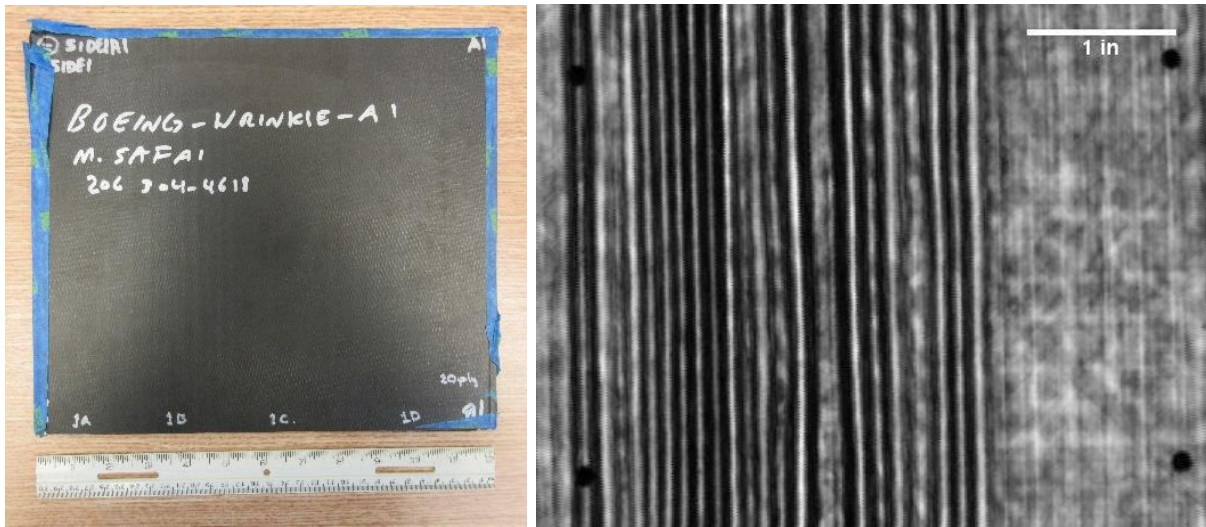
Figure 4.5-5. (Left) Photograph of Specimen #31: Boeing Wrinkle A1. (Right) PEUT image showing indications of fiber waviness within the material bulk.

4.5.2.2 Thermography

While AFP fiber twists were not detected with thermography, other AFP fiber defects such as folds and missing tows were detected using thermography. Thermography is also a very effective method to detect ply layup fiber defects such as wrinkles.

Thermography results for NDE standard #57 (photographs in Figure 4.5-1) are shown in Figure 4.5-6. The twisted tows are not visible in this image. Based on the UT data shown in Figure 4.5-2, the most likely reason for thermography not being able to detect the twisted tows has the do with the width of the tow being extremely narrow as the tow is turned vertically compared to the depth of the twist. The variation in contrast across the specimen is consistent with thermography indications of resin rich and resin poor areas.
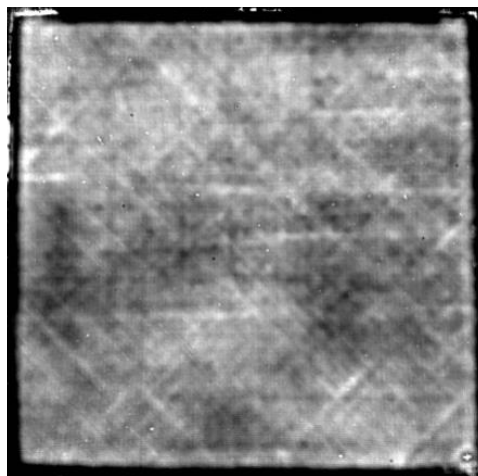
Figure 4.5-6. Thermographic Signal Reconstruction (TSR) 2nd derivative at 9.20 sec of #57-Twisted Ply standard.
No twisted plies detected.

Thermography results for NDE standard #60 (photographs in Figure 4.5-3), a folded tow AFP standard, show three easily observed subsurface indications. The folded tows were confirmed to

77

be subsurface by their late divergence in the logarithmic temperature time plot. The 1st derivative at 21.36 seconds was used to produce the final inspection images shown in Figure 4.5-7.
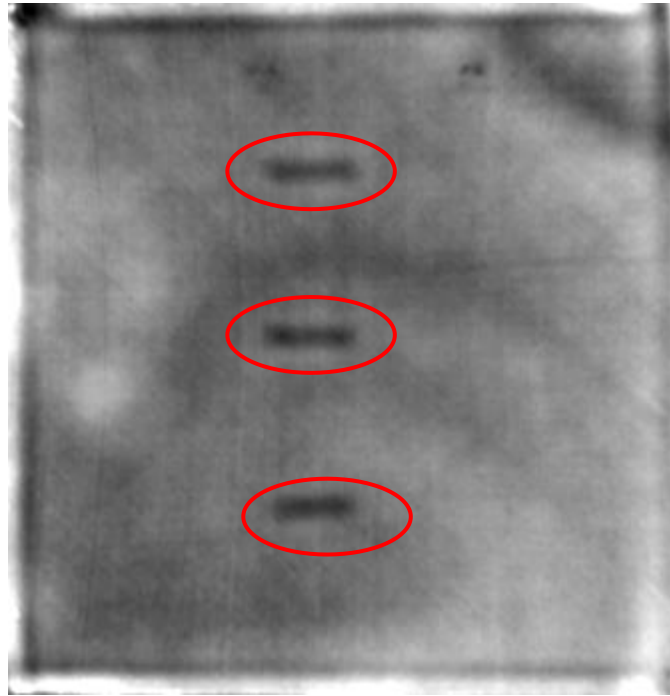
Figure 4.5-7. TSR 1st derivative at 21.36 sec of #60-Folded Tow NDE Standard.

Another type of AFP fiber defect is a missing tow. NDE standard #62 contains three missing tows as shown in Figure 4.5-8.

Figure 4.5-8. Photographs of specimen #62: Missing Tow.

Three subsurface indications were observed and are shown in Figure 4.5-9. The indications are confirmed to be subsurface by their late divergence in the logarithmic temperature time plot. The 1st derivative at 20.18 seconds was used to produce the final inspection images shown in Figure 4.5-9.
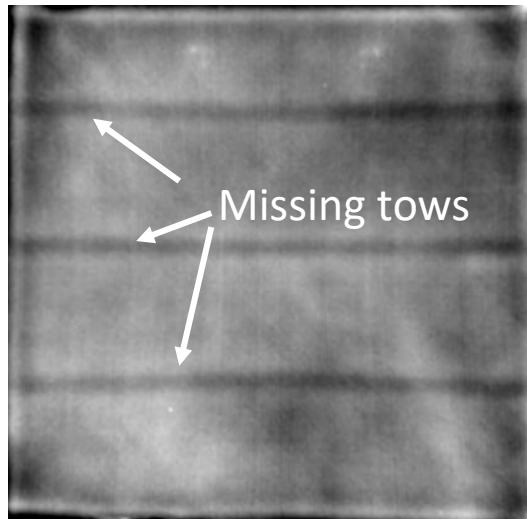
Figure 4.5-9. TSR 1ˢᵗ derivative at 20.18 sec of #62-Missing Tow Ply #23.

Thermography results for the same specimen #31 shown in Figure 4.5-5 (left) are detailed in Figure 4.5-10. These figures show the IR image of the sheet layup (non-AFP) panel at 1.6 seconds. As anticipated, hot and cold spots can be observed (circled in red), corresponding with the manufactured wrinkle locations. Because the panel was uniformly heated on the side that the camera observed, the strongest thermal gradient will come from the wrinkles on that side. Because of this, one can observe fainter, mirrored indications of the wrinkles when observed from the opposite side, such as the left side grouping of wrinkles in Figure 4.5-10a appearing fainter on the right side in Figure 4.5-10b. From these data, it is possible to measure the wavelength of the wrinkles, though the amplitudes cannot be determined from these data.

a) Side 1.   *b) Side 2.*
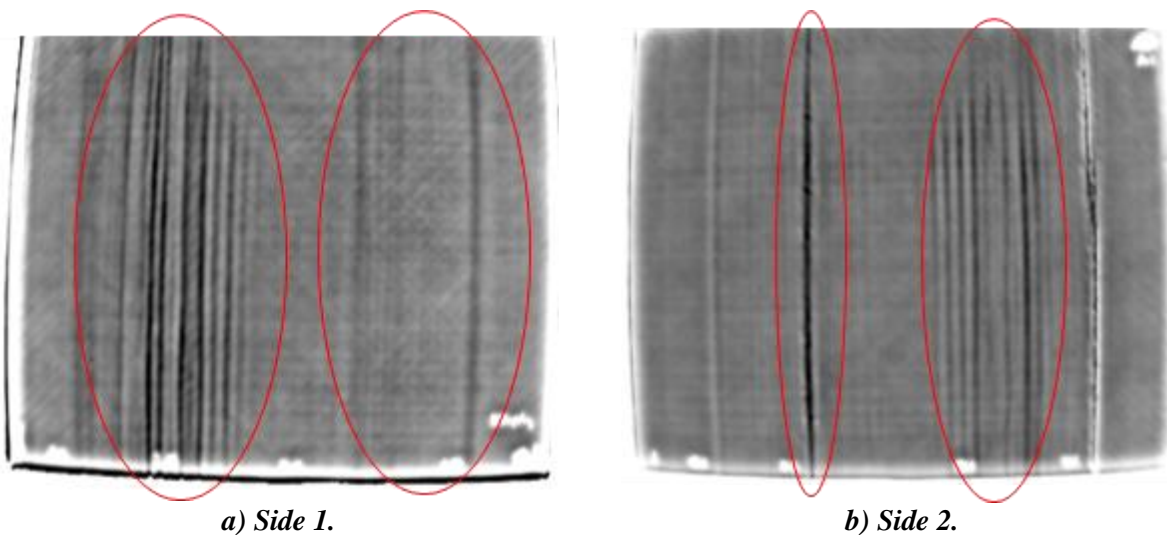
Figure 4.5-10. IR image 1.6s after flash of Wrinkle Standard #31.

4.5.2.3   XCT

Depending on the size of the specimen (which determines the achievable resolution), fiber defects are generally detectable with XCT. Visualization of fiber tow damage is facilitated by rotating the data volume such that the surface of the composite aligned with the x-, y- or z-plane. In this orientation, data from an interface between two plies are easily viewed as a 2D slice of the data.

For panels with some curvature, it is normally possible to map the coordinate system to a coordinate system where the ply interface is contained in a single plane.

XCT data are shown for Specimen #31, A1 (Figure 4.5-13), a wrinkled fiber NDE standard, the CT enables a quantitative measurement of the waviness.
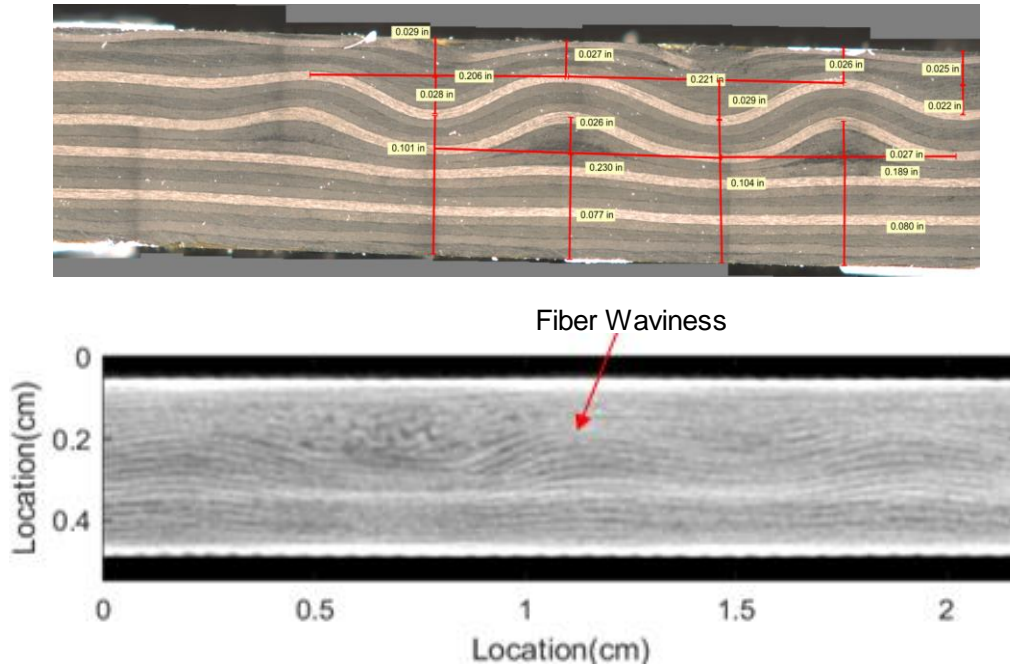
Figure 4.5-13. Microscope photograph of typical fiber waviness (top), and XCT slice of fiber waviness (bottom).

4.5.2.4   Shearography

None of the round-robin fiber defect standards were inspected with shearography. However, shearography systems have been shown to detect some fiber defects such as wrinkled fibers and fiber bridging.

4.5.3   Fiber Defects Standards

A summary of fiber defect standards and test methods is provided in Table 4.5-2. Due to number and breadth of samples and inspection methodologies, not all methods described above were tested. Instead, the Handbook along with Appendix E acts as a preliminary guide to fiber defect inspection.

Table 4.5-2. Summary of fiber defect standard specimens tested by consortium.

#	Reference Standard	Structure	Material	Configuration/ Radius	Defects and features	Dimensions (inches)	Partner: Tests
57	NASA-03-Twisted-Tow-001	Fiber Placed Panel	IM7/8552-1 Slit Tape	Flat panel	Twisted Tow - 1 ply	$16 \times 16 \times 0.15$	NASA: PEUT, SSIR, TTIR
58	NASA-03-Twisted-Tow-002	Fiber Placed Panel	IM7/8552-1 Slit Tape	Flat panel	Twisted Tow - Mid	$16 \times 16 \times 0.15$	NASA: PEUT, SSIR, TTIR
60	NASA-03-Folded-Tow-001	Fiber Placed Panel	IM7/8552-1 Slit Tape	Flat panel	Folded Tow - 1 ply	$16 \times 16 \times 0.15$	NASA: PEUT, SSIR, TTIR
61	NASA-03-Folded-Tow-002	Fiber Placed Panel	IM7/8552-1 Slit Tape	Flat panel	Folded Tow - Mid	$16 \times 16 \times 0.15$	NASA: PEUT, SSIR, TTIR
62	NASA-03-Missing-Tow-001	Fiber Placed Panel	IM7/8552-1 Slit Tape	Flat panel	Missing Tow - 1 ply	$16 \times 16 \times 0.15$	NASA: PEUT, SSIR, TTIR
63	NASA-03-Missing-Tow-002	Fiber Placed Panel	IM7/8552-1 Slit Tape	Flat panel	Missing Tow - Mid	$16 \times 16 \times 0.15$	NASA: PEUT, SSIR, TTIR
64	NASA-03-Bridged-Joggle-001	Fiber Placed Panel	IM7/8552-1 Slit Tape	Flat panel	Bridging - Joggle	$12 \times 9 \times 1.3$	
65	NASA-03-Bridged-Joggle-002	Fiber Placed Panel	IM7/8552-1 Slit Tape	Flat panel	Bridging - Joggle	$12 \times 9 \times 1.3$	
66	NASA-03-Bridged-Joggle-003	Fiber Placed Panel	IM7/8552-1 Slit Tape	Flat panel	Bridging - Joggle	$12 \times 9 \times 1.3$	
67	NASA-03-Bridged-Joggle-004	Fiber Placed Panel	IM7/8552-1 Slit Tape	Flat panel	Bridging - Joggle	$12 \times 9 \times 1.3$	
59	NASA-03-Steered-Tow-003	Fiber Placed Panel	IM7/8552-1 Slit Tape	Flat panel	Tow Orientation	$46.5 \times 46.5 \times 0.15$	
31	Wrinkle A1	thin laminates	8552-1 slit tape	flat panel	flat wrinkles	$1.5 \times 12 \times 0.15$	USC: GWUT NASA: XCT, PEUT
32	Wrinkle A2	thin laminates	8552-1 slit tape	flat panel	medium wrinkles	$1.5 \times 12 \times 0.15$	USC: GWUT NASA: XCT, PEUT
33	Wrinkle A3	thin laminates	8552-1 slit tape	flat panel	significant wrinkles	$1.5 \times 12 \times 0.15$	USC: GWUT NASA: XCT, PEUT
34	Wrinkle A4	thin laminates	8552-1 slit tape	flat panel	significant wrinkles	$1.5 \times 12 \times 0.15$	USC: GWUT NASA: XCT, PEUT

#	Reference Standard	Structure	Material	Configuration/ Radius	Defects and features	Dimensions (inches)	Partner: Tests
75	NASA-005-Wrinkle-001	Quasi-isotropic	IM7/8552 satin weave fabric and unidirectional	Rotorcraft blade spar tube	Out of plane wrinkle	$11.5 \times 8.5 \times 2.8$	
76	NASA-005-Wrinkle-002	Quasi-isotropic	IM7/8552 satin weave fabric and unidirectional	Rotorcraft blade spar tube	Out of plane wrinkle	$11.5 \times 8.5 \times 2.8$	NASA: PEUT
74	NASA-005-STANDARD-002	Quasi-isotropic	IM7/8552 satin weave fabric and unidirectional	Rotorcraft blade spar tube	Pristine	$11.5 \times 8.5 \times 2.8$	
51	NASA-TAB-SNAG13-FLAT	Triaxial Braid, 0/+60/-60	T-800SC Triaxial Braid 0/+60/-60 with 3M AMD-825	Flat panel	Fabric Snag	$12 \times 13 \times 0.5$	
56	NASA-TAB-SNAG1-FLAT	Triaxial Braid, 0/+60/-60	T-800SC Triaxial Braid 0/+60/-60 with 3M AMD-825	Flange	Fabric Snag	$9 \times 12 \times 2$	NASA: XCT

4.6 Impact Damage Inspection Guidance

4.6.1 Impact Damage Detection and Characterization Executive Summary

Imapact-induced damage is one of the most complex damage scenarios, containing delaminations, matrix cracks, and broken fibers/tows. The damage typically gets wider as the damage spreads deeper into the composite (away from the impacted side). Structures with impacts that produce little to no surface deformation are referred to as BVID structures. Unlike metals, BVID in composites can create significant subsurface damage; therefore, it is important to characterize any possible impact to a CFRP composite. Eighteen specimens of various sizes and ply layers were manufactured and impacted to create BVID as part of the ACP specimen library.

UT, thermography, shearography, and XCT are typical NDE techniques used to detect and characterize impact damage. Within the scope of this Handbook, BVID in manufacturing of CFRP composites most likely results from tool drops or handling damage.

A brief overview of NDE methods is provided in Table 4.6-1. The impact damage standards tested in a round-robin assessment in this program as well as the experience of SMEs among the Consortium members resulted in evaluation of NDE methods effective for the detection and evaluation of impact damage as follows:

Effective Methods
- UT
- Thermography
- XCT

Marginally Effective Methods
- Shearography
- Visual

Ineffective Methods
- CR
- DR
- X-ray Backscatter

Participating Partner(S)
- NASA
- Boeing

Table 4.6-1. Advantages and disadvantages of various methods on detecting impact damage in composites.

Effective Detection and Characterization Methods for Impact Damage		
Detection Method	**Advantages**	**Disadvantages**
Ultrasound	- Manufacturing maturity, widely supported in industry, numerous equipment and supplier options - Inexpensive options - Can be highly portable - Several automated systems available - Both single-sided and transmission configurations - Safety - Defect detection, discrimination, and depth determination techniques - Capable of quantitative measurement of width and depth of damage	- Typically requires coupling fluid that may contaminate or compromise the structure - Requires surface contact - Requires relatively smooth surface for good surface coupling - Automated systems and software for C-scan, B-scan imaging can be expensive - Manual and automated raster scanning for 100% inspection can be time consuming - May require complex contour following robotics and software for curved geometries
Single-Sided Thermography	- Relatively fast/large area inspection - Non-contact - No harmful radiation or surface heating - Relatively insensitive to changes in part contours, angles, and thicknesses—contour following robotics generally not required - Possible to determine delamination widths	- Deeper layers of damage masked by damage closer to surface - Depth of damage approximate - IR camera requires direct line of sight
XCT	3-dimensional view of complete volume promises detection of impact damage. - Capable of discerning delaminations, fiber breakage, and matrix cracking - Non-contact - Excellent potential for spatial fidelity, sizing, shape definition - Provides permanent visual digital scan record - Full volume density map with cross-sectional image slices and depth information - Relatively insensitive to changes in part contours, angles, and thicknesses—contour following robotics generally not required - Images are relatively easy to interpret	- Radiation/shielding safety concerns - Typically, not portable - Requires access to all sides of the part - High initial equipment cost - Computationally intensive - Scans, software reconstruction, and data evaluation are time consuming - Requires large data storage capabilities - Not typically applicable to scan large parts or assemblies at high enough resolution. - Resolution related to part size.

Marginally Effective Detection and Characterization Methods of Impact Damage		
Detection Method	**Advantages**	**Disadvantages**
Shearography	• Relatively fast/large area inspection • Non-contact • Single sided inspection • No harmful radiation or surface heating • Relatively insensitive to changes in part contours, angles, and thicknesses—contour following robotics generally not required	• Subsurface defects must be sufficiently large to cause surface deformations • Requires direct line-of-sight with imager • Defect depth determination is not straight forward without a-priori knowledge of the structure • May require surface coating or modification on glossy surfaces for successful inspection
Visual Inspection	• Direct and rapid inspection • Non-contact • Low-cost • Can be performed without instrumentation or with inexpensive equipment such as cameras, borescopes, and magnifiers • Can find imperfections inside radii and complex curvatures • Direct reporting with photographs	• Limited to surface inspections • Insensitive to bulk features • Requires direct line of sight • Observation data can be user-dependent • Impact damage may or may not result in and surface indentation for composites, while subsurface damage can be significant.

Ineffective Detection and Characterization Methods for Impact Damage		
Detection Method	**Advantages**	**Disadvantages**
Computed Radiography	• Sensitive to density variations, caused by material differences, voids, or other defects effecting the density of material the X-rays pass through. • Suitable for complex parts • Resolution generally better than DR • Faster results than film X-ray • Results dependent on FOD material (metallic inclusions can be detected while materials close in density to the composite cannot)	• 2D image - the results are superimposed images of the defects • Sensitive to defect orientation • Radiation safety concerns • Detection depends on density of inclusion • Cannot normally identify impact damage
Digital Radiography	• Sensitive to density variations, caused by material differences, voids, or other defects effecting the density of material the X-rays pass through • Results dependent on FOD material (metallic inclusions can be detected while materials close in density to the composite cannot)	• 2D image - the results are superimposed images of the defects • Sensitive to defect orientation • Radiation safety concerns • Detection depends on density of inclusion • Cannot normally identify impact damage
X-ray Backscatter	• Sensitive to material density changes that can be correlated to porosity	• Radiation safety concerns, particularly in portable applications

• Non-contact • Single sided • Method is real-time or near-real-time • Provides permanent visual record (film or digital image) • Can be portable with adequate safety precautions • Relatively insensitive to changes in part contours, angles, and thicknesses—contour following robotics generally not required	• High initial equipment cost • Cannot normally identify impact damage

4.6.2 Impact Damage Inspection Technologies

A listing of inspection methods is provided in the following sections along with brief descriptions of common inspection strategies. A more extensive overview of the inspection methods is covered in Section 5 of this Handbook. Individual test reports for selected inspection methods for the NDE standards tested are provided in Appendix E, which include method, partners, samples descriptions, measurement setups, test results, and technique applicability ranking.

A brief overview of inspection methodologies used for impact damage detection is provided below and includes a general listing of advantages and disadvantages for each general method.

4.6.2.1 Ultrasound

PEUT is generally a highly effective method for impact damage detection, as shown in Figures 4.6-1 and 4.6.2. Water-coupled PEUT scans were performed on standard #81 to demonstrate the capability of detecting impact damage defects. Figure 4.6-1 shows a back side surface amplitude image of the sample in its post-impacted state. The impact damage region is identified with measurements. An air bubble on the under side of the sample in the immersion tank is also noted. No surface indication of impact damage was visible.
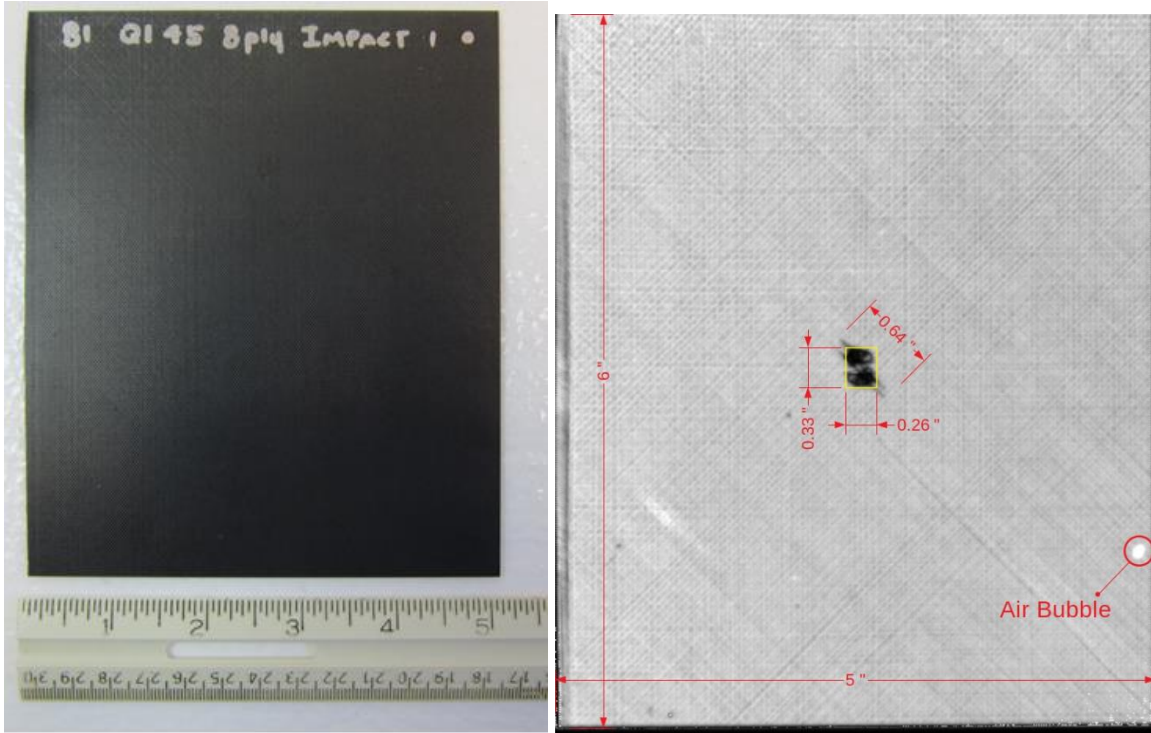
Figure 4.6-1. NDE Standard #81 photography (left). 10MHz Post-impact image (right).

Figure 4.6-2 is an internal reflection amplitude image. The gate region is selected to highlight reflections from the delaminations caused by the impact.
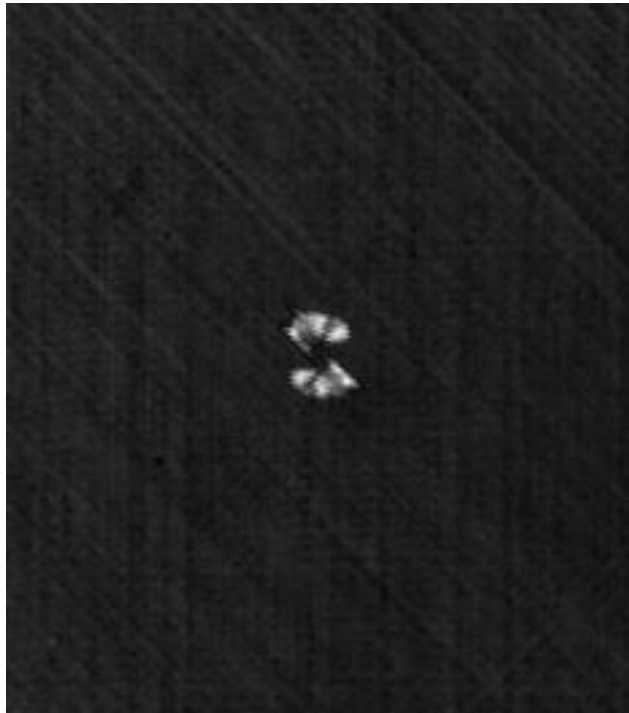
Figure 4.6-2. Internal reflection amplitude image of NDE standard #81 with the gate region selected to highlight reflections from the delaminations caused by the impact.

Figure 4.6-3 below is another example of UT data for an impacted standard, in this case a thicker, 24-ply panel. No surface indication of impact damage was visible.
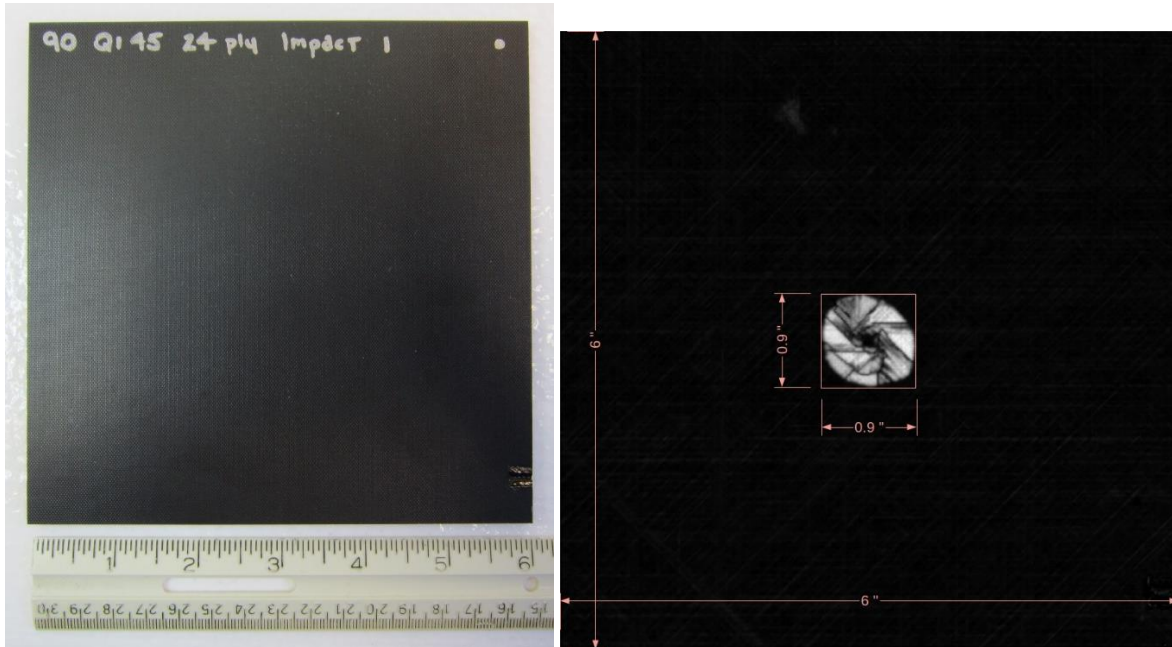
Figure 4.6-3. NDE Standard #90, a 24 ply [(45/90/-45/0)3]ₛ quasi-isotropic 6- x 6-inch low-energy impacted panel photograph (left). 10MHz post-impact image (right).

4.6.2.2   Thermography

Given its fast, non-contact capabilities, thermography is often used as a preliminary inspection tool for impact damage. Thermography works particularly well for CFRP composites, which have diffusivities low enough to easily capture thermal responses of the impacted specimen at frame rates available in today's hardware, and diffusivities high enough that responses can be quantified with good signal-to-noise ratio (SNR).

Figure 4.6-4 shows thermography results for three of the NDE impact standards (#81,82, and 83), which are all eight plies thick. The impacts were low-energy impacts that are possible in manufacturing environments, typically due to tool drops or as a result of transportation damage for example. Thermal data were taken from both sides of the specimens—the impacted side and the non-impacted side. Higher resolution can be achieved by changing the lens on the IR camera, although this also reduces the field of view (FOV) of the image—negating one of the major benefits of thermography (large area inspection). However, in the case of BVID, it may be likely that the location of the impact is known a priori from visual inspection, making a higher-resolution lens appropriate. The data below were taken with a 25-mm lens.
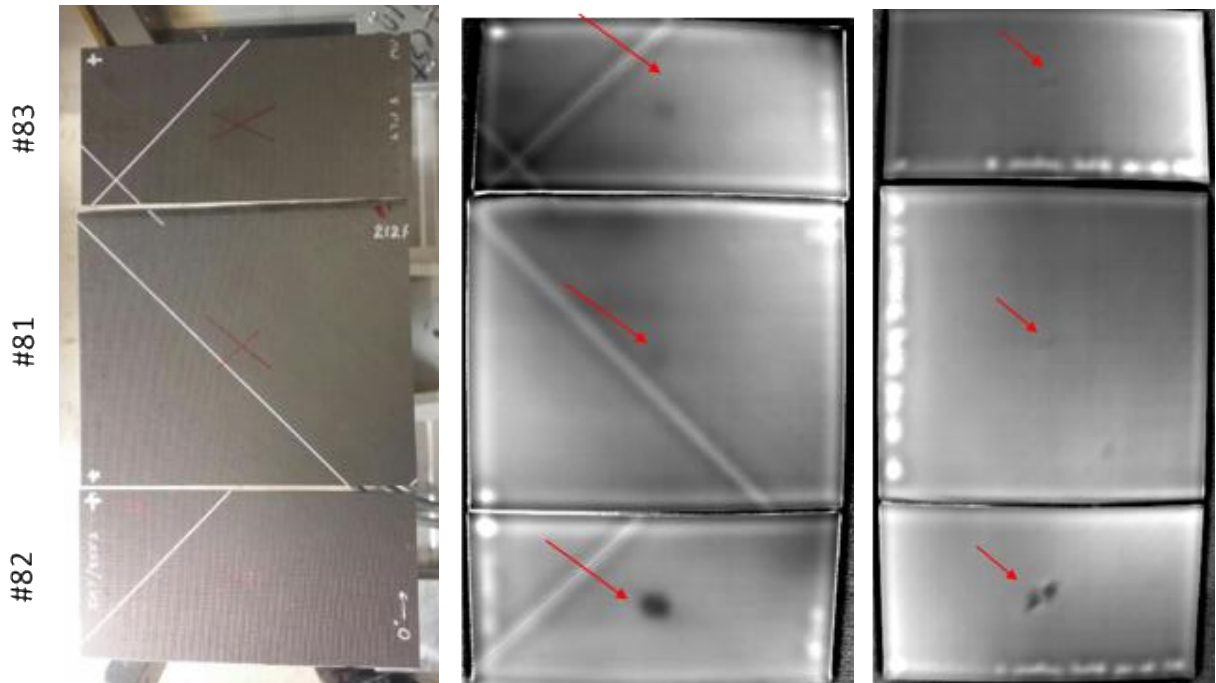
Figure 4.6-4. Thermography results for NDE impact standards #81,82, and 83.
(Left) Picture of front of samples 81, 82, and 83. (Middle) Thermography results from front side of specimens. (Right) Thermography results from back side of specimens. Red arrows point to subsurface impact damage. Impact damage can be better resolved by using a higher resolution lens.

4.6.2.3   Radiography

4.6.2.3.1   *Computed Radiography (CR) and Digital Radiography (DR)*

CR and DR imaging is dependent on the superimposed density of the part being imaged. In the case of the impact damage, the damaged portion tends to get indented, slightly compressing the material underneath the indent. Therefore, the superimposed density remains approximately the same as prior to impact. This makes the detection of impact damage by an operator using 2D radiography such as CR very difficult. As seen in Figure 4.6-5, the impact damage is not easily visible. Given knowledge of the locations, an operator may be able to discern damage but contrast from the damage is not enough to be detected in a general case.
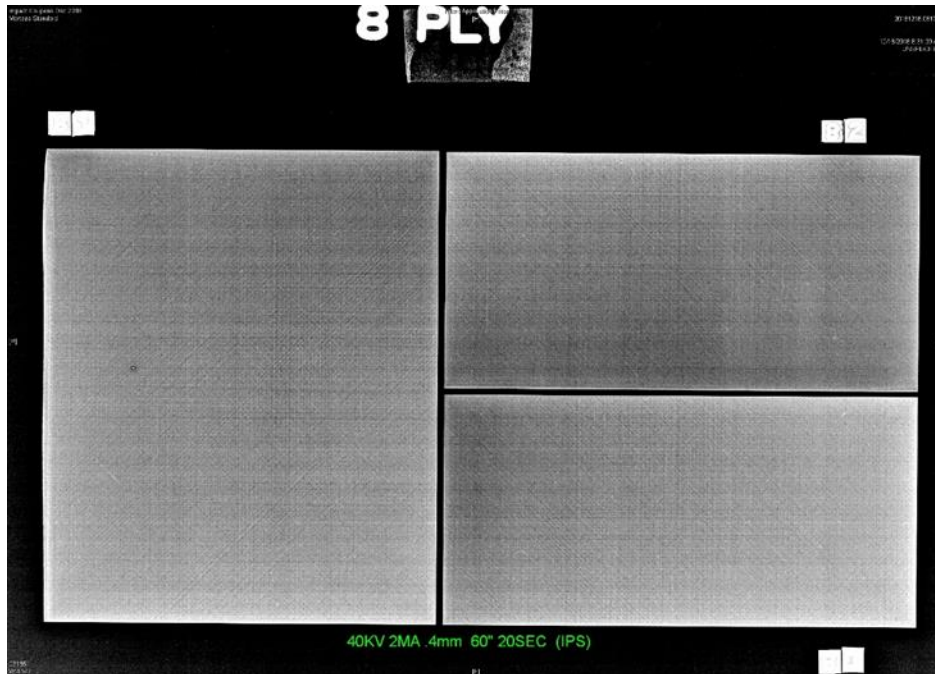
Figure 4.6-5. Flash filtered CR image of 8-ply impact panels.

4.6.2.3.2   X-ray Backscatter

Backscatter X-ray is particularly sensitive to material differences that cause large variations in scatter. Changes in surface orientation such as the indents from impact damage are theoretically detectable, if they cause a large enough change in scatter. Figure 4.6-6 shows NDE standard #85, a 22- × 22-inch 8-ply CFRP with four impacted locations. This figure shows no visible indent indications, however. The lack of detectability in this case may be caused by the limited resolution of this imaging method or an insufficient difference in X-ray scatter that cannot be effectively detected. In this case, X-ray backscatter imaging is not able to detect the small impact damage that is present in this panel.

The faint horizontal lines in this image are the metal pipes along the wall located behind the panel (+10 ft.). The black rectangle at the bottom of the image is the clamp holding the panel in place.

Figure 4.6-6. NDE standard #85, a 22"x22" 8-ply CFRP with four impacted locations.
(Left) Photograph of NDE standard #85, a 22"x22" 8-ply CFRP laminate with four low-energy impact locations. (Right) X-ray backscatter image of 8-ply impact damage panel shows no detectable damage.

4.6.2.3.3   XCT

Unlike 2D X-ray imaging, XCT produces a full 3D volume of data and can display interior slice views of the object. This allows for detailed detection of flaws. In the case of the impact panels, XCT is capable of detecting fiber tow breakage, matrix cracking, and delaminations—giving a full picture of the damage state.

Depending on the size of the specimen, which determines the achievable resolution, impact damage is generally detectable with XCT. Visualization of the disbonds, fiber tow breakage, and matrix cracking, all typical of impact damage in composites, is facilitated by rotating the data volume such that the surface of the composite is aligned with the x-, y- or z-plane of the CT slice direction. In this orientation, data from an interface between two plies are easily characterized as a 2D slice of the data.

This effect is shown below in Figure 4.6-7 and Figure 4.6-8. In the first Figure 4.6-7, the data is presented as-collected in the CT system without fine-tuning the rotation of the specimen so that the specimen plies align to an image slice. On the left, the front surface of the specimen is half in and half out of the CT slice. The ply is not aligned to the coordinate system. Several plies are visible in the single CT slice, evident by the changing directions of the 0º/ 90º/ 45º degree lines in the image as well as the front surface of the specimen going out of the slice at the bottom of the image. The right image in Figure 4.5-7 shows the top view of the panel, illustrating the off-angle rotation of the specimen to the CT slice. The red vertical line is the CT slice location.

Front View   **Top View**

Changing ply
directions within
slice

Partial view of
delamination
crossing slice

Ply not aligned with CT Slice
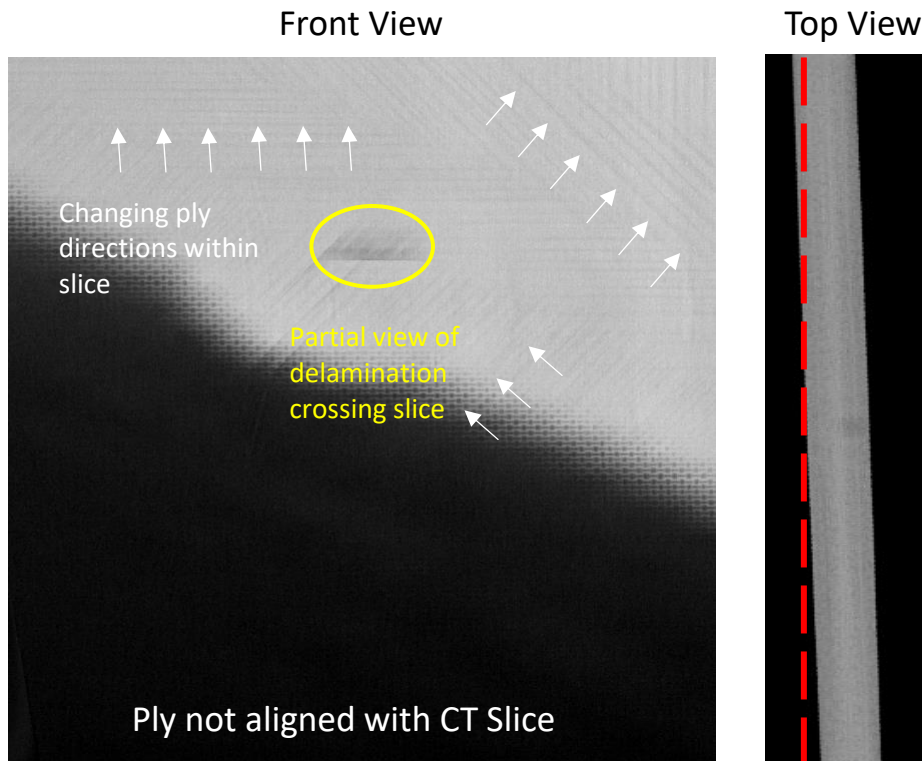
Figure 4.6-7. (Left) Specimen not aligned to the coordinate system. Plies do not remain in a single CT slice. (Right) Plies not aligned with the coordinate systems so that the plies remain in a single CT slice. The vertical red dashed line is the location of the CT slice.

Figure 4.6-8 shows the panel rotated so that the entire ply is displayed on the same CT slice and the rotation performed so that the plies are aligned with the coordinate system. On the left, the front surface of the specimen is fully within the CT slice. The ply is aligned to the coordinate system. Note the horizontal features within the image that correspond to the fiber direction. Visible in the upper left corner and the lower right corner are 45° lines indicating that the panel may have some very slight curvature or not be perfectly aligned. While in the image on the right in Figure 4.5-8 shows the top view of the panel, with the corrected rotation of the panel to the coordinate system. For panels with some curvature, it is normally possible to map the coordinate system to a coordinate system where the ply interface is contained in a single plane.

Front View

Top View

Full view of
delamination
within slice

unchanging ply
directions within
slice

Ply aligned with CT Slice
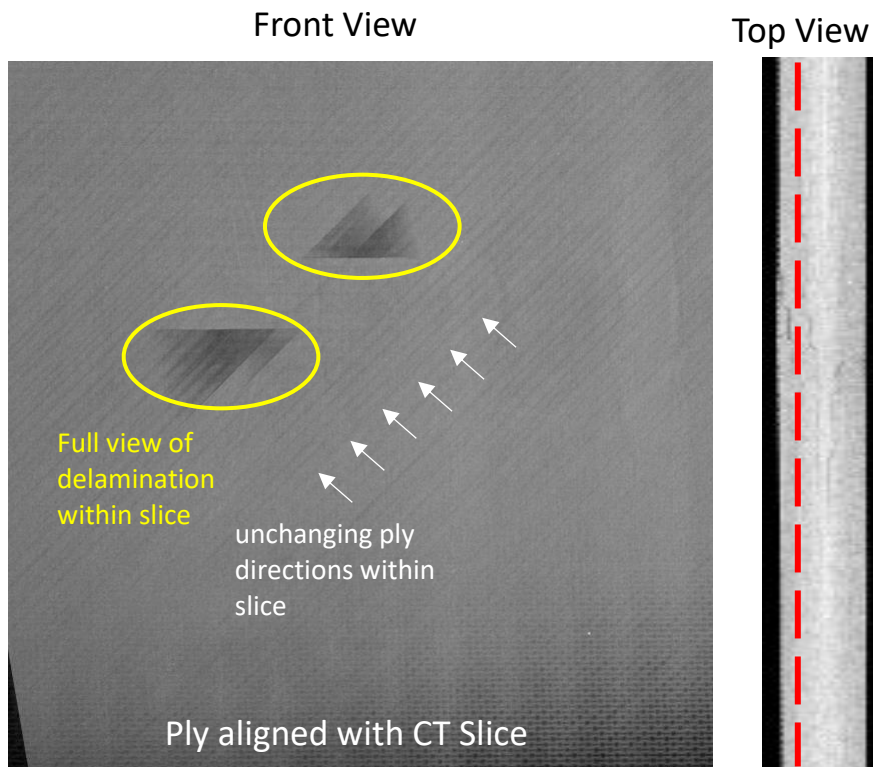
Figure 4.6-8. (Left) Specimen aligned to the coordinate system. Plies remain in a single CT slice. (Right) The data have been rotated to keep the plies aligned with the coordinate system.
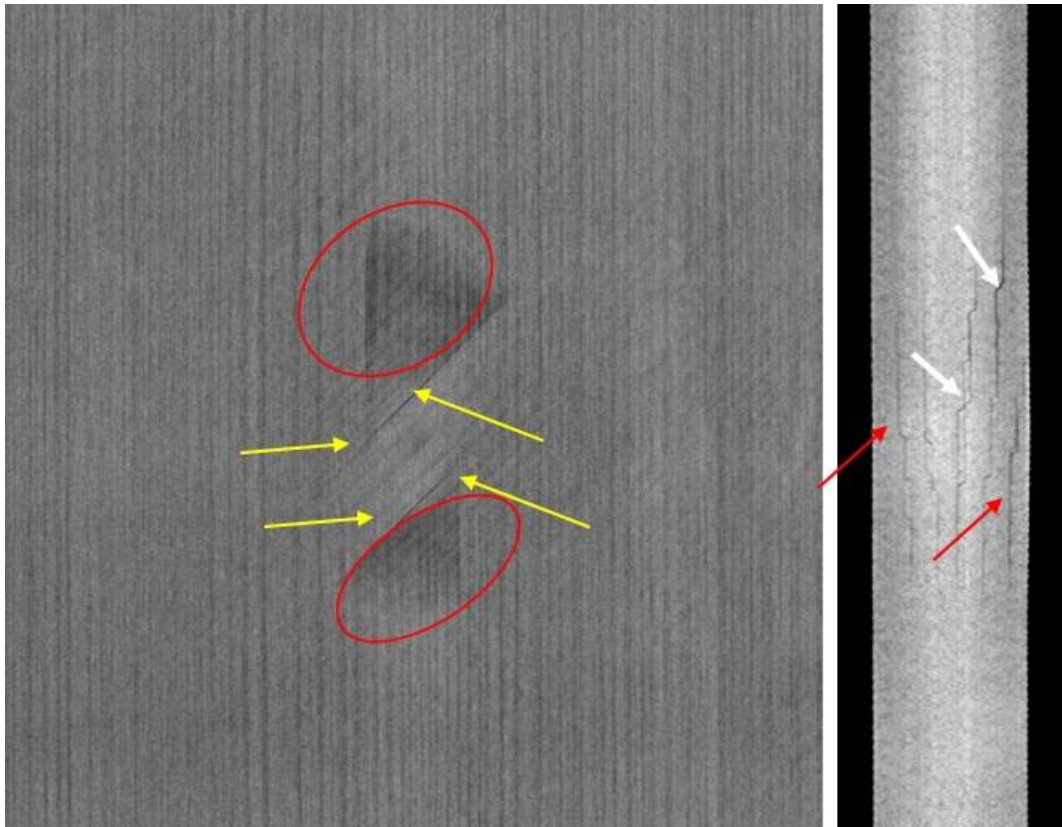
Figure 4.6-9. XCT data of NDE standard #91, a 3- × 5-inch 24 ply [(45/90/-45/0)3]_S.
CFRP laminate with low energy impact. The image on the left show delaminations between plies (red circles) and cracks (yellow arrows) between fibers. The image on the right shows the delaminations (red arrows) between plies and matrix cracks within the plies (white arrows). These data have been rotated to align the plies with the slice coordinate system.

4.6.2.4 Shearography

Two CFRP panels were made for impact NDE standards large enough for shearography testing. They were both 22×22 inches with one panel being 8 plies thick and the other 16 plies thick. Each of these two specimens were impacted in four locations delineated at the corners of a square centered in the panel. For these two panels, the vacuum shearography tests buckled the panel before indications due to impact were detected. However, in general shearography has been shown to be capable of detecting impact damage in composite panels.

4.6.3 Impact Damage Standards

A summary of BVID impact damage standards and test methods is provided in Table 4.6-2. Due to number and breadth of samples and inspection methodologies, not all methods described above were tested. Instead, the Handbook along with Appendix E acts as a preliminary guide to impact damage inspection.

Table 4.6-2. Summary of impact damage standards specimens tested by consortium.

#	Reference Standard	Structure	Material	Configuration/ Radius	Defects and features	Dimensions (inches)	Partner: Tests
81	QI_45 8ply 6x5 Impact 1	[(45/90/-45/0)]S	IM7/8552	Flat panel	1 impact 0.34 inch	6 × 5	NASA: SSIR, PEUT Boeing: XCT, CR
82	QI_45 8ply 3x6 Impact 1	[(45/90/-45/0)]S	IM7/8552	Flat panel	1 impact 0.82 inch	3 × 6	NASA: SSIR, PEUT, XCT Boeing: XCT, CR
83	QI_45 8ply 3x6 Impact 2	[(45/90/-45/0)]S	IM7/8552	Flat panel	1 impact 0.37 inch	3 × 6	NASA: SSIR, PEUT, XCT Boeing: XCT, CR
84	QI_45 8ply 11x11 Impact 1	[(45/90/-45/0)]S	IM7/8552	Flat panel	Spare-no impact	11 × 11	Spare - not tested
85	QI_45 8ply 22x22 Impact 1	[(45/90/-45/0)]S	IM7/8552	Flat panel	4 impacts 0.22 inch to 0.54inch	22 × 22	NASA: SSIR Boeing: CT, CR, Backscatter, Shearography
86	QI_45 16ply 6x6 Impact 1	[(45/90/-45/0)2]S	IM7/8552	Flat panel	1 impact 0.2 inch	6 × 6	NASA: SSIR, PEUT Boeing: XCT, CR
87	QI_45 16ply 3x5 Impact 1	[(45/90/-45/0)2]S	IM7/8552	Flat panel	1 impact 1.28 inches	3 × 5	NASA: SSIR, PEUT, XCT Boeing: XCT, CR
88	QI_45 16ply 3x5 Impact 2	[(45/90/-45/0)2]S	IM7/8552	Flat panel	1 impact 0.88 inch	3 × 5	NASA: SSIR, PEUT, XCT Boeing: XCT, CR
89	QI_45 16ply 22x22 Impact 1	[(45/90/-45/0)2]S	IM7/8552	Flat panel	4 impacts 0.22 inch to 0.75inch	22 × 22	NASA: SSIR Boeing: XCT, CR, Shearography
90	QI_45 24ply 6x6 Impact 1	[(45/90/-45/0)3]S	IM7/8552	Flat panel	1 impact 1"	6 × 6	NASA: SSIR, PEUT Boeing: XCT, CR
91	QI_45 24ply 3x5 Impact 1	[(45/90/-45/0)3]S	IM7/8552	Flat panel	1 impact 1.11 inches	3 × 5	NASA: SSIR, PEUT, XCT Boeing: XCT, CR
92	QI_45 24ply 3x5 Impact 2	[(45/90/-45/0)3]S	IM7/8552	Flat panel	1 impact 1 inch	3 × 5	NASA: SSIR,PEUT, XCT Boeing: XCT, CR
93	QI_45 32ply 6x6 Impact 1	[(45/90/-45/0)4]S	IM7/8552	Flat panel	1 impact 0.23 inch	6 × 6	NASA: SSIR, PEUT Boeing: XCT, CR
94	QI_45 32ply 3x5 Impact 1	[(45/90/-45/0)4]S	IM7/8552	Flat panel	1 impact 1.12 inches	3 × 5	NASA: SSIR, PEUT, XCT Boeing: XCT, CR
95	QI_45 32ply 3x5 Impact 2	[(45/90/-45/0)4]S	IM7/8552	Flat panel	1 impact 0.25 inch	3 × 5	NASA: SSIR, PEUT, XCT Boeing: XCT, CR
96	TC1 18ply 6x6 Impact 1	[45/90/-45/0/0/45/90/-45/0]S	IM7/8552	Flat panel	1 impact 0.3 inch	6 × 6	NASA: SSIR, PEUT Boeing: XCT, CR
97	TC1 18ply 3x5 Impact 1	[45/90/-45/0/0/45/90/-45/0]S	IM7/8552	Flat panel	1 impact 0.92 inch	3 × 5	NASA: SSIR,PEUT, XCT Boeing: XCT, CR
98	TC1 18ply 3x5 Impact 2	[45/90/-45/0/0/45/90/-45/0]S	IM7/8552	Flat panel	1 impact 0.96 inch	3 × 5	NASA: SSIR, PEUT, XCT Boeing: XCT, CR

5.0 Inspection Technology Summaries and Capabilities

This section of the Handbook is organized by inspection technology. Each NDE technique includes a brief technical explanation of the physics of the technique. It also covers some of the specifics important to the inspection of solid laminate CFRP composites. The intent of this section is to facilitate determining which NDE technique might work for a specific inspection application and which will not, where to start and what to consider. Types of defects that have successfully been analyzed with the techniques are discussed. Additionally, the important parameters for each technique, along with technique limits, differences in application of the technique for composites versus metals are provided. The benefits and drawbacks of the technique, and some of the data analysis techniques that have been used to quantify damage are covered. Specific examples shown are for illustrative purposes.

Predominately discussed are the techniques used to inspect each of the NDE standards developed for the ACP. However, also included are well known NDE techniques that are not typically used for inspection of CFRP composites, why they are not used, and the kind of composites for which that technique might be more suitable.

For a discussion of the applicability of each inspection technology for specific defects in the specimens used for this Handbook, see Section 4.0.

5.1 Ultrasound

5.1.1 Fundamentals of Ultrasonic NDE

In ultrasonic NDE, the probing energy used for inspection is in the form of a stress wave that propagates into the material. The term 'ultrasonic wave' refers to an acoustic pressure wave or elastic stress wave that encompasses the frequency ranges above the hearing frequencies of the human ear (~20 kHz). The higher the ultrasonic frequency, the shorter the wavelength, and correspondingly, the higher the attenuation. Attenuation can lead to lower depth penetrability. Ultrasonic frequencies between 1 and 10 MHz are the common range for hand-held NDE inspection, which typically uses a liquid couplant or immersion methods (immersing the component and probes in a tank of water). These are the most commonly used frequencies for traditional bulk wave ultrasonic inspection. Ultrasonic frequencies below the MHz range have comparatively lower wavelengths and attenuation, and are adequate for GWUT testing. See Section 5.6.6 for a more in-depth explanation of this technique. Frequencies between 10 and 400 MHz is used for localized investigation of the materials with very precise scan control within a rugged system with the capability of isolating the surrounding vibration (e.g., scanning acoustic microscopy). These frequencies are suitable for underwater ultrasonic imaging. Frequencies above 400 MHz do not have much use for general-purpose material inspection but are used for biological material applications because the resolution of the scans can go well below ~5µm.

Ultrasonic NDE has a long history for the characterization of macroscale damage/defects in metallic materials/structures. Ultrasonic methods have also been successfully used to investigate the morphology or crystalline structure of a material. Metallic materials/structures are isotropic in nature and the ultrasonic stress wave velocities are similar in all directions. The physics of ultrasonic wave propagation in traditional metals (i.e., metal not created via additive processes) has led to well-established and understood methods for ultrasonic NDE inspection.

With the increased use of composite materials, NDE engineers and researchers have tried to apply conventional metallic ultrasonic NDE methods to composite materials and found that the material properties of composites lead to challenges. Since composite materials are often anisotropic, wave speeds vary with propagation direction. Furthermore, attenuation in composites is higher than in metallic materials. This chapter is dedicated to identifying and understanding the uniqueness of the ultrasonic waves in composite materials and discusses best practices in performing NDE of composite.

UT is the method most frequently used to inspect composite components for the most common types of defective conditions: delaminations, porosity, wrinkles, and FOD. Ultrasonic inspection typically takes the form of a single element transducer emitting a burst of sound into the component, then the echoes, which are returned to that or another transducer, are interpreted to identify the quality of the component. Because echoes are created at each interface where the density or stiffness of the component changes, it is especially well suited to respond to the defective conditions mentioned above. At the same time, considerable complications in the form of extraneous noise and sound beam disruption are caused by the complex construction of high-stiffness fibers (carbon, glass, etc.) inside a low-stiffness matrix (polymers such as epoxy). This section describes how UT can be effectively used to assess component quality and contains information on limitations to be aware of during inspection.

Technically speaking, the probing energy used for ultrasonic inspection is in the form of a stress wave that propagates into the material. UT propagation occurs in one of three distinct wave modes (a quasi-pressure mode or one of two quasi-shear modes), analogous to one pressure and one shear mode in metals. When a sound wave encounters an abrupt shift in properties, (density or modulus), the break in material property continuity causes wave reflection and transmission at that interface. The energy which is reflected typically takes on multiple forms, transforming into any or all of the media's three propagating mode types along with changes in propagation direction. Likewise, transmitted energy can also change modes and direction. The change in direction upon transmission at a material interface is referred to as refraction. UT can change directions due to material anisotropy even in the absence of an interface, the change in direction known as beam steering.

The types of composite materials commonly inspected with UT include a variety of polymer matrix but also ceramic matrix composites. This document focuses on PMCs, but structures filled with core (honeycomb or foam) are included. In addition, ultrasonic inspection applies to various types of structures including "stringers" (e.g., composite I-Beam structures bonded to panels), composite wedge inserts between panels, or bent plies (e.g., L-shape or U-shape).

5.1.2 Principles of Ultrasonic Inspection

5.1.2.1 Wavelength, Frequency and Velocity

UT inspection of a composite component is generally done at frequencies between 0.2 and 10 MHz. This is because the wavelength at those frequencies is matched to detect flaw sizes in the material being inspected. Wavelength is a function of sound velocity and frequency per Equation 1.

$$\lambda = \frac{C}{F} \qquad\qquad \text{Equation 1}$$

where, C= Velocity (in/ μsec), F = Frequency (MHz), λ = wavelength (in)

Resolution is optimized by using a smaller wavelength, but the complex internal structure of composites degrades sound penetration and thus inspectability as wavelength decreases. At the high end of this frequency range, features as small as .025-inch diameter can be resolved in thin samples, and individual plies can even be imaged. However, 10 MHz is unable to penetrate thicknesses greater than eight plies. At 0.2 MHz, even relatively thick PMC component can be inspected. See Figure 5.1-1 for guidance on the highest frequency that can be used for a component of a given thickness.
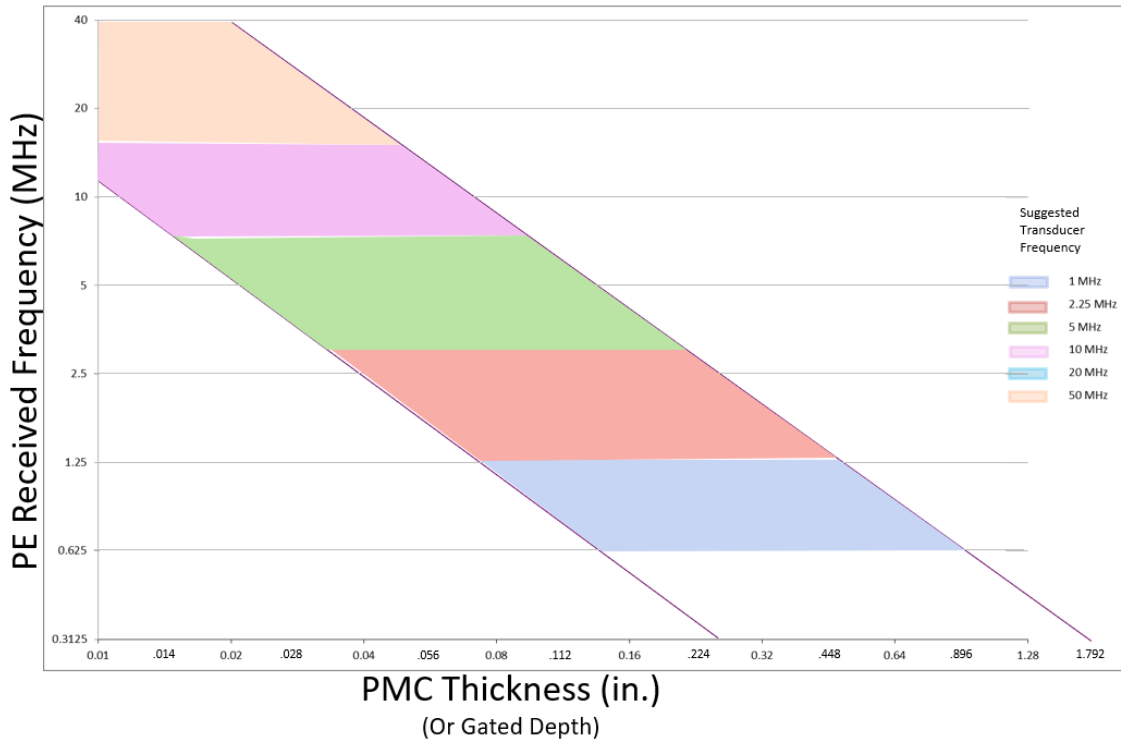
Figure 5.1-1. Frequency selection guideline for Pulse-echo (PE) ultrasonic inspection of laminar PMCs of various thickness.

Velocity plays a role in discriminating features at different depths. Inspecting in pulse echo mode, a burst of sound energy is transmitted into the component, and is reflected by the interface at the back surface of the part. If the time between the front surface and back surface is 3 µsec, for example, then given the velocity of 0.110 inch/µsec, it can be calculated that the sound traveled 0.330 inch in the sample. Because in pulse-echo mode the sound must travel down to the back surface and then return to the front of the component, the distance traveled represents twice the part thickness, so the part thickness would be 0.165 inch. Similar calculations can be made for internal features and defective conditions, so that the depth of the feature can be determined.

5.1.2.2 Reflectivity and Transmission

Anytime a sound wave encounters an interface between two materials having differing density or modulus, some sound energy is reflected at that interface. The amplitude of the signal reflected is a function of the impedances of the two materials as shown in Equation 2[1]. For example,

$$R = \frac{(Z2 - Z1)}{(Z2 + Z1)} \qquad \text{Equation 2}$$

98

where Z1 and Z2 are acoustic impedance values in material 1 and material 2, respectively and given by $Z = \rho*C$.

Water has an impedance of 1.5, and PMC has an impedance of approximately 3.5, so a 100% signal traveling through water and impinging on a PMC would have $(3.5-1)/(3.5+1) = 55\%$ reflected back into the water.

Similarly, a 100% signal in PMC reflecting off water at the back surface would have an amplitude of -55%. The negative sign signifies that the signal would be reflected upside down; that the polarity would be reversed. This can be a useful effect when looking at echoes from inside a component. If the internal echo has the same appearance as the back wall, then the cause of that echo has an impedance lower than the PMC, likely air or water. If the signal is upside down, then the feature is a high impedance material, such as metal or ceramic, (Z>25, or ~15, respectively). Materials inside a PMC component, which are bonded to the PMC, are able to transmit sound in addition to reflecting it. The amplitude of the transmitted signal (T) can be calculated from the reflection coefficient, R, of Equation. 2. This relationship is shown in Equation 3 and Equation 4.

$$T^2 = 1 - R^2 \qquad\qquad \text{Equation 3}$$

$$T = \sqrt{\frac{2Z1Z2}{(Z2+Z1)^2}} \qquad\qquad \text{Equation.4}$$

Note that air has an impedance close to 0, so all the sound is reflected at a delamination interface, and no sound is transmitted through that interface.

5.1.2.3 Beam Size

The ability to measure defective conditions is directly linked to the diameter of the sound beam entering the component. The beam diameter can be estimated using the transducer wavelength, focal length and element diameter. Using the frequency and sound velocity in water, the wavelength is determined according to Equation 5[2]. A key feature of this relationship is that for a given frequency, any transducer with the same (Focal Length/Element Diameter) ratio will result in the same beam size at its focus (see Figure 5.1-2). Therefore, a 5-MHz transducer with an 8-inch focal length and 1-inch diameter has the same focal zone properties as a 5-MHz transducer with a 6-inch focal length and a 0.75-inch diameter. The natural consequence of this is that a scan using the first transducer at 8-inch water path will yield the same image as the second transducer operated at a 6-inch water path.

$$\text{Beam diameter} = \lambda \text{ (F/D) (F= Focal length, D=element Diameter)} \qquad \text{Equation 5}$$
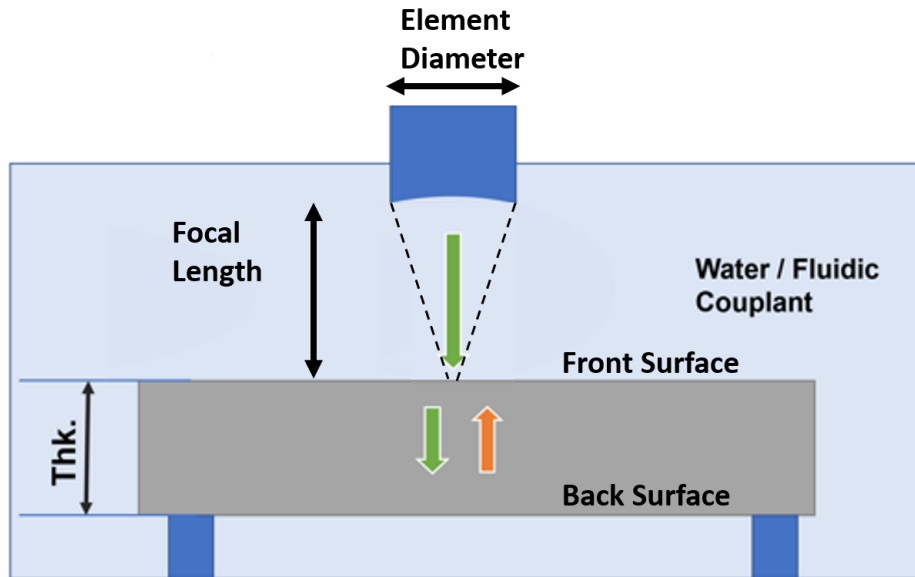
Figure 5.1-2. Sketch of a transducer with focal length and element diameter.

The relationship in Equation 5 is a good approximation of the beam size, except when the focal length is less than half of the Near Field Distance (Equation 6)[1]. For smaller element diameters, the transducer should be treated as unfocused, with a focal length equal to the Near Field Distance, and the beam diameter approximately equal to one quarter of the element diameter.

$$\text{Near Field Distance} = D^2/4\lambda \quad (\text{D=element diameter}) \qquad \text{Equation 6}$$

The relationships described in Sections 5.1.2.2 and 5.1.2.3 are useful "rules of thumb" and can be used to solve most inspection challenges. However, it should be noted that the exact solutions require higher order math and careful consideration of material properties.

5.1.2.4   UT Interactions with Composite Architecture

Composite components are inherently complex structures because of the design intent to use that complexity to benefit component behavior. Because component behavior is generally linked to its stress/strain properties, that complexity naturally affects ultrasonic inspection behavior. Ultrasonic inspection of PMC components is best done with the sound beam oriented perpendicular (at 90°) to the plane of the laminate. As a general rule, if the angle between the two is less than 75°, the sound beam will be guided to a new angle by the fiber orientation. This wave guide or beam steering action prevents pulse-echo signals from returning to their source transducer, and makes TT reception location unpredictable. This behavior effect needs to be considered, whether the angle misalignment occurs at the component surface or deep inside the component. The beam steering behavior is more severe at the higher frequencies; so if ply orientation is an unavoidable issue, lower frequency (longer wavelength) scans are more likely to be effective.

This effect can influence an inspection even when the plies are perpendicular to the beam. Fiber waviness within a ply, such as in braided samples, or ply drops can cause low-level beam disruption at each ply, leading to severe beam disruption after several plies. In a sample made of unidirectional plies, sound beams behave very well, and properties of refraction can even be applied to achieve sub-surface focusing. In braided samples, however, a sound beam only expands

as it travels through the component. For these samples, the highest resolution scan will be achieved by placing the focal spot on the surface of the component.

An extreme case of beam disruption comes in the form of chopped fiber samples. In this type of material, the fibers are randomly oriented and the orientation is mixed within the sample. A sound beam incident on the surface of such a part is quickly and randomly disrupted, making the material virtually inspectable with UT for any defect type except large delaminations.

5.1.3   Commonly Used Ultrasonic Techniques

5.1.3.1   Through-Transmission Ultrasound (TTUT)

The TT approach uses a transducer to transmit sound into the component, and a second transducer to receive the sound after it has passed through the component (Figure 5.1-3d). A component with no defective conditions will allow the sound to pass through in a predictable manner. Once a good part is inspected, subsequent parts can be compared to that for variance, which might be attributed to defects. Delaminations, porosity, wrinkles, and most types of FOD will cause sound to be scattered or absorbed, so less sound is returned to the receiving transducer. That reduced sound is often referred to as a "shadow." Normal variation in ply layup can also cause shadows, so the inspector must be aware of how much shadowing should be expected from normal component variation, and how much indicates a risk of having a defective condition. Defining this threshold is typically based on a calibration standard, which is most effective when it is made from an actual component laid up with synthetic defects placed inside. If a defect standard is not available, another means of calibration is to start with a reference signal, perhaps one that passed from the transmitting transducer to the receiving transducer, with only water in between. After scanning a variety of parts, the inspector becomes accustomed to how much sound typically passes through a component of a certain material and thickness, so if less sound is received, it is known to be outside the normal range for good material.

In its most common form, the transmitting and receiving transducers are the same frequency and have the same focal properties. The focal spot can be placed at mid-thickness in the component, or they can be placed on the outer surfaces of the component. These arrangements are tolerant of variation in part thickness and water path; however, sometimes inspections can be improved by changing this arrangement. If the inspector knows the transmitted sound is affected by the component, the receiving transducer can have different properties or be placed in a different location to improve signal reception.
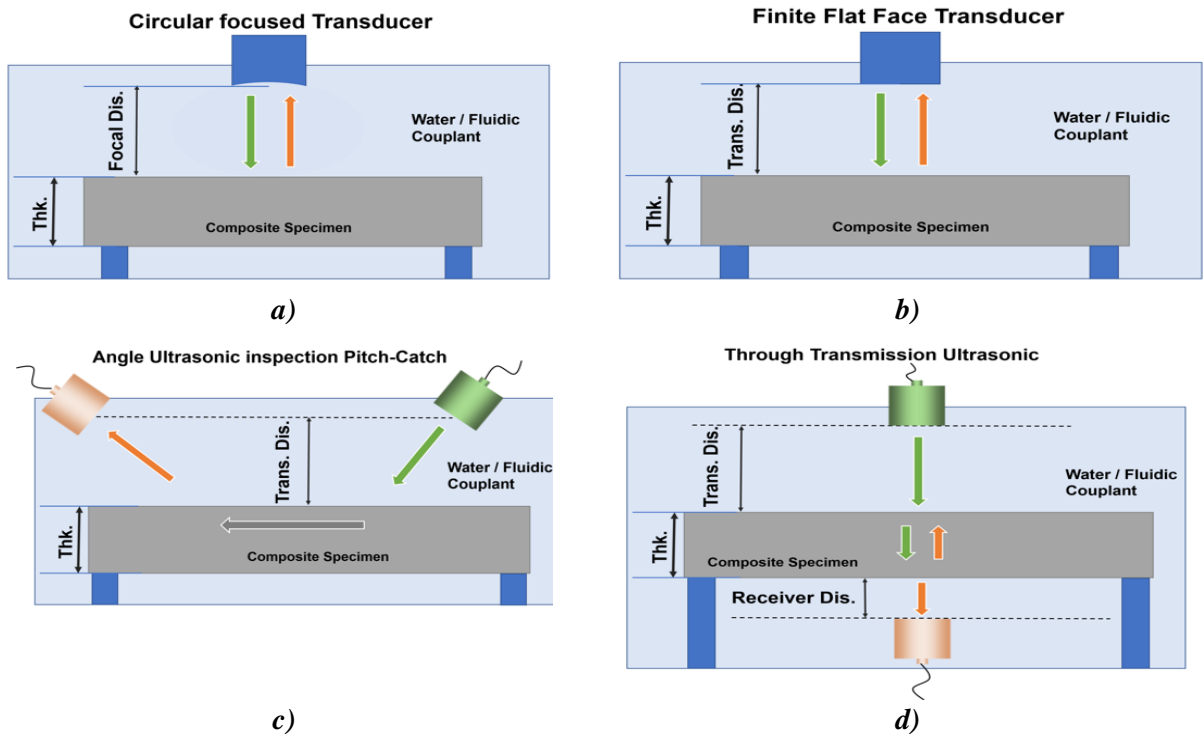
***Figure 5.1-3. Typical arrangements of ultrasonic transducers in a water tank.
a) Focused transducer in pulse-echo mode. b) Flat surface transducer in pulse-echo mode. c) Guided
wave inspection under water in pitch-catch mode. d) TT arrangement in pitch-catch mode.***

5.1.3.2   Pulse-Echo Ultrasound (PEUT)

The pulse echo approach uses a single transducer to transmit sound into the part, (Figure 5.1-3a, and b) then echoes are returned to the same transducer. As long as the plies are all perpendicular to the beam, echoes from laminar defects can be detected, including delaminations and foreign material. In addition, shadows from those plus porosity and wrinkles can be observed by measuring the amplitude of the back surface echo. One benefit of pulse-echo over TT is that access is only needed from one side of the component. If the component has an internal cavity, it may be difficult to get a second transducer inside that cavity for a TT scan. In that case, pulse echo is likely to be the only option.

5.1.3.3   Immersion

Because almost all sound is reflected at an interface between the component and air, a couplant is needed between the transducers and the component. The simplest arrangement is to simply put everything in a water bath. With water completely surrounding the component and transducer, it is easy to move transducers around the part and observe signals without concern for continuity of couplant. While immersion is preferred, there are reasons to use other approaches. For example, a honeycomb component may be at risk of water ingress, or a component may be too large for available tanks.

5.1.3.4   Squirter

Large components with honeycomb are often too buoyant to immerse in a water tank. An alternate means of doing a water-based inspection is to use a squirter system. This uses the same type of

transducers, except they are placed inside a column of water, so that a continuous stream of water is being sprayed on the component, and the sound beam is fully contained within that water. The end result is essentially the same as an immersion scan, although there is a risk of getting extraneous echoes from air bubbles in the water column. Also, the beam diameter may be affected; for very small water columns, the beam diameter can be assumed to be the same size as the water column.

5.1.3.5   Laser

Very large parts or parts that have complex geometry, which cannot be scanned with conventional motion control systems can benefit from Laser UT. A high-power laser is aimed at the surface of the component to heat the surface rapidly enough to launch a sound wave, then a low-power laser picks up vibrations resulting from that excitation. The receiving laser works on the principle of interferometry. The end results are very similar to pulse-echo, with the benefit that the scan is done by steering the laser around the surface of the component without couplant. When setting up this type of scan, the operator must be careful that the component surface is not ablated by the laser; sometimes a layer of sacrificial tape is used.

5.1.3.6   Air Coupled

Air-coupled UT is sometimes used when water is not allowed to contact the component. Custom-designed air-coupled transducers are used, which have better coupling by acoustic impedance matching for air. Because air severely attenuates UT above 0.5 MHz, lower-frequency transducers are used, often in the range of 0.1 to 0.2 MHz. The consequence of this is a large sound beam and lower resolution. This is most often used in TT mode, but challenges arise with sound passing around the component's edges, making the outer edge of the component uninspectable unless special sound shielding is used to surround the component.

5.1.3.7   Apparatus: Scanning Systems and Fixtures

Composite parts offer a few unique challenges to the practical aspects of setting up a scan. Because sound transmits so easily through the composite-water interface, it is common for echoes arising from outside the component to show up in a scan. This is most common for support structures, which touch the back surface in various locations. Another version of this same effect is air bubbles on the back surface: a back surface amplitude image will show high-amplitude locations where air is trapped.

TT scans require careful alignment between the transmitting and receiving transducers. For large parts, this is accomplished by using precise motion of two robotic scanners moving in tandem. For smaller parts, a "yoke" can be used. This is a U-shaped device, which is able to reach around to the front and back sides of a part at the same time.

5.1.3.8   Transducers

The most common type of transducer is a single piezoelectric element made of a ceramic material, such as lead zirconate titanate (piezoelectric sensors/transducer (PZT)), as in Figure 5.1-4. These are easy to make in a repeatable manner and they last a long time. They can come in narrowband or broadband configurations. Narrowband probes create a burst of sound, which has a long duration. This long duration can penetrate complex materials better than short bursts, so it is often preferred for TT applications. The broadband version has a short burst of sound, which provides better time of flight (depth) resolution, and allows for detection of defective conditions nearer the

surface in pulse-echo mode. The short pulse duration is minimized when using a probe made with a different piezoelectric material: polyvinylidene fluoride (PVDF) or copolymer. The drawback of these latter probes is that they tend to transmit weaker signals.

Handheld transducers with a flat face are effective for contact inspections, where a transducer is manually slid across the surface of the component, with a couplant such as glycerin or mineral oil on the surface. Dry-contact ultrasonic transducers, (roller probes), area also available, but they are only effective for low-frequency applications. Higher-resolution images can be achieved by scanning with a focused transducer, with a separation, (water path), between the component and the transducer, which is no greater than the focal length of the transducer.

As seen in the medical UT community, phased array transducers are becoming more common in the industrial inspection community. For metal component applications, phased array transducers are able to steer a sound beam around the internal volume of the component and focus at multiple depths simultaneously, but for composites, the primary advantage is the ability to sweep a sound beam over a wide scan area for increase productivity. In general, the sound beam produced by an array transducer mimics that of a single element transducer.
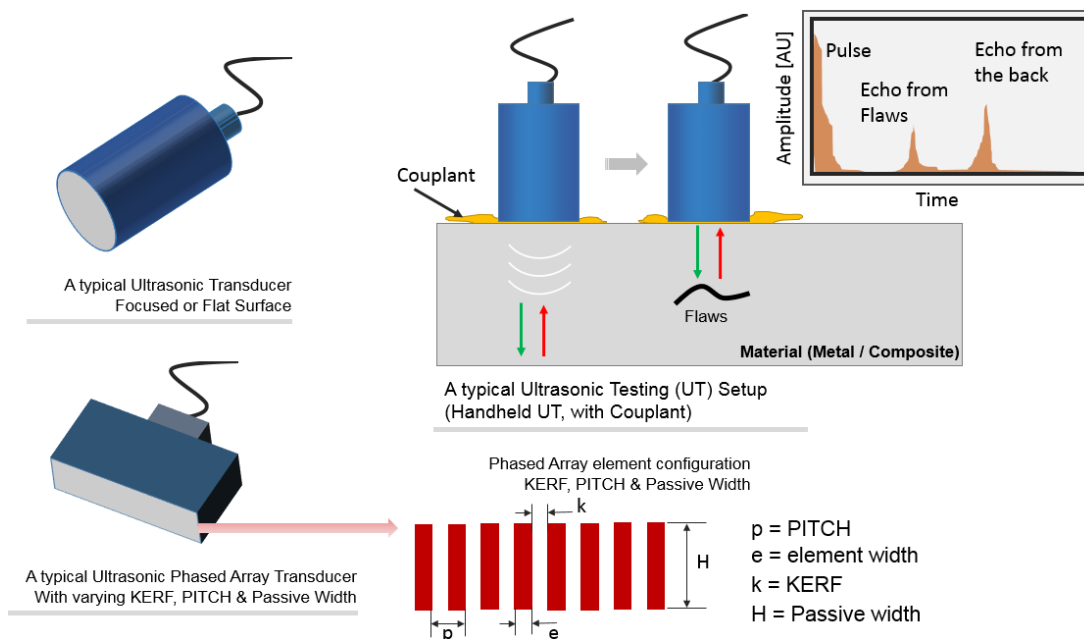
Figure 5.1-4. Typical ultrasonic transducers used in NDE of metal and composites.
These transducer arrangements are transmit receiver type, operating in pulse-echo mode, and used with couplants to send the ultrasonic energy into the test specimen.

5.1.3.9 Calibration Methods

While the metals community often will use a single set of flat bottom hole or side-drilled hole calibration standards for a large variety of parts, composite part designs are unique enough that a custom standard is needed for each design. In order to assess inspection capability and set meaningful limits, a component is needed that contains defective conditions at the requested threshold of detection. For example, if a 0.5-inch delamination needs to be detected, a target near that size (equal to or slightly smaller) needs to be placed in that same type of component to help determine the reject threshold. If the defective condition to be detected is delamination, then the target type should be one that does not bond, so a piece of Teflon might be inserted into the

component prior to cure. Because sensitivity often varies by depth, it is best to include targets at the range of depths that need inspection. These targets can also identify sensitivity risks at ply drops or other geometry features.

When a standard cannot be made with intentionally placed targets, pulse-echo sensitivity can be established by drilling flat-bottomed holes into a PMC component. TT sensitivity can be established by placing foam tape of the required size on the surface of the part. This latter solution must be practiced with care, as it has been shown that foam targets outside the component are easier to detect than real defective conditions inside the component.

Similar to delaminations, FOD can be placed in a component to assess the ability of UT to detect different material types within the laminate. Artificially made wrinkles are difficult to create, as is porosity. Often inspection capability for this is based on naturally occurring, rejected hardware.

5.1.4   Analysis of Ultrasonic Data

5.1.4.1   Detection Based on Amplitude

Regardless of the method of sound generation, the use and interpretation of signals is the same. The signal strength or amplitude of the received signal provides information about features in the sound path, which absorb or scatter sound. By mapping detected signal amplitudes over the area of the component, an image of the internal structure is generated, which is often intuitive to interpret by an inspector who is familiar with composite components.

In TT mode, signal strength is diminished by any disruption in the laminate. Delaminations block sound entirely from passing through the component, while porosity will scatter and absorb sound in a more subtle, yet detectable manner. Wrinkles contain fibers that are not perpendicular to the sound beam so they steer the sound away from the receiving probe. The result is that wrinkles cause a reduced signal strength at the receiving transducer. FOD can cause significant loss of signal as well, but some types, when bonded to the laminate, do not cause a measureable loss of signal strength.

One exception to the above description is the detection of surface-connected delaminations. It is possible for water to penetrate the delamination, and then sound is able to pass through multiple layers of composite and water. The transmission coefficient between water and composite is high enough that a water-filled delamination can be difficult to detect in TT mode.

Using pulse-echo mode, various target types reflect sound, and the characteristics of the targets affect the amplitude of the returned signal. Delaminations, large voids, and FOD will return sound energy to the receiving transducer for amplitude-based detection. While porosity and wrinkles will not return sound energy to the receiving transducer, if there is a signal available from the back surface, it can be monitored for loss of amplitude caused by porosity and wrinkles. Because of the behavior of the reflection coefficient, many types of FOD can be detected with higher sensitivity in pulse-echo than TT, including thin metal shim and water-filled delaminations.

Often amplitude-base indications are best detected in relation to their surroundings. A signal strength of 10%, for example, means nothing until one knows that the typical response at that same location is 3%. For this reason, C-Scan images and known calibration standards are important for amplitude-based evaluations.

5.1.4.2 Detection Based on Time of Flight

The time at which a signal arrives is also useful in detecting and characterizing defective conditions because in pulse echo, the time of arrival is proportional to the depth of the feature causing the echo. In addition to being a descriptive measure for indication evaluation, it can also provide detection in situations where pulse echo might miss an indication. Some defective conditions that produce a weak reflection, for example, may not be visible in an amplitude C-scan image, but if a preponderance of those low-amplitude signals came from the same depth, that might indicate the presence of laminar porosity. Another example is the case where a defective condition is very close to the back surface. A pulse-echo scan might pick up the signal with a normal amplitude, but time of flight image would show an abrupt change in depth, indicating the signal is not from the back surface at that location.

5.1.4.3 Data Presentation

Ultrasonic signals can be displayed as an A-scan, B-scan, or C-scan (see Figure 5.1-5). The C-scan is a common means of reporting data, showing in two dimensions, how the parameter of interest (amplitude or time of flight) varies over the area of the component. This is an intuitive display, which allows the inspector to understand the condition of the component. The A-scan is the one-dimensional (1D) display, which is essentially an oscilloscope trace, allowing the operator to dissect the various signals detected. The relationship between time and amplitude are available for analysis. The B-scan display is a stack of A-scans, color-coded for 2D display. This is effective for displaying a cross-sectional slice of the component under test.
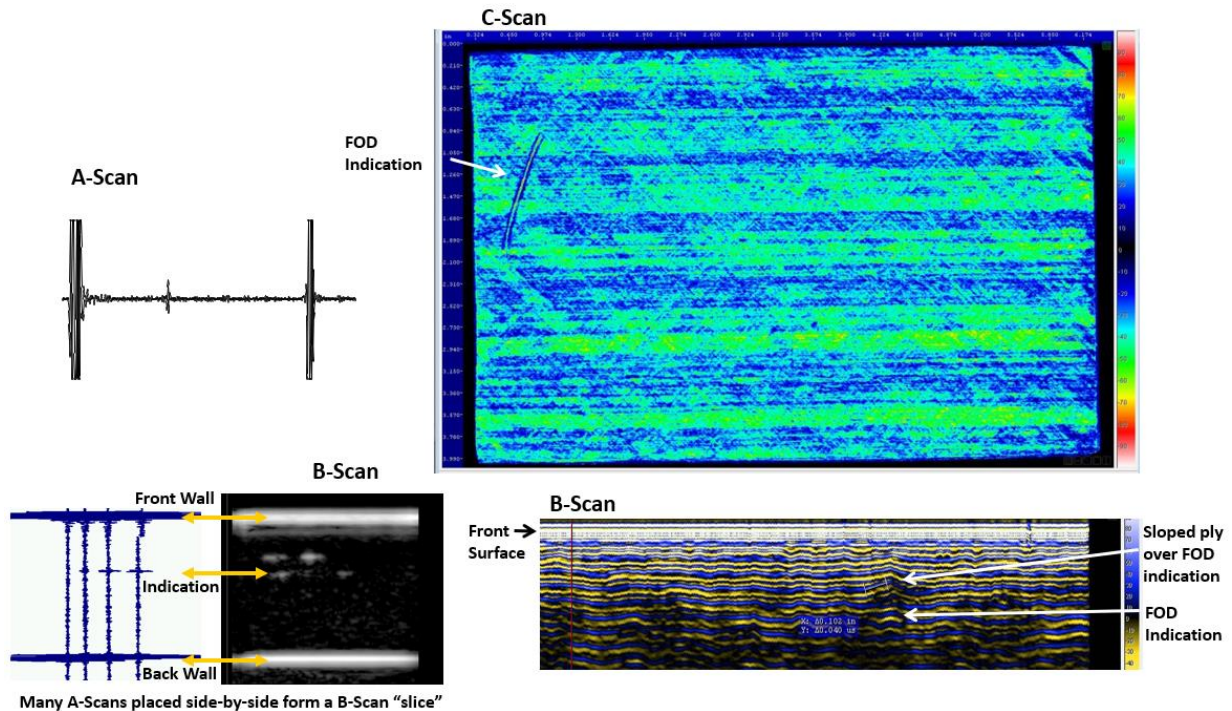
Figure 5.1-5. Examples of display options for ultrasonic data.

5.1.5 Applications

5.1.5.1 Delaminations

Delamination is the most common type of defect called out for detection. As discussed in prior sections, delaminations are relatively easy to detect because they block/reflect all incident sound. Because of this, they are high-amplitude features in pulse-echo scans, and low (zero) amplitude features in TT scans. The one reason for caution is when the delamination fills with water, it can be missed in TT. See Section 4 for a more detailed analysis of delaminations.

5.1.5.2 Spectrum of Voids and Porosity

Voids and porosity come in many configurations. At one end of the spectrum is fine, bulk porosity, which is a population of small voids uniformly distributed throughout a volume. At the other end is a single large void, which might be equated to a delamination. Several intermediate levels of voiding also exist. Laminar porosity is made up of small voids all lying within a single ply. "Bridging" is a series of voids/delaminations lying along a corner of an "L" or "U" structure. Each of these increasingly prevents the transmission of sound as severity increases, but measurement of each can differ. Delaminations, large voids, and laminar porosity can be measured as an area defect with a length and width. Smaller, distributed voids can be measured as a percent of volume, and that percentage is proportional to the sound loss (attenuation) per unit thickness (dB/in). See Section 4 for a more detailed analysis of porosity.

5.1.5.3 Spectrum of Foreign Object Debris (FOD)

FOD also exhibits a range of behavior, generally dictated by the effect that PMC cure cycle has on the material. Many polymer-based FOD transforms into a delamination or laminar porosity, while fibrous materials (e.g., breather) can be absorbed into the matrix like another fiber. Obviously, the ultrasonic response for the former will be much more detectable than the latter. The best way to determine which category a particular FOD will fall into is to put one in a component and run it through a cure cycle, followed by an ultrasonic scan. See Section 4 for a more detailed analysis of FOD.

5.1.5.4 Spectrum of Wrinkles and Fiber Alignment

Wrinkles can take multiple shapes, ranging from a small step over a ply drop to a "W" shape. In all cases, the loss of signal increases as the angle to the surface increases and as the length of the off-angle fiber increases. Ply drops are observed in an ultrasonic C-scan as a subtle stripe. Such stripes are reassurances of the ply orientation and coherent sound penetration. For the more severe case of a "W" shaped wrinkle, the sound transmission is modulated by the change in angle, where most of the signal is lost for the steep sides of the "W", but a full signal is able to pass through the wrinkle at the top and bottom peaks of the "W", leading to a striped appearance in a C-scan. See Section 4 for a more detailed analysis of wrinkles.

5.1.6 Emerging Concepts with Research Activity

5.1.6.1 Modeling to Predict UT Response

From the previous discussion, it is apparent that ultrasonic NDE of composites can be complicated compared to NDE of traditional materials, and is covered in depth in Section 5.6.1. Simulation tools can greatly aid in understanding ultrasonic wave propagation in complex components, along

with the tradeoffs between scan setup and detection of various types of defective conditions. Programs are being generated from several sources that are able to predict the signal returned for a given inspection configuration enabling a cost effective route to explore a large number of varying damage scenarios and geometries. Reference 3 discusses modelling methods, (finite element method (FEM), multi-Gaussian beam model (MGBM), etc.), with their respective pros and cons.

5.1.6.2 Artificial Intelligence for Automated Defect Recognition

Once a physics-based understanding is in place, employment of sophisticated data analysis and feature extraction methods can reduce the exorbitant amount of ultrasonic data into meaningful features. Development and implementation of machine-learning algorithms may enable real-time data reduction. However, a challenge is that machine-learning methods require large amounts of training data. Data sets may need labeling for some machine learning methods and must contain sufficient amounts of both "defect" and "pristine" data. Simulated data may be able to add to the available training data for more robust and cost-effective machine-learning algorithms. This is an area that will need careful consideration prior to use because of the consequences of getting a wrong answer on whether a component is defective or not. Testing protocols will need to be established to ensure automated decisions are as good as a human operator for novel indications.

5.1.6.3 Phased Array with FMC/TFM/PWI

While the inspection community is working through the details of how to use phased array, the next generation of phased array is already being created. This is a shift away from beam forming, moving towards firing on all elements of the array and then receiving on all elements. In its most basic form, it is called Full Matrix Capture, (FMC), to convey the idea that all elements are being used. Two sub-techniques are Total Focus Method, (TFM), and Plane Wave Imaging (PWI). Under these umbrellas fall additional nuances of signal processing, in order to receive data comparable to traditional UT scans, but with far less data acquisition time.

5.1.6.4 Surface Adaptive Contour following

In conjunction with phased array, FMC is surface adaptive scanning. In this scenario, the scanning system is no longer required to follow the contour of the component. Instead, the array of transducers is used with FMC to first predict the location and shape of the front surface then recalculate the image reconstruction to accommodate for refraction in the complex geometry of the component. It is only effective to the point where the individual elements can steer to the angles needed for such geometries, but where it applies, it is a powerful idea for increasing inspection throughput.

5.1.7 References

1. Krautkramer, J.; and Krautkramer, H.: "Ultrasonic testing of Materials," *Springer-Verlag*, 1990.
2. Gilmore, R. S.; Tam, Q. C.; Young, J. D.; and Howard, D. R.: Acoustic Microscopy from 10 to 100 MHz for Industrial Applications, *Phil. Trans. R Soc. London*, A320 215-235, 1986.
3. Michel Bouchon; and Francisco J. Sánchez-Sesma: "Boundary Integral Equations and Boundary Elements Methods in Elastodynamics, Chaper 3 in Advances in Wave Propagation in Heterogeneous Earth," *Advances in Geophysicis*, Ru-Shan Wu, Valerie Maupin, Renata Dmowska, Editors. 2007, Elsevier-Academic Press: New York, Boston.
4. Auld, B. A.: "Acoustic Fields and Waves in Solids," *Wiley*, 1990.

5. Rokhlin, S. I. C., D. E.; and Nagy, P. B.: *Physical Ultrasonics of Composites*, Oxford, UK: Oxford University Press, 2011.

5.2 Thermography

5.2.1 Introduction

The thermal NDE technique discussed in this Handbook is commonly referred to as "active thermography" [refs. 1 and 2]. Active thermography integrates IR thermal imaging with external heating to assess subsurface structure via the thermal response of the specimen. It is important to distinguish this approach from that of passive thermography used by the predictive maintenance community where temperature distributions of operating machinery or electrical systems are used to isolate localized heating indicative of operational problems. Additionally, passive thermography is routinely used to characterize infrastructure, such as roof temperature distributions, to look for potential degradation in structural performance. While these applications are very important in their own right, they do not involve the use of externally controlled heating as required for active thermography. Active thermography involves the detection of subsurface structures and defects based on the variation in thermal properties between the defect and the host material. During and/or following the active heating of the specimen, a measurement of the temporal evolution of the specimen surface temperature is performed by recording a time series of images with an IR camera allowing subsurface defects to be revealed. Figure 5.2-1 shows a diagram of a typical active thermography experimental setup.
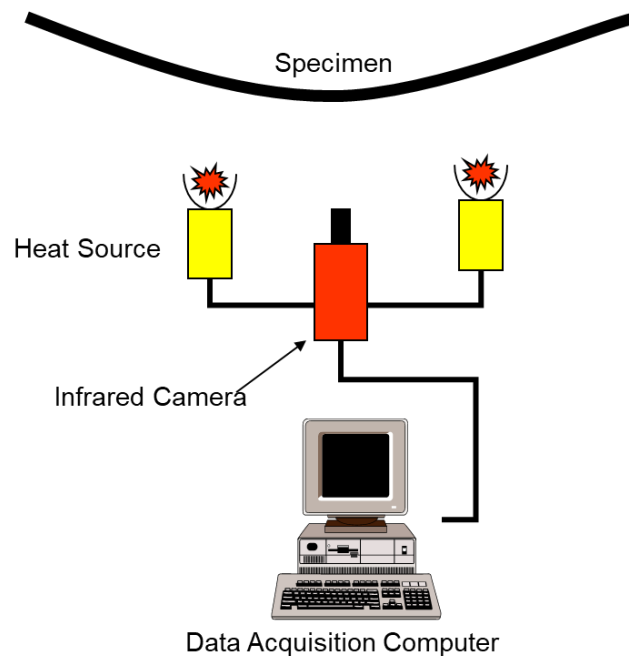
Figure 5.2-1. Diagram of a typical active thermography experimental setup.

To induce a temperature change in the specimen, various types of energy sources are used. The most common forms being divided into optical (xenon flash, quartz…), mechanical (vibrothermography, thermoelasticity…), and electromagnetic (eddy current, microwaves, terahertz…) [ref. 3]. There are two main classical types of active thermography techniques if we consider the way to deliver the energy, which are pulsed thermography, and modulated or lock-in thermography [ref. 2]. Khodayar provides a good overview, discussion, and examples of each of

these types of active thermography [ref. 4]. Generally, the differences between active thermography techniques arise either from different heating methods, as mentioned previously, or from different approaches to analyzing the data acquired. The remainder of the section will discuss techniques successfully applied to the inspection of aerospace composites.

5.2.2 Common Thermography Techniques for Composites

5.2.2.1 Single-sided Flash Thermography (SSFT)

The most commonly used means of inspecting graphite epoxy composites materials and structures is single-sided pulsed or flash thermography. The heating, typically excited using a very short duration (flash) heating pulse, usually produced by photographic type xenon flash bulbs. This method is routinely referred to as "flash thermography." The technique is single-sided because the flash heat source is on the same side of the specimen as the IR camera as illustrated in Figure 5.2-1. ASTM International has developed a standard practice for flash thermography of composite panels and repair patches used in aerospace applications. This standard practice describes the "established flash thermography test methods that are currently used by industry, and have demonstrated utility in quality assurance of composite structures during post-manufacturing and in-service examinations" [ref. 5].

5.2.2.1.1 *General Considerations*

One of the most critical elements of a flash thermography system is good synchronization between the triggering of the flash and the acquisition of the IR data, allowing for quantitative analysis of the data. Most commercial flash thermography systems provide very accurate synchronization, but if a system is developed from individual components and software, care must be taken to ensure that the application of the heat is tightly synchronized to the start of data acquisition from the IR camera. For heating purposes, commercial off-the-shelf xenon photographic flash-type lamps are used, but exercise caution must be exercised to make sure that the total energy deposited on the surface of the specimen is sufficient. Typically, raising the surface temperature by 3–5 °C above ambient will produce acceptable SNR in the resulting thermal images. Efforts should be made to keep the heating as uniform as possible across the inspection area of the specimen. This will reduce effects in the final thermal images that can be difficult to interpret. Also, note that injecting too much heat could result in damage to the specimen. To assist with heating and imaging by the IR camera, it is desirable for the inspection surface to have as high an emissivity as practical[6]. This could mean coating the surface of the specimen with a coating (black paint, lamp black, etc.) to raise the emissivity. Finally, both the angle of heating and the angle of the IR camera's optical axis with the inspection surface deserve consideration. Since thermal emissivity exhibits a cosine dependence on angle of incidence (off normal) [ref. 6], then both the energy applied to the surface and the temperature sensed by the camera will be affected by the angle of inspection.

As the inspection reports in this Handbook (Appendix E) demonstrate, there are a number of flaw types that can be detected by thermography when inspecting graphite-epoxy composites. Delaminations (discontinuities within the plies of a composite laminate), disbonds (discontinuities between two adhesively bonded composites), out-of-plane fiber wrinkling, FOD of some types,

---

[6] Emissivity is defined as the ratio of the energy radiated from a material's surface to that radiated from a blackbody (a perfect emitter) at the same temperature and wavelength and under the same viewing conditions. It is a dimensionless number between 0 (for a perfect reflector) and 1 (for a perfect emitter).

changes in thickness and porosity can all be detected using thermography. Thermography can typically detect flaws in a composite panel or repair patch, or at the bonded interface between the panel and a supporting sandwich core or solid substrate. It does not necessarily apply to detecting discontinuities in the sandwich core, or at the interface between the sandwich core and a second panel on the far side of the core (with respect to the inspection system). It has been noted that for a defect to be detectable by SSFT, the ratio of the diameter of the defect to its depth below the surface (also called the aspect ratio) must be greater than one [ref. 7]. While this assumption does not hold in all cases, it is a reasonable starting point for ensuring that flaws of interest are detected. Other considerations such as flaw type (porosity, disbonding, delamination, or impact damage, etc.), size, and severity also play a role.

In all cases, the individual performing the inspection must be thoroughly familiar with the underlying structure to avoid false calls during the evaluation. The underlying structure will absorb heat in varying degrees, which is can be falsely interpreted as other defects such as water absorption.

5.2.2.1.2   *Analysis Methodologies*

Flash IRT is a widely applied NDE technique for composite materials, because thermography it offers significant improvements advantages in both ease of application and speed of inspection over as compared to other commonly utilized NDE methods (e.g., tap, visual, UT, radiography, etc.). These improvements; however, are typically associated with increased cost. A notable limitation for flash IRT is its restricted depth of penetration, which typically limits its application to components less than 15 mm in thickness in single-sided applications (like defect aspect ratio, this is just a "rule of thumb" and not an absolute physical limit). Stemming from a combination of factors, the depth restriction is rooted in the exponential rate of attenuation of a defect signature with depth. This is a consequence of the dependence of thermography on the processes of heat conduction to convey information about internal structural anomalies. Thus, as a result, defect signatures for defects deeper into the material can be subtle, often amounting to temperature changes of tenths of a degree or less. From the standpoint of remote IR detection, this amounts to a, resulting in a difficult technical challenge. Therefore, to overcome this issue, image enhancement techniques become critical to the success of flash IRT inspection efforts. At the most basic level these enhancement measures consist of adaptations of conventional filtering approaches widely used in the visible image-processing field [ref. 8]. It is, however, possible to construct better analysis methods by exploiting aspects of heat-conduction physics, thus enhancing the signal of the data and allowing for better imaging of more subtle defects. Additionally, physics-based analysis methods, in some cases, can provide more rapid and accurate flaw detection, delineation [ref. 9], and quantitative material property measurements.

There are a number of common techniques for analyzing single-sided flash IRT data. For example, Shepard describes a means of analyzing flash thermography data called TSR [refs. 10 and 11]. This approach involves a polynomial regression of the thermal response in log-time space of each pixel in the time series. Reconstruction of the original thermal response is possible from the coefficients of the polynomial. There are several distinct advantages to this approach. First, the polynomial regression acts as a low pass filter of the thermal response, therefore reducing noise in the reconstructed data. Additionally, this regression is used as a lossy compression scheme, since it is only necessary to store the coefficients therefore greatly reducing the file size of the saved data. Finally, some analysis algorithms, such as first and second derivatives with respect to time, is are calculated very quickly from the stored coefficients, thus allowing rapid analysis of the data.

One drawback of polynomial regression is that the basic functions are not orthogonal and are therefore "non-local," meaning the fitted value of the thermal response at one point in time can depend strongly on thermal response values from other points in time [ref. 12]. Figure 5.2-2 shows a comparison between raw frames of SSFT data with no data processing, reconstructed frame of thermography data, and first and second time derivative images calculated from the polynomial regression. The specimen was a graphite epoxy composite (IM7/8552) 7.7 cm wide by 15.2 cm long by 0.33 cm in thickness with three impact damage sites that are visible in the thermography data. Figure 5.2-2 also highlights the benefits achieved by the application of analysis algorithms. While the three impact locations are visible in the raw thermal data, the quantified size (width) of the damage is difficult to determine without further image processing. When displaying raw thermal images with no data processing, hotter (disbonded) regions are typically shown as white and colder (undamaged) regions shown as grey. Because the heat transfer equation is a diffusion equation, the extent of the damage (width) is difficult to determine as the scaling in the image can be adjusted and the data are highly dependent on the time after the flash and the depth of the defect. Once processed, the color displayed in the image no longer represents hot or cold, but is a representation of the parameters of the processing (such as high and low values of the first or second time derivative). In Figure 5.2-2c, the first time derivative shows delamination damage in the 0° ply direction at two different depths (the thin black regions noted with red arrows surrounded by the bright white regions). If Figure 5.2-2d, the delaminations as detected in the second time derivative (noted with blue arrows) are aligned with the 45° fiber direction. Note that in both Figure 5.2-2c and 5.2-2d the edges of the delaminations are crisp and well defined as opposed to the unprocessed data in Figure 5.2-2a, allowing for quantification of the defect size.

a)   *b)*   *c)*   *d)*
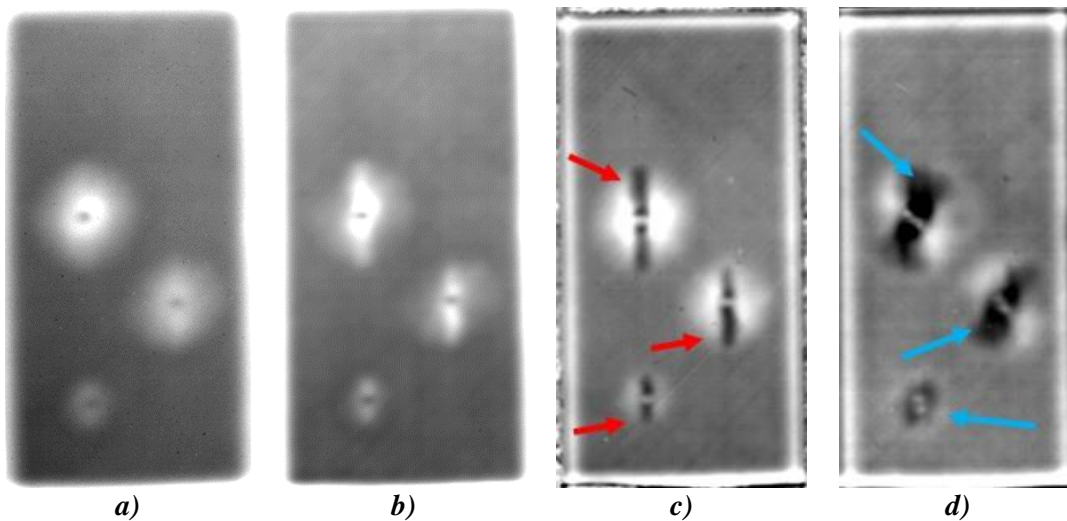
Figure 5.2-2. SSFT data from composite specimen.
All four images are from 1.10s after flash heating. a) Raw thermal image no data processing, b) thermal image after TSR analysis, c) first time derivative image using TSR analysis showing delamination indications at two different depths (red arrows highlighting delamination at one depth while the surrounding white regions consistent with deeper delamination) delaminations aligned with 0° ply direction and d) second time derivative image using TSR analysis. (blue arrows highlighting delamination indications aligned with 45° ply direction).

A second commonly used data analysis technique for SSFT is Principal Component Analysis (PCA) [ref. 13]. The application of PCA to the reduction of transient thermographic data consists

of calculating the principal components of the temporal data through singular value decomposition (SVD) of the experimental data itself. For example, Rajic [refs. 14 and 15] and Valluzzi [ref. 16] both use PCA as a contrast enhancement technique for defect detection. Genest [ref. 17] and Vavilov [ref. 18] provide comparisons between PCA and various other data-reduction techniques for defect sizing. Zalameda [ref. 19] discusses PCA's use for temporal compression of the thermal data. Finally, Marinetti [ref. 20] suggests the use of an experimentally derived training set to calculate the principal components. While this technique is quite effective in reducing thermal data, the singular value decomposition required for PCA can be computationally intense especially with large 3D arrays of thermal data typically produced during an inspection. Additionally, PCA can experience problems when very large defects are present (defects that dominate the FOV). The first eigenvector accounts for as much of the variability in the data as possible therefore if defective material dominates the FOV, the first eigenvector may reflect the response of the defect, not the "good" material. If material responses captured by the first eigenvector are considered a nominal material response, this results in a misclassification of the defect region. To increase the processing speed and eliminate issues arising from the presence of large defects, Cramer [ref. 21] proposed an alternative method of PCA where a fixed set of eigenvectors, generated from an analytic model of the thermal response of the material under examination, is used to process the thermal data from composite materials. Figure 5.2-3 demonstrates the results of PCA processing where the eigenvectors are calculated from the data acquired. The images show the projection of the data onto the first four eigenvectors from the same data set shown in Figure 5.2-2. Figure 5.2-3a predominantly accounts for the response of the 'good' material, while the higher eigenvectors reflect more discrete responses due to the damage. Projection of the raw thermal data onto the fourth eigenvector presents the best, quantitative view of the delamination (red arrows). To detect the deeper delaminations aligned to the 45° fiber direction the, PCA analysis would be performed on a later set (to highlight differences in thermal response of the specimen due to deeper delaminations) of time series images.
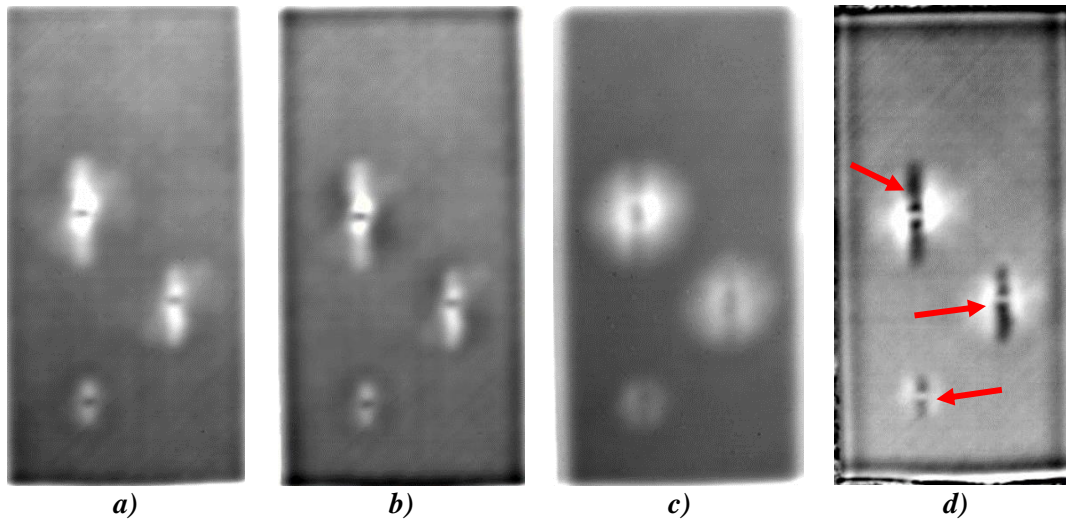
***Figure 5.2-3. SSFT data from composite specimen analyzed using PCA over the time
window from 0.6s to 4.0s after flash heating.
Each image is the projection of the raw thermal data onto: (a) first eigenvector, (b) second
eigenvector, (c) third eigenvector and (d) fourth eigenvector, with the red arrows pointing
to the delamination indications.***

Another common technique is PPT [refs. 22 and 23]. In this analysis approach, the data are transformed from the time domain to the frequency domain using the 1D discrete Fourier transform, yielding an amplitude and phase value for each pixel in the acquired thermal data. The major attraction to PPT over other data analysis routines is that the phase information produced by the technique tends to be less affected than raw thermal images by environmental reflections, emissivity variations, and non-uniform heating. Notwithstanding these advantages, phase data in PPT are very sensitive to high-frequency noise, typically due to the Gibbs Phenomenon.

Other techniques for analyzing SSFT data exist. Lopez [ref. 24] provides a good overview of a number of these techniques such as Thermal Contrast, Differential Absolute Contrast, and Peak SNR. D'Accardi [ref. 25] further provides a comparison of a five of different algorithms, highlighting their strengths and weaknesses on a single aluminum specimen.

5.2.3   TT Flash Thermography (Diffusivity Imaging)

Thermal diffusivity is the thermal conductivity divided by the density and specific heat capacity for a material at constant pressure. It measures the rate of transfer of heat in a material from the hot end to the cold end of a specimen. Changes in porosity, delaminations, disbonding, and fiber volume fraction can all affect the thermal diffusivity. Thermal diffusivity is typically measured by flash heating one side of a specimen and measuring the thermal response, as a function of time, of the opposite (or back) side. Because it is a two-sided measurement, it can be difficult to implement on large, fully assembled structures. However, it is an extremely useful tool for quantitative characterization of changes in a specimen.

Several methods were developed to compute thermal diffusivity (α) from standard IRT experimentation [refs. 26 and 27]. Probably the best-known technique to compute thermal diffusivity was derived by Parker [ref. 28]. Parker's method consists of heating a sample and observing the temperature evolution of either the front or back face. If the back face is monitored, Parker showed that for a sheet of thickness L, the time $t_{1/2}$ (this is the time for the back surface to

114

rise to half its maximum value) can be expressed (assuming a one-dimensional heat flow within a semi-infinite medium, an acceptable hypothesis if experimental conditions can reproduce such a scheme) by:

$$t_{1/_2} = \frac{1.38L^2}{\pi^2 \alpha}$$

Parker's method, while very straightforward and easy to implement, can be quite noisy especially when applied to an entire image. Therefore, Winfree [ref. 27] developed a method for reducing thermographic data to diffusivity images using a nonlinear least squares routine that fits experimental thermal data to an analytical representation of the thermal response of a single layer in a form that is computationally efficient to calculate. Because Winfree's method is using the entire thermal response, rather than a single point on the response curve, it is less susceptible to systemic noise. Using Winfree's approach, Zalameda showed how thermal diffusivity imaging is used to measure both changes in fiber volume fraction [ref. 29] and changes in porosity [ref. 30] in carbon fiber reinforced composites. Figure 5.2-4 shows diffusivity images of the same specimen as shown in Figures 5.2-2 and 5.2-3 calculated using both Parker's method and Winfree's nonlinear least squares routine. The region outlined in green is a "good" or defect free region, the region outline in red is a damaged region. Table 5.2-1 contains the average diffusivity calculated using each technique for the two regions noted in Figure 5.2-4. The uncertainty of the measurements is one equal to one standard deviation. As can be seen from Table 5.2-1, while the two methods give similar values, the standard deviation of Parker's method is more than an order of magnitude larger than Winfree's method.

a)   *b)*
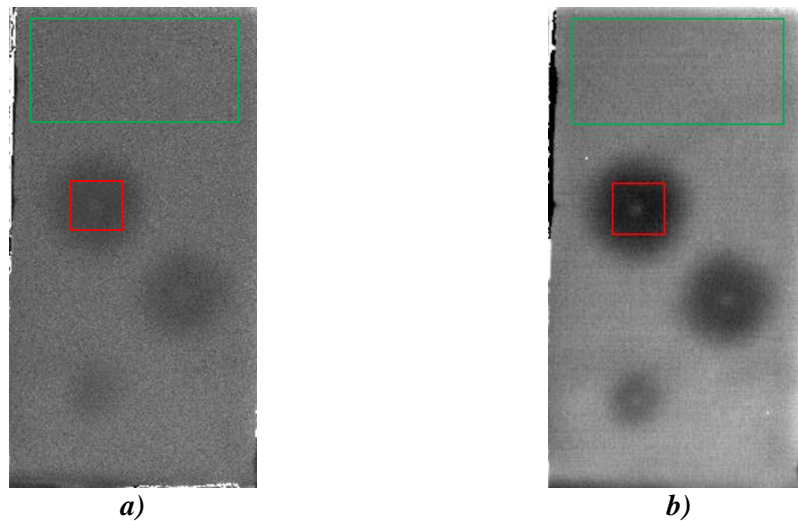
Figure 5.2-4. TT flash thermography data from composite specimen analyzed using two different thermal diffusivity imaging techniques.
a) Parker's Method, b) Winfree's routine. The green region represents 'good' material while the signal within the red box represents a damaged region.

Table 5.2-1. Thermal diffusivity values for the outlined regions of Figure 5.2-4.
The uncertainty of the measurement is equal to one standard deviation over the region.

Thermal Diffusivity cm^2/s		
	Parker's Method	Winfree's Routine
Good Region (Green)	0.0044 ± 0.00037	0.00474 ± 0.000025
Damaged Region (Red)	0.0030 ± 0.00025	0.00321 ± 0.000025

5.2.4 Other Heating Methods

A number of other heating methods are possible for the inspection of composite materials with IRT. Eddy Current Thermography (ECT), also called induction thermography, is a combination of eddy current heating and thermography, which is based on electromagnetic induction and Joule effect heating. ECT has many advantages, such as being non-contact, fast, full-field and high resolution. ECT is a kind of volume heating thermography for graphite composites due to low conductivity and great skin depth [refs. 31−34].

Related to ECT, Active Microwave Thermography (AMT) is a relatively new approach to thermal NDE, which takes advantage of unique aspects of microwave NDE and thermography, thereby offering the potential for improved inspections. In this approach, the specimen is exposed to microwave energy, since carbon fiber composites are electrically conductive, current is induced in the composite. The presence of a defect (i.e., delaminated portion of the composite) will affect the diffusion of heat through the structure, and will be evident in the surface temperature profile [refs. 35−38].

Line scanning thermography (LST) is a dynamic thermography technique, which has successfully applied to the inspection of metallic surfaces and composites. In LST, the heat source is moved across the sample's surface at a constant speed and an IR imager is used to record the temperature changes on the surface during the heating protocol. The IR detector moves at the same velocity as the heat source and the imager's FOV is set to contain a region behind the location where heat is deposited. The temperature recorded in the heated region is used to analyze the cooling behavior after heat deposition detecting the presence of defects or material property changes. This technique has the advantage that when robotically implemented very large structures are interrogated very quickly [refs. 39−45].

Long pulse heating, usually achieved with quartz heat lamps, is used to successfully inspect carbon fiber composites [ref. 46]. Other less common heating methods include hot (or cold) air [ref. 47], laser pulse heating [ref. 48] and even solar heating [ref. 49].

A variation of long pulse heating is lock-in thermography (LT) or modulated thermography. In LT, the heat source (usually a quartz lamp) is modulated as a sine or square wave, synchronized the frame rate of the camera. Images are recorded with the IR camera and synchronous demodulation is performed [ref. 50]. Similar to PPT (discussed earlier), the results yield amplitude and phase images.

Finally, in contrast to classical thermography in which the energy is delivered to the sample surface by convection (i.e., via hot air) or radiation (i.e., via xenon lamps), in vibrothermography, the sample is mechanically excited by an elastic wave from a mechanical vibration, such as sonic or ultrasonic oscillations. In general, the propagation of the damped acoustic waves through the material converts mechanical energy into thermal energy, but near a defect, the energy dissipation is greater due to friction between the faces of the defect and/or stress concentration in the

surrounding material. This mechanical excitation acts as a selective inner heat source, located just at the defect, which diffuses inside the material and is detected as a temperature variation on its surface by means of an IR camera [refs. 51−53].

5.2.5 References

1. Shull, P. J.: "Nondestructive evaluation: theory, techniques, and applications," *CRC press*, 597-644, 2016.
2. Maldague, X. P. V.: "Nondestructive Evaluation of Materials by Infrared Thermography," *NDT and E International*, 6(29), 6, 1996.
3. Ibarra-Castanedo, C.; Genest, M.; Piau, J. M.; Guibert, S.; Bendada, A.; and Maldague, X. P.: *Active Infrared Thermography Techniques for the Nondestructive Testing of Materials*, in *Ultrasonic and Advanced Methods for Nondestructive Testing and Material Characterization*, 325-348, 2007.
4. Khodayar, F.; Sojasi, S.; and Maldague, X.: "Infrared thermography and NDT: 2050 horizon," *Quantitative InfraRed Thermography Journal*, 13(2), 210-231, 2016.
5. ASTM International: *Standard Practice for Infrared Flash Thermography of Composite Panels and Repair Patches Used in Aerospace Applications*, ASTM, A. E., 2582, West Conshohocken, Pennsylvania, 2007.
6. Howell, J. R.; Menguc, M. P.; and Siegel, R.: "Thermal radiation heat transfer," *CRC press*, 2015.
7. Milne, J. M.; and Reynolds, W. N.: "The non-destructive evaluation of composites and other materials by thermal pulse video thermography," in *Thermosense VII: Thermal Infrared Sensing for Diagnostics and Control*, Vol. 520, pp. 119-123, International Society for Optics and Photonics, 1985, March.
8. Maldague, X.; and Moore, P. O.: *Infrared and thermal testing nondestructive testing Handbook*, Columbus, OH, 2001.
9. Rajic, N.: "Principal Component Thermography for Flaw Contrast Enhancement and Flaw Depth Characterisation in Composite Structures," *Composite Structures*, 58(4), 521-528, 2002.
10. Shepard, S. M.: U.S. Patent No. 6,751,342. Washington, DC: U.S. Patent and Trademark Office, 2004.
11. Shepard, S. M.; Lhota, J. R.; Rubadeux, B. A.; Wang, D.; and Ahmed, T.: "Reconstruction and enhancement of active thermographic image sequences," *Optical Engineering*, 42(5), 1337-1343, 2003.
12. Magee, L.: Nonlocal behavior in polynomial regressions. The American Statistician, 52(1), 20-22, 1998.
13. Winfree, W. P.; Cramer, K. E.; Zalameda, J. N.; Howell, P. A.; and Burke, E. R.: Principal Component Analysis of Thermographic Data," in *Thermosense: Thermal Infrared Applications XXXVII* (Vol. 9485, p. 94850S), International Society for Optics and Photonics, 2015, May.
14. Rajic, N.: Principal Component Thermography for Flaw Contrast Enhancement and Flaw Depth Characterisation in Composite Structures," *Composite Structures*, 58(4), 521-528, 2002.
15. Rajic, N.: *Principal component thermography* (No. DSTO-TR-1298), Defence Science And Technology Organisation Victoria (Australia) Aeronautical And Maritime Research Lab, 2002.

16. Valluzzi, M. R.; Grinzato, E.; Pellegrino, C.; and Modena, C.: "IR Thermography for Interface Analysis of FRP Laminates Externally Bonded to RC Beams," *Materials and Structures*, 42(1), 25-34, 2009.
17. Genest, M.: "Image Processing for Automated Flaw Detection in Pulsed Thermography," in *Proceeding of 6th International Workshop-NDT Signal Processing* (pp. 1-9), 2009, November.
18. Vavilov, V. P.; and Marinetti, S.: "Comparative Analysis of the Thermal Testing of Corrosion in High and Low Heat-Conducting Metals," *Russian Journal of Nondestructive Testing*, 44(12), 841-846. 2008.
19. Zalameda, J. N.; Howell, P. A.; and Winfree, W. P.: "Compression techniques for improved algorithm computational performance," in *Thermosense XXVII* (Vol. 5782, pp. 399-407). International Society for Optics and Photonics, 2005, March.
20. Marinetti, S.; Grinzato, E.; Bison, P. G.; Bozzi, E.; Chimenti, M.; Pieri, G.; and Salvetti, O.: "Statistical analysis of IR thermographic sequences by PCA," *Infrared Physics and Technology*, 46(1-2), 85-91, 2004.
21. Cramer, K. E.; and Winfree, W. P.: "Fixed Eigenvector Analysis of Thermographic NDE Data," in *Thermosense: Thermal Infrared Applications XXXIII* (Vol. 8013, p. 80130T). International Society for Optics and Photonics, 2011, May.
22. Ibarra-Castanedo, C.; and Maldague, X.: "Pulsed Phase Thermography Reviewed," *Quantitative Infrared Thermography Journal*, 1(1), 47-70, 2004.
23. Maldague, X.; Galmiche, F.; and Ziadi, A.: "Advances in Pulsed Phase Thermography," *Infrared Physics and Technology*, 43(3-5), 175-181, 2002.
24. Lopez, F.; Ibarra-Castanedo, C.; Maldague, X.; and de Paulo Nicolau, V.: "Analysis of Signal Processing Techniques in Pulsed Thermography," in T*hermosense: Thermal Infrared Applications XXXV* (Vol. 8705, p. 87050W), International Society for Optics and Photonics, 2013, May.
25. D'Accardi, E.; Palumbo, D.; Tamborrino, R.; and Galietti, U.: "Quantitative Analysis of Thermographic Data Through Different Algorithms," *Procedia Structural Integrity*, 8, 354-367, 2018.
26. Welch, C. S.; Winfree, W. P.; Heath, D. M.; Cramer, K. E.; and Howell, P. A.: "Material property measurements with post-processed thermal image data," in *Thermosense XII: An International Conference on Thermal Sensing and Imaging Diagnostic Applications*, Vol. 1313, pp. 124-134, International Society for Optics and Photonics, 1990, March.
27. Winfree, W. P.; and Heath, D. M.: "Thermal diffusivity imaging of aerospace materials and structures," in *Thermosense XX*, Vol. 3361, pp. 282-291, International Society for Optics and Photonics, 1998, March.
28. Parker, W. J.; Jenkins, R. J.; Butler, C. P.; and Abbott, G. L.: "Flash Method of Determining Thermal Diffusivity, Heat Capacity, and Thermal Conductivity," *Journal of Applied Physics*, 32(9), 1679-1684, 1961.
29. Zalameda, J. N.; and Winfree, W. P.: "Quantitative Thermal Diffusivity Measurements on Composite Fiber Volume Fraction (FVF) Samples," in *Review of Progress in Quantitative Nondestructive Evaluation*, pp. 1289-1295. Springer, Boston, MA, 1993.
30. Zalameda, J. N.: "Measured through-the-thickness thermal diffusivity of carbon fiber reinforced composite materials," *Journal of Composites, Technology and Research*, 21(2), 98-102, 1999.

31. Sakagami, T.; and Ogura, K.: "New flaw inspection technique based on infrared thermal images under Joule effect heating," *JSME International Journal, Ser. A, Mechanics and Material Engineering*, 37(4), 380-388, 1994.

32. Cheng, L.; and Tian, G. Y.: "Surface Crack Detection for Carbon Fiber Reinforced Plastic (CFRP) Materials Using Pulsed Eddy Current Thermography," *IEEE Sensors Journal*, 11(12), 3261-3268, 2011.

33. He, Y.; Tian, G.; Pan, M.; and Chen, D.: "Impact Evaluation in Carbon Fiber Reinforced Plastic (CFRP) Laminates Using Eddy Current Pulsed Thermography," *Composite Structures*, 109, 1-7, 2004.

34. Yang, R.; and He, Y.: "Polymer-Matrix Composites Carbon Fiber Characterization and Damage Inspection Using Selectively Heating Thermography (SeHT) Through Electromagnetic Induction," *Composite Structures*, 140, 590-601, 2016.

35. Foudazi, A.; Donnell, K. M.; and Ghasr, M. T.: Application of Active Microwave Thermography to Delamination Detection," in *2014 IEEE International Instrumentation and Measurement Technology Conference (I2MTC) Proceedings*, pp. 1567-1571, IEEE, 2014, May.

36. Pieper, D.; Donnell, K. M.; Ghasr, M. T.; and Kinzel, E. C.: "Integration of Microwave and Thermographic NDT Methods for Corrosion Detection," in *AIP Conference Proceedings*, Vol. 1581, No. 1, pp. 1560-1567, AIP, 2014, February.

37. Levesque, P.; Deom, A.; and Balageas, D.: "Nondestructive Evaluation of Absorbing Materials Using Microwave Stimulated Infrared Thermography," in *Review of Progress in Quantitative Nondestructive Evaluation*" pp. 649-654, Springer, Boston, MA, 1993.

38. Prost, D.; Issac, F.; Lemaître, F.; and Parmantier, J. P.: "Infrared Thermography of Microwave Electromagnetic Fields," in *International Symposium on Electromagnetic Compatibility-EMC EUROPE*, pp. 1-4, IEEE, 2012, September.

39. Woolard, D. F.; and Cramer, K. E.: "Line Scan Versus Flash Thermography: Comparative Study on Reinforced Carbon-Carbon," in *Thermosense XXVII*, Vol. 5782, pp. 315-324, International Society for Optics and Photonics, 2005, March.

40. Cramer, K. E.; and Winfree, W. P.: "Thermal Characterization of Defects in Aircraft Structures Via Spatially Controlled Heat Application," in *Thermosense XVIII: An International Conference on Thermal Sensing and Imaging Diagnostic Applications*, Vol. 2766, pp. 202-210, International Society for Optics and Photonics, 1996, March.

41. Peeters, J.; Ibarra-Castanedo, C.; Khodayar, F.; Mokhtari, Y.; Sfarra, S.; Zhang, H.; and Steenackers, G.: "Optimised Dynamic Line Scan Thermographic Detection Of CFRP Inserts Using FE Updating and POD Analysis," *NDT and E International*, 93, 141-149, 2018.

42. Khodayar, F.; Lopez, F.; Ibarra-Castanedo, C.; and Maldague, X.: "Parameter Optimization of Robotize Line Scan Thermography for CFRP Composite Inspection," *Journal of Nondestructive Evaluation*, 37(1), 5, 2018.

43. Ibarra-Castanedo, C.; Servais, P.; Ziadi, A.; Klein, M.; and Maldague, X.: "RITA-Robotized Inspection by Thermography and Advanced Processing for the Inspection of Aeronautical Components," in *12th International Conference on Quantitative InfraRed Thermography*, 2014, July.

44. Peeters, J.; Verspeek, S.; Sels, S.; Bogaerts, B.; and Steenackers, G.: "Optimized Dynamic Line Scanning Thermography for Aircraft Structures," *Quantitative Infrared Thermography*, 687-695, 2018.

45. Ley, O.; Butera, M.; Godinez, V.; and Chung, S.: "Assessing Impact Damage on Composites Using Line-Scanning Thermography," *Advanced Materials and Processes*, 170(6), 20-25, 2012.
46. Cramer, K. E.: (2002). *Thermal Nondestructive Evaluation Report: Inspection of the Refurbished Manipulator Arm System in the Manipulator Development Facility at Johnson Space Center 10–12 January 2001*, NASA/TM–2002-211732, 2002.
47. Valluzzi, M. R.; Grinzato, E.; Pellegrino, C.; and Modena, C.: "IR Thermography for Interface Analysis of FRP Laminates Externally Bonded to RC Beams," *Materials and Structures*, 42(1), 25-34, 2009.
48. Junyan, L.; Yang, L.; Fei, W.; and Yang, W.: "Study on Probability of Detection (POD) Determination Using Lock-In Thermography for Nondestructive Inspection (NDI) of CFRP Composite Materials," *Infrared Physics and Technology*, 71, 448-456, 2015.
49. Howell, P. A.; Winfree, W. P.; and Cramer, K. E.: "On-Orbit Passive Thermography," *Nondestructive Testing and Evaluation*, 23(3), 195-210, 2008.
50. Zweschper, T.; Dillenz, A.; and Busse, G.: "NDE of adhesive Joints and Riveted Structures With Lock-In Thermography Methods," in *Thermosense XXIII*, Vol. 4360, pp. 567-574, International Society for Optics and Photonics, 2001, March.
51. Rantala, J.; Wu, D.; and Busse, G.: "Amplitude-Modulated Lock-In Vibrothermography for NDE of Polymers and Composites," *Research in Nondestructive Evaluation*, 7(4), 215-228, 1996.
52. Salazar, A.; Mendioroz, A.; Apiñaniz, E.; Oleaga, A.; Venegas, P.; and Sáez-Ocáriz, I.: "Characterization of delaminations by lock-in vibrothermography," in *Journal of Physics: Conference Series*, Vol. 214, No. 1, p. 012079, IOP Publishing, 2010.
53. Yi, H.; Peng-Cheng, M.; Zhong-Ning, Z.; Shu-Yi, Z.; Li, S.; Xiu-Ji, S.; and Zhi-Bing, Z.: "The Ultrasonic Infrared Thermography and its Application in NDE [J]," *Journal of Nanjing University (Natural Sciences)*, 4, 014, 2003.

5.3   Radiography

Radiography is an NDE method that utilizes penetrating X-rays, gamma rays, or neutrons to inspect materials. However, the following sections of this Handbook will only focus on the use of X-rays. X-rays are high-energy photons, which pass through material and attenuate roughly proportional to density of the material. TT radiography consists of a source generating X-rays, which pass through the part being inspected and excite an imaging material (film) or device (digital detector). A resulting image corresponding to the density variations of the part is created, which allows for inspection for internal flaws and features. Most methods are 2D, generating a superimposed image of the part. CT creates a reconstructed 3D volume, greatly increasing the flexibility and applicability of radiography. X-rays are commonly generated by accelerating electrons in a vacuum with high voltage from a hot filament to a tungsten or similar material target. This generates heat and X-rays, which exit the vacuum tube through a window in a cone or fan beam spread. Quality sharp images require a fine focal spot size from which the X-ray originates.

Radiography has advantages over many other NDE methods with improved resolution, penetrating power, and variety of parts that can be inspected. It has distinct disadvantages, however, in safety and cost. The ionizing radiation used in radiography requires that inspections take place in a cleared safety zone or shielded vault/cabinet. Additionally, X-ray systems are often extremely expensive compared to other NDE systems. 2D methods are very sensitive to defect orientation.

Defects parallel to the beam do not produce enough change in density over enough pixels of the detector to be quantified.

5.3.1 Computed Radiography (CR)

CR is a 2D TT X-ray inspection method. It uses a phosphor imaging plate to acquire a digital X-ray image instead of traditional X-ray film. It system consists of a standard X-ray source generating X-rays, which pass through a part and expose an imaging plate for a period ranging from seconds to minutes. After exposure to X-rays, the incoming radiation is stored in the phosphor layer of the imaging plate. A red laser from the scanner stimulates the plate and causes it to emit visible blue light that is detected by a photomultiplier tube. The light is converted to digital signal/image, and is stored on a computer. The imaging plate is erased by high-intensity white light and is ready for next exposure. The images, usually 16-bit greyscale, are then reviewed digitally with brightness and contrast controls and a variety of filters and tools available. CR X-ray imaging is sensitive to density variations, caused by material differences, voids, or other defects effecting the density of material the X-rays pass through. Because this imaging is 2D, the results are superimposed internal images of the specimens. Figure 5.3-1 shows a diagram of a CR imaging setup.
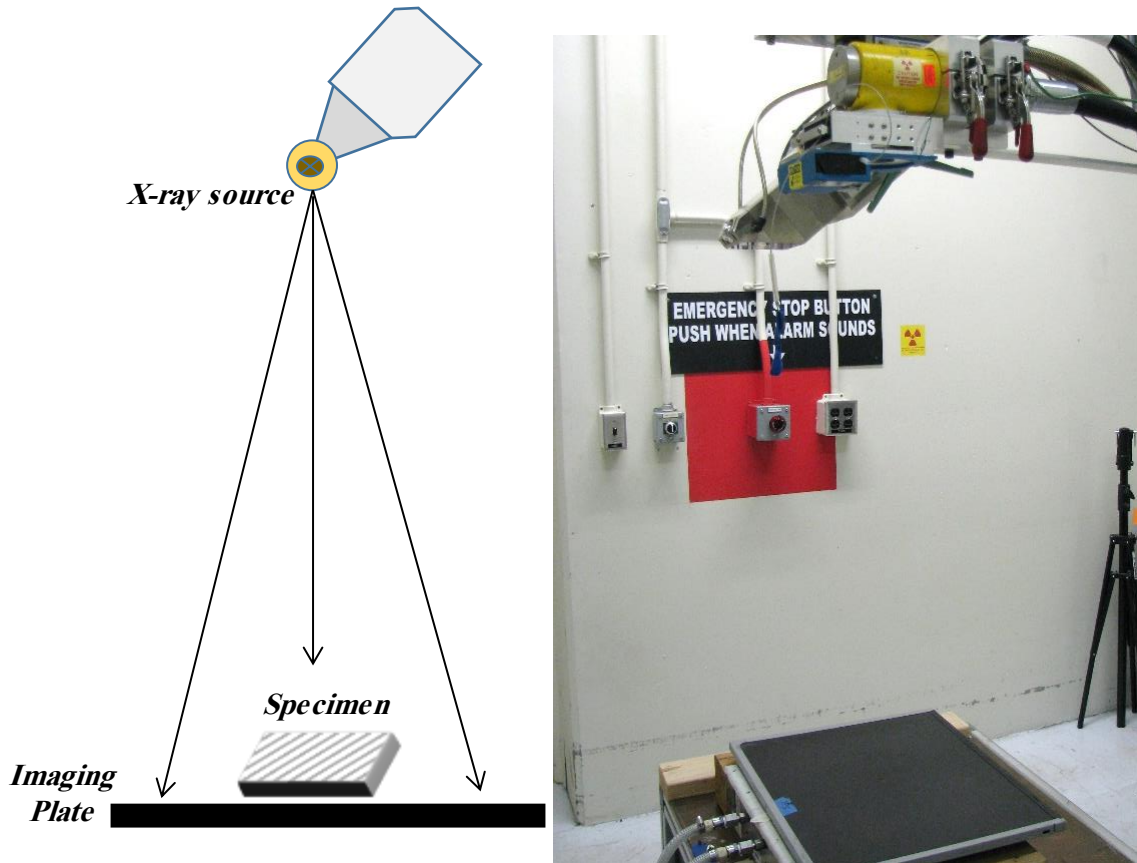
Figure 5.3-1. CR imaging setup.

CR performs very similar to DR on composites. Figures 5.3-2 and 5.3-3 show excellent sensitivity to the high-density brass inserts but poor contrast for the low-density change of RPF inserts.
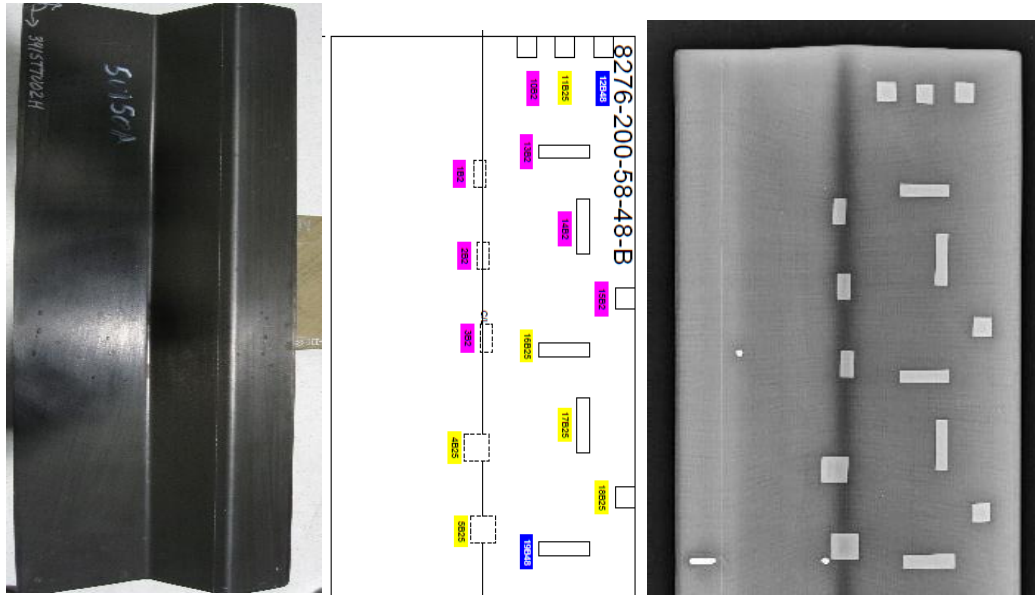
Figure 5.3-2. Photo of S-curve panel (left), defect map where purple denotes locations of 0.001-inch brass foil inserts, (middle), and CR image (filter applied) (right) of brass inserts in S-curve composite panel.
The dark line down the center of the image is located at the curvature of the specimen where the X-ray path has less material to pass through before reaching the detector.
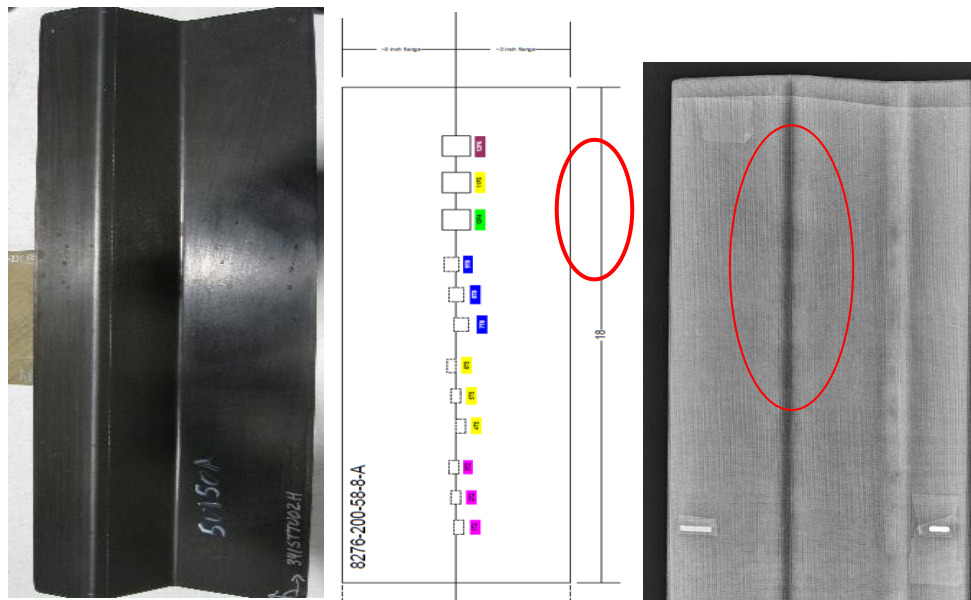
Figure 5.3-3. Photo of S-curve panel (left), defect map where top three squares denotes RPF inserts at three different ply depths (middle), and CR image (filter applied) of RPF material (circled) in composite panel (right), showing poor contrast for the low-density change of RPF inserts.

The parameters that effect CR are source energy kilovolt (kV), source current milliamp (mA), source distance, focal spot size, imaging plate type, exposure time, and scanner resolution. The scanner resolution has the largest effect on the resulting image resolution. Although image plate type and focal spot size, can affect the noise, contrast and geometric unsharpness. Composites have the advantage of requiring less source energy to penetrate due to their lower density and therefore

122

can achieve a higher contrast sensitivity. This also allows a large selection of potential sources for use in the field.

CR shares advantages and disadvantages with the other X-ray methods. It provides high-resolution results with good sensitivity to a variety of defects and is used to measure various features of parts. It produces images that are easier to interpret than many other NDE methods. This makes CR more suitable for complex parts than other methods such as UT. It provides a resolution generally better than DR, but tends to result in more noise. CR provides faster results than film X-ray while also providing some of the field flexibility of film. The imaging plates do wear down slowly over time due to cumulative exposure to ionizing radiation and handling.

CR is currently seeing developments similar to other areas of X-ray technology. Assisted Defect Recognition (ADR) is being developed for many applications to improve speed and consistency of inspection for production settings. This often involves algorithms, image processing, and measurement tools to automatically or nearly automatically identify and measure defects of concern to determine if the part in question meets passing criteria. Tools to improve the image quality of CR by reducing noise or image plate artifacts are in development. Improved resolution CR scanners are available to improve that limiting factor in CR technology.

5.3.2   Digital Radiography (DR)

DR is a 2D TT X-ray inspection method. It consists of a standard X-ray source generating X-rays, which pass through a part and expose a DDA, as shown in Figure 5.3-4. The object-to-detector distance is often used to magnify the image. The individual detector elements that make up this array take the photons of the X-rays and convert them to electrical signals corresponding to the incoming radiation. It is typical to take many short exposure frames from the detector and average them to produce a reduced noise image. The images, usually 16-bit greyscale, are reviewed digitally with brightness and contrast controls, a variety of filters, and functions such as panning, zooming, inverting the gray scale, and measuring distances and angles. DR X-ray imaging is sensitive to density variations, caused by material differences, voids, or other defects effecting the density of material the X-rays pass through. Because this imaging is 2D, the resulting images are the integrated absorption of the X-rays along their path before reaching the detector.
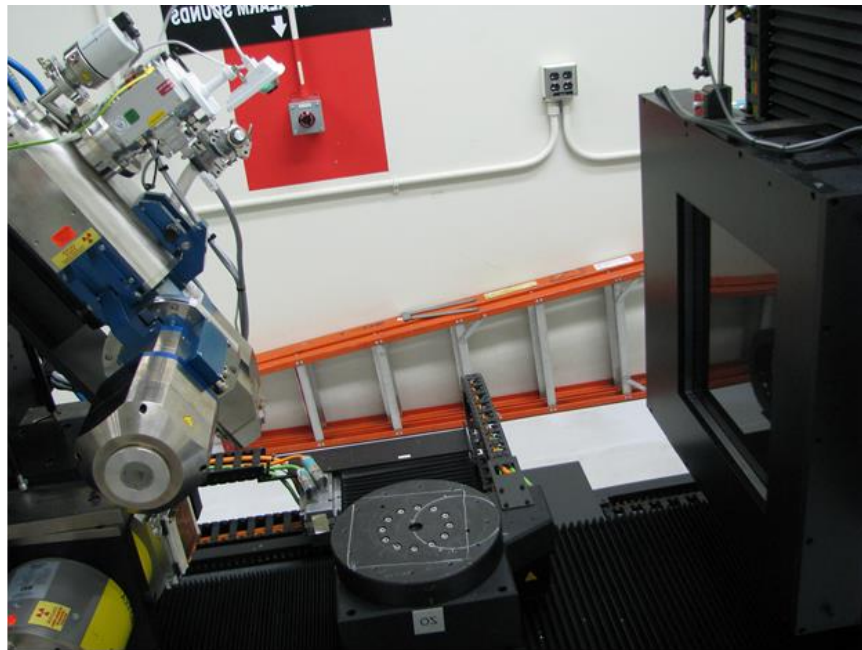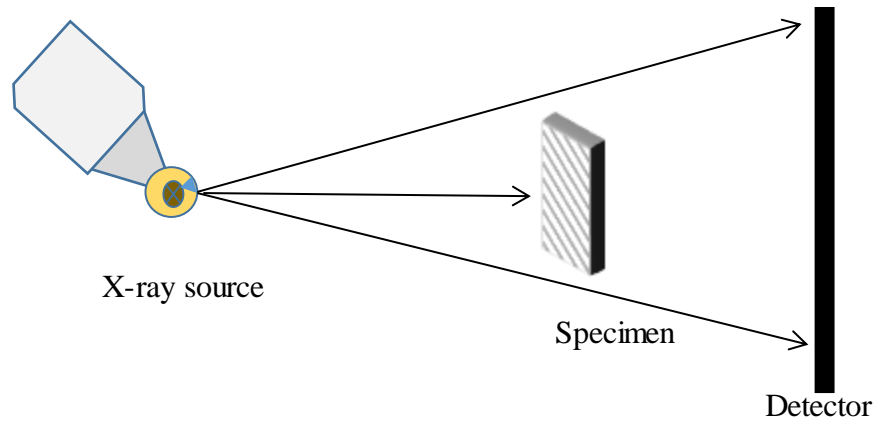
Figure 5.3-4. DR imaging setup.

DR performs on composites similar to other X-ray methods. It is excellent at identifying high-density foreign material because of its sensitivity to density differences. Thus, metal heavily contrasts with the relatively low-density composite materials. Figure 5.3-5 shows brass inserts (dark rectangles) clearly contrasting with the low-density composite. However, DR is sensitive to defect orientation. If a defect such as a delamination that is tightly closed does not cause a density change large enough in the direction of the X-rays, such as closed contact, DR will not be sensitive to it. The RPF inserts in Figure 5.3-6 cause a very limited density change, resulting in low contrast. Being generally spherical, porosity is often detected by DR from multiple directions. DR is capable of evaluating sandwich panels and core defects such as core crushing, which can occur in honeycomb composites with CFRP face sheets when damage occurs to the face sheet causing the core to indent and sometimes detach from the face sheet. Radiography is better suited to the detection of volumetric defects than linear defects such as cracks or tightly closed delamination.
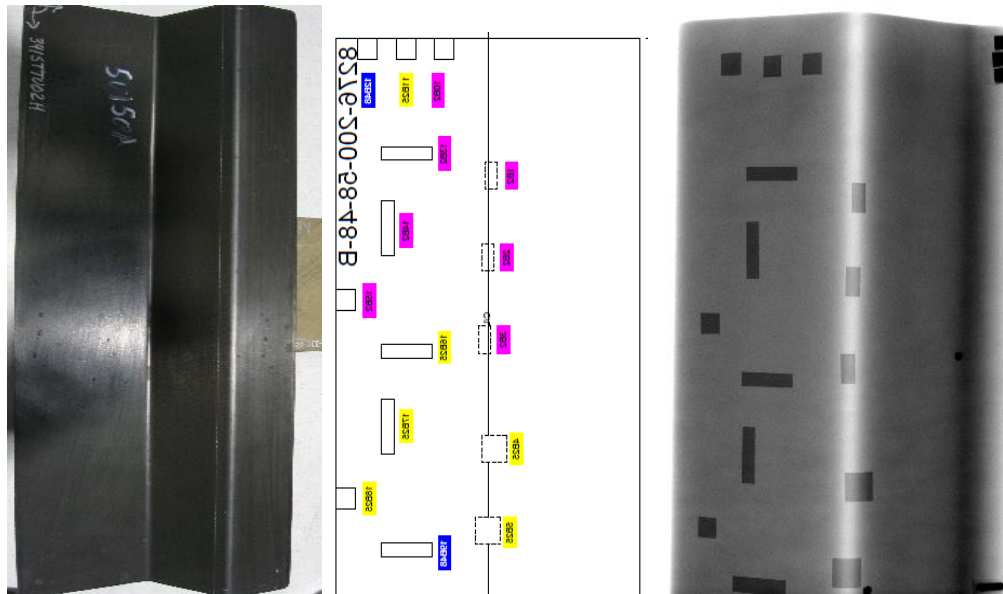
Figure 5.3-5. Photo of S-curve panel (left), defect map where purple denotes locations of 0.001-inch brass foil inserts, (middle), and DR image (right) of brass inserts in S-curve composite panel.
The white line down the center of the image is located at the curvature of the specimen where the X-ray path has less material to pass through before reaching the detector. Similarly, the vertical black line is the curvature in the opposite direction where fewer X-rays are able to reach the detector as they pass through more material.
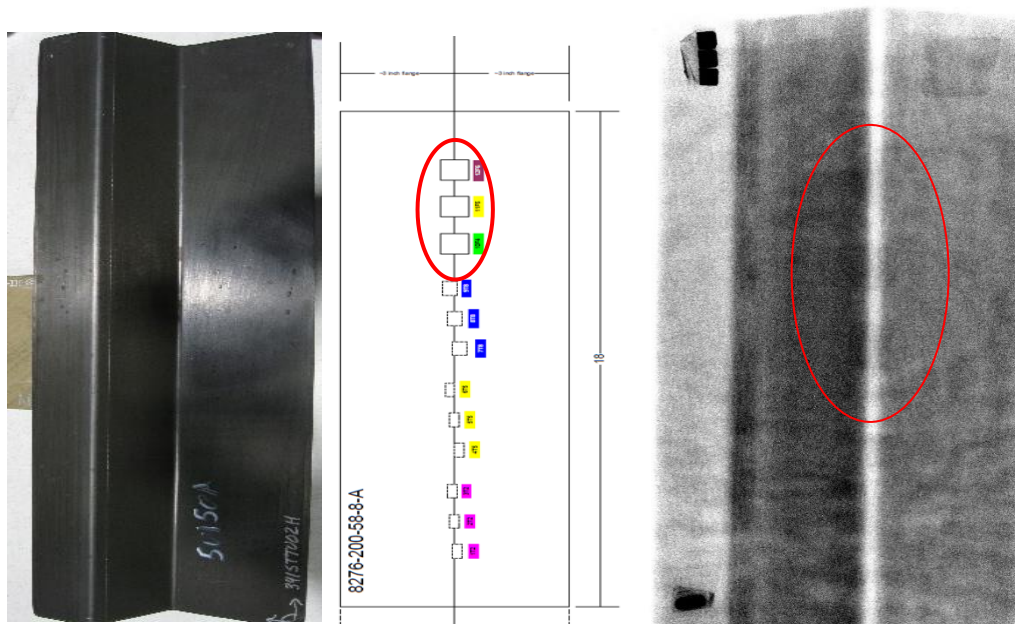
Figure 5.3-6. Photo of S-curve panel (left), defect map where top three squares denotes RPF inserts at three different ply depths (middle), and DR image of RPF material (circled) in composite panel (right), showing poor contrast for the low density change of RPF inserts.

The parameters that affect DR are the X-ray source energy (kV), source current (mA), source distance, geometric magnification, focal spot size, detector type, number of frames averaged, and detector resolution. The use of geometric magnification and the detector resolution affect the

125

resulting resolution of the object in the image. Composites have the advantage of requiring less source energy to penetrate, due to their lower density (lower atomic number of constituents), than metals and therefore can achieve a higher contrast sensitivity. This also allows a large selection of potential sources for use in the field.

DR shares advantages and disadvantages as compared to other NDE methods with the other X-ray methods. It provides high resolution to enable the detection of a variety of defect types. DR is used to measure various features of parts such as geometrical dimensions. It produces images that are easier to interpret than many other NDE methods. This can make DR more suitable for complex parts than other methods such as UT.

While DDAs generally have a lower resolution than CR scanners, the frame averaging of DR results in reduced noise. Geometric magnification is often employed to make up for the lower resolution. DR is useful for *in situ* (in process) applications such as structural testing. DR is cost prohibitive especially because DDAs are expensive and delicate, therefore limiting field use (though their reusabiliy over film can offer cost savings in the long term). The rigid nature of DDAs hinders their ability to fit the curves of parts such as pipes. Detector electronics also wear down over time due to cumulative exposure to ionizing radiation.

Similar to other areas of X-ray technology, advancements in DR are evolving and continue to be pursued and demonstrated. Durable detectors that are smaller and higher in resolution are becoming more available and are improving over time. Flexible detectors for improved field X-ray application are a near future development. ADR is also advancing for many applications to improve speed and consistency of inspection for production settings. This often involves algorithms, image processing, and measurement tools to automatically or nearly automatically identify and measure defects of concern to determine if the part in question meets passing criteria.

5.3.3 Backscatter X-ray

Unlike most other X-ray methods that are TT, Backscatter X-ray is a method of 2D imaging that only requires one-sided access as shown in Figure 5.3-7. When X-rays interact with a material, most pass through with some attenuation; however, a small fraction scatters back and can be detected (Compton Scattering). Backscatter uses this by exposing a small area of a specimen to a rotating collimated X-ray beam. The scattered X-rays are collected with detectors and used along with the swept area of the beam to construct a column of an image. By translating the whole source, another column is made and sequentially a full 2D image is created as seen from the source side. Figure 5.3-8 shows a photo of S-curve panel and an X-ray Backscatter image of 8276-200-58-26 standard with brass inserts in S-curve composite panel.
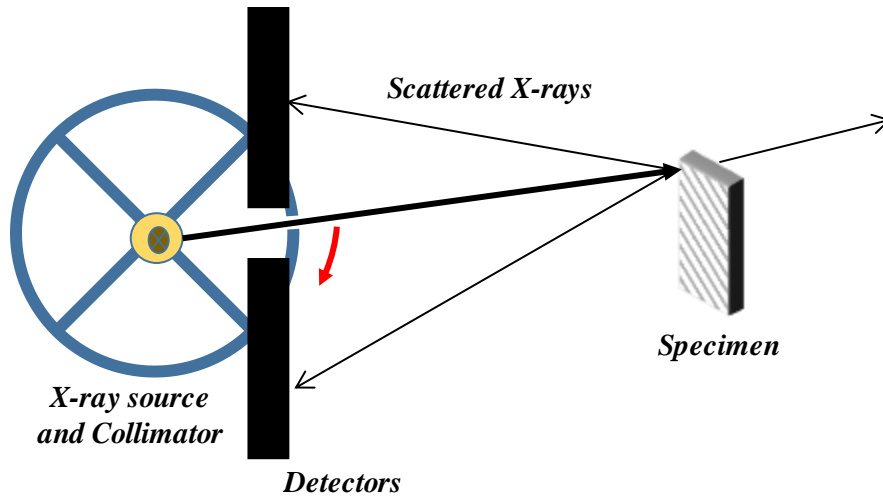
Figure 5.3-7. Backscatter imaging setup.
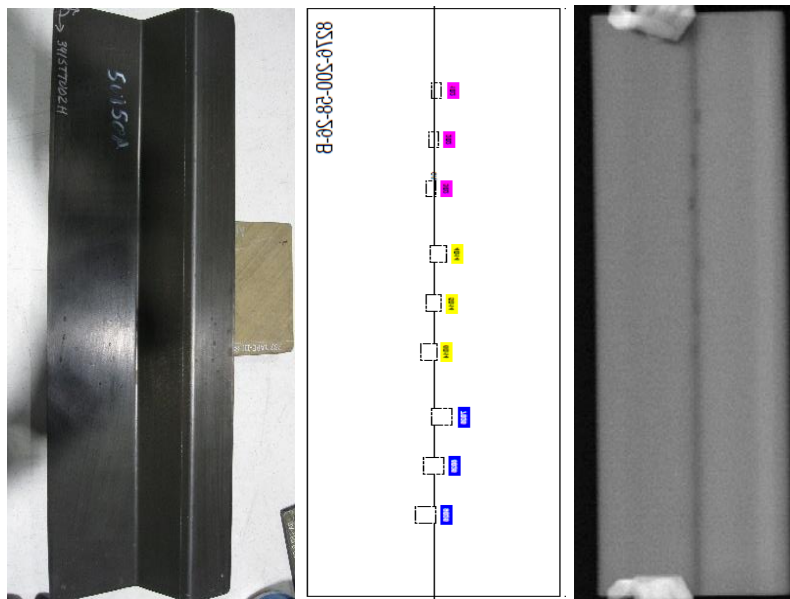
Figure 5.3-8. Photo of S-curve panel (left), defect map where purple denotes locations of 0.001-inch brass foil inserts, (middle), and X-ray Backscatter image of 8276-200-58-26 standard (right) with brass inserts in S-curve composite panel.
The dark line down the center of the image is located at the curvature of the specimen where the scattered X-ray path pass through more material due to the part geometry.

Parameters that effect Backscatter are source energy (kV), source current (mA), aperture size, scan speed, and standoff. A finer resolution scan is achieved with a low-scan speed at the cost of increased time, or a smaller aperture at the cost of reduced signal. Increase in kiloelectron volt (KeV) can contribute in density penetration, while mA can increase contrast. Composites have the advantage of requiring less source energy to penetrate due to their lower density than metal therefore can achieve a higher contrast sensitivity.

Backscatter has the distinct advantage over other X-ray methods of only needing access to one side of the part. This makes it a suitable candidate for use in inspections where two-sided access is difficult or impossible. It has a special sensitivity to material differences, allowing for good

127

foreign material detection. Because of the high collimation of the X-rays, it has a lower radiation footprint and is safe for use in the field with a reduced safety zone. This, along with its ability to image large areas, has made it applicable to many law enforcement use applications such as vehicle inspection for contraband, utilizing both large-scale scanners and handheld units. Disadvantages include a generally lower resolution compared to other X-ray methods and reduced penetration power. If the surface of the object is highly scattering, it is unlikely backscatter will be able to resolve internal features reliably.

Backscatter imaging is currently evolving in both resolution and portability. These two advances can be difficult to achieve simultaneously because large detectors assist with increasing resolution without increasing scan time. These detectors are large and heavy, therefore, limiting portability and increasing size.

5.3.4 Computed Tomography (CT)

XCT is a powerful and versatile inspection method. It generates three-dimensional volumetric representations of the component under inspection and reveals internal conditions or flaws, often with unrivaled accuracy relative to other nondestructive methods. XCT is capable of providing information at µm resolution. One of its largest limitations is that during normal implementation it requires a minimum of 180° rotation of the specimen within the inspection window, limiting component size. Therefore, large components assembled into an aircraft are normally not inspectable with XCT. A second consideration is the requirement that CT is performed in an X-ray shielded environment or in a significantly remote region to limit human exposure. While not practical for inspection of large components, CT is very useful during material development and certification for understanding the morphology of flaws. It also facilitates the development of other less costly inspection techniques that are more applicable on assembled aircraft. XCT is often used as the "ground truth" inspection data and assists in validating other techniques such as thermography or UT.

CT reconstruction is performed by collecting enough data with different orientations of the relative locations of the source, detector, and specimen to effectively define a set of simultaneous linear equations to enable the estimation of a value proportional to the average density for a set of small volumes that combine to make the entire scanned volume. These volume pixels are referred to as voxels. For industrial CT, this is normally performed by a 360° rotation of the specimen with data acquired at discreet, incremental angles to enable reconstruction of the data via an integral transform.

A typical cone beam XCT system used for NDE is shown in Figure 5.3-9. As can be seen in the figure, the principal components are a source, a rotation stage for the scanned object and an X-ray detector. This is different from a medical system where the scanned object is stationary and the source and detector are rotated. For composites, commercial off the shelf systems normally consist of microfocus X-ray source (spot size 5 µm or less), a precision rotation stage and a flat panel detector with a pitch of approximately 100 µm. Systems are sold both in shielded cabinets or can be installed in a shielded room.
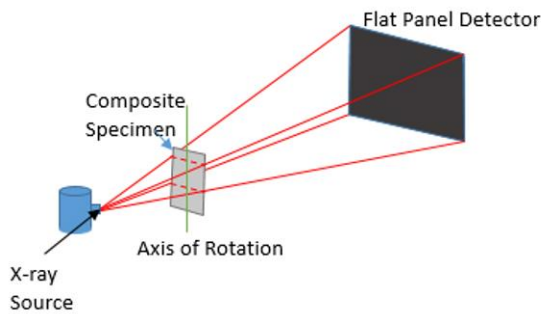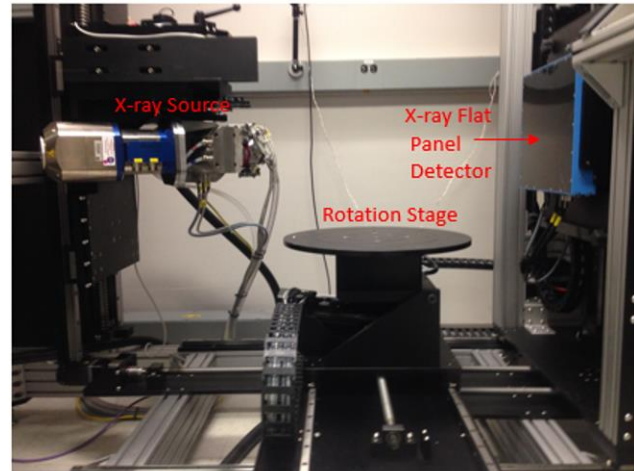
a)   b)

Figure 5.3-9. Typical cone beam XCT system used for NDE.
a) An Illustration of a cone beam X-ray tomography system. The dashed red lines approximately
indicate the portion of the specimen for which CT data are acquired. b) A picture of a NASA CT
system.

The spatial resolution in a system is limited by element and panel size of the flat-panel detector; the X-ray focal spot size and the distance between the source, specimen, and detector. For commercial systems source-to-detector distance, the element and panel size of the flat panel detector are typically fixed. The spot size of the source is often adjustable and reducing the spot size normally requires a reduction in source accelerating voltage. Spatial resolution is also limited by the alignment of the source, detector and rotation stage, and the precision of the rotation.

XCT is similar to X-ray radiography. For X-ray radiography, a single image of the specimen is projected onto an X-ray detector array. The image is approximately a function of the integral of the X-ray attenuation (Z) path between an X-ray source and a point on the detector array. CT reconstruction assumes the log of this projection is proportional to the sum of all the masses along the path. This can be a poor approximation if there are high Z materials in the specimen or there are long paths through the specimens. For composites, this can be an issue when the specimen contains both metallic and composite components, particularly if the metallic components have significant amounts of high Z metals such as iron, nickel, copper, or titanium. Inclusion of these high Z materials can create a well-known CT artifact known as "beam hardening" and iterative reconstruction techniques are used to reduce its impact on the quality of the data.

The "optimal" spatial resolution for a specimen depends on the size of the specimen. It is obtained by placing the center of rotation of the specimen at a location where the largest projection of the specimen on the flat panel detector fills the width of the panel as is shown in Figure 5.3-10b. This assumes the separation of the source and detector is large enough, such that a full rotation of the specimen without hitting either the source or detector is possible at that location. The size of a voxel of data in the data cube is given by the size of the pixel pitch of the flat panel detector divided by the magnification. As seen from the geometry of Figure 5.3-10b, the magnification is the distance from the source to detector divided by the distance from the source to the center of rotation. A second method of calculating the "optimal" magnification is dividing the width of the detector by the largest lateral dimension of the specimen. For most operating conditions, the voxel size is an estimation of the spatial resolution of the system.

129
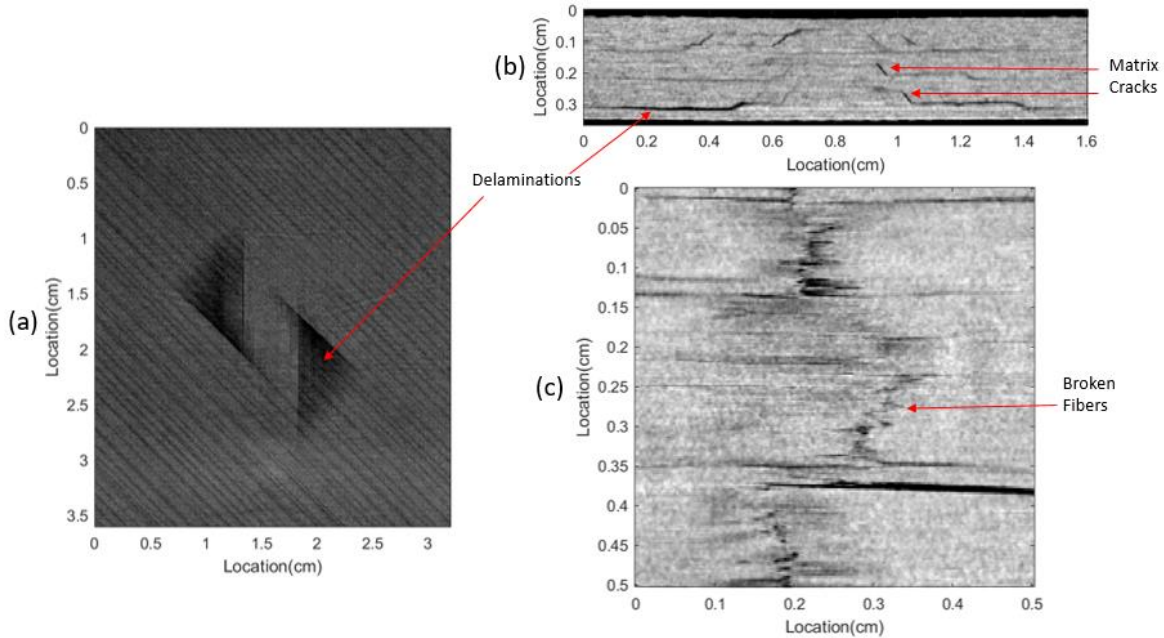
Figure 5.3-10. CT images acquired on impacted composites.
a) and b) showing clear indications of delaminations, b) indications of matrix cracks and
c) indications of fiber/tow breakage.

For composite specimens, the smaller the voxel size, the better the spatial resolution of the data. If detection of delaminations is of interest, a desirable size of the voxels is approximately one-fourth the ply thickness or smaller. If the ply thickness is ~0.01 cm (100 μm) and the flat panel detector is ~ 20 cm wide (~100-μm pitch, 2048 by 2048 detectors), the specimen width should be no greater than 5.0 cm. The same spatial resolution is possible with wider specimens with a wider flat panel detector, multiple flat panel detectors, or translating a single flat panel detector. However, it is expensive to assemble a system with a voxel size of 25 μm for a composite 30 cm wide. The measurement resolution also depends on the spatial resolution of the flat panel detector, which varies from panel to panel, and the spot size of the X-ray source. Since micro-focus X-ray source commonly have spot sizes of 5 μm or less, the spot size of the source is typically not critical for the composite panels of interest. It is possible to measure the spatial resolution of a system with fabricated specimens as is described in the literature [refs. 1 and 2].

A flaw in the composite need not be larger than the system resolution for detection. Detectability of feature is a function of the system resolution, the relative X-ray absorption of the feature and the surrounding material, and the SNR in the data. This is very noticeable if small metallic particles during composite fabrication (intentionally or unintentionally) are incorporated. These metallic particles can be much smaller than the volume of a voxel and still have the greatest intensity in an image. To experimentally improved detectability, the easiest factor to improve is the SNR, which is done by either increasing the integration time for each projection or acquiring more projections with the cost being longer times for data acquisition. This also assumes the primary noise sources are uncorrelated random noise and X-ray scatter.

For composites, the material itself typically has significant variations within plies at the microscopic level, because of the variations in fiber and resin content. This results in a "material clutter" in the images, which may limit detectability. This is evident in Figure 5.3-10a, a slice of the CT data acquired from an impacted composite. It is relatively easy to visualize the

130

delamination; however, the diagonal features, which are the fiber directions of the ply, have approximately the same contrast in the images as the delaminations. Visualization of delaminations is facilitated by rotating the data volume such that the surface of the composite aligned with the x-, y- or z-plane. In this orientation, data from an interface between two plies is easily viewed as a 2D slice of the data and images such as the one shown in Figure 5.3-10a are obtained. For panels with some curvature, it is normally possible to map the coordinate system to a coordinate system where the ply interface is contained in a single plane.

Reviewing the large volume of XCT data obtained from a single specimen is very time consuming. Signal processing is employed to both reduce the time required for review and increase the detectability of some flaws, particularly in cases where the flaws are significantly larger than a single voxel. Traditional signal processing methods have been effective in removing the smooth variations in the CT data, thus enhancing the visualization of delaminations [ref. 3]. By digital processing of the data then employing neural networks, automatic detection of impact-induced delaminations is possible, which provides a similar level of detectability as that of a human reviewer of the CT data. Moreover, the automated processing can take place much faster than human review. In one case for example, the machine-learning algorithms reduced a set of $2000 \times 2000 \times 360$ volumetric CT data, each slice of which was manually analyzed by an SME and taking an entire day, to a display of all slices identified with damage in less than 30 minutes. This is only one example, without a discussion of the accuracy, reliability, and false calls of the algorithm, but the potential for increased productivity is clear. Automated sizing of the flaws has been extremely difficult to achieve and is an evolving research area [refs. 4−6].

One of the primary uses of CT for composites is the characterization of the physical dimensions and shapes of flaws. Limitations are imposed by the characteristics of the flaw. As an example, delaminations are detectable even when the delamination gap is much smaller than the width of the voxel. However, when a gap becomes too small, the contrast between it and the surrounding material may not be great enough for it to be detectable. For a delamination where the gap gets progressively smaller towards the edge, it may appear to be smaller than it is. It should also be noted that it is not possible to measure characteristics such as the width of a delamination gap by simply measuring its width in a CT image.

For composites, types of anomalies that are detectable are resin-rich areas, resin-poor areas, delaminations, matrix cracking, broken fibers, and fiber waviness. Shown in Figure 5.3-11 are delamination, matrix cracks, and broken fibers/tows—all examples of impact-induced damage. Not pointed out in Figure 5.3-10a, but clearly seen, are the −45° variations suspected to be the result of varying fiber/resin content.

Figure 5.3-11 shows CT images from composites manufactured to illustrate fiber waviness and porosity. For the fiber waviness, the CT enables a quantitative measurement of the waviness without destroying the specimen. This facilitates the development of other nondestructive techniques that are more feasible on aircraft components. XCT is often used as the "ground truth" inspection data and assists in validating other techniques such as thermography or UT. In Figure 5.3-11b, the porosity is clearly visible. Finally, Figure 5.3-11c illustrates how XCT is able to characterize damage hidden from other techniques, such as ultrasonic scans, and present a 3D visualization of the damage.
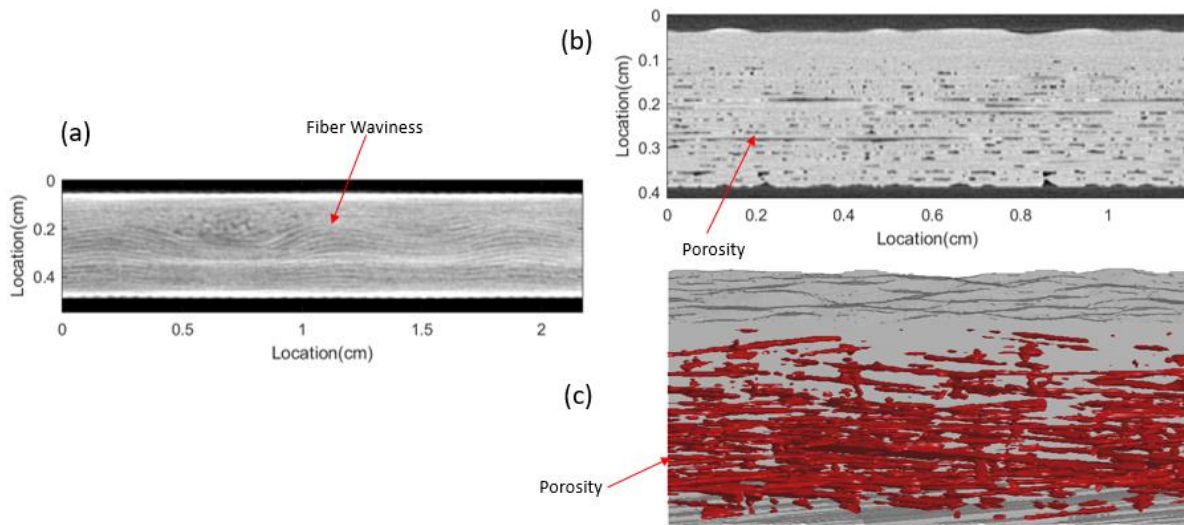
Figure 5.3-11. CT images acquired on composites fabricated to illustrate (a) fiber waviness and porosity (b and c).

5.3.5　References

1. ASTM Internationsl: *Standard Guide for Computed Tomography (CT) Imaging*, ASTM E1441 - 11.
2. Hiller, J.; Maisl, M.; and Reindl, L. M.: "Physical characterization and performance evaluation of an X-ray micro-CT system for dimensional metrology applications," *Measurement Science and Technology*, 23, pages-085404, 2012,https://doi.org/10.1088%2F0957-0233%2F23%2F8%2F085404.
3. Lockard, C. D.: *Anomaly Detection in Radiographic Images of Composite Materials Via Crosshatch Regression*, Master's thesis, Old Dominion University, 2015.
4. de Albuquerque, V. H. C.; Tavares, J. M. R.; and Durão, L. M.: "Evaluation of Delamination Damages on Composite Plates Using Techniques of Image Processing and Analysis and a Backpropagation Artificial Neural Network," in *Eng Opt 2008-International Conference on Engineering Optimization*, 2008.
5. Sammons, D.; Chen, L.; and Milletich, R.: S*ummary of Results from Application of CNN to NASA Image Data*, white paper, NASA Langley Research Center, Office of the Chief Information Officer, Hampton, Virginia, October 2016.
6. Delelegn, D. T.: *Non-Destructive Evaluation for Composite Material*, Master's thesis, Old Dominion University, 2018.

5.4　Shearography

5.4.1　Introduction

A high throughput optical inspection technique, shearography uses a common path, laser-based imaging interferometer to detect, measure, and locate anomalies by imaging submicroscopic changes to a test part surface when an appropriate stress is applied. The shearography camera inspects a full field at a time, rather than a scanning a single point sensor or an array of sensors as with phased array ultrasonic testing. It is non-contact (except for portable vacuum shearography), non-contaminating and near real-time. While laser light is a non-penetrating radiation, shearography systems are capable of inspecting composite structures for both surface and

subsurface discontinuities such as impact damage, disbonds, delaminations, near surface porosity, wrinkled fibers, fiber bridging, FOD, heat damage and cracks.

Shearography NDT is based on the phenomenon that when an object is subjected to a change in load, subsurface anomalies can produce slight local deformations on the surface. These out-of-plane deformations may be as small as several nanometers but are easily imaged by a shearography camera. For example, when a carbon fiber laminate panel is exposed to IR radiation, the change in temperature causes primarily in-plane thermal expansion. In a panel with a delamination, the laminate on the heated side of the panel expands more and sooner than the laminate on the cooler side of the panel away from the heat. This differential expansion coupled with the discontinuity boundary causes the material over the discontinuity to deform out of plane. A shearography camera is used to capture a Reference Image before the application of the thermal stress to the panel and then a second image as the heat is flowing through the laminate plies. These images are processed to produce an image of the delamination that can be measured and located on the part. In addition to thermal stress, the range of shearography techniques include pressure changes, vacuum stress, vibration stress using both sonic and ultrasonic signals, mechanical load changes, varying magnetic field loads and microwave stress changes. Figure 5.4-1 shows the set up for shearography inspection of a composite over-wrap pressure vessel (COPVs) and an aircraft radome.
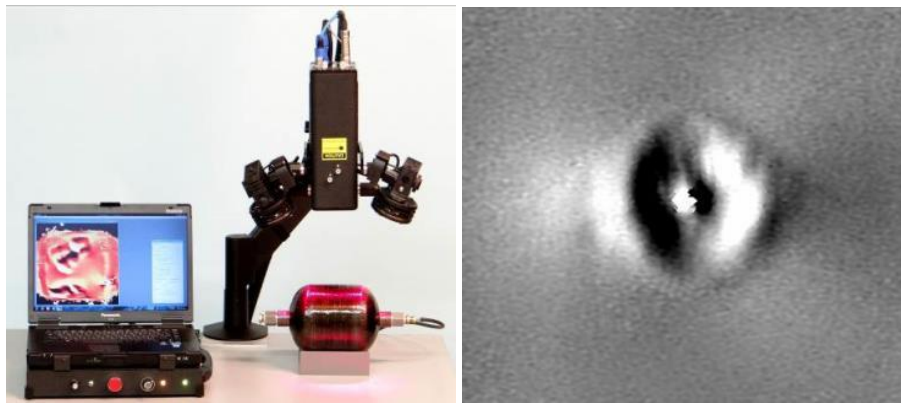
Figure 5.4-1. Set up for shearography inspection of a COPV and an aircraft radome.
At left, a shearography test set up for a small carbon fiber COPV is shown. The tank is rated for 7,250 psi (50 Mpa) but using a small pressure change of only 5 psi (0.03 MPa) we can image non-visible impact damage as shown on the right. The small impact strike is in the center of the circular delamination which measures 3.2 inches (81.3 cm) in diameter. No visual evidence of damage was seen on this COPV.

Shearography is an evolutionary development from holographic interferometry first developed by Karl Stetson in 1964 [ref. 20]. Initial shearography techniques invented by Y. Y. Hung in 1982, [ref. 12] was further enhanced with the development of electronic phase detection by S. Nakadate, [ref. 13] in 1988. Commercialization of electronic shearography NDT began in 1986 with the first integration of the technology into a major aircraft manufacturing program by J. Newman [ref. 2].

Shearography NDT methods can be highly effective solutions for a wide range of composite NDT applications. Common successful applications include metal and composite honeycomb, foam cored panels, bonded elastomers or cork, solid composite laminates, fiber wound structures such as COPVs, solid propellant rocket motors and liquid propellant regeneratively cooled rocket engines. Test objects ranging from less than an inch in width to very large composite structures have been successfully inspected.

133

The benefits of shearography include very high throughput. Large production systems easily achieve throughput rates of 300–700 sq. ft/hr. (27-65m²/hr.) compared to typically only 10 sq. ft/hr. (0.93 m²/hr.) with TTUT C-Scan. Portable vacuum shearography cameras are able to inspect up to 150 sq. ft/hr. In many cases, shearography NDT methods are non-contact—ideal for space applications. Production shearography cameras do not require precision contour following and can inspect a structure at an offset angle, eliminating the costs associated with precision gantries such as required for UT C-Scan systems. In addition, because many shearography NDT methods are non-contact composite structures manufactured with multiple cure cycles can be inspected in-process allowing repairs or scrapping of the part with the lowest possible cost implications. The technology lends itself to a wide range of configurations to meet the discontinuity detection and logistical requirements.

As with all NDT methods in use, a critical element is operator training and certification to recognized standards. For shearography, NDT operators are trained and tested to the requirements of the American Society of Nondestructive Testing (ASNT) SNT-TC-1A and CP105, National Aerospace Standard NAS410 or European Standard EN 4179. Shearography operator training courses meeting these requirements are commercially available.

Shearography instruments have a range of tools for measuring indication sizes, area, linear dimensions, and z-axis deformation resulting from the stress change. These measurements compensate for the shear vector in every image (except image integration) and are used to accept or reject indications against the test part discontinuity accept/reject criteria.

5.4.2 Advantages and Limitations

The advantages of shearography NDT over conventional methods include high throughput. The time required to gather the raw data is typically determined by the time required to induce the load change be it thermal flow in a carbon fiber laminate or pressurization of a rocket engine thrust chamber. The data processing is generally accomplished in less than 60 to 200 msec. A second advantage is no requirement for part contour following. Tilted test part surfaces can be inspected, greatly reducing the cost of a scanning shearography system. Third, shearography methods can employ many different test part stress methods and often several in the same test. This diversity of techniques often leads to a positive NDT solution. Shearography can test a number of materials such as bond cork and foam that are extremely difficult for conventional NDT methods. Also, shearography does not require water couplant as with TTUT, a big advantage when testing parts for spacecraft. Finally, shearography techniques and interpretation tend to be simpler than other NDT methods. For example, in NAS 410, the recommended training hours for Level 2 Shearography is 60 hours and for Ultrasonic Testing is 80 hours.

A major drawback of shearography is that it is possible to damage the structure by applying too great a load during testing. Other limitations of the shearography method include reduced defect sensitivity at depth. The deeper the flaw is from the surface the larger it must be to be detected. Extensive testing of matrix NDT standards for carbon fiber laminates has shown detection of 0.28-inch-diameter void through 18 plies. Another limitation is the challenge of shearography inspecting black glossy curved surfaces. The use of penetrant developer or other approved coating to increase the surface reflectivity or changing the viewing angle to the part can reduce glare. Finally, shearography images can be degraded by environmental vibration and sound.

5.4.3 Laser Safety

Laser shearography NDT systems utilize laser light to illuminate the surface of a test article being inspected. The laser provides a convenient source of monochromatic-coherent light that makes the implementation of shearography NDT possible. With the exception of extremely low powered laser systems, virtually all laser products pose some form of hazard [ref. 19]. The most common hazards associated with lasers come from the direct exposure of the eyes and skin. Within the United States, laser systems are classified in accordance with the regulations set forth by the Center for Devices and Radiological Health (CDRH) division of the Food and Drug Administration (FDA). Additional Federal, State, and Local regulations may also apply to further regulate the use of a laser product for a given application. Many of these secondary regulations are based on classification data provided by the American National Standards Institute (ANSI) [refs. 15 and 16]. In the European community, laser system standards are overseen primarily by the International Electrotechnical Commission (IEC) and the British Standards Institution (BSI).

5.4.4 Theory and Principles of Operation

A shearography NDT system consists of a laser light source, a shearing image interferometer, an image-processing computer, display monitor, and a means to provide a controlled and repeatable stress to the test object [refs. 2, 4–12]. Shearography cameras are relatively resistant to environmental vibration and motion. Large production systems with 30-ft (9.14-m) gantry scanners have been built as well as portable systems for on-vehicle inspection. Shearography is relatively insensitive to test part bending or deformation due to the applied stress but still highly sensitive to local deformation caused by a discontinuity.

Shearography cameras are sensitive to changes in the distance from the object surface to the camera and in practice these z-axis surface deformation sensitivity may be as small as 1 nm depending on environmental noise. Test parts can be inspected with a few images using a large FOV camera lens setting or for greater resolution. Many images with a smaller FOV can be recorded and automatically stitched together. The optimal FOV for a shearography test depends on the maximum allowable defect size, camera resolution, laser illumination power, the ability to uniformly apply a stress change to the test part over the FOV. Figure 5.4-2 shows a schematic diagram of a thermal shearography system that includes the laser and optical elements for test part illumination, an imaging shearing optical system consisting of a beam splitter with a 2-axis tilting mirror, a second mirror with a piezoelectric phase stepper to translate the mirror in half wavelength steps at video frame rates, and finally the charge-coupled device (CCD) camera. The laser light is expanded through lenses to illuminate the test area on the panel. Light from point P1 is reflected from the panel surface, where it is well bonded to the core. Light from point P2 is reflected from the surface above a skin-to-core disbond.
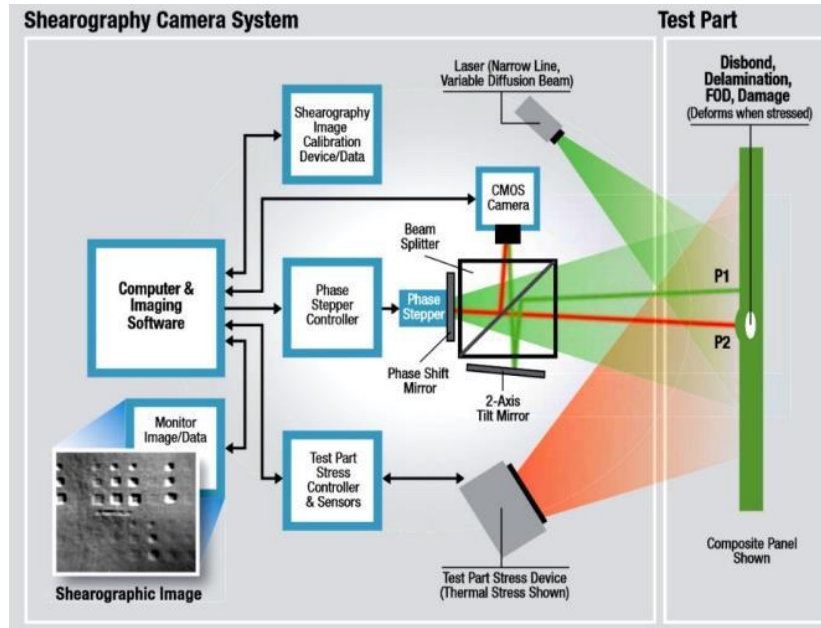
Figure 5.4-2. Schematic of a thermal shearography system.
Includes laser, optical elements for test part illumination, imaging shearing optical system consisting of beam spitter with 2-axis tilting mirror, a second mirror with piezoelectric phase stepper to translate mirror in half wavelength steps at video frame rates and CCD camera.

If the panel is stressed with a small temperature change or a partial vacuum, the panel face sheet above the disbond will deform out-of-plane towards the shearography camera. This shorter distance traveled by light from point P2 causes a phase shift with respect to light from point P1. Light from both P1 and P2 are combined by the shearing interferometer at a single pixel in the complementary metal oxide semiconductor (CMOS) array. Figure 5.4-3 contains a diagram showing change in phase and resulting change in light summation intensity. Figure 5.4-4 shows shearography images.

The piezoelectric phase stepper applies a $\pi/2$ phase shift on one leg of the interferometer at video frame rates (typically from 30 to 120 frames/second) to generate a phase map and subsequent quantitative determination of the deformation derivatives between two strain states [refs. 2, 9, 13, and 14]. As the applied load on the test object is changed from one stress another, two sets of phase stepped images (I1–I4) and (I5–I6) are captured and the phase calculation is performed for each pixel in the image, using the following equation for the four-phase step method shown below:

Equation 7:
$\Delta(x, y) = Tan^{-1}[I_8(x, y) - I_6(x, y)/ I_5(x, y) - I_7(x, y)]$ - $Tan^{-1}[I_4(x, y) - I_2(x, y)/[I_1(x, y) - I_3(x, y)]$

where I_1 through I_8 are eight sequentially phase stepped captured images, described by:

$I_1(x, y) = I'(x, y) + I''(x, y) \cos[\Phi(x, y)]$,

$I_2(x, y) = I'(x, y) + I''(x, y) \cos[\Phi(x, y)+\pi/2]$,

$I_3(x, y) = I'(x, y) + I''(x, y) \cos[\Phi(x, y)+\pi]$,

$I_4(x, y) = I'(x, y) + I''(x, y) \cos[\Phi(x, y)+3\pi/2]$,

$I_5(x, y) = I'(x, y) + I''(x, y) \cos[\Phi(x, y)+\Delta(x, y)]$,

136

$I_6(x, y) = I'(x, y) + I''(x, y) \cos[\Phi(x, y) + \Delta(x, y) + \pi/2]$,

$I_7(x, y) = I'(x, y) + I''(x, y) \cos[\Phi(x, y) + \Delta(x, y) + \pi]$,

$I_8(x, y) = I'(x, y) + I''(x, y) \cos[\Phi(x, y) + \Delta(x, y) + 3\pi/2]$,

where,

I' = the bias intensity

I'' = the modulation intensity

Φ = the random phase variable due to reflection of the laser light from test object

Δ = a quantity directly proportional to the differential displacement due to the test part deformation from the applied load change
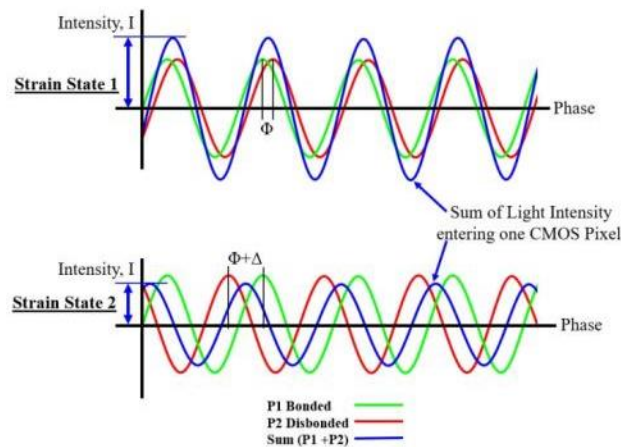
Figure 5.4-3. Diagram showing change in phase and resulting change in light summation intensity.

137
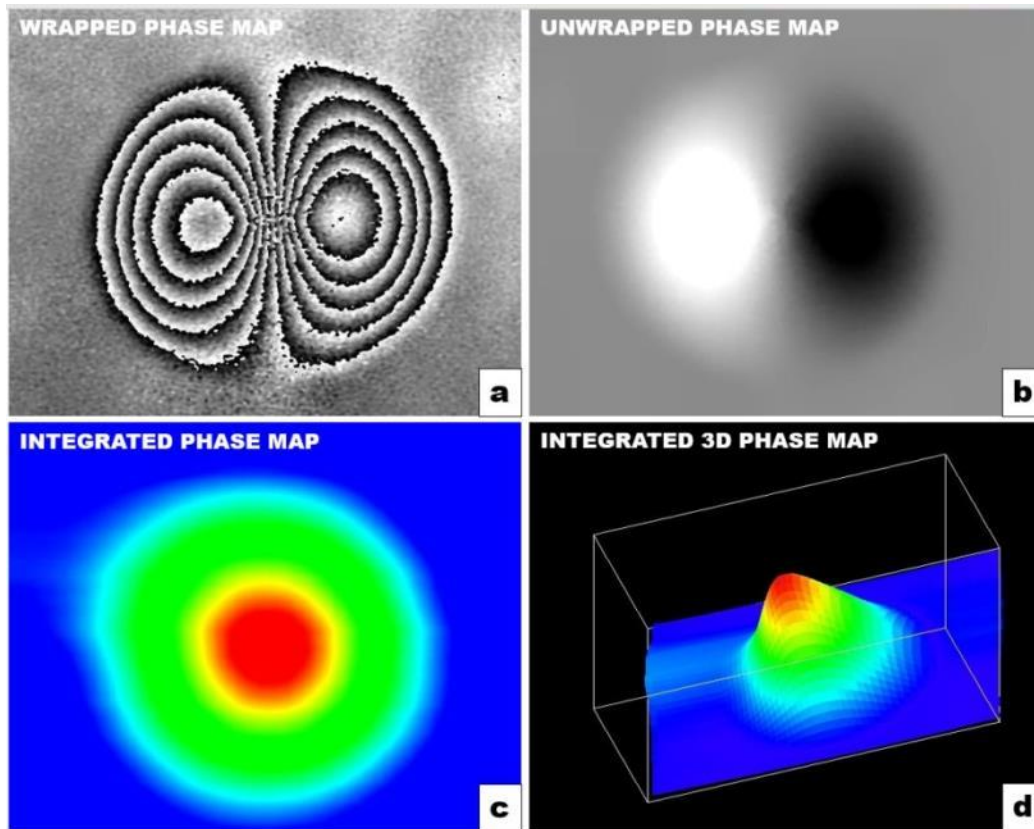
Figure 5.4-4. Shearography images.
a) phase map of the deformation derivative, b) unwrapped phase map, c) integrated unwrapped phase map and d) a 3D representation of the plate deformation. Numerical values of deformation over the entire FOV can be exported as a .csv file for analysis and comparison to finite element models.

Shearography images also include quantitative calibration data for the image scale and the image offset or shear vector. These data are used to obtain accurate discontinuity dimensions (D) by subtracting the shear vector component from the measured dimension (Dm). For example, if the shear vector, Sv, is in the horizontal (or 0°) direction with a shear of 0.5 inches (5 mm), the total horizontal uncorrected measured dimension (Dm) of any indication with be greater by Sv. The measured dimension (D) in the vertical direction, perpendicular to the direction of Sv, will equal the measured dimension (Dm). For any measured dimension at any angle (α) to the shear vector D and be calculated a D= (Dm – cosα). The calibration data are also used during calculation of the integrated shearogram to extract the Z-axis deformation of the part surface anywhere in the FOV.

The shear vector, illustrated in Figure 5.4-5, is designated Sv, is defined as the separation distance and direction of the two images formed by the shearing interferometer. The shear vector convention, adapted in ASTM E-2581-14 Standard Practice for Shearography NDT [ref. 14], starts with the zero order shear and then measures the offset distance in inches or mm in the plane of the surface of the test object. In the case shown, this is written as Sv= D@ +45°, where D is the distance between like points in each image. The shear vector, as determined by the NDT Engineer is a key parameter is setting up a shearography test as it determines the defect detection sensitivity, resistance to ambient vibration, and image clarity.
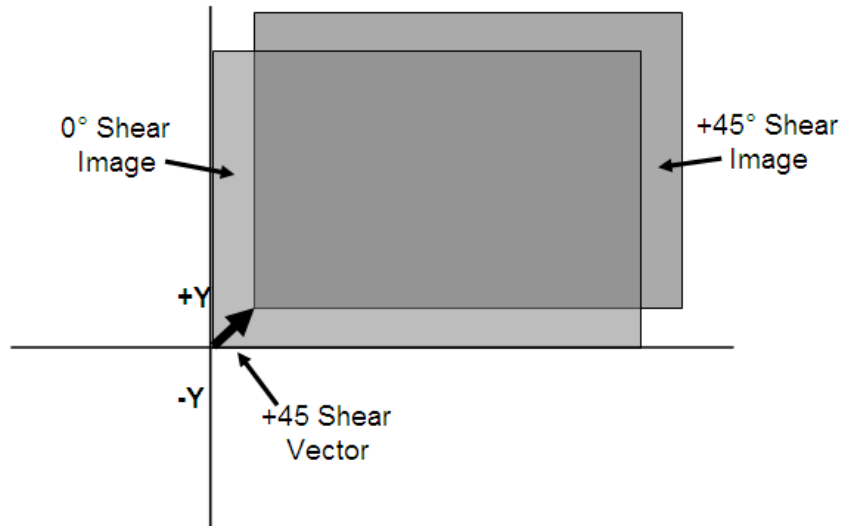
Figure 5.4-5. Illustration of shear vector convention as adapted by ASTM E-2581-14.

Finally, the calibration data can be combined with the stress data to measure discontinuity deformation rates as a function of the applied stress change. This technique has been used for example to establish a model for grading impact damage to honeycomb distinguishing between crushed core and disbonds. Applications using thermal stress can us a non-contact remote temperature sensor to measure the test part temperature change and the resulting discontinuity thermal deformation.

Real-time phase maps and unwrapping algorithms can be performed at video frame rates and quantitative measurement of the Z-axis deformation can be computed. For NDT, shearography images can provide details of surface damage and subsurface discontinuities and structural features. Figure 5.4-6 shows a vacuum stress shearogram of a 14- × 24-inch (36 × 61cm) section of a metal spacecraft honeycomb radiator panel manufactured with aluminum honeycomb, aluminum ammonia tubes with bonded face sheets 0.025 (0.63 mm) inches thick. The cells, disbonds and voids are detected. With the panel and the camera placed inside a shearography test chamber, two sets of phase stepped interferograms were captured, one set at ambient pressure and the second set 10 seconds later when the pressure was reduced by 0.5 psi. (3.4 KPa) below ambient. The metal face sheet over the honeycomb cells and disbonds develop submicroscopic dimples as the air pressure in the test chamber is reduced. One indication in particular (large arrow on the left side) is a disbond on top of a coolant tube. This disbond was not detected with TTUT NDT, due to the presence of the coolant tube beneath it blocking the ultrasonic signal. Shearography is frequently used for spacecraft composites because of its high throughput that can be 10 times greater than UT C-Scan. Shearography does not use any liquid couplant so the test parts remain dry and uncontaminated. In addition, Shearography NDT in many cases is able to detect anomalies in areas with complex geometry or conditions that prevent the use of traditional NDT techniques.
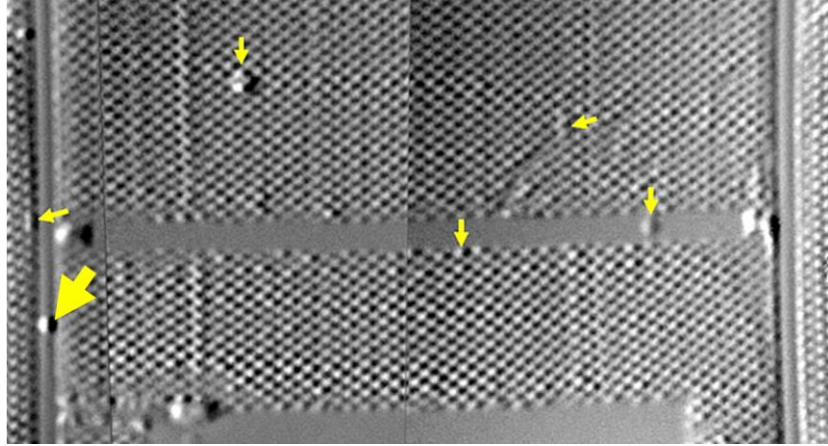
Figure 5.4-6. Shearogram of a 24- × 14-inch (61 × 35.6 cm) section of honeycomb spacecraft radiator panel.
This hearogram shows the honeycomb cells, disbonds, and embedded coolant tubes. A disbond is seen at near the left edge on top of an embedded coolant tube (large arrow) and was not detected with TTUT C-Scan as it is masked by the coolant tube.

5.4.5 Shearography Equipment and Accessories

Shearography cameras usually are built with integrated stressing equipment such as thermal or vacuum stress. The detect detection Probability of Detection (PoD) for each type of camera and stressing mechanism must be determined for the structures and defect types expected for a given application. The development and production of accurate representative NDT Standards is a part of every shearography NDT process.

Shearography systems are divided into two main types: Portable instruments and Production Systems. Portable shearography instruments are manually manipulated over the surface of the test part and have built-in stressing devices, which may include thermal lamps, vacuum blowers or both. Figure 5.4-7a, b, and c show three different portable shearography systems: a tripod-mounted shearography camera with thermal stress lamps; a portable vacuum/thermal stress systems used during construction of large composite naval ships; and Production shearography systems that may have automated scanning and part stressing equipment that may include scan gantries, robots and/or vacuum stress shearography chambers. Figures 5.4-8 shows a typical production shearography system.

a)   *b)*   *c)*
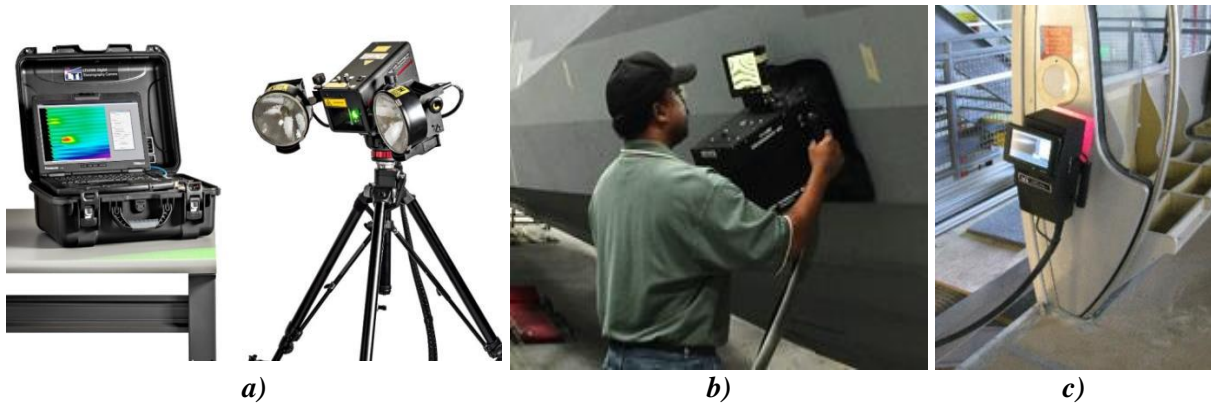
Figure 5.4-7. Three portable shearography systems.
a) A tripod-mounted shearography camera with thermal stress lamps. Instruments with this configuration are used on bench top mounts, tripods, gantries or robots depending on the application. All the shearography electro-optical components and the single frequency laser are built into the sealed housing. Thermal stress is achieved with the 2-1kw quartz thermal lamps. The system shown in b) A portable vacuum shearography system. c) A small thermal shearography camera being used to inspect a mass transit rail car interior for disbonds. The camera includes tools for measuring size and area of indications.
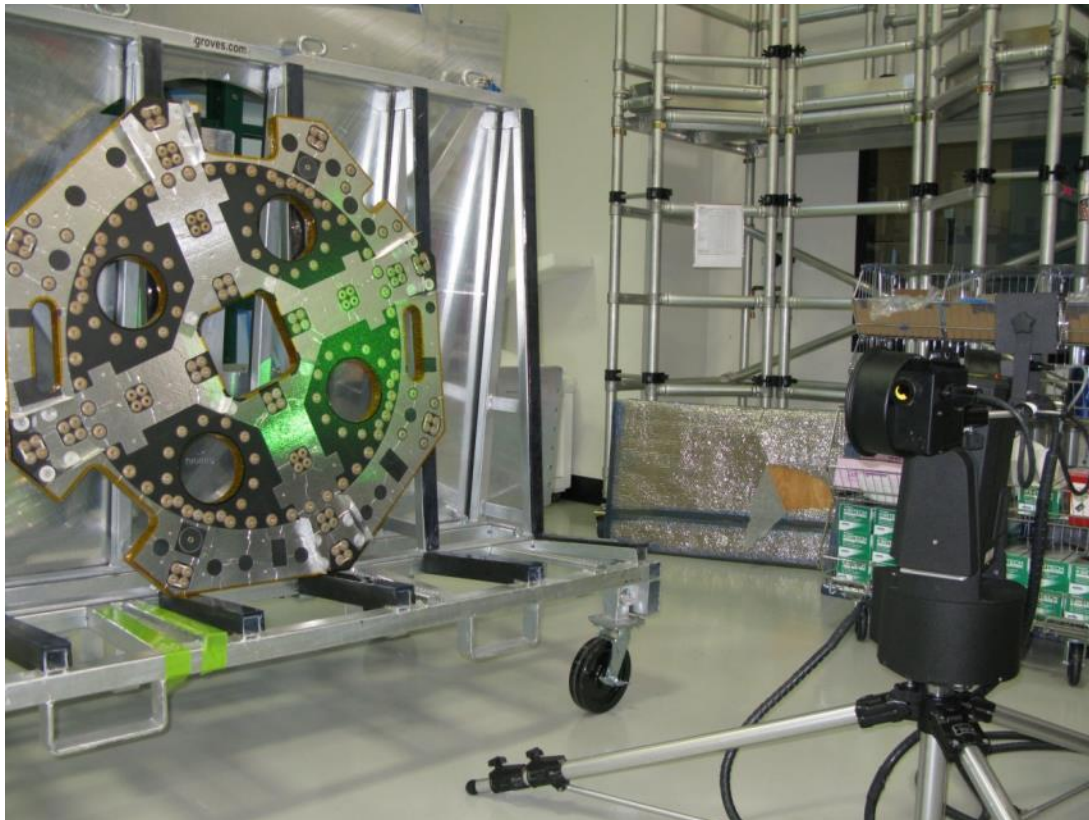
Figure 5.4-8. Stand-alone production shearography camera, bottom right, with programmable pan/tilt scan capability performing automated thermal shearography test on large composite honeycomb panel. Disbond sensitivity was validated even through the solar reflecting foil.

Large vacuum shearography test chambers such, as shown in Figure 5.4-9, use robotic scan gantries to inspect large aircraft and spacecraft structures and are often paired with thermal stress

141

lamps. The air pressure inside this chamber can be reduced from ambient by up to 10 psi (-0.035 kg/cm^2) below ambient in less than 15 sec. Subsurface disbonds, unbonds, FOD, delaminations, core splice disbonds, and surface deformations can detected with a shearography camera. The shearography test results are automatically stitched, documenting both the indication measurement and location. Test part scan speeds of 400 sq. ft/hr. are easily achieved by these systems.

Figure 5.4-9. Shearography camera mounted on large x/y scan gantry in large vacuum test chamber. This system is used for shearography NDT of large honeycomb aircraft components. The author is standing at the back wall for scale.

5.4.6   References

1. "New York's Bronx-Whitestone Bridge Span to Feature 390 Composite Wind Fairings," NetComposites, http://netcomposites.com/news/2003/october/22/new-york-s-bronx-whitestone-bridge-span-to-feature-390-composite-wind-fairings/, 2003.
2. Newman, J. W.: "Laser Testing: Shearography & Holography," P. O. Moore, editor, *The Nondestructive Testing Overview*, Columbus Ohio, American Society for Nondestructive Testing, 2012.
3. Newman, J. W.: "Shearographic & Holographic Testing," R. H. Bossi, editor, *ASNT Industry Handbook Aerospace NDT*, Columbus Ohio, American Society for Nondestructive Testing, 2012, https://www.asnt.org/MajorSiteSections/Publications/NDT_Handbooks/Industry_Handbook_Aerospace.aspx.
4. Caufield, H. J.; and Lu, S.: *Applications of Holography*, New York, NY, Wiley-Interscience, 1970.
5. Chatters, T.; Pouet, B.; and Krishnaswamy, S.: "Shearography With Synchronized Pressure Stressing," D. O. Thompson and D. E. Chimenti, editors, *Review of Progress in Quantitative NDE*, La Jolla, CA, Plenum Press, p. pgs. 19-426, 1992
6. Deaton, J. B., Jr.; and Rogowhi, R. S.: "Optimization of Image Shearing Parameters in Electronic Shearography for Nondestructive Evaluation," D. O. Thompson and D. E. Chimenti, editors, *NDE: An Answer for an Aging World*, Columbus OH, American Society for Nondestructive Testing, p. 204-206, 1994.

7. Gryzagoridis, J.; Oliver, G.; and Findeis, D.: "Modal Frequency Versus Shearography in Detecting and Locating Voids/Delaminations in Sandwich Composites," *Insight*, Vol. 55, No. 5, p. 249-252, 2013.
8. Post, D.: "Optical Interference for Deformation Measurements - Classical Holographic and Moire' Interferometry," W. W. Stinchcomb, editor, *Mechanics of Nondestructive Testing*, New York, NY, Plenum Press, 1980.
9. Spicer, J. B.; Champion, J. L.; Osiander, R.; and Spicer, J. W. M.,: "Time Resolved Shearography and Thermographic NDE Methods doe Graphite Epoxy/Honeycomb Composites," *Materials Evaluation*, Vol. 54, No. 10, p. 1210-1213, 1996.
10. Vest, V. M., Holographic Interferometry, New York NY, John Wiley, 1979.
11. Gryzagoridis, J.: "Laser Based Nondestructive Inspection Techniques," *Journal of Nondestructive Evaluation*, Vol. 31, No. 4, p. 295–302, 2012.
12. Hung, Y. Y.: "Shearography: A New Optical Method for Strain Measurement and Nondestructive Testing," *Optical Engineering*, Vol. 21, No. 3, p. 391-395, 1982.
13. Nakadata, S.: "Phase Detection of Equidistant Fringes for Highly Sensitive Optical Sensing," *Journal of the Optical Society of America A*, Vol. 5, No. 8, p. 1265-1269, 1988.
14. ASTM International: "Standard Practice for Shearography of Polymer Matrix Composites and Sandwich Core Materials in Aerospace Applications," ASTM E2581-14, American Society for Testing and Materials, web page: https://www.astm.org/Standards/E2581.htm.
15. ASTM International: "Standard Guide for Nondestructive Testing of the Composite Overwraps in Filament Wound Pressure Vessels Used in Aerospace Applications," ASTM E2981, American Society for Testing and Materials, 2015, web page: https://www.astm.org/Standards/E2981.htm.
16. Timoshenko, S. P.; and Goodier, A. N.: *Theory of Elasticity*, *3rd Edition*, New York, McGraw-Hill Classic Textbook Reissue Series, 1970.
17. Timoshenko, S. P.; and Woinowsky-Krieger, S.: *Theory of Plates and Shells*, *2nd Edition*, McGraw-Hill Book Company, 1959.
18. Prescott, J.: *Applied Elasticity*, New York, Dover, 1946.
19. Sliney, D. H.: *Safety with Lasers and Other Optical Sources: A Comprehensive Handbook*, New York, Springer Science, 1980.
20. Stetson, K. A.: "50 Years of Holographic Interferometry," *SPIE Optics and Measurement Conference Proceedings*, Vol. 9442, 2014.

5.5   Visual Inspection, Tap Testing, and Liquid Penetrant Testing

As stated in the introduction, this Handbook concentrates on instrumented inspection techniques. While visual inspection, tap testing, and liquid penetrant testing are performed on composites, they were not the focus of the ACP Rapid Inspection and Characterization task. Disbonds, voids, AFP defects and fiber tow failures are typically buried within the composite, making visual inspection of limited use. Visual inspection is also extremely slow and tedious, not lending itself to automation techniques, which would reduce the time to design and develop validated composite components. Where visual inspection is suitable, it is noted in Section 4 of this Handbook where appropriate methods to detect a given defect type are discussed.

Tap testing has been demonstrated successfully on composite components, but like visual inspection does not lend itself to rapid inspection techniques like automation and is therefore not discussed in this Handbook.

Although commonly applied to metallic materials, liquid penetrant testing methods have applications in NDT and NDE of composite materials as well. Liquid penetrant testing can be implemented as an aid to visual inspection and can enhance the visual assessment of damage to the composite matrix or gel-coat from impact. Radiopaque liquid penetrants have proven useful when applied to composite materials prior to X-ray radiography to improve the contrast of inspection [ref. 1], particularly in the assessment of the depth and extent of impact damage [ref. 2]. Liquid penetrant testing is often a useful NDE tool for inspection of metallic components used in composite systems. One such example is the use of liquid penetrant to inspect thin-walled metallic liners used in COPVs [ref. 3]. Liquid penetrant testing has also proven a useful technique to monitor the performance of erosion and oxidation protective coatings in polymer-matrix and ceramic-matrix composites used in aircraft engines [ref. 4]. Given its relative low costs and ease of implementation, liquid penetrant testing remains a useful NDE tool for engineers and technicians working with carbon reinforced composite materials.

The principle of liquid penetrant testing relies on specially formulated liquid dyes designed to infiltrate surface-breaking discontinuities. After application of liquid dye penetrant to the part, discontinuities are filled with liquid through capillary forces. Excess liquid is then removed from the surface of the part leaving only the liquid trapped within the discontinuity. A developer is then added to the surface of the part, which draws in the liquid out of the discontinuities and provides a contrast background to aid in the examination of indications. Parts are visually inspected and indications are interpreted based on the base material, process, and associated suspected defects. Rigorous pre-cleaning and proper surface preparation and conditions are critical to the success of a liquid penetrant test. Often parts are also rigorously post-cleaned in order to remove any residual dye and developer. Table 5.5-1 provides an overview of the liquid penetrant process with advantages and limitations of the liquid penetrant testing technique.

Table 5.5-1. Overview of liquid penetrant testing process with identified advantages and limitations.[7]

Liquid Penetrant Process	Advantages of Liquid Penetrant Testing	Limitations of Liquid Penetrant Testing

[7] American Society of Nondestructive Testing*, Tracy, N. A., Moore, P. O. (1999) *Nondestructive Testing Handbook Volume 2, Liquid Penetrant Testing.* Columbus, Ohio: American Society of Nondestructive Testing

Liquid Penetrant Application Liquid Penetrant Removal Developer Application Inspection	• Can be implemented on complex part geometries • Sensitive to small surface discontinuities • Can be applied to a wide range of materials • Use of relatively inexpensive, non-sophisticated equipment and adaptable to high-volume processing, allowing for 100% surface inspection • Can often be implemented in the field • Sensitivity can be adjusted through material selection and process control and allows for focus on specific defects of interest for a given material, process, or service condition • Technique is direct visual, not sensor based and does not require measurement of a signal output in comparison to a reference standard	• Will only reveal discontinuities open to the surface • Coatings and contaminants must be removed from the surface • Residual or unremoved organic surface contamination can affect inspection • Mechanically disturbed surfaces (e.g., machined, peened, buffed, brushed, etc.) smear the surface of most metals and can mask defects. Etching of the surface is often required for materials with mechanically disturbed surfaces to ensure a reliable test • A reliable test and inspection requires a well-controlled process for pre-cleaning, penetrant application and dwell-time, penetrant removal, intermediate drying, and developer application

Owing to the sensitivity of an established, controlled, and verified process for liquid penetrant testing, the requirements of ASTM-E1417, Standard Practice for Liquid Penetrant Examination, are commonly employed and often required per NASA standards and requirements [ref. 2]. ASTM-E1417 standardizes a detailed classification system of liquid penetrant materials and processes, personnel qualifications, process and equipment controls, and quality control provisions, thus ensuring a well-controlled and reliable liquid penetrant testing process [ref. 3]. Liquid penetrant testing is a useful NDE technique often applied to monolithic materials and is particularly useful in the identification of weld defects. Figure 5.5-1 shows a fluorescent penetrant inspection of a weld showing micro-cracking in the heat-affected zone of the weld.
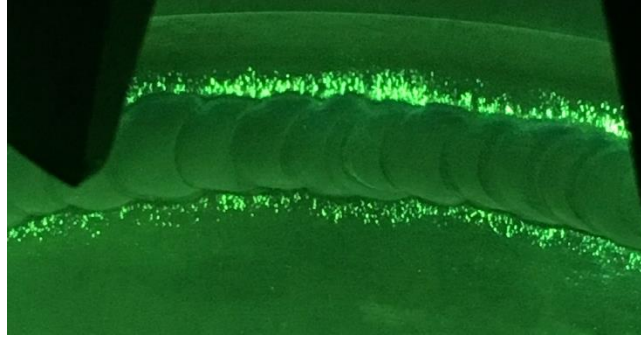
Figure 5.5-1. Fluorescent liquid penetrant indications of micro-cracking in weld heat-affected zone.[8]

5.5.1 References

1. SAE International: *Composite Repair NDT/NDI Handbook*, SAE Recommended Practice ARP 5089, 2011.
2. Rummel, W. D.; Tedrow, T.; and Brinkerhoff, H. D.: *Enhanced X-ray Stereoscopic NDE of Composite Materials*, AFWAL-TR-80-3053, 1980.
3. ASTM International: *Standard Guide for Nondestructive Testing of Thin-Walled Metallic Liners in Filament-Wound Pressure Vessels used in Aerospace Applications*, ASTM-E2982, 2014.
4. National Aeronautics and Space Administration: *Erosion Coatings Developed To Increase the Life and Durability of Composites*, NASA Glenn Research Center Research and Technology Report, pg. 45, 2004.
5. Tracy, N. A.; and Moore, P. O.: *Nondestructive Testing Handbook Volume 2, Liquid Penetrant Testing.* Columbus, Ohio: American Society of Nondestructive Testing, 1999.
6. National Aeronautics and Space Administration: *Nondestructive Evaluation Requirements for Fracture-Critical Metallic Components*, NASA-STD-5009A, 2018.
7. ASTM International: *Standard Practice for Liquid Penetrant Inspection*, ASTM-E1417, 2016.
8. Smith, Nathan A.: *Liquid Penetrant Testing at Goddard Space Flight Center*, Greenbelt, Maryland: National Aeronautics and Space Administration Goddard Space Flight Center, 2019.

5.6 Other NDE Techniques and Tools

NDE inspection of composites has matured significantly in recent years. As the use of composites in aerospace structures increases it has become necessary to develop techniques and tools to speed inspections, evaluate and disposition defects, predict the effect of defects on the inspection of complex components, and evaluate techniques without expensive (or difficult to produce) representative standards. This section of the handbook presents some of the useful and emerging NDE tools and laboratory inspection techniques that, while not currently widely used, are enabling techniques for critical NDE inspections. NDE Simulations and Robotics are enabling tools applicable to many NDE techniques. Commercially available profilometry systems are becoming useful NDE tools when coupled with machine learning algorithms. *In situ* thermography, bond strength NDE, polar backscatter UT and GWUT are representative of evolving techniques

---

[8] Smith, Nathan A., (2019). *Liquid Penetrant Testing at Goddard Space Flight Center.* Greenbelt, Maryland: National Aeronautics and Space Administration Goddard Space Flight Center

currently employed in laboratory environments with approaching field applicability for composite inspection.

5.6.1 NDE Simulations

NDE simulation entails the use of commercial or custom software codes to implement mathematical approaches/algorithms that model the physics of an inspection. For example, UT simulation tools are used to model wave propagation (wave speed, propagation direction, etc.) and interaction with defects (scattering, mode conversion, etc.). Simulation tools are used to model any physics based NDE technique. Some benefits of using NDE simulation tools include:

- Aiding in the optimization of NDE techniques with reduced experimental testing
- Analyzing the inspection coverage (i.e., inspectability) for a given NDE method on a specific structural configuration
- Aiding in the determination of the capability (i.e. probability of detection) again with reduced experimental testing
- Providing an understanding of inspection data through insight into the energy interaction with the structure
- Increasing capability of detection of flaw size or type by optimizing techniques

In regards to increasing NDE capability, simulation is used to augment and expand the experimental data available for NDE technique assessment typically required; it is feasible to simulate many more scenarios that would otherwise not be cost-effective for a purely experimental investigation. This approach can be particularly beneficial for highly complex, unique parts or scenarios with low part-counts, where sufficient numbers of flawed specimens for experimental characterization of capability are either not available or affordable. In such cases, the use of NDE simulation tools is necessary to yield a relevant assessment (for example, aiding the establishment of a probability of detection [ref. 1]).

The rest of this section discusses the practice of NDE simulation. The following is a brief section on thermography modeling, followed by several sections covering UT modeling. Simulation and analytical modeling for other NDE techniques can be found in the references provided at the end of this section.

5.6.1.1 Thermography Simulation

Thermography modeling has a number of well-established approaches since modeling of thermal NDE is essentially heat-transfer modeling. In a solid, homogeneous, isotropic body, these transfers are governed by the equation of heat conduction [ref. 2]:

$$\frac{\partial T}{\partial t} = \frac{K}{\rho C_p}\left(\frac{\partial^2 T}{\partial x^2} + \frac{\partial^2 T}{\partial y^2} + \frac{\partial^2 T}{\partial z^2}\right) \qquad \text{Equation 10}$$

Where T is the temperature, t the time, ρ the density, K the thermal conductivity and C_p the specific heat at constant pressure. In the case of very simple geometries, this equation is reduced to (or approximated by) one dimension and an analytic solution can be developed [refs. 2–5]. However, in most practical cases, the analytical approach rapidly degenerates into unworkable situations with the introduction of both anisotropic properties and subsurface defects, especially if 1D approximation cannot be retained. Therefore, numeric methods such as finite difference or FEM

techniques are typically employed to solve the heat equation. An example using COMSOL® simulation software is shown in the section 'NDE Simulation Examples' (below).

5.6.1.2   UT Simulation

Commonly employed types of UT simulation techniques include the FEM, spectral FEM, and finite difference (FD) method. Commercial packages that can simulate UT propagation include Abaqus®, ANSYS®, COMSOL®, OnScale®, Pogo, CIVA, among others. Most of these software packages use explicit and/or implicit FEMs for 3D simulation (Abaqus®, ANSYS®, COMSOL®, OnScale®, Pogo). CIVA software contains multiple UT modeling modules that are based on 2D and 3D semi-analytical methods, 2D FD method, and 2D FEM. Custom simulation tools can be used to fill in the gaps of commercial tools, or may provide computational benefit over commercial codes (such as more rapid simulation times or simulation of larger components). This includes work at NASA Langley Research Center (LaRC) in a computationally efficient 3D FD UT simulation code targeted for anisotropic composite materials, based on a rotated-staggered grid (RSG) technique [ref. 6].

5.6.1.3   Incorporation of Material Damage

As discussed in the state-of-practice survey (Appendix A) and other sections of this Handbook, damage types occurring in composites include delamination, cracking, foreign material, porosity, wrinkling, and waviness. Since all of these damage types can create a challenge to inspection and damage characterization methods, NDE simulation is used as a tool to inform what inspection method(s) are most promising for a specific inspection problem. Regardless of the NDE simulation method in use, the scale of energy interaction with the size of defect needs consideration when selecting an appropriate representation of defect for the model.

For ultrasonic NDE, consideration of the ratio of UT wavelength compared to the defect size is necessary when deciding on the scale of details included in the UT model. For example, for typical bulk wave or guided wave inspections, modeling each ply layer as a homogeneous medium is likely the most practical route. A simulation that models each carbon fiber and the matrix resin material in a CFRP is not practical or reasonable since the wavelength for a typical inspection is too large to create significant scattered signals from individual fibers. Similarly, through-thickness homogenization of multiple layers is done [refs. 7 and 8]. However, it has a strong potential to oversimplify wave interaction phenomena (for example, wave scattering effects depend on local material properties that are modified through homogenization).

In UT modeling, foreign material is incorporated into an UT simulation by changing the elastic properties (e.g., density, stiffness) in the region containing foreign material. Both cracking and delamination damage can be represented in an UT simulation by using stress-free boundaries at the edges of the damage site [refs. 9 and 10]. This approach assumes that no sound propagates into the stress-free region (i.e., into the 'gap' space of the crack or delamination). For defect scenarios, with a 'closed' defect (e.g., closed crack or disbond) some amount of energy transfer can occur across the defect boundaries. In these cases, a change in material properties may be a more accurate representation of the defect (e.g., changes resulting in an increase in reflectivity and decrease in transmission across the boundary). However, the choice of specific values used for the equivalent/degraded material properties may be subjective unless the selected values are based on rigorous experimentation on representative samples. Alternatively, a validated representative

148

volume element (RVE) model is used to determine the degraded property that is relevant to incorporate into the UT simulation.

The approach of using degraded material properties is likely also the most reasonable method for defects such as fiber breakage and porosity [ref. 11]. Since the wavelength to defect ratio in those cases is large (for typical UT inspection frequencies), modeling the wave scattering from individual pores/voids or broken fibers is not a reasonable approach for the UT simulation (and is also likely not feasible computationally if a realistically sized composite component is being modeled). This is another case where validated RVE models are used to inform an equivalent material property.

In thermal modeling, cracking and delamination damage is modeled via a change in thermal resistivity. For small-scale void type defects, such as porosity, changes to thermal diffusivity is used to model heat flow in the presence of defects. As shown in Equation (10), changes in material properties due to degradation or foreign material is represented by changing density, specific heat, and or thermal conductivity.

5.6.1.4 Discretization, Stability, and Convergence

To produce stable, converged simulation results, care is taken to use appropriate spatial and temporal discretizations. As a starting point for spatial discretization, it is common to use 'rules of thumb' based on number of discretizations per shortest ultrasonic wavelength, often ranging from 10–20+ steps per wavelength depending on the order of the technique and degree of accuracy required. Since wavelength has a directional dependence due to anisotropy in composites, compute memory savings are achieved using elongated discretizations in the (stiffer/faster) fiber-direction. Mapped meshing techniques can extend this for curving laminates.

For guided waves, which have a standing wave component perpendicular to the propagation direction, the wavelength of the guided wave (obtained via calculating a dispersion curve) is often used instead of the bulk propagation wavelength. In this case, an additional criterion of number of elements in the direction perpendicular to the propagation (e.g., through-thickness direction) is needed. Spatial discretizations may also need to be smaller at interfaces, free boundaries, and when accounting for defects within the part thickness, depending on the simulation technique.

It is important for a person performing a simulation to have a positive proof of convergence when using results from a model. This is because convergence requirements are difficult to know *a priori*, depending on a number of factors (e.g., order of approximation, geometric/interface effects, and metrics of interest). Best practice is to perform relevant benchmarks and/or convergence studies not only when using a new simulation approach, but also when using new software as internal implementation details may vary. However, extremely high degrees of computational accuracy may be unnecessary, and even if they are of interest, in most cases, elastic properties exhibit significant degrees of uncertainty that may make high degrees of accuracy unrealistic (unless a statistical approach is taken). Even with careful measurements of quasi-static elastic properties, they exhibit frequency-dependent effects that are typically not measured. High-frequency measurements can provide properties that are more applicable for ultrasonic modeling. For example, water tank measurements for IM7-8552 are shown to differ from static-elastic constants of approximately 5-10% [ref. 12].

The choice of temporal discretization depends on the use of explicit or implicit time-domain solution technique. Explicit technique solves for state variables at the current time step entirely in

terms of previous time steps. This provides a faster solution per time step, with the drawback that these techniques require smaller time steps for numerical stability. Commercial UT simulation software (e.g., Pogo, OnScale®) has been trending towards explicit time solvers, reporting high simulation speedups as the high per-time-step computational efficiency more than makes up for the smaller time steps.

5.6.1.5   Representing Composite Simulation Domains

Incorporation of damping effects into composite UT models is important, as composites generally exhibit damping effects significantly stronger than metallic materials. Damping models include linear viscoelastic models (e.g., Maxwell, Rayleigh [ref. 13], or Kelvin-Voigt [ref. 14]) and hysteresis damping (incorporation of a loss factor via complex elastic moduli). For further reading, Treviso et al. [ref. 15] published a comprehensive review of damping parameter estimation and damping modeling for composites.

When compute memory savings are needed, one of the first approaches should be reducing the size of the domain, (e.g., simulation of an infinite domain with absorbing boundaries, such as perfectly matched layer (PML)) [ref. 16] or gradually increasing damping absorption techniques [ref. 17]. For cases where large-scale simulation domains are critical, the use of semi-analytical techniques are a highly efficient alternative (although more difficult to employ). Examples of approaches include semi-analytical finite element (SAFE) modeling [ref. 18] and the combined analytical finite element approach (CAFA) [ref. 19]. These types of techniques incorporate analytical components for regions or aspects of wave propagation with simple geometries and properties, and use numerical techniques as needed to represent damage or geometrically complex regions.

5.6.1.6   Incorporation of a Transducer

When an end-to-end UT scan simulation is needed, coupled field piezoelectric equations are employed, for example [refs. 20 and 21]. This is supported in each of the commercial codes mentioned above. This approach allows direct modeling of transmission and reception of waveforms by a transducer. It is common practice to omit the transfer function of transducer and data-acquisition equipment circuitry, instead normalizing amplitude results and using relative comparisons. Such relative comparisons are useful in time of flight comparisons for bulk or guided wave scenarios, in guided wave analysis relying on dispersion curves, or after calibrating relative to the noise floor from bulk wave results.

A common approach for elastodynamic solvers is to implement excitation purely in mechanical terms (e.g., time-varying displacement, body force, or moment rate tensor). To employ these techniques, various techniques are used to represent transducer excitation in terms of mechanical forces. For commonly employed thin PZT transducers, in-plane radial motion is prescribed in various manners, for example by analytical theories of a perfectly bonded transducer ([refs. 10 and 20]). Another approach includes experimental measurements, such as obtaining velocities for a transducer via laser Doppler vibrometer. A piezoelectric coupled field model can also be set up in a separate code, and the mechanical state at an interface imported into an elastodynamic solver [ref. 22].

5.6.1.7   NDE Simulation Examples

In this section, example cases of UT and thermography simulation in composites are briefly discussed.

Under the NASA ACP, benchmark cases were generated for guided ultrasonic wave propagation in a composite laminate. Ideally, a benchmark case represents a well-defined specimen and defect scenario that has associated experimental data. The benchmark case shown below is for an eight-ply $[0_2/90_2]$s IM7-8552 CFRP laminate. Both a pristine and a delamination-type scenario were studied. For the delamination case, the experimental specimen contained a Teflon insert of a simple geometry rather than a real delamination. Full details on the benchmark studies are found in [ref. 23]. Figure 5.6-1 shows an example of simulated versus experimental guided wave propagation for the 'delamination' type defect and a 300 kHz excitation source. In the simulated image (Figure 5.6-1b), the white box represents the defect region. It was observed that the wavelength decreases in the damage region, with simulation and experiment yielding similar wavenumber values (see [ref. 23] for more details). The simulation was implemented using the Elastodynamic Finite Integration Technique (EFIT) method. The example below demonstrates the ability of simulation tools to provide guidance on the type and degree of wave-defect interaction that are expected. Such simulations can thus provide guidance on inspection and data analysis methods.
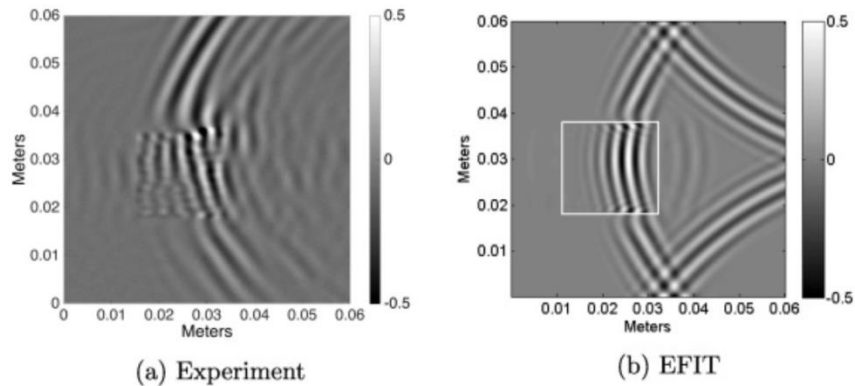
Figure 5.6-1. Guided wave propagation in composite laminate containing a delamination type defect. a) Experimental wavefield data taken using a laser Doppler vibrometer, b) simulated wavefield data.

Simulation of UT in complex geometry composites is highly relevant for aerospace applications. This is an area of active research. NASA LaRC is currently working to adapt in-house custom codes to include the ability to simulate UT in complex composites with each ply layer modeled individually to allow for realistic incorporation of defects (which can often occur between plies). Researchers at NASA Ames Research Center (ARC) have tested commercial codes, such as Abaqus®, ANSYS®, and COMSOL® to model UT in composite laminates [ref. 23]. An example using Abaqus® for a hat-stiffened composite is shown in Figure 5.6-2 as a snapshot of a wavefield. Upon wave interaction with a rectangular defect (white box), the simulation predicts aberrations in the nearfield and scattered wavefield which carry information pertaining to the damage location and state. Other researchers have also used Abaqus® to simulate guided waves in stiffened composites [ref. 24]. NASA is working towards performing validations between simulated hat-stiffened composites and experimental data. Such validations are of key importance to establish reliability and accuracy for UT simulation tools.
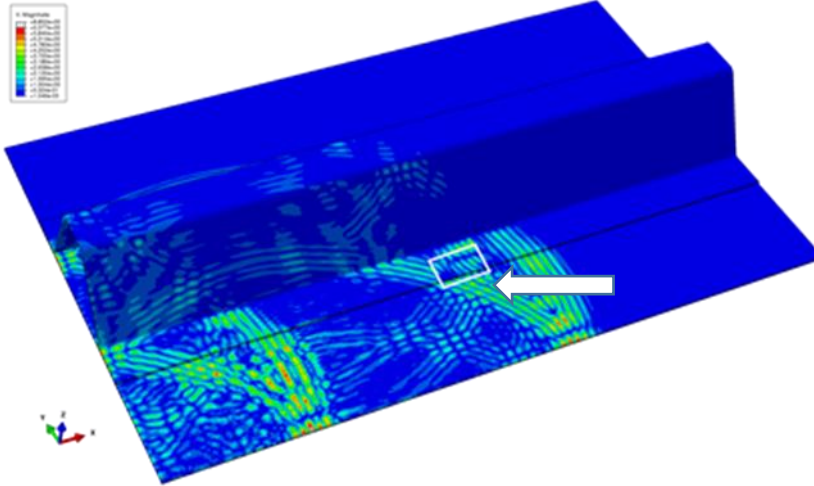
Figure 5.6-2. Single snapshot in time of simulation showing guided wave interaction with hat-stiffened composite containing rectangular delamination (box outlined in white).

As stated in the introduction, the simulation of thermal NDE to represent real-world scenarios often requires the use of FEM numerical modeling. Figure 5.6-3 shows a 2D FEM of the heat flow in a complex geometry, complex material specimen. Utilizing FEM models, as NDE predictive tools provides a resource to easily perform parametric studies. Figure 5.6-4 illustrates a parametric study varying both delamination width and gap thickness. Delamination widths above 2 cm do not affect the thermal signal while gap thicknesses (contact resistance) increase the slope of the thermal response. The model of Figure 5.6-3 was produced using the commercial FEM software COMSOL®.
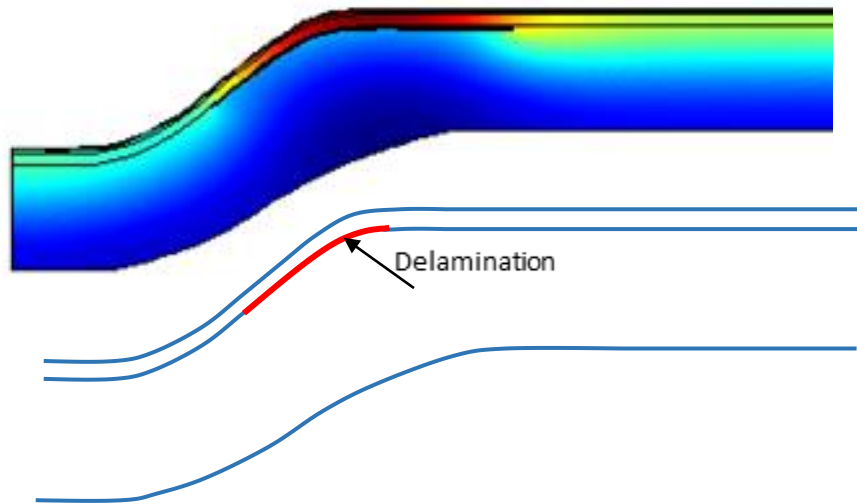
Figure 5.6-3. 2D finite element simulation of heat flow in complex geometry specimen showing increased heating over delamination region (top), and geometry showing location and size of delamination (bottom).

152
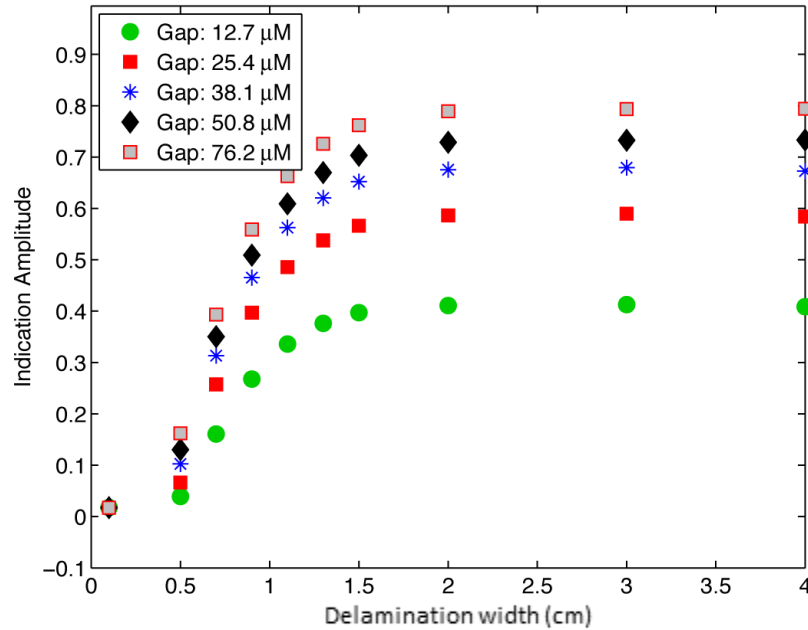
Figure 5.6-4. Effect of delamination width and gap thickness on thermal signal for above configuration.

5.6.1.8   References

1. Chapuis, Bastien; Calmon, Pierre; and Jenson, Frédéric: "Best practices for the use of Simulation in POD Curves Estimation," *IIW Collection*, 2016.
2. Carslaw, H. S.; and Jaeger, J. C.: *Conduction of Heat in Solids*, Clarenon Press, Oxford, 1986.
3. Maillet, D.; et. al.: *Thermal Quadrupoles*, John Wiley & Sons, Chichester, 2000.
4. Vavilov, V. P.: "Modeling and Characterizing Impact Damage in Carbon Fiber Composites by Thermal/Infrared Non-Destructive Testing," *Composites Part B: Engineering* 61, 1-10, 2014.
5. Winfree, W. P.; Zalameda, J. N.; Howell, P. A.; and Cramer, K. E.: "Simulation of Thermographic Responses of Delaminations in Composites with Quadrupole Method," in *Thermosense: Thermal Infrared Applications XXXVIII*, Vol. 9861, p. 98610N, International Society for Optics and Photonics, 2016.
6. Frankforter, Erik; Leckey, Cara; and Schneck, William III: "Comparison of staggered grid finite difference schemes for ultrasound simulation in curving composites," *AIP Conference Proceedings*, Vol. 2102, No. 1, AIP Publishing, 2019.
7. Wang, L.; and Rokhlin, S. I.: "Floquet Wave Homogenization of Periodic Anisotropic Media," *The Journal of the Acoustical Society of America*, 112.1, 38-45, 2002.
8. Schoenberg, Michael; and Muir, Francis: "A Calculus for Finely Layered Anisotropic Media," *Geophysics*, 54.5, 581-589, 1989.
9. Leckey, Cara A. C.; Rogge, Matthew D.; and Parker, F. Raymond: "Guided Waves in Anisotropic and Quasi-Isotropic Aerospace Composites: Three-Dimensional Simulation and Experiment," *Ultrasonics*, 54.1, 385-394, 2014.
10. Yu, Lingyu; Tian, Zhenhua; and Leckey, Cara A. C.:. "Crack Imaging and Quantification in Aluminum Plates with Guided Wave Wavenumber Analysis Methods," *Ultrasonics*, 62, 203-212, 2015.

11. Tavaf, Vahid; et al.: "Effect of Multiscale Precursor Damage on Wave Propagation Through Modulated Constitutive Properties of Composite Materials," *Health Monitoring of Structural and Biological Systems XII*, Vol. 10600, International Society for Optics and Photonics, 2018.

12. Barazanchy, Darun; Roth, William; and Giurgiutiu, Victor: "A New Ultrasonic Immersion Technique to Retrieve Anisotropic Stiffness Matrix for Dispersion Curves Algorithms," *Structural Health Monitoring 2017*, shm 2017.

13. Gresil, M.; and Giurgiutiu, Victor: "Guided Wave Propagation in Composite Laminates Using Piezoelectric Wafer Active Sensors," *The Aeronautical Journal*, 117.1196, 971-995, 2013.

14. Shen, Yanfeng; and Cesnik, Carlos E. S.: "Local Interaction Simulation Approach for Efficient Modeling of Linear and Nonlinear Ultrasonic Guided Wave Active Sensing of Complex Structures," *Journal of Nondestructive Evaluation, Diagnostics and Prognostics of Engineering Systems*, 1.1, 011008, 2018.

15. Treviso, A; et al.: "Damping in Composite Materials: Properties and Models," *Composites Part B: Engineering*, 78, 144-152, 2015.

16. Collino, Francis; and Tsogka, Chrysoula: "Application of the Perfectly Matched Absorbing Layer Model to the Linear Elastodynamic Problem in Anisotropic Heterogeneous Media," *Geophysics*, 66.1, 294-307, 2001.

17. Shen, Yanfeng; and Giurgiutiu, Victor: "Effective Non-Reflective Boundary for Lamb Waves: Theory, Finite Element Implementation, and Applications," *Wave Motion*, 58, 22-41, 2015.

18. Marzani, Alessandro; et al.: "A Semi-Analytical Finite Element Formulation for Modeling Stress Wave Propagation in Axisymmetric Damped Waveguides," *Journal of Sound and Vibration*, 318.3, 488-505, 2008.

19. Shen, Yanfeng; and Giurgiutiu, Victor: "Combined Analytical FEM Approach for Efficient Simulation of Lamb Wave Damage Detection," *Ultrasonics*, 69, 116-128, 2016.

20. Giurgiutiu, V.: *Structural Health Monitoring with Piezoelectric Wafer Active Sensors, 2ndEdition*, Elsevier Academic Press, 1032 pages, ISBN 9780124186910, 2014

21. Marklein, René: "The Finite Integration Technique as a General Tool to Compute Acoustic, Electromagnetic, Elastodynamic, and Coupled Wave Fields," *Review of Radio Science*, 2002, 201-244, 1999.

22. Shen, Yanfeng; and Cesnik, Carlos E. S.: "Hybrid Local FEM/Global LISA Modeling of Damped Guided Wave Propagation in Complex Composite Structures," *Smart Materials and Structures*, 25.9, 095021, 2016.

23. Leckey, Cara A. C.; et al.: "Simulation of Guided-Wave Ultrasound Propagation in Composite Laminates: Benchmark Comparisons of Numerical Codes and Experiment," *Ultrasonics*, 84, 187-200, 2018.

24. Panda, Rabi Sankar; Rajagopal, Prabhu; and Balasubramaniam, Krishnan: "Rapid Guided Wave Inspection of Complex Stiffened Composite Structural Components Using Non-Contact Air-Coupled Ultrasound," *Composite Structures*, 206, 247-260, 2018.

25. Fernandez, Roman; et al.: "Simulation Studies of Radiographic Inspections with CIVA," 2008.

26. Fernandez, Roman; et al.: "CIVA Computed Tomography Modeling," *proceedings of the World Conference of NDT*, 2012.

27. Sarens, Bart; et al.: "Investigation of Contact Acoustic Nonlinearity in Delaminations by Shearographic Imaging, Laser Doppler Vibrometric Scanning and Finite Difference Modeling," *IEEE Transactions on Ultrasonics, Ferroelectrics, and Frequency Control*, 57.6, 1383-1395, 2010.
28. Cheng, Jun; et al.: "Numerical Analysis of Correlation Between Fibre Orientation and Eddy Current Testing Signals of Carbon-Fibre Reinforced Polymer Composites," *International Journal of Applied Electromagnetics and Mechanics*, 39.1-4, 251-259, 2012.
29. Lopato, Przemyslaw; et al.: "Full Wave Numerical Modelling of Terahertz Systems for Nondestructive Evaluation of Dielectric Structures," *COMPEL-The International Journal for Computation and Mathematics in Electrical and Electronic Engineering*, 32.3, 736-749, 2013.

5.6.2 Robotics

The application of robotics to NDE inspection tools is a rapidly growing effort. Robotic systems offer increased inspection speed, repeatability, and reliability especially for large structures. The sheer volume of inspection data being created and the necessity to automate and track inspections are ideally suited to robotic systems. These systems can also enable location identification and lifetime NDE data assessments, directly comparing the state of specific locations within a structure during multiple discrete inspections. Robotics systems also offer improved inspection capabilities for safety purposes in cases where inspections require access to dangerous areas such as those involving radiation hazards, enclosed spaces, or difficult access scenarios. The Boeing Giraffe system and the NASA Collaborative Robot Line Scanner systems are two examples of robotic systems used in Aerospace NDE are described in more detail in the following sections.

5.6.2.1 Examples

Example A: Boeing Giraffe system

The Giraffe is a ground-based robotic inspection platform for use on the structures like the fuselage of an airplane during production. This system is a self-supported, holonomic platform that is able to reach to inspection locations on large structure, and is relative easy to set up and use. A vertical mast with a pivoting end effector on an extension arm allows a large inspection envelope. For commuter-sized airplanes, the current model can reach and inspect up to the centerline of the top and bottom of the fuselage from either side of the airplane. Larger Giraffe systems are built to handle larger aircraft or different structures.

The holonomic base allows quick and efficient repositioning of the robot sensor unit along the length of the fuselage. Motion-control software with sensor feedback enables automatic capture overlapping grid pattern scans. Also captured is reference position data to align the NDE scans with appropriate airplane coordinate system. The Giraffe is configured to accept various types of NDE units mounted to its end effector, which includes IRT, UT, and eddy current NDE sensors.

As stated above, the Giraffe system includes a holonomic base, vertical extension mast, pivoting end effector, proximity sensors, and support for multiple types of NDE devices mounted on the end effector. To reduce development costs, an existing Mecanum-wheeled holonomic base platform was reconfigured to carry the vertically extendable support mast (Figure 5.6-5).
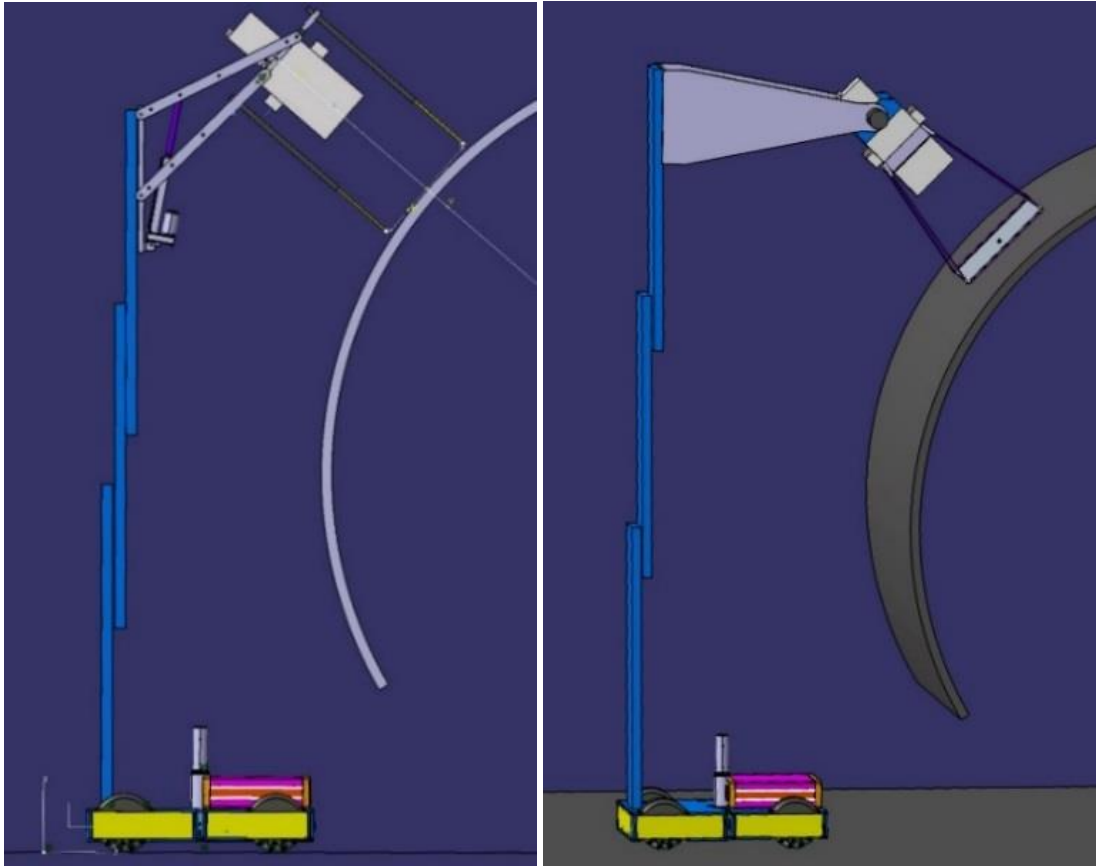
Figure 5.6-5. Candidate designs of vertical mast and end effector concepts mounted to holonomic base.

The concept on the left incorporated a four-bar linkage arm mechanism to control the position and orientation of the end effector, while the concept on the right used a rigid extension arm and a motor control rotational joint for end effector placement. A variation of the design shown on the right in Figure 5.6-5 was chosen for the current Giraffe system due to its relative mechanical simplicity, which allowed independent programmable control over the extension height, and end effector pitch rotation using position control motors with non-back drivable gearboxes.

The system configuration of the mobile platform, extension arm, end effector, IRT scanner, and distance sensors is shown in Figure 5.6-6.

Figure 5.6-6. System configuration of ground-based robotic inspection platform with IRT unit.

During typical operation, this system can be driven (tele-operated) by an operator to an approximate starting location, after which it is set to automatically acquires grid scans arranged in an operator defined vertical and horizontal pattern along either side of the airplane fuselage.

The automated grid-scanning feature of the motion control algorithm used here involves feedback of distance data from three laser range meters to the motion control algorithm, which sets the horizontal and vertical placement, and the yaw and pitch orientation of the platform, and end effector, respectively. After the automated scanning sequence is complete, the individual images from each IRT scan (Figure 5.6-7b) can then be stitched together to produce a single representation of the inspection region. The lower image in Figure 5.6-7b is the scan taken from the location shown in Figure 5.6-7a, and the light gray vertical strip in the center of that image is a 7-inch long "flaw" attached to the back of the 0.375-inch-thick composite panel that was used for testing. Figure 5.6-7c, shows the IR marking detected, which is placed on the backside of the panel.
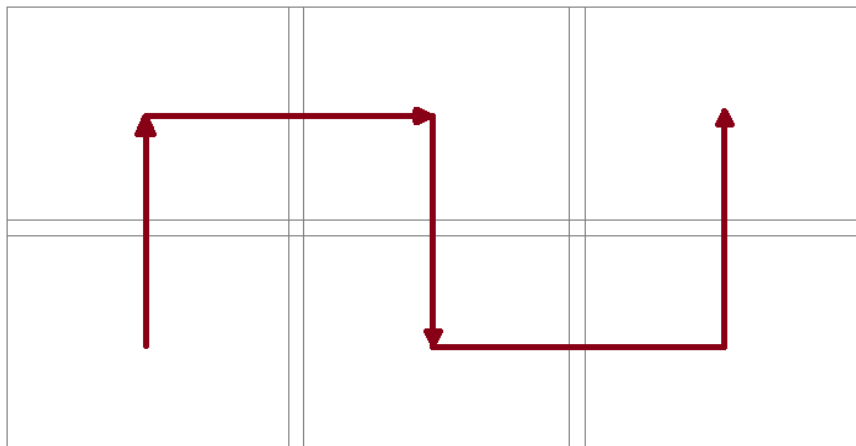
a)
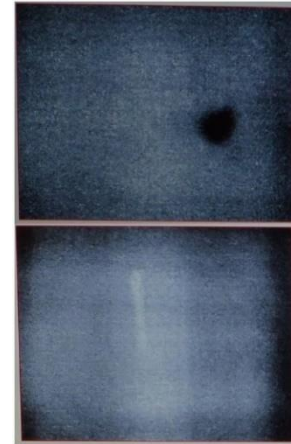
b)
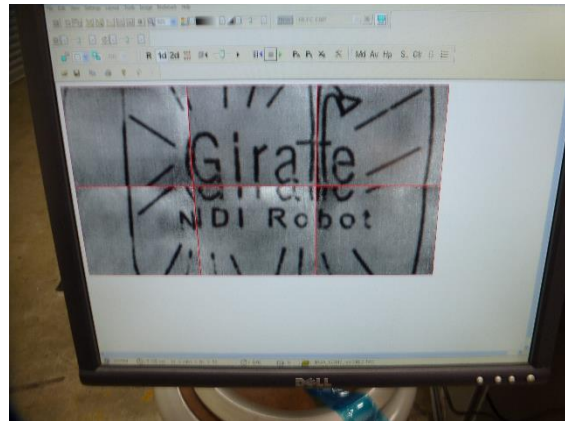
c)

Figure 5.6-7. a) Scan pattern (3 × 2) for IRT-based inspection, b) examples of individual IRT scans, c) example of written defect from backside of the part.

The system is fully controlled in a teleoperation mode to allow operators to acquire data manually. A semi-automated mode is also possible (although not yet implemented), where the user controls the platform position and mast height, and the system automatically adapts the end-effector pitch orientation to maintain a perpendicular alignment with the surface in front of it.

In order to locate the scans in the coordinate system of the airplane, 3D position measurements are taken of the boundary regions of the scans. This boundary reference allows the combined scan image placement in the same coordinate system as the airplane and its associated computer-aided design (CAD) models. This enables association acquired scans with the respective 3D models of the airplane, and provides location data for future reference. A Local Positioning System (LPS), shown in Figure 5.6-8, is used to acquire 3D position data in the coordinate system of the airplane.

Figure 5.6-8. LPS used to acquire scan position data in airplane coordinates.

Example B: NASA Dual Collaborative Robot Line Scanner

NASA's Dual Collaborative Robot uses the LST technique described in Section 5.2.4 of this handbook. The heat source is mounted on one robot and moved across the sample's surface at a constant speed. An IR imager is mounted on a second robot closely following the first and used to record the temperature changes on the surface. The IR detector moves at the same velocity as the heat source and the imager's FOV is set to contain a region behind the location where heat is deposited. The temperature recorded in the heated region is used to analyze the cooling behavior after heat deposition detecting the presence of defects or material property changes. This technique has the advantage that when robotically implemented very large structures are interrogated very quickly [refs. 39–45].

This system is a low cost (~ $100 K total), human safe robot system that automates the inspection without dedicated "keep-out" areas (see Figure 5.6-9). The synchronized robots enable thermal inspection of large-area, complex geometries with high throughput, with a scan speed of 105 mm/s depending on geometry. The system contains preplanning simulation for verification of feasibility. It is more than ten times faster than manual flash thermography and approximately two times faster than robotic flash thermography. The dual collaborative robot system is adaptable to other inspection modalities and provides automated export of inspection data that are registered to the structure by linking it to a CAD file for analysis.

a)

b)

c)
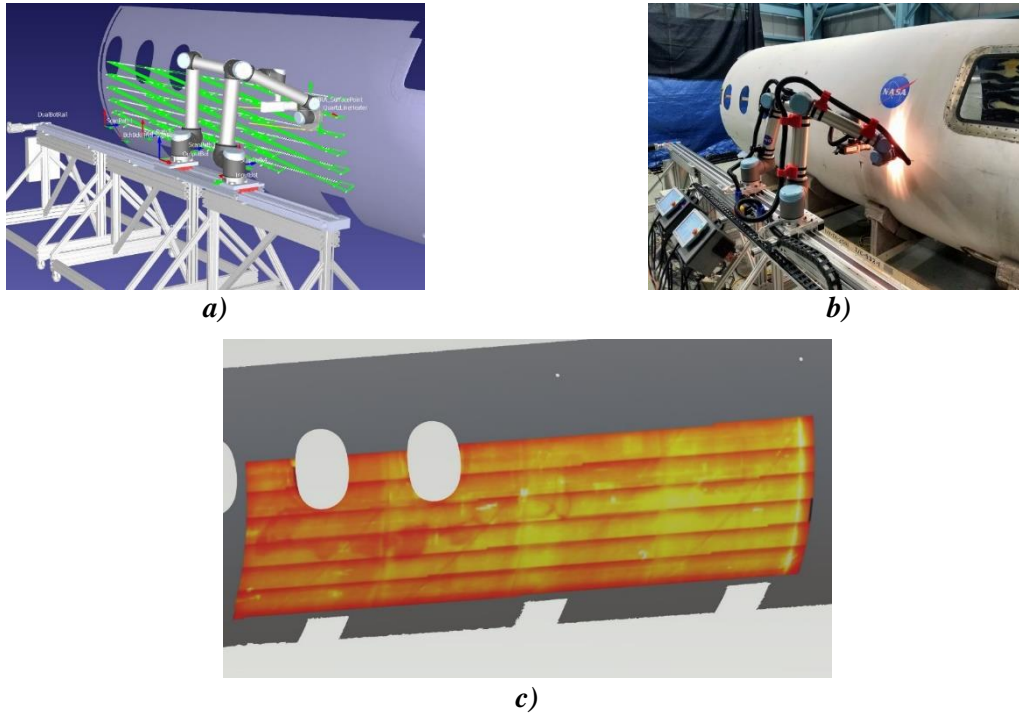
***Figure 5.6-9. NASA's Collaborative Robot System inspecting a small fuselage section.
a) Interactive path planning, b) data collection on composite fuselage, and c) thermography data
mapped onto CAD geometry.***

5.6.3 In-process Inspection

AFP is a complex method of composite fabrication that drastically reduces the variability of part quality compared to hand layup. The use of robots to place material limits some types of flaws but can result in other flaws such as tow overlaps and gaps, tow twists or peel-up, and FOD. These types of flaws may result in significant reduction in mechanical capability (e.g., strength, stiffness, etc.) [refs. 1–4].

Inspecting AFP parts after each ply reduces the likelihood that entire parts will be rejected as flaws are detected and fixed in a new ply with minimal effect on previous plies. Waiting until the part is complete or only inspecting after few plies, leads to additional waste and longer time for repair. This also leads to a stronger likelihood of missing indications flaws upon final inspection of the part. Although AFP can position composite prepreg material on a tool faster than humans can, AFP also requires a significant amount of manual inspection after placing each ply. This inspection time can be up to 42% of total manufacturing time [ref. 5]. To reduce the time spent inspecting and to make these inspections less prone to human error *in situ*, inspection has become a topic of research in the field of AFP.

Two examples of inspection techniques being developed for AFP inspection include profilometry coupled with machine learning and *in situ* thermography presented in the next sections.

5.6.3.1 Profilometry

Profilometry is a commercially available optical NDE technique most often utilized that provides a 3D rendering of a surface. It can be used as an NDE method by detecting deviations in the surface shape from the expected shape provided, either from a model of the component or a previous

measurement on a component with no known flaws. The deviations from the expected shape can provide indications of defects such as errors in the fabrication process or damage (e.g., impact damage). It is a non-invasive imaging method based on the concept of light reflection to locate objects and measure distance. A pattern is projected down onto a surface, through which surface features are inferred from deviations in the pattern [ref. 1]. The advantages of profilometry are that it is non-contact, high resolution, can be rapidly acquired, and provides indications of surface damage and other non-conformances not readily observable by simple visual inspection.

In general, laser profilometry is utilized in instances of surface profiling where non-contact requirements are imposed. In addition, optical scanning processes such as profilometry have a high accuracy and high resolution compared to other methods [ref. 2].

Common profilometry methods include Time of Flight, Shape-form-shading Methods, and Stereoscopic Methods [ref. 3]. Time of flight, the method employed in the ACSIS Keyence profilometers, projects a laser signal from a source and measures the time it takes for the signal to reach an object and is reflected back to a receiver. Shape-form-shading methods infer surface shapes from the gradual variations in greyscale in an image. Stereo methods employ a dual or multi-camera system to mimic the shape rendering capabilities of human vision.

Several key issues to overcome with profilometry are the stability of the scanning platform and the potential of data loss through material signal attenuation. Thus, calibration and system performance indicators are key to proper functioning. Chen et al. [ref. 4] contains an overview of analytic calibration techniques. Sacco et al. [ref. 5] observes that material type in AFP inspection can have a direct effect on data loss and artifact production in profilometry-based inspection.

Profilometry has been used for imaging of manufactured parts made from different materials such as rubber, plastics, and metals. Implementation of profilometry on composites inspection is relatively new and unexplored. Post-acquisition data can be used for machine learning implementations for recognition, cloud of point comparison with original/intended shape and hard coded algorithms. Profilometers react differently according to material type and the reflectiveness of the surface plays a role in the effectiveness of the inspection.

Sacco et al. [ref. 6] presents a detailed study on the usage of profilometry in inspection of composite parts manufactured with Automated Fiber Placement. Profilometers were used to obtain the grayscale image shown in Figure 5.6-10. These images were then analyzed with software based on machine learning to recognize the AFP defects.
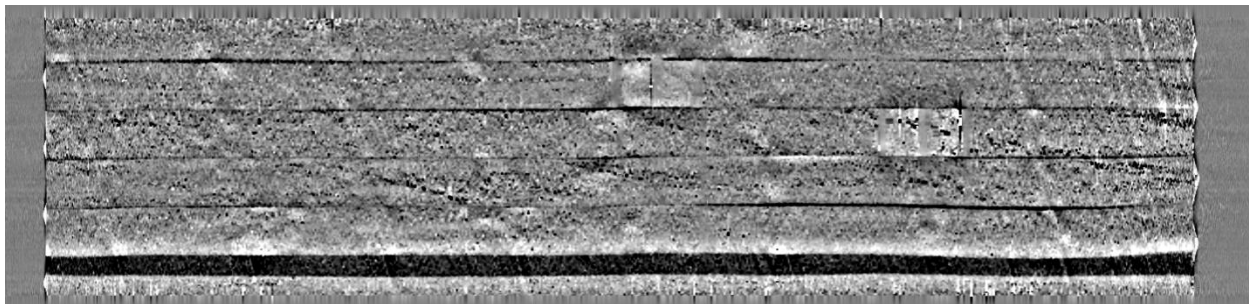
Figure 5.6-10. Grayscale image of AFP from profilometer scan [ref. 6].

Figure 5.6-11 demonstrates the output from the machine-learning-based software and the algorithm-detected indications. Figure 5.6-12 shows the results of applying the machine learning results to the profilometry scans resulting in classified AFP defect indications.
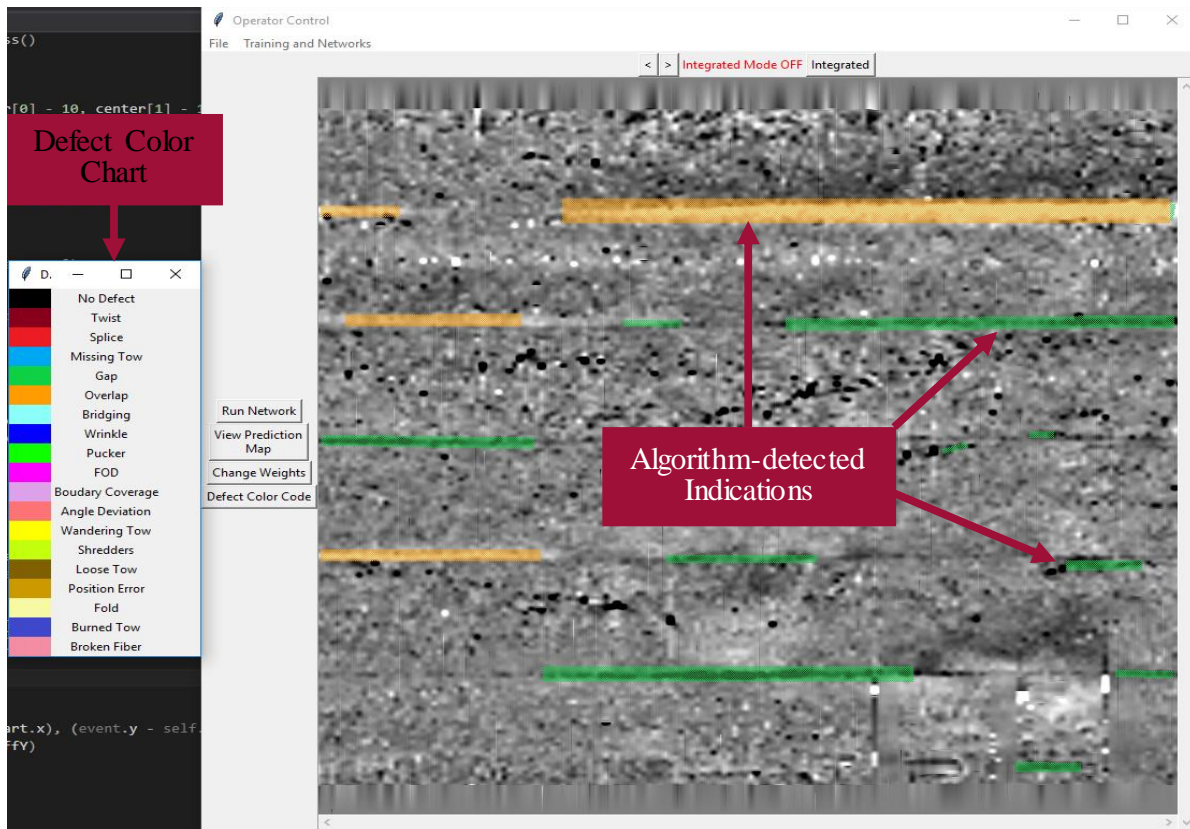
Figure 5.6-11. Algorithm-detected indications in AFP materials [ref. 6].
Green identifies gaps between tape layers and orange represents overlapped tape layers.
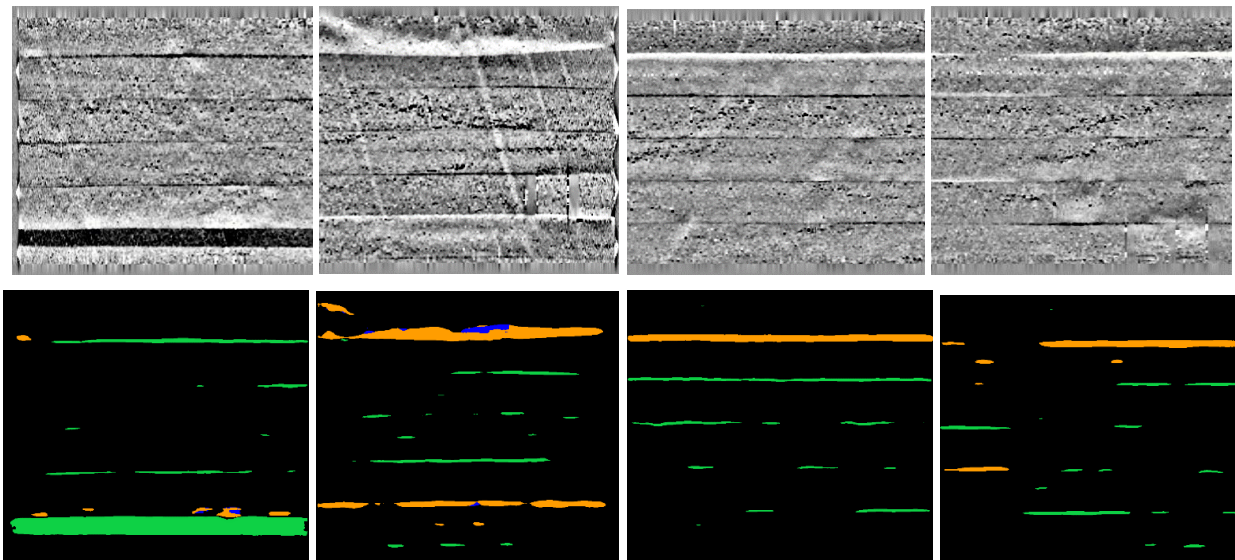
Figure 5.6-12. Algorithm-classified indication map of profilometry data [ref. 6].
Green identifies gaps between tape layers and orange represents overlapped tape layers. The dark purple is identifying FOD.

5.6.3.1.1 References

1. Hu, E.; and Haifeng, F.: "Surface Profile Inspection of a Moving Object By Using Dual-Frequency Fourier Transform Profilometry," *Optik (Stuttg)*, vol. 122, no. 14, pp. 1245–1248, 2011.
2. Sert, E.; Tas, D.; and Alkan, A.: "Three stepped calibration of structured light system with adaptive thresholding for 3D measurements," *Optik (Stuttg)*, vol. 126, pp. 5176–5181, 2015.
3. Van der Jeught, S.; and Dirckx, J. J. J.: "Real-Time Structured Light Profilometry: A Review," *Opt. Lasers Eng.*, vol. 87, no. 2016, pp. 18–31, 2015.
4. Chen, X.; Xi, J.; Jin, Y.; and Sun, J.: "Accurate Calibration for a Camera-Projector Measurement System Based on Structured Light Projection," *Opt. Lasers Eng.*, vol. 47, no. 3–4, pp. 310–319, 2009.
5. Sacco, C.; Radwan, A. B.; Harik, R.; and Van Tooren, M.: "Automated Fiber Placement Defects: Automated Inspection and Characterization," *SAMPE 2018 Conf. Proceeding*, 2018.
6. Sacco, C.; Radwan, A. B.; Beatty, T.; and Harik, R.: "Machine Learning Based AFP Inspection: a Tool for Characterization and Integration," *SAMPE 2019 Conf. Proceeding*, 2019.
7. https://www.compositesworld.com/blog/post/real-time-automated-ply-inspection-rtapi-system-cws-series-on-automated-inspection-methods.
8. Cemenska,J.; Rudberg, T.; and Henscheid, M.: *Automated In-Process Inspection System for AFP Machines*, .EI whitepaper: https://www.electroimpact.com/WhitePapers/2015-01-2608.pdf

5.6.3.2 In-situ Thermography

5.6.3.2.1 Introduction

Thermography provides a visual representation of the thermal conductivity of a part. A fundamental aspect of thermography is that information about underlying structure is obtained or deduced by observing the surface temperature of a volume over time in the presence of known heating conditions. The AFP process already utilizes a heat source to aid with compaction and adherence. Immediately before placing new material on the tool or a previous layer, the surface is heated as shown in Figure 5.6-13. The heat source is often a lamp but can also be a laser or heat gun. This heat source thus provides the excitation needed for the thermographic NDE method. By observing and analyzing the time, history of the surface temperature after a new course is applied and subsequently heated, one can assess part quality using established thermographic NDE techniques and image processing algorithms. This type of assessment is significantly faster and less subjective than visual inspection and allows repairs to be made during fabrication, reducing the risk of curing a part of unacceptable quality.
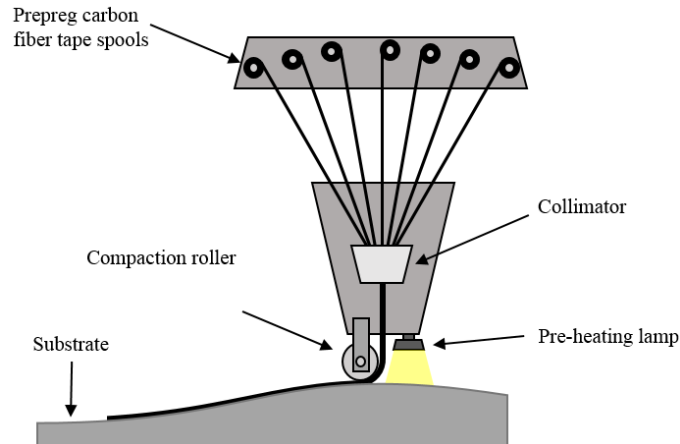
Figure 5.6-13. Simplified diagram of typical AFP robotic platform.

5.6.3.2.2   Data Collected by In Situ Thermal Inspection

AFPs use of a heat source makes it an ideal candidate for thermal inspection. The underlying substrate is heated and then cold material is placed on top. The substrate acts as a heat source and the top surface of the new material is observed as heat moves from the bottom surface, as is illustrated in Figure 5.6-14. If there is a gap between tows, it will manifest as a hot spot, as the camera will see the substrate at a higher temperature than the newly placed tow. Overlaps will show as a cold spot in the thermal data, as the heat from the substrate is now conducting through two layers of material instead of one. FOD that was on the surface during heating may show up as a hot spot and FOD that was placed along with the material (such as backing paper) will be cooler. Areas of poor adhesion will be cold as there will be insufficient heat conduction between the new material and the substrate.

Figure 5.6-14 shows a single thermal image gathered during fabrication of a part by the *In Situ* Thermal Inspection System (ISTIS) on the AFP system at NASA LaRC. The compaction roller is visible at the top of the image. The part of the roller where the new tape is pressed into the substrate is much cooler than the area of the roller that was pressed directly into the heated substrate. There are ten tows in this course. The third and fourth tows from the left have slipped to the right causing a gap between the second and third tow from the left and causing the fourth tow to overlap the fifth tow slightly and the sixth tow from the left to overlap the seventh tow. This course is being placed over non-flat geometry, which caused the edges of the tows to "bubble" up on the left sides. This course is not straight; it is "steered," meaning it is an arch. This steering geometry also causes the "bubbling" to be on one side. The underlying surface consists of previous ply drop-offs resulting in a stair step geometry. When a new course is placed over this geometry, it results in bridging between steps, causing poor adhesion.
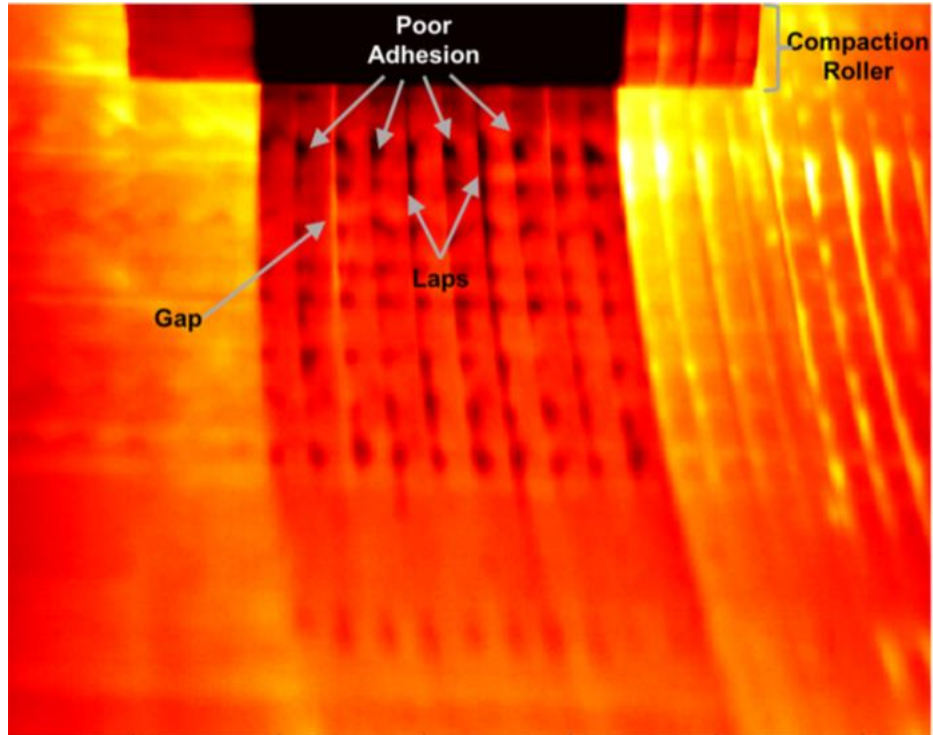
Figure 5.6-14. Single thermal image collected during AFP.
The yellow areas are hotter than the red areas and the black areas are the coldest. Areas of poor adhesion appear as "Bubbles" of cooler areas, a single gap results in two laps.

After plies are placed, it is also possible to use the AFP robot as a moving heat source and camera for a more traditional thermographic inspection where the surface is heated and the heat diffusion is observed.

Data can be spatially registered with the geometry of the part if the position of the robot head is known for each frame. Figure 5.6-15 through Figure 5.6-17 show an example of this line scan process after the data are spatially registered.
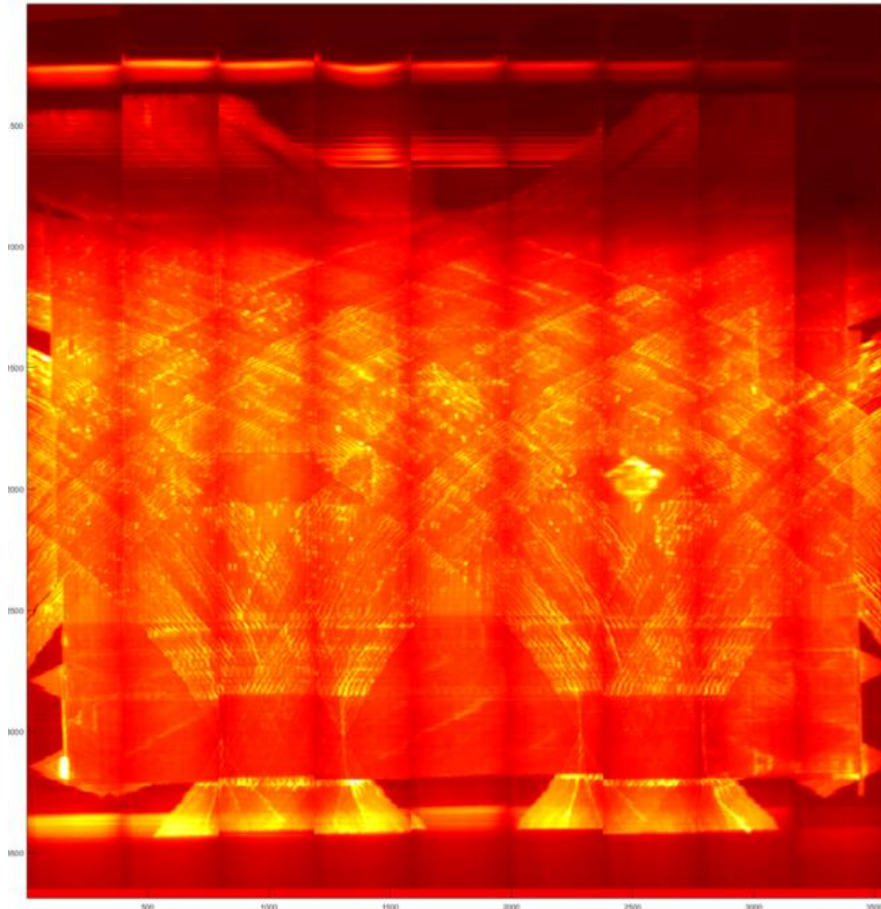
Figure 5.6-15. Spatially registered and temporally aligned in situ thermography data for Go-1 risk mitigation panel collected after layup using lamp as heat source and following line scan path [ref. 9].
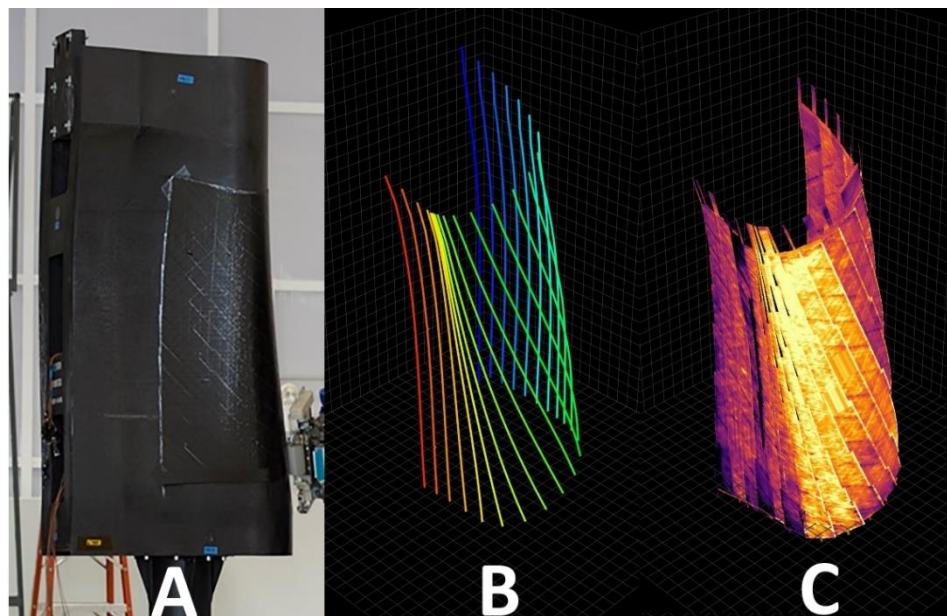
Figure 5.6-16. a) Photo of the complex contour tool, b) image depicting tool path for each course, and c) 3D reconstruction of ply layup thermal data.

166
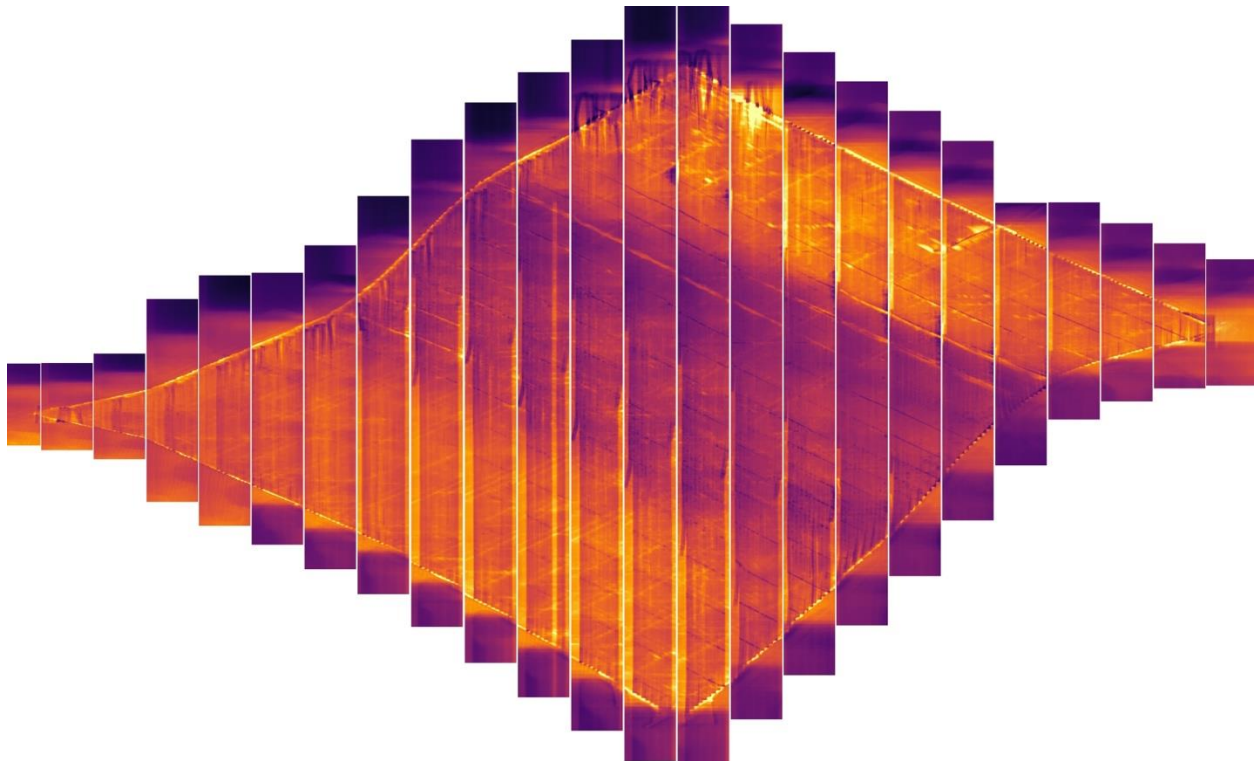
Figure 5.6-17. Flat image of thermal data taken from 45° ply layup.
Each vertical path corresponds to a course. Colder region on the center is the result of inadequate heat lamp exposure due to the complex geometry.

It is also possible to develop a Deep Learning neural network to create masks or bounding boxes to localize specific flaws. Figure 5.6-18 shows an example of the type of masks that can be used to train these neural networks and the outputs these networks will provide.

a)

b)
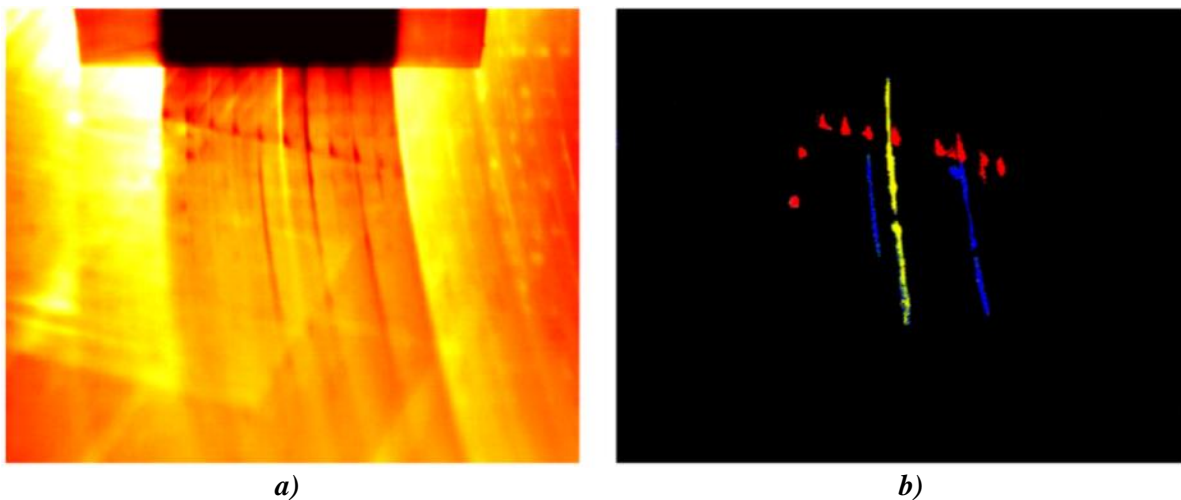
Figure 5.6-18. Example of a) original image and b) a mask for overlaps in blue, gaps in yellow, and poor adhesion in red.

5.6.3.2.3   References

1. Croft, K.; Lessard, L.; Pasini, D.; Hojjati, M.; Chen, J.; and Yousefpour, A.: "Experimental Study of the Effect of Automated Fiber Placement Induced Defects on Performance of

167

Composite Laminates," *Composites Part A: Applied Science and Manufacturing*, vol. 42, no. 5, pp. 484–491, 2011.

2. Fayazbakhsh, K.; Nik, M. Arian; Pasini, D.; and Lessard, L.: "Defect Layer Method To Capture Effect of Gaps and Overlaps in Variable Stiffness Laminates Made by Automated Fiber Placement," *Composite Structures*, vol. 97, February 2014, pp. 245–251, 2013.

3. Heinecke, F.; van den Brink, W.; and Wille, T.: "Assessing the Structural Response of Automated Fibre Placement Composite Structures with Gaps and Overlaps By Means of Numerical Approaches," in *20th International Conference on Composite Materials*, July, 2015, p. 12.

4. Elsherbini, Y. M.; and Hoa, S. V.: "Experimental and Numerical Investigation Of The Effect Of Gaps On Fatigue Behavior Of Unidirectional Carbon/Epoxy Automated Fiber Placement Laminates," *Journal of Composite Materials*, 2016.

5. Rudberg, T.: "Electroimpact's Vision for Fiber Placement, Industry Standards, Predictive Maintenance and Reduced Inspection Requirements," Tysons Corner, VA, 2018.

6. Denkena, B.; Schmidt, C.; Völtzer, K.; and Hocke, T.: "Thermographic Online Monitoring System for Automated Fiber Placement Processes," *Composites Part B: Engineering*, 97, 239–243, 2016.

7. Schmidt, C.; Denkena, B.; Völtzer, K.; and Hocke, T.: "Thermal Image-based Monitoring for the Automated Fiber Placement Process," *Procedia CIRP*, Vol. 62, pp. 27-32, 2017.

8. Winfree, W. P.; Heath, D. M.; and Cramer, K. E.: "Thermal Diffusivity Imaging with a Moving Line Source," *Thermosense XXIII*, 4360, pp. 606-615, 2001.

9. Grenoble, R.; Nguyen, T.; Przekop, A.; McKenney, M.; Juarez, P.; Gregory, E.; and Jegley, D.: "Fabrication of a Composite Tow-Steered Structure for Air-Launch Vehicle Applications," in *59th AIAA/ASCE/AHS/ASC Structures, Structural Dynamics, and Materials Conference*, AIAA SciTech Forum, no. January, Kissimmee, FL, 2018, pp. 1–14.

10. Shepard, S.: Enhancement and Reconstruction of Thermographic NDT Data," *AeroSense*, International Society for Optics and Photonics, 4710, 531-535, 2002.

11. Shepard, S.: "Flash Thermography of Aerospace Composites," *IV Conferencia Panamericana de END Buenos Aires*, 7 pages, 2007. http://www.ndt.net/article/panndt2007/papers/132.pdf

12. Lu, L.; Shin, H.-c.; Roth, H. R.; Gao, M.; Lu, L.; Member, S.; Xu, Z.; Nogues, I.; Yao, J.; Mollura, D.; and Summers, R. M.: "Deep Convolutional Neural Networks for Computer-Aided Detection: CNN Architectures , Dataset Characteristics and Transfer Learning Deep Convolutional Neural Networks for Computer-Aided Detection: CNN Architectures , Dataset Characteristics and Transfer," *IEEE Transactions on Medical Imaging*, vol. 35, no. 5, pp. 1285–1298, 2016.

13. Liu, L.; Gadepalli, K.; Norouzi, M.; Dahl, G. E.; Kohlberger, T.; Boyko, A.; Venugopalan, S.; Timofeev, A.; Nelson, P. Q.; Corrado, G. S.; Hipp, J. D.; Peng, L.; and Stumpe, M. C.: "Detecting Cancer Metastases on Gigapixel Pathology Images," pp. 1–13, 2017. [Online]. Available: http://arxiv.org/abs/1703.02442

14. Esteva, A.; Kuprel, B.; Novoa, R. A.; Ko, J.; Swetter, S. M.; Blau, H. M.; and Thrun, S.: "Dermatologist-Level Classification of Skin Cancer with Deep Neural Networks," *Nature*, vol. 542, no. 7639, pp. 115–118, 2017. [Online]. Available: http://dx.doi.org/10.1038/nature21056

15. Shelhamer, E.; Long, J.; and Darrell, T.: "Fully Convolutional Networks for Semantic Segmentation," *Proceedings of the IEEE Conference on Computer Vision and Pattern Recognition*, pp. 3431–3440, 2015.
16. Sammons, D.; Winfree, W. P.; Burke, E.; and Ji, S.: "Segmenting De-Laminations in Carbon Fiber Reinforced Polymer Composite CT Using Convolutional Neural Networks," *AIP Conference Proceedings*, vol. 1706, 2016.
17. Cemenska, J.; Rudberg, T.; and Henscheid, M.: "Automated In-Process Inspection System for AFP Machines," *SAE International Journal of Aerospace*, vol. 8, no. 2, pp. 2015–01–2608, 2015. [Online]. Available: http://papers.sae.org/2015-01-2608/

5.6.4   Bond Strength

NDE plays a critical role in ensuring the safe and reliable performance of aerospace structures, both during manufacturing and in-service. However, a critical shortcoming of NDE methods has been the inspection of bonded joints to validate bond strength. The certification of the structure requires total confidence in the as manufactured strength of the adhesive joint. Unfortunately, no standard NDE methods exist that can return a quantitative value for the bond strength.

Laser bond inspection (LBI) utilizes a stress wave to interrogate the bonded structure. A high-power short-pulse laser beam is used to deliver energy that is absorbed in a sacrificial overlay such as black paint or tape at the incident surface of the sample. See Figure 5.6-19. No sample heating takes place, and there is no surface damage. Vaporization of some elements of the overlay produces locally high pressure that is enhanced by inclusion of a transparent overlay layer, such as a water film or clear tape that briefly confines vapor expansion. This pressure pulse duration is tailored to a few hundredths of nanoseconds. The magnitude of the pressure is a function of the laser input irradiance, which facilitates generation of calibrated stress waves. The shock from the laser pulse produces a compression wave that propagates to the back surface of the sample where it reflects from the free surface as a tension wave. This tensile wave propagating through the sample provides a proof-test type loading to the bond layer. For laser bond inspection, the laser-pulse failure fluency is used as the parameter for comparing evaluating bond strengths tested with LBI. See Figure 5.6-20.

Figure 5.6-19. Laser inspection system.
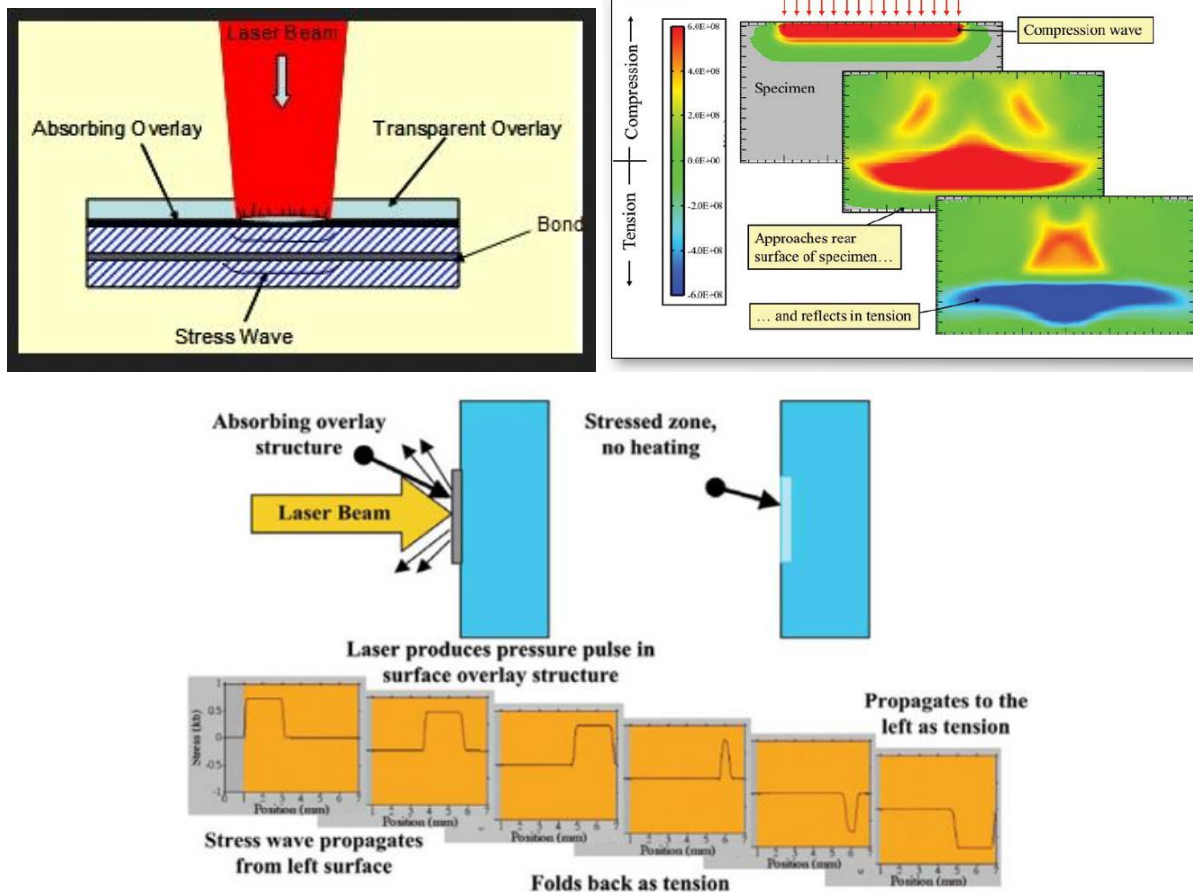
Figure 5.6-20. Laser pulse transformation.

In order to test bond strength with a dynamic loading process such as LBI, it is necessary to have a calibrated bond standard that represent different levels of bond quality. Controlled, weak bond standards were created following processes defined in Boeing patents. The bonds show the same elastic behavior, but the failure strength is clearly different. These bonds are tested by other means, including double cantilever beam and flat wise tension. The results of LBI testing have demonstrated a very reasonable correlation to the relative strengths of bonds obtained through mechanical methods.

LBI was used to evaluate the strength of bonded composite laminate panels for the NASA ACC Program. Testing was performed using a commercial Neodymium Glass (Nd:Glass) laser at 1054 nm wavelength. The laser is capable of producing up to 45 Joules per pulse with very high reproducibility. The pulse is tailored to provide Gaussian-like temporal shape with 200 ns full width at half maximum. The beam is delivered with an 8-mm-diameter, flat top profile to generate a plane pressure wave in the standard. Different fluence levels in terms of Joules per square centimeter (J/cm^2) are applied at each test location. UT is used to detect indications following an LBI inspection at each location. Indications are plotted as a function of incident laser fluence and POD analysis following MIL-HDBK-1823 is applied to the data.

5.6.4.1 Reference

1. https://www.lsptechnologies.com/laser-bond-inspection-lbi-faqs/

5.6.5   Polar Backscatter UT

Standard immersion ultrasonic inspection is performed using a sound beam incident normal to the surface of the part, i.e., parallel to the Z-axis, having a polar angle θ = 0 (see Figure 5.6-21). In this orientation, the magnitude of the sound reflected from the surfaces, and any flaws oriented parallel to the surfaces, is maximized. When the transducer is rotated to a non-zero polar angle θ > 0, the surface-reflected sound does not return to the source transducer, allowing the typically much smaller-magnitude, internally scattered sound to be better observed. The term "Polar Backscatter" derives from measuring ultrasonic backscatter at a non-zero polar angle.
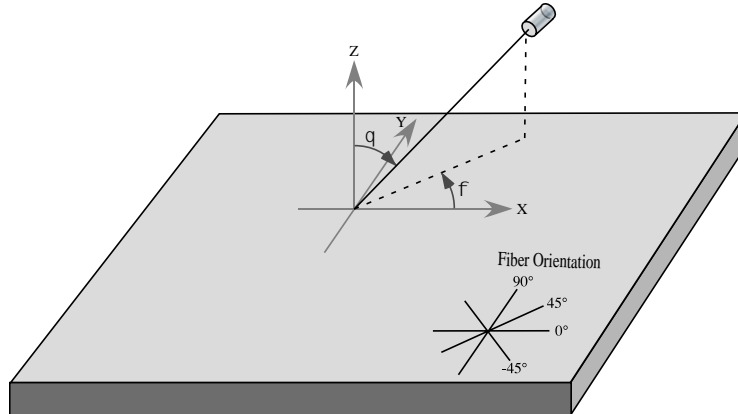
Figure 5.6-21. Immersion ultrasonic backscatter measurement geometry, showing polar coordinate system.

Standard, normal-incidence interrogation exhibits sensitivity to variations of material properties through the thickness of the specimen. Damage states, such as delaminations, inclusions and large voids, which are oriented horizontally, produce reflections detected by the transmitting transducer (pulse-echo mode). These flaws, as well as volumetric flaws, such as porosity, also cause shadowing, which is measured as signal reduction by a receiving transducer opposite the transmitting one (pitch-catch, transmission mode), or as reduction in the back-surface reflection as observed by the transmitting transducer (pulse-echo mode). Ply wrinkling or out-of-plane waviness produces variations in B-scan image texture, which are subtle, but detectable, signal indications. In-plane fiber misorientation or waviness yields even more subtle textural variations in C-scan images. Vertically oriented flaws, such as transverse matrix cracks, produce little or no signal in the normal-incidence case. Practically, in-plane waviness and transverse cracks are generally not detectable using normal-incidence UT.

Oblique, non-normal incidence interrogation results in the sound refracted inside the composite to have an in-plane component, which provides sensitivity to in-plane variations of material properties. Within each ply of composite, the fibers lie along some defined direction, and the ultrasonic scattering properties of the fibers are similarly aligned. The same is true of transverse ply cracks, which tend to follow the direction of the fibers. The azimuthal angle, ϕ, of the incident UT beam then becomes important. The scattering produced by an extended target (fiber, crack) is maximum when the sound beam is incident perpendicular to the target's direction. Therefore, if the polar angle of the UT is fixed, and the azimuthal angle is varied, the backscattered signal received will peak whenever the beam becomes perpendicular to a fiber direction or a transverse ply crack.

Example waveforms are presented in Figure 5.6-22 for normal incidence and polar backscatter.

172

Normal Incidence Waveform

Polar Backscatter Waveform

Front   Back   Reverberations
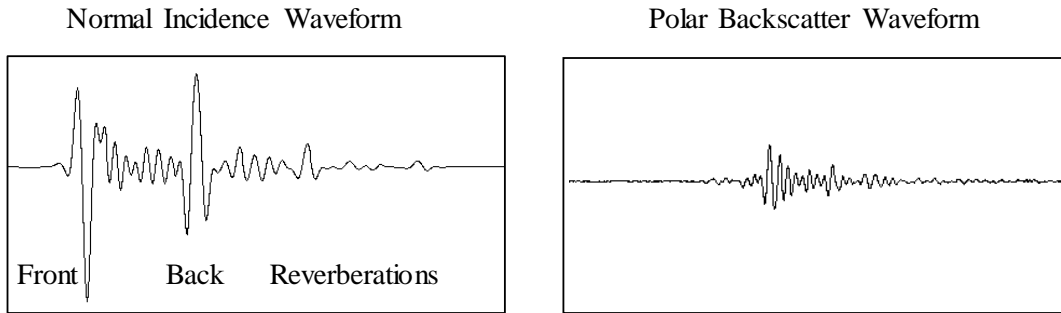
Figure 5.6-22. Example waveforms for ultrasonic backscatter measurement.
Left-hand side shows wave measured at normal-incidence. Indicated are the relatively large echoes arising from the front and back surfaces, and the decreasing-in-amplitude reverberations. Between the surface reflections are the smaller-magnitude backscattered signals arising from the fibers and interlaminar resin layers. Right-hand-side shows a waveform measured at a polar angle of 20°, with the azimuthal angle adjusted to maximize the signal arising from an apparent transverse crack and the fibers aligned in the same ply. The surface-reflected echoes (and their reverberations) do not return at this angle.

5.6.5.1 Examples of Polar Backscatter

Figure 5.6-23 presents examples of polar backscatter results for three different ply layups. For small polar angles, the large-magnitude surface reflection dominates (and is saturated in this figure). At polar angle large enough to miss the surface reflection, the scattered signal gets very small, but exhibits peaks at azimuthal angles where the angle of incidence is perpendicular to a fiber direction in the laminate. For a unidirectional panel, where the fibers are positioned along the 0° direction, there are backscattering peaks at ϕ equal to 90° and 270°, i.e., at angles where the sound beam is perpendicular to the 0° fibers, from either side. Similarly, for the cross-ply panel, backscatter peaks occur at 90° and 270°, corresponding to the 0° fibers, and at 180° and 360°, corresponding to the 90° fibers. For the quasi-isotropic laminate, there are eight backscattering peaks corresponding to angles perpendicular to the four different fiber directions, separated by 45° increments.
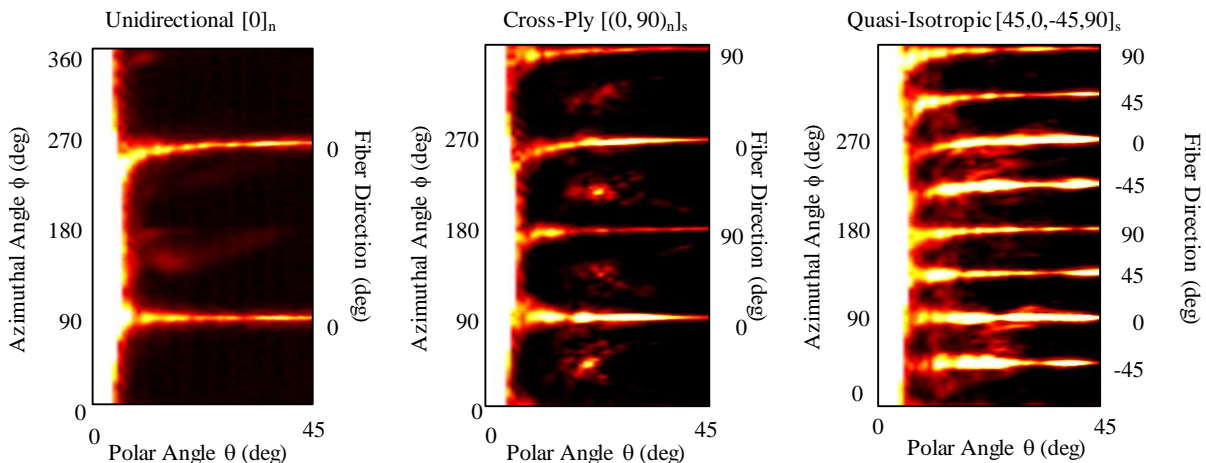
Figure 5.6-23. Polar backscatter from three different ply layups.
Unidirectional (all fibers lying in the 0° direction), cross-ply (fiber direction alternating between 0° and 90°), and quasi-isotropic (fiber directions including 0°, 90°, and ±45°). Note: The signals located between fiber directions in the cross-ply image arise from the bleeder cloth impression on the surface of the composite. The surfaces of the unidirectional and the quasi-isotropic panel were smooth.

173

Figure 5.6-24 presents data obtained from a laminate containing intentional in-plane fiber waviness. During hand layup of a quasi-isotropic specimen, the surface ply was subjected to shearing forces, resulting in a sine-wave-like distortion in that ply. A photograph of the cured laminate is shown on the left-hand side of Figure 5.6-24. Polar backscatter measurements were made at points along a line parallel to the nominal direction of the surface ply. At each point, the azimuthal angle was scanned through 0°−360°, holding the polar angle at 25°. On the right-hand side of Figure 5.6-24, the polar backscatter peaks arising from the surface ply are observed to vary in angle as the measurements moved along the path. Backscatter from the deeper non-wavy plies remain at constant angles.
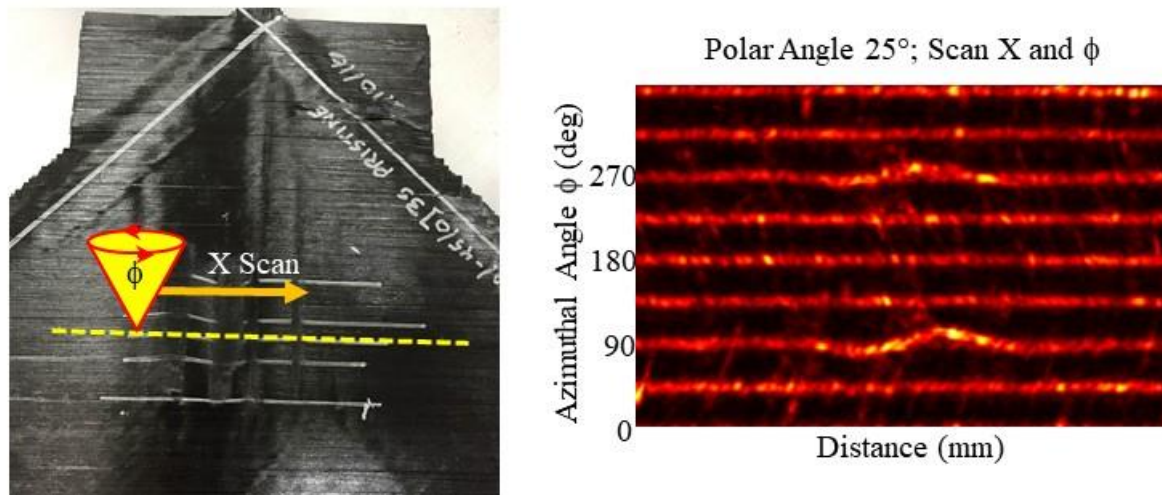
Figure 5.6-24. Polar backscatter measurement of wavy fibers.
The left-hand side is a photograph of a laminate in which the surface ply contains intentional waviness. Polar backscatter measurements were made over azimuthal angles 0•−360• along the dashed yellow line, with a fixed polar angle of 25•. The azimuthal-distance plot of backscatter is shown on the right-hand side. The wavy surface ply results in backscatter appearing at variable azimuthal angle. Undisturbed lower plies appear at constant angles.

The inclusion of polar backscatter scans together with a normal-incidence scan provides a more complete understanding of the damage state of the composite laminate than the normal-incidence scan alone. However, either mechanical positioning of the transducer at different angles and repeatedly scanning the same area repeatedly, or remaining at a single point while scanning through azimuthal and/or polar angles, are not satisfactory approaches for practical inspections.

5.6.5.2 Polar Backscatter Using Two-Dimensional Arrays

When the concept of polar backscatter was first identified and studied in the 1980s, the use of phased array ultrasonics had not yet migrated substantially from medical applications into the realm of NDI. Cost-per-channel for multiple channel systems was prohibitive, and technical limitations existed. Therefore, even if imagined, those polar backscatter measurements could have been implemented using multi-dimensional arrays; it was not yet practical to attempt to do so.

Over the decades since, many things have changed. Technological advances in computational capacity and speed, RF electronics (signal-to-noise, bandwidth, miniaturization), transducer array manufacturing, mechanical manufacturing (CAD, computer-aided machining, 3D printing), etc.,

174

have enabled the realization of practical multidimensional ultrasonic arrays. Just as importantly, application of ultrasonic phased array to NDE has become widely accepted as emerging, if not mainstream.

In this environment, the ACP began exploring the ultrasonic array approach for polar backscatter in an immersion system. The concept is illustrated in Figure 5.6-25. An array, shaped as a portion of the surface of a sphere, is populated with some number of ultrasonic transducer elements. An element (or set of elements) at the center of the array are used to perform a conventional normal-incidence pulse-echo measurement (Figure 5.6-25a). In rapid succession, backscatter measurements are made using elements (or sets of elements) positioned on the array at an appropriate non-zero polar angle, and at a sequence of azimuthal angles (Figure 5.6-25b–d).
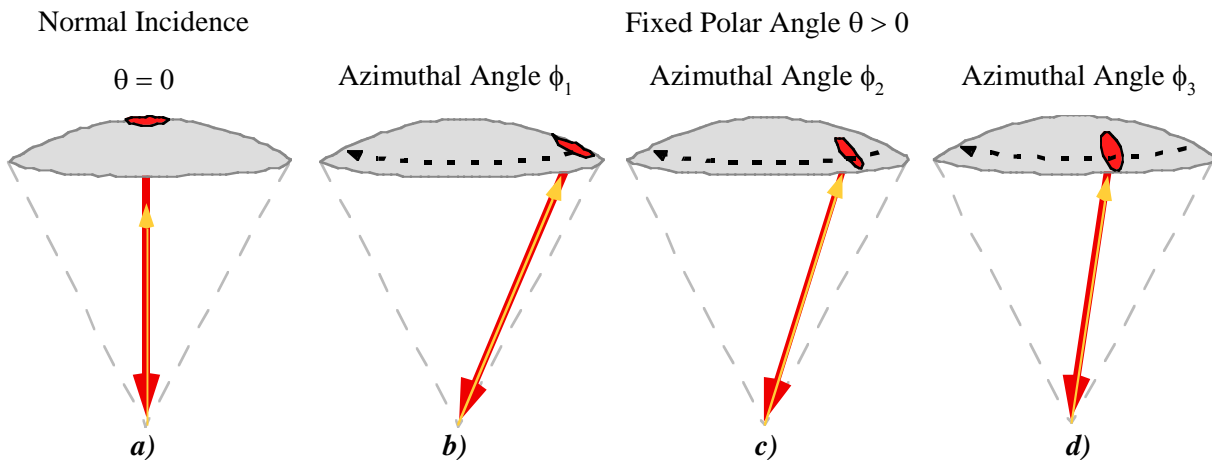
Figure 5.6-25. Concept for performing polar backscatter measurements using 2D ultrasonic array. The array, as imagined, can perform standard, normal-incidence pulse-echo measurements using its central element(s), while elements around the perimeter, at a non-zero polar angle, can sequentially measure polar backscatter as a function of azimuthal angle.

5.6.5.3 References

1. Bar-Cohen, Y.; and Crane, R. L.: "Acoustic Backscattering Imaging of Subcritical Flaws in Composites," *Materials Evaluation*, 40, pp. 970-975, 1982.
2. Van Dreumel, W. H. M.; and Speijer, J. L.: "Non-destructive composite laminate characterization by means of ultrasonic polar-scan," *Materials Evaluation* 39, pp. 922–925, 1981.
3. Bar-Cohen, Y.; and Mal, A. K.: "Characterization of Composite Laminates Using Combined LLW and PBS Methods," *Review of Progress in Quantitative Nondestructive Evaluation* 10B, pp. 1555-1560, 1991.
4. Johnston, P. H.: "Ultrasonic Polar Backscattering for NDE of Stitched Graphite-Epoxy Composites," *Proc. IEEE International Ultrasonics Symposium*, pp. 819-824, 1992.
5. Kersemans, M.; Van Paepegem, W.; Lemmens, B.; Van Den Abeele, K.; Pyl, L.; Zastavnik, F.; Sol, H.; and Degrieck, J.: "The Pulsed Ultrasonic Backscatter Polar Scan and its Applications for NDT and Material Characterization," *Experimental Mechanics*, 54, pp. 1059–1071, 2014.
6. Johnston, P. H.; Appleget, C. D.; and Odarczenko, M. T.: "Characterization of Delaminations and Transverse Matrix Cracks in Composite Laminates Using Multiple-Angle Ultrasonic Inspection," *Review of Progress in Quantitative Nondestructive Evaluation*, 32B, pp. 1011-1018, 2012.

7. Handley, S. M.; Miller, J. G.; and Madaras, E. I.: "Effects of Bleeder Cloth Impressions on the Use of Polar Backscatter to Detect Porosity," *Review of Progress in Quantitative Nondestructive Evaluation*, 8B, pp. 1581-1587, 1989.
8. Madaras, E. I.; Brush, E. F.; Bridal, S. L.; Holland, M. R.; and Miller, J. G.: "Measured Effects of Surface Cloth Impressions on Polar Backscatter and Comparison with a Reflection Grating Model," *Review of Progress in Quantitative Nondestructive Evaluation*, 12B, pp. 1799-1806, 1993.
9. Smith, B. T.; Heyman, J. S.; Buoncristiani, A. M.; Blodgett, E. D.; Miller, J. G.; and Freeman, S. M.: "Correlation of the Deply Technique with Ultrasonic Imaging of Impact Damage in Graphite-Epoxy Composites," Materials Evaluation 47, pp. 1408-1416, 1989.
10. Qu, J.; and Achenbach, J. D.: "Backscatter From Porosity in Cross-Ply Composites," *Review of Progress in Quantitative Nondestructive Evaluation*, 7B, pp. 1029-1036, 1988.
11. Roberts, Ronald A.: "Characterization of Porosity in Continuous Fiber-Reinforced Composites with Ultrasonic Backscatter," *Review of Progress in Quantitative Nondestructive Evaluation*, 7B, pp. 1053-1062, 1988.
12. Gorman, M. R.: "Ultrasonic Polar Backscatter Imaging of Transverse Matrix Cracks," *J. of Composite Materials,* 25, pp. 1499-1514, 1991.
13. Aymerich, F.; and Meili, S.: "Ultrasonic Evaluation of Matrix Damage in Impacted Composite Laminates," *Composites: Part B*, 31, pp. 1-6, 2000.

5.6.6   Guided Wave Ultrasound (GWUT)

5.6.6.1   Introduction to NDE Applications of Ultrasonic Guided Waves in Composites

Guided waves can be used to scan a composite to detect defects and damage either in a water tank or with special wedge contact transducers. By using transducers permanently mounted onto composite structures, guided waves can be employed in-situ to perform SHM. Guided wave techniques have been shown to be effective for damage detection in plate-like metallic and composite structures due to their ability to inspect a large area while maintaining sensitivity to small defects in the structure [refs. 1−6]. Guided waves are ultrasonic waves that propagate along waveguides by its boundaries (e.g., pipes, rods, and plate-like structures), which allows the waves to propagate a long distance with little energy loss. When propagating in thin-wall structures they are often referred to as Lamb waves. Advances in guided wave-based NDE technologies over the last decade have demonstrated the feasibility of detecting and locating damage in composite structural components [refs. 7−21].

The fundamental of guided wave NDE of damage detection consists of evaluating the characteristics of wave propagation along the wave path between wave actuator and receiver, as illustrated in Figure 5.6-26a. Prior work has found that subsurface damage will affect various characteristics of the interrogation waves (such as amplitude and travelling propagation time). In addition, this damage can cause wave scattering, mode conversion, and multiple reflections in the delamination region. Compared to guided waves in isotropic materials, wave propagation in composite structures presents additional complexity for efficient damage identification [ref. 22]. The guided wave complexity increases significantly due to anisotropic and inhomogeneous properties inherent in composite materials (Figure 5.6-26b). In addition, defects in composites are often unique. For example, when ultrasonic waves propagate in a delaminated composite, multiple reflections within the delamination region can occur, as shown in references [refs. 23−27]. Therefore, a considerable amount of ultrasonic energy can be "trapped" above, below, and between

delaminated regions until eventually, the energy dissipates [ref. 28]. and As a result, quite often the traditional metal-based guided wave NDE methods are inappropriate, sometimes even misleading [refs. 29−31], and shall should be modified toward for applications in composite structures.
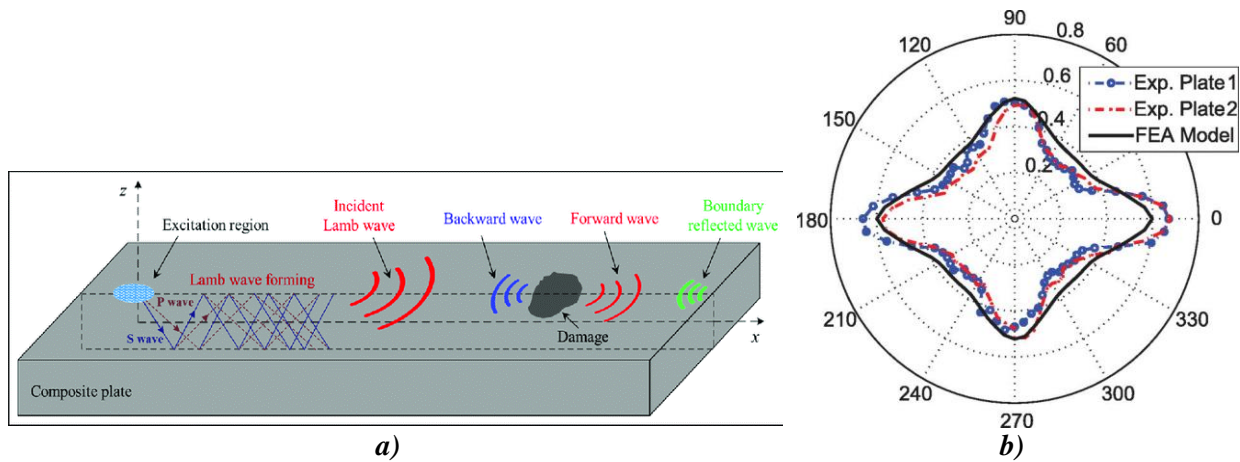
Figure 5.6-26. Guided wave NDE inspection method for composites.
a) Illustration of guided waves inspection method [ref. 33], b) guided waves in composites is highly directional compared to omnidirectional in metal structures [ref. 34].

To initiate and detect guided wave on CFRP composites, utilization of a variety of transducers, such as wedge transducers, air-coupled transducer, piezoelectric thin wafers, fiber optics, and laser transducers are used. One of the most commonly used guided wave transducers is the wafer-type piezoelectric sensors (referred to PZT in the rest of this section) [ref. 32]. As a laboratory tool to remotely (non-contact) characterize guided wave propagation, the scanning laser Doppler vibrometer (SLDV) has been successfully used as a means for non-contact remote sensing in ultrasonic wavefield measurement due to the fact that these systems can make non-contact accurate surface velocity or displacement measurements over a spatially dense grid and provide high time and spatial resolution image sequences of wave propagation [ref. 32]. The wave propagation visualization provides deeper understanding of Lamb waves in the structures and their interactions with structural features. However, they are not applicable as part of an *in situ* monitoring system for aircraft. Other than being a non-intrusive method, the specific benefit of the SLDV over other ultrasonic sensors is that SLVD can provide rapid and precise measurements of all the scanning points with a very high spatial resolution [ref. 32].

5.6.6.2 PZT-SLDV Guided Wave Techniques for Composites NDE

5.6.6.2.1 Experimental setup

The PZT-SLDV system described in the following was implemented utilized to inspect the 14 chosen standards in the Handbook study. The chosen standards included porosity and delaminations in flat plates and radii for layered laminates and woven CFRP as well as specimens with embedded wrinkles. The system employed one contact type PZT as an actuator to excite guided waves in the testing plate specimens. Traditionally, the PZT bonds to the surface of the specimen using chemical adhesives, and it can generate guided waves by coupling its in-plane motion with the structure through the adhesive layer [ref. 5]. For the guided wave sensing and visualization, a noncontact, rapid and high-spatial-resolution SLDV was employed. The Displacement or velocity of the particle motion was measured along the laser beam based on the

Doppler effect. The SLDV is capable of scanning a predefined area by directing the laser beam to multiple points through two mirrors inside the laser head driven by galvanometric actuators.

Shown in Figure 5.6-27, is the schematic design of the PZT-SLDV system. The excitation signal (e.g., Hanning window modulated N-count sine waves) is generated by an arbitrary waveform generator (AWG) and amplified through a voltage amplifier. The SLDV is synchronized with the AWG and the guided waves (velocity/displacement with respect to recorded time) at each scanning point are captured for post-processing and analysis. The scan is user predefined so that various configurations, such as line distribution for 1D scanning and rectangular grid distribution for 2D scanning, can be achieved.
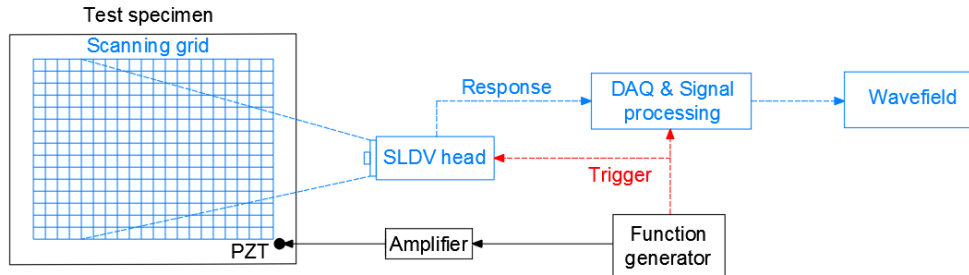
Figure 5.6-27. PZT-SLDV system layout [ref. 32].

5.6.6.3   Implementation Considerations

Traditionally, the PZT would be bonded to the surface of the specimen using an adhesive, which serves to couple the sensors in-plane motion into the structure [ref. 5]. Also, reflective tape would be applied on the sensing surface to improve the SLDV signal quality [ref. 32]. However, for aeronautic applications, additions of foreign materials to the existing composite structures would not be permitted. Also, removing the PZT or the tape could modify the condition of the structure surface. Hence, a completely non-invasive PZT-SLDV installation and setup was necessary. Commercially available honey was used as the couplant for the PZT with good results. A wipe-off reflective spray for SLDV enhancement, previously developed and validated for the guided wave NDE applications was also used. Using a syringe, a tiny drop of honey is placed at a defined excitation point on the sample. Then, the PZT is carefully placed at the honey drop and gentle pressure is applied to evenly distribute the honey on the contact surface between the PZT and the plate. Removable tape affixing the PZT wires on the specimen to guarantee the PZT rests firmly on the target point is used. Figure 5.6-28a shows the finished setup for using honey to attach the PZT.

a)   *b)*
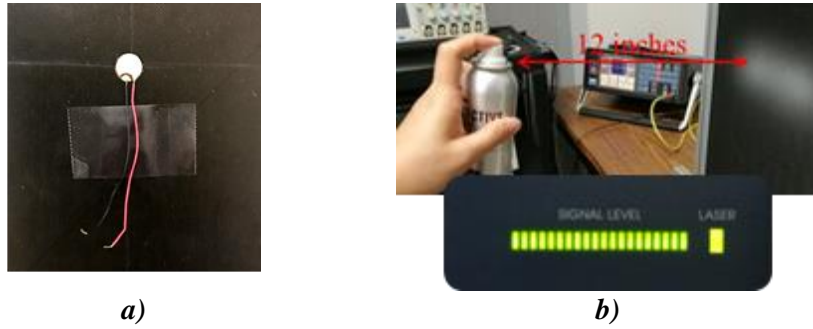
Figure 5.6-28. Noninvasive PZT-SLDV system setup.
a) PZT attached using honey couplant, b) spray applying illustration and related signal strength.

On the SLDV sensing side, wipe-off type reflective spray (Figure 5.6-28b) was selected and tested. To apply, the spray nozzle is held twelve inches away normal to the specimen surface (Figure 5.6-28b). Application of approximately 20 layers of spray is suggested to give a full-signal level on the laser head indicating that the SLDV has achieved good signal quality.

5.6.6.4   Inspection method

For guided wave inspection with PZT-SLDV system, line inspection (measurements along a straight line) and area inspection (measurements along a rectangular grid) is performed rapidly. The user can select the spatial distance between the points and how many points to measure. The arrangement of inspection on composite structures indeed is material and sample composition dependent. The explanation will be easy by using a specific sample that is reported in Appendix E. The wrinkle sample A1 is used in the subsequent description. Sample A1 is a 26.5- $\times$ 30.6- $\times$ 0.4-cm CFRP solid laminate with imbedded wrinkles. A typical wrinkle example is shown below in Figure 5.6-29. More details of A1 are found in Appendix D.
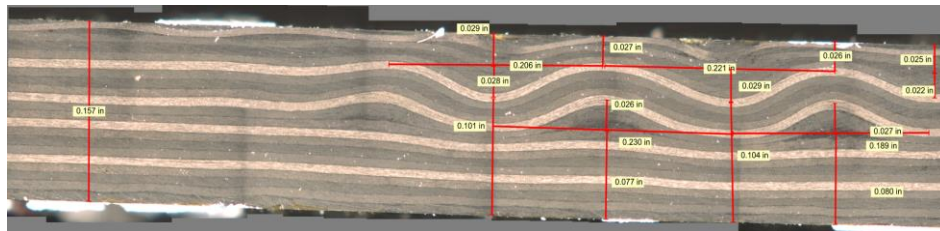
Figure 5.6-29. Cross-section of typical wrinkle specimen showing imbedded ply wrinkles.

To assist subsequent data analysis algorithms, it is recommended to define a Cartesian coordinate in the sample first. The predefined coordinates is shown in Figure 5.6-30. Two regions are usually selected for inspection: reference (marked as red) and defected (wrinkle in this case, marked as green) region. The wrinkling creates a local change in the form of the stiffness matrix and can also lead to resin rich regions. Overall, this means a local change in material properties that affects wave propagation. Before inspection, the plate's dispersion curves need to be acquired, either through theoretical study, if material properties are known, or experimentally by line scanning using a chirp excitation. Multiple scans are recommended to get more accurate velocity information along different direction of the plate, such as the three line scanning approach performed for A1. The inspection can be along various fiber directions, such as 0°/180° direction (Figure 5.6-30a), or along 90° (Figure 5.6-31a).

179
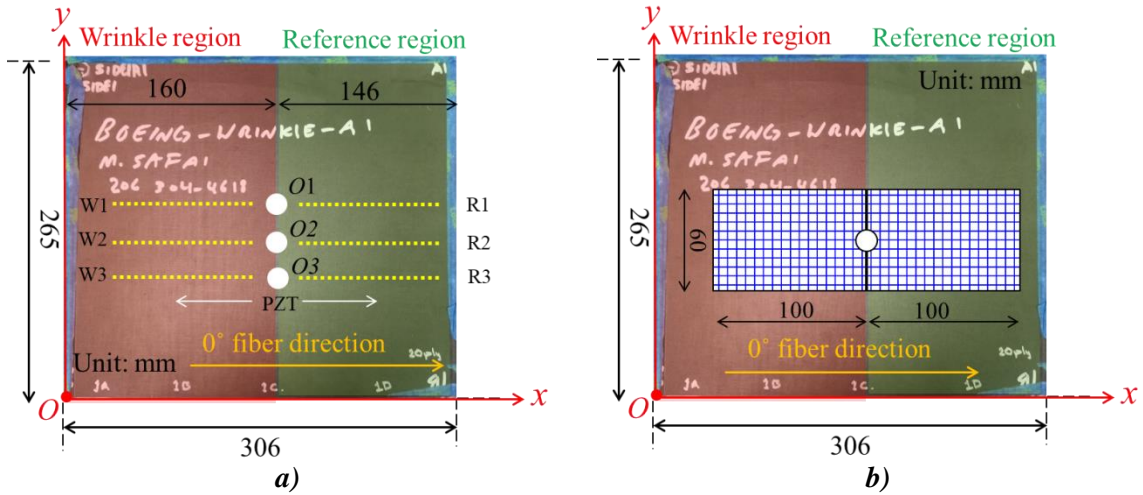
***Figure 5.6-30. Experimental setup for specimen A1 along 0°/180° direction w.r.t actuation on side 1.
a) Line inspection and b) area inspection.***

Performing an area scan will give a quick overall inspection. For A1, location O_2 is selected as the excitation point, and a rectangular area scan is performed in the area 60 mm × 100 mm (Figure 5.6-30b) with 1-mm spatial resolution. It can also be performed separately in a reference and defected region as illustrated in Figure 5.6-31b.
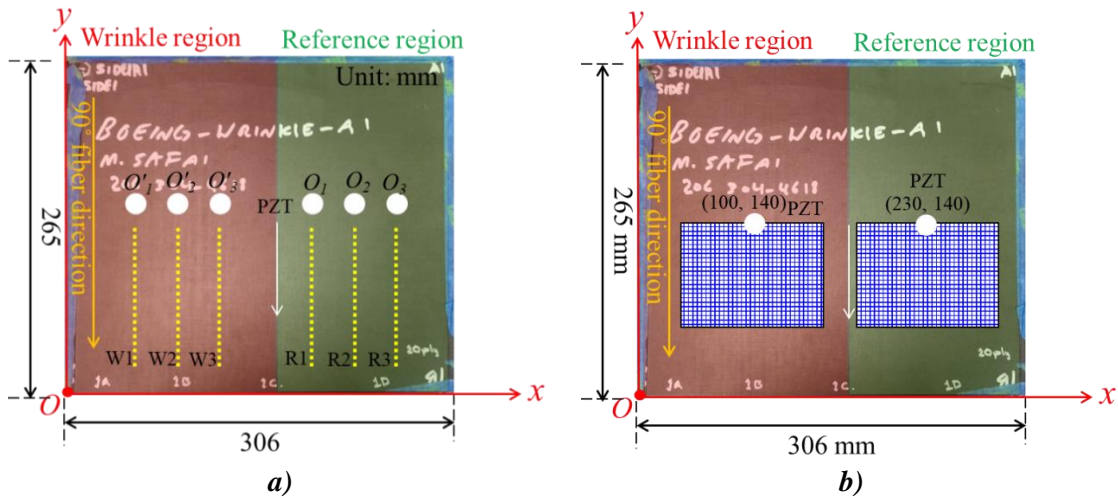
***Figure 5.6-31. Experimental setup for specimen A1 along 90°/270° w.r.t actuation on side 1.
a) Line inspection and (b) area inspection.***

5.6.6.5 Analysis methodologies

5.6.6.5.1 *Line scan data analysis*

With wavefield data acquired by line scan (2D data) or area scan (3D data), various signal processing methods can be reported in literatures that can be applied to analyze the data. In this study, multidimensional Fourier analysis based methods are used. For line scanned data (2D data), they are presented as the time-space wave motion velocity wavefields as $v(t, x)$. Here, t is time

and x is the space information along the scanning line. The frequency-wavenumber spectrum $v(f,k)$ are obtained through 2D Fourier transform [ref. 32], as

$$v(f,k) = \int_{-\infty}^{\infty} \int_{-\infty}^{\infty} v(t,x) e^{-j(2\pi ft - k \cdot x)} \mathrm{d}t \mathrm{d}x \qquad \text{Equation 11}$$

By examining the wavefields directly or the frequency-wavenumber representations, differences are identified in regions where a defect is present as compared to those acquired where there is no defect. Examples of wavefields produced by line scans and the corresponding frequency-wavenumber representations obtained for the specimen with wrinkle defects are given in Figure 5.6-32.

a)   *b)*
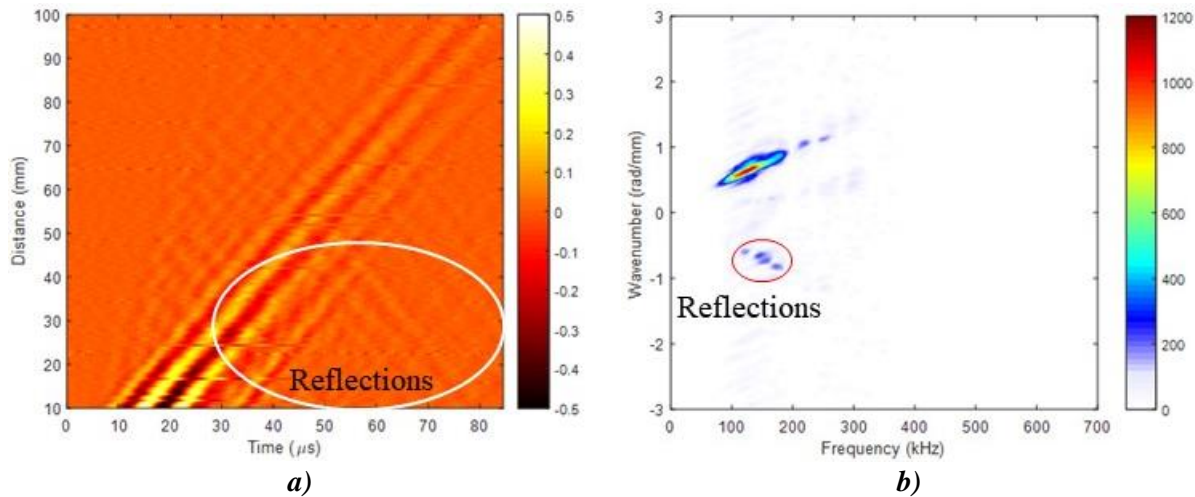
Figure 5.6-32. Examples of wavefields and corresponding frequency-wavenumber representations obtained for specimen with wrinkle defects.
Examples of data in a) time-space original domain as wavefield showing weak reflections caused by wrinkle, where the color scale represents the amplitude of the wavefield and b) frequency-wavenumber representation after Fourier transform indicating the presence of reflections as components with negative wavenumbers, where the scale represents the frequency wavenumber amplitude.

Although the frequency-wavenumber analysis provides the frequency and wavenumber information, the spatial information is lost during the process, which would show the location of the structural defect that causes the wavenumber change. To address this issue, a short space Fourier transform can be used to retain the spatial information through a windowing process [ref. 32], resulting in a space-frequency-wavenumber spectrum. An example of the resulting spatial distribution of wavenumber in a wrinkle specimen is given in Figure 5.6-33. The incident wave mode is defined as Mode1$^+$, and the corresponding reflected wave mode as Mode1$^-$. It shows the reflections caused by the wrinkles start at 50 mm, determining the location of the wrinkle defect indication.
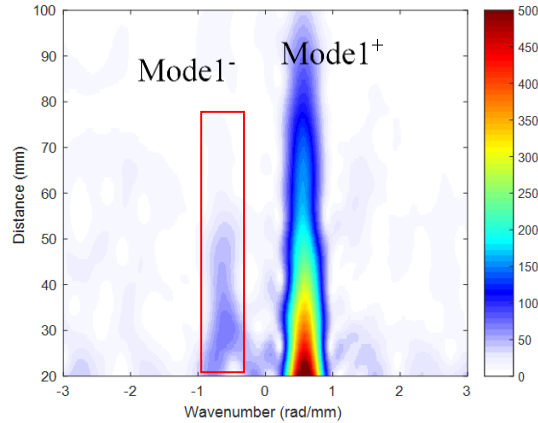
Figure 5.6-33. Short-space Fourier transform shows wavenumber changes as a wave propagates. Mode1⁺ is the incident wave mode and Mode1⁻ is the corresponding reflected wave mode. The reflections caused by the wrinkles start at 50 mm, quantifying the location of the wrinkle defect indication.

5.6.6.5.2   *Area scan data analysis*

To obtain more information and observe the wave propagation directly and more clearly, an area scan is performed, although at the cost of longer inspection time and longer data processing time.

With an area scan, the 3D time-space wavefield $v(t, \mathbf{x})$ are obtained. Here, t is time and $\mathbf{x}$ is the space vector (x, y). Snapshots of the wavefield in the wrinkle sample A1 at 22 microseconds (µs) and 60 µs is illustrated in Figure 5.2-34 as examples. In the wavefield at 22 µs, first mode arrives at the wrinkle area and mode conversions (change of wavelength) are observed. Alternatively, in the wavefield at 60 µs, obvious reflections are observed in the wrinkle region. Hence, images generated from the area scan wavefield directly can indicate the presence of defects such as the wrinkles in sample A1.

a)   *b)*
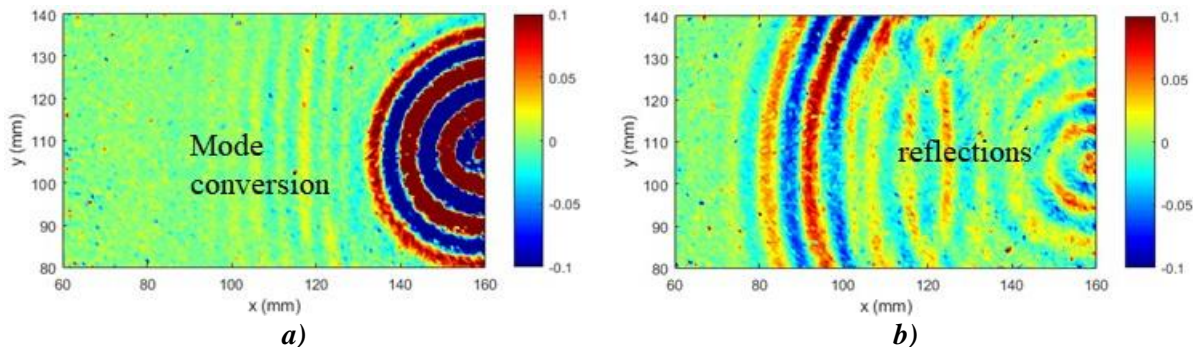
Figure 5.6-34. Wavefield of wrinkle standard A1.
a) At 22 μm. The first mode arrives at the wrinkle are and mode conversions are observed and
b) 60 μm. Refections are observed in the wrinkle region.

The limitation with the wavefield images is that frames are recorded at multiple time stamps and are hard for inexperienced operators to identify or extract for damage detection. A simple but

effective imaging method was developed by presenting the energy distribution on the subject plate using the entire wavefield data. The algorithm is simply:

$$v_{mag}(\mathbf{x}) = \max\left(\text{abs}\left(v(t,\mathbf{x})\right)\right)$$

Equation 12

which defines the pixel values at a spatial location **x**. Figure 5.6-35 shows an example of the generated image. A clear wrinkle pattern is observed in the wrinkle region, while no obvious wrinkle pattern is observed in the reference region.

Figure 5.6-35. Energy image indicating and profiling the region of wrinkles (red rectangle) using the entire wavefield data.

5.6.6.6 Alternative Noncontact Excitation Source for Guided Wave NDE

Alternative to the PZT-SLDV system, the guided wave NDE can also be implemented through other methods such as the newly d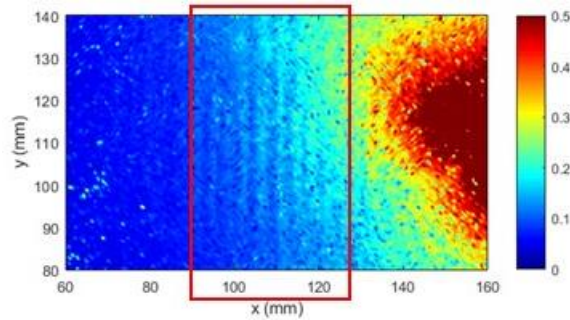eveloped and fully noncontact air-coupled transducer (ACT)-SLDV system. The overall setup is similar except that the PZT is replaced with ACT for Lamb wave excitation. The fundamental difference between ACT-SLDV and PZT-SLDV systems is that the former excites highly narrow-band Lamb waves focused around 120 kHz while the latter can be operated over a wide range of excitation frequencies and the resulting Lamb waves often have wider bandwidth.

As a non-contact type actuation, ACT uses the air as the couplant between the transducer and the specimen and excites the Lamb waves in plate based on Snell's law [ref. 33]. The typical overall schematic setup of the ACT-SLDV is given in Figure 5.7-36a, and the notations of the main parameters (focal length *d*, incident angle *θ*, sampling spatial resolution Δ*x*, etc.) of the ACT-SLDV system are given in Figure 5.6-36b. An ACT with a center frequency at 120 kHz and a bandwidth from 113 kHz to 125 kHz is used for the A1 wrinkle specimen inspection as an example.

For ACT actuation of Lamb waves, the ACT incident angle, θ, with respect to the normal of the plate is a critical parameter. It determines what Lamb wave mode is actuated in the subject plate for a given ACT resonant frequency. Theoretical dispersion relations can be used to provide an initial indication of incident angles appropriate for particular modes. Then, when testing, the angle can be tuned experimentally to provide optimal excitation. For the A1 specimen, the angle θ tuning finds that strongest A0 mode actuation is achieved when angle θ is set at 15° for both 0° and 90° fiber directions excitations.

a)   *b)*
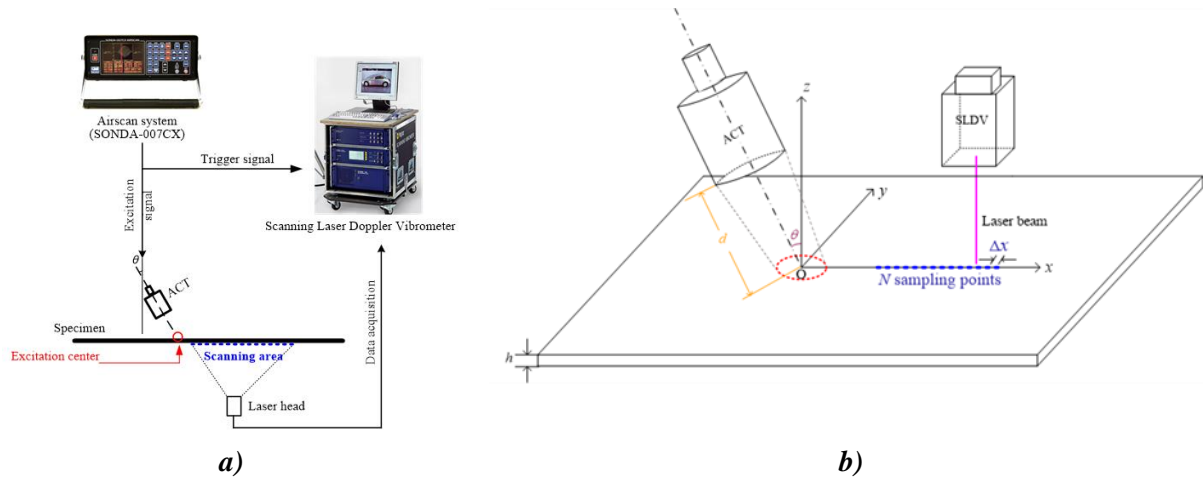
Figure 5.6-36. ACT-SLDV setup.
a) System layout and b) notations used in the ACT-SLDV system.

Similar to the data acquisition and analysis used by the PZT-SLDV system, line scan of ACT-SLDV Lamb waves and corresponding frequency-wavenumber spectrum on the A1 wrinkle sample is obtained, as shown in Figure 5.6-37. Compared to those acquired by PZT-SLDV system, the bandwidth of this excitation is significantly narrower. The energy map using the entire wavefield data to detect wrinkle indications is given in Figure 5.6-38. Though weaker compared to PZT-SLDV (since ACT actuation is much less efficient compared to PZT's), the wrinkle area is successfully detected by the fully non-contact ACT-SLDV system.

a)   *b)*
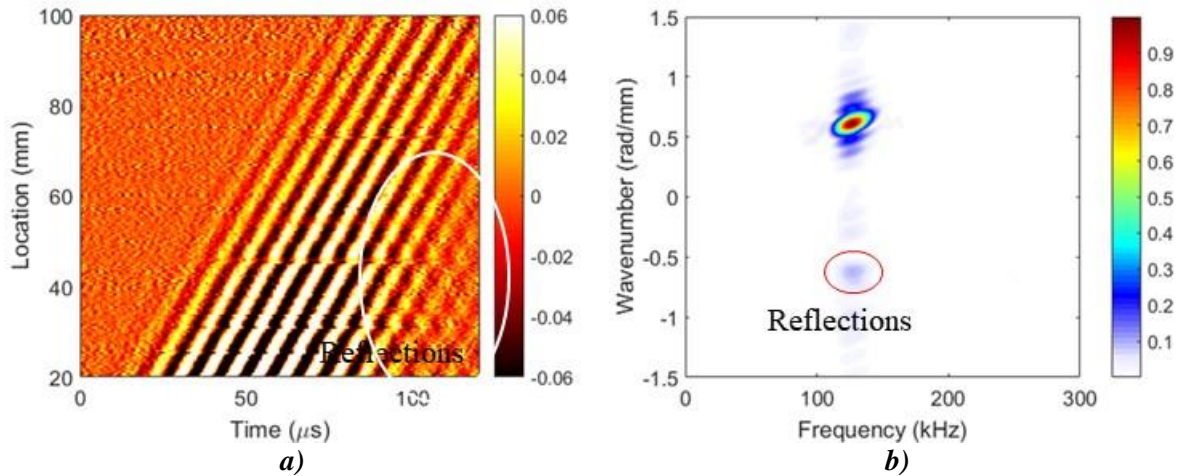
Figure 5.6-37. Examples of ACT-SLDV data.
a) In time-space original domain as wavefield showing weak reflections caused by wrinkle, and
b) frequency-wavenumber representation after Fourier transform indicating the presence of reflections
as components with negative wavenumbers.

184
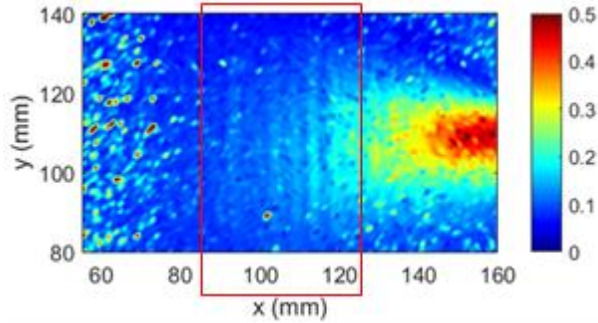
Figure 5.6-38. Energy image generated by ACT-SLDV system indicating and profiling wrinkles.

5.6.6.7 References

1. Alleyne, D. N.; and Cawley, P.: "The Interaction of Lamb Waves with Defects," *IEEE Transactions on Ultrasonics Ferroelectrics and Frequency Control*, vol. 39, pp. 381-397, 1992.
2. Rose, J. L.: *Ultrasonic Waves in Solid Media*, Cambridge: Cambridge University Press, 1999.
3. Boller, C.: "Next Generation Structural Health Monitoring and Its Integration into Aircraft Design," *International Journal of Systems Science*, vol. 31, pp. 1333-1349, 2000.
4. Staszewski, W. J.; Boller, C.; and Tomlinson, G. R.: *Health Monitoring of Aerospace Structures*, Chichester: John Wiley and Sons, 2004.
5. Giurgiutiu, V.: *Structural Health Monitoring with Piezoelectric Wafer Active Sensors*, Boston, MA: Academic Press, 2008.
6. Ong, W. H.; and Chiu, W. K.: "Redirection of Lamb Waves for Structural Health Monitoring," *Smart Materials Research*, vol. 2012, p. 718686, 2012.
7. Wang, L.; and Yuan, F. G.: "Group Velocity and Characteristic Wave Curves of Lamb Waves in Composites: Modeling and Experiments," *Composites Science and Technology*, vol. 67, pp. 1370-1384, Jun 2007.
8. Kundu, T.; Das, S.; Martin, S. A.; and Jata, K. V.: "Locating Point of Impact in Anisotropic Fiber Reinforced Composite Plates," *Ultrasonics*, vol. 48, pp. 193-201, Jul 2008.
9. Su, Z. Q.; Cheng, L.; Wang, X. M.; Yu, L.; and Zhou, C.: "Predicting Delamination of Composite Laminates Using an Imaging Approach," *Smart Materials and Structures*, vol. 18, p. 074002, Jul 2009.
10. Castaings, M.; and Hosten, B.: "Ultrasonic Guided Waves for Health Monitoring of High-Pressure Composite Tanks," *Ndt and E International*, vol. 41, pp. 648-655, Dec 2008.
11. Salamone, S.; Bartoli, I.; di Scalea, F. L.; and Coccia, S.: "Guided-Wave Health Monitoring of Aircraft Composite Panels under Changing Temperature," *Journal of Intelligent Material Systems and Structures*, vol. 20, pp. 1079-1090, Jun 2009.
12. Salas, K. I.; and Cesnik, C. E. S.: "Guided Wave Structural Health Monitoring Using Clover Transducers in Composite Materials," *Smart Materials and Structures*, vol. 19, p. 015014, Jan 2010.
13. Song, F.; Huang, G. L.; and Hu, G. K.: "Online Guided Wave-Based Debonding Detection in Honeycomb Sandwich Structures," *Aiaa Journal*, vol. 50, pp. 284-293, 2012.
14. Giurgiutiu, V.; and Soutis, C.: "Enhanced Composites Integrity through Structural Health Monitoring," *Applied Composite Materials*, vol. 19, pp. 813-829, 2012.

15. Leckey, C. A. C.; Rogge, M. D.; and Parker, R.: "Guided Waves in Anisotropic and Quasi-Isotropic Aerospace Composites: Three-Dimensional Simulation and Experiment," *Ultrasonics*, vol. 54, pp. 385-394, 2014.
16. Guo, N.; and Cawley, P.: "The Interaction of Lamb Waves with Delaminations in Composite Laminates," *Journal of Acoustic Society of America*, vol. 94, pp. 2240-2246, 1993.
17. Petculescu, G.; Krishnaswamy, S.; and Achenbach, J. D.: "Group Delay Measurements Using Modally Selective Lamb Wave Transducers for Detection and Sizing of Delaminations in Composites," *Smart Materials and Structures*, vol. 17, p. 015007, Feb 2008.
18. Purekar, A. S.; and Pines, D. J.: "Damage Detection in Thin Composite Laminates Using Piezoelectric Phased Sensor Arrays and Guided Lamb Wave Interrogation," *Journal of Intelligent Material Systems and Structures*, vol. 21, pp. 995-1010, Jul 2010.
19. Michaels, T. E.; Michaels, J. E.; and Ruzzene, M.; "Frequency-Wavenumber Domain Analysis of Guided Wavefields," *Ultrasonics*, vol. 51, pp. 452-466, 2011.
20. Yeum, C. M.; Sohn, H.; Ihn, J. B.; and Lim, H. J.: "Instantaneous Delamination Detection in a Composite Plate Using a Dual Piezoelectric Transducer Network," *Composite Structures*, vol. 94, pp. 3490-3499, 2012.
21. Rogge, M. D.; and Leckey, C. A. C.: "Characterization of Impact Damage in Composite Laminates Using Guided Wavefield Imaging and Local Wavenumber Domain Analysis," *Ultrasonics*, vol. 53, pp. 1217-1226, 2013.
22. Ricci, F.; Mal, A. K.; Monaco, E.; Maio, L.; Boffa, N. D.; Di Palma, M.; and Lecce, L.: "Guided Waves in Layered Plate with Delaminations," presented at the *Proceedings of 7th European Workshop on Structural Health Monitoring*, La Cite, Nantes, France, 2014.
23. Hayashi, T.; and Kawashima, K.: "Multiple Reflections of Lamb Waves at a Delamination," *Ultrasonics*, vol. 40, pp. 193-197, 2002.
24. Ramadas, C.; Balasubramaniam, K.; Joshi, M.; and Krishnamurthy, C. V.: "Interaction of the Primary Anti-Symmetric Lamb Mode (A0) with Symmetric Delaminations: Numerical and Experimental Studies," *Smart Materials and Structures*, vol. 18, p. 085011, Aug 2009.
25. Sohn, H.; Dutta, D.; Yang, J. Y.; Park, H. J.; DeSimio, M. P.; Olson, S. E.; and Swenson, E. D.: "Delamination Detection in Composites through Guided Wave Field Image Processing," *Composites Science and Technology*, vol. 71, pp. 1250-1256, 2011.
26. Sohn, H.; Dutta, D.; Yang, J. Y.; DeSimio, M.; Olson, S.; and Swenson, E.: "Automated Detection of Delamination and Disbond from Wavefield Images Obtained Using a Scanning Laser Vibrometer," *Smart Materials and Structures*, vol. 20, p. 045017, 2011.
27. Glushkov, E.; Glushakova, N.; Golub, M. V.; Moll, J.; and Fritzen, C. P.: "Wave Energy Trapping and Localization in a Plate with a Delamination," *Smart Materials and Structures*, vol. 21, p. 125001, 2012.
28. Tian, Z.; Yu, L.; Lecky, C.C.: "Guided Wave Imaging for Detection and Evaluation of Impact Induced Delamination in Composites," *Smart Materials and Structures*, Vol. 24, No. 10, 2015.
29. Su, Z. Q.; Cheng, L.; Wang, X. M.; Yu, L.; and Zhou, C.: "Predicting Delamination of Composite Laminates Using an Imaging Approach," *Smart Materials and Structures*, vol. 18, p. 074002, Jul 2009.
30. Castaings, M.; and Hosten, B.: "Ultrasonic Guided Waves for Health Monitoring of High-Pressure Composite Tanks," *Ndt and E International*, vol. 41, pp. 648-655, Dec 2008.

31. Salamone, S.; Bartoli, I.; di Scalea, F. L.; and Coccia, S.: "Guided-Wave Health Monitoring of Aircraft Composite Panels under Changing Temperature," *Journal of Intelligent Material Systems and Structures*, vol. 20, pp. 1079-1090, Jun 2009.
32. Yu, L.; and Tian, Z.: "Lamb Wave Structural Health Monitoring Using a Hybrid PZT-Laser Vibrometer Approach," *Structural Health Monitoring – an International Journal*, Vol. 12, No. 5-6, pp. 469-483, 2013.
33. Harb, M. S.; and Yuan, F. G.: "Barely Visible Impact Damage Imaging Using Non-Contact Air-Coupled Transducer/Laser Doppler Vibrometer System," *Structural Health Monitoring*, Vol. 16, No. 6, 2016.
34. Murat, B. I. S.; Khalili, P.; and Fromme, P.: "Scattering of Guided Waves at Delaminations in Composite Plates," *Journal of the Acoustical Society of America*, Vol. 139, No. 6, 2016.

5.7   Techniques Not Suitable for Inspection of CFRP Composites

This section describes NDE techniques not typically suitable for inspection of CFRP composites—the focus of this Handbook. Each section briefly describes the technique, discusses why it is not generally suited to inspection of CFRP solid laminate composites, and discusses which composite materials that have been shown to be appropriate for inspection using that particular technique.

5.7.1   Terahertz

The word "terahertz" refers to electromagnetic radiation that has frequencies of approximately 10^{12} Hz. The wavelength of the electromagnetic radiation at that frequency in free space is about 300 µm. In operational use, some terahertz generation mechanisms often produce radiation over rather broad frequencies from as low as 100s of gigahertz (GHz) to several terahertz (THz), which translates into wavelengths of 100 µm to a few mm.

For terahertz radiation, some systems such as Time Domain Reflectometry Systems (TDRS) are used to look at the phase reflected signals or through transmitted signals. Images are built by scanning the transmitter/detector system similar to how ultrasonics is typically applied, including pulse echo and pitch-catch methods. Alternatively, there are terahertz camera systems on the market that can emulate a thermography camera system and hence, would use thermography and optical appropriate data processing methods.

One of the first successful uses of terahertz as an NDE tool was by NASA LaRC as a solution to imaging flaws in sprayed on foam on the Space Shuttles' external tank using a TDRS, which was successfully applied by NASA Marshall Space Flight Center (MSFC) and Michoud Assembly Facility [refs. 1, 2, and 3] (See Figure 5.7-1.). Another NDE application pursued was imaging under the Space Shuttle heat shield tiles and thermal blankets for hidden corrosion and looking for the location of various hidden wing components [ref. 4]. The method is also evaluated for corrosion detection on Al metal surfaces hidden by paint [ref. 5].

a) b)

c)
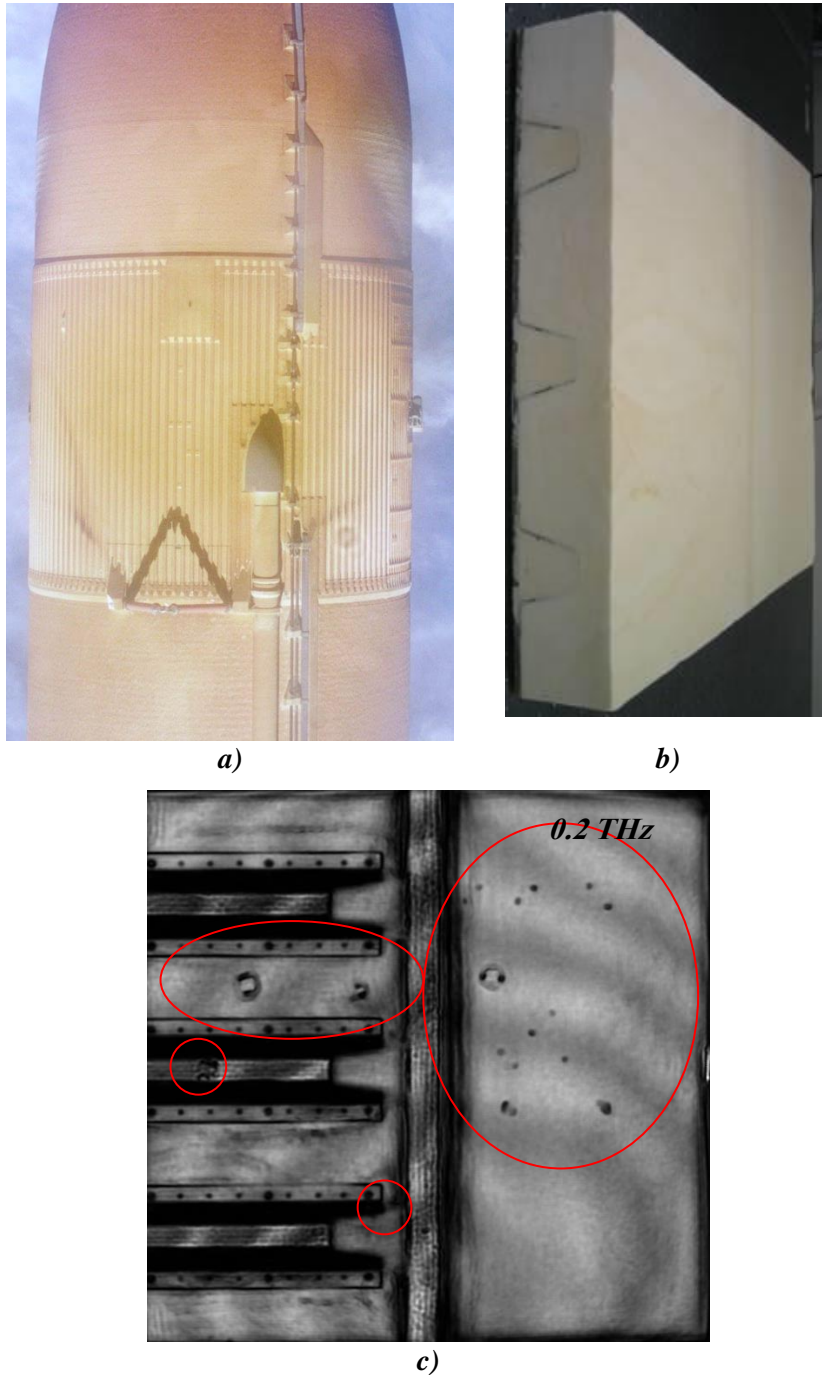
Figure 5.7-1. LaRC use of terahertz as NDE tool as solution to imaging flaws in sprayed-on foam on Space Shuttles' external tank using a TDRS.
a) Section of the space shuttle external tank, b) mockup of a section of the external tank containing manufactured flaws. c) Terahertz image of the mockup section with flaws highlighted with red ovals.

For NDE imaging of composite materials used in aviation, as with any electromagnetic radiation, the radiation's penetration into a material depends on its permittivity properties. For metals or any conducting material, the penetration depth of terahertz is very shallow. Hence, for conducting materials, terahertz imaging is generally surface constrained. Some work by Hsu at Iowa State

University has characterized some of the limitations of the application of terahertz to graphite based composites [ref. 6]. Alternatively, ceramic composites, which are not conductive, were more, fully characterized with terahertz [ref. 4]. Similarly, glass fiber composites will allow the penetration of terahertz into the material [refs. 7 and 8]. Materials like Kevlar and Nomex fabrics are imaged with terahertz for damage [ref. 6]. In aviation, structures such as Radomes are imaged with terahertz, as they are transparent to microwaves. Terahertz radiation can also help in detecting the presence of moisture in Radomes and non-conducting honeycomb layups, and detect the presence of some types of chemicals and foreign materials [ref. 9].

In summary, while terahertz NDE is valuable in many instances, for the purpose of graphite or carbon fiber materials typical of the majority of modern aircraft skins and structures, terahertz NDE imaging is generally not expected to be a major testing modality due to the conductivity of the material and therefore the rather limited penetration of terahertz into composites.

5.7.1.1   References

1. Chiou1, Chien-Ping; Thompson, R. Bruce; Winfree, William P.; Madaras, Eric I.; and Seebo, Jeffrey: "Modeling and Processing of Terahertz Imaging in Space Shuttle External Tank Foam Inspection Review of Progress in Quantitative Nondestructive Evaluation," D. O. Thompson and D. E. Chimenti, eds., v 894, 401-407, 2006.
2. Zimdars, D.; Valdmanis, J. A.; White, J. S.; Stuk, G.; Williamson, S.; Winfree, W. P.; and Madaras, E. I.: "Technology and Applications of Terahertz Imaging Non-Destructive Examination: Inspection of Space Shuttle Sprayed on Foam Insulation," *AIAA*, eds., v. 24A, 570-577, 2005.
3. Winfree, W. P.; and Madaras, E. I.: "Detection and Characterization of Flaws in Sprayed on Foam Insulation with Pulsed Terahertz Frequency Electromagnetic Waves," *41st AIAA/ASME/SAE/ASEE Joint Propulsion Conference and Exhibit*, AIAA-2005-3629, 2005.
4. Anastasi, Robert F.; Madaras, Eric I.; Seebo, Jeffrey P.; Smith, Stephen W.; Lomness, Janice K.; Hintze, Paul E.; Kammerer, Catherine C.; Winfree, William P.; and Russell, Richard W.: "Terahertz NDE Application for Corrosion Detection and Evaluation under Shuttle Tiles," *Proc. SPIE* 6531, 2007.
5. Anastasi Robert F.; and Madaras, Eric I.: "Terahertz NDE for Under Paint Corrosion Detection and Evaluation," *AIP Conference Proceedings* 820, p. 515, 2006.
6. Hsu, David K.; Im, Kwang-Hee; Chiou, Chien-Ping; and Barnard, Daniel J.: "An Exploration of the Utilities of Terahertz Waves for the NDE of Composites," *AIP Conference Proceedings*, 1335, p. 533, 2011.
7. Chady, T.; Lopato, P.; and Szymanik, B.: "Terahertz and Thermal Testing of Glass-Fiber Reinforced Composites with Impact Damages," *Journal of Sensors*, Article ID 954867, 2012.
8. Dong, Junliang; Kim, Byungchil; Locquet, Alexandre; McKeon, Peter; Declercq, Nico; and Citrin, D. S.: "Nondestructive Evaluation of Forced Delamination in Glass Fiber-Reinforced Composites by Terahertz and Ultrasonic Waves," *Composites Part B: Engineering*, v 79, pp 667-675, 2015.
9. Friederich, Fabian; May, Karl Henrik; Baccouche, Bessem; Matheis, Carsten; Bauer, Maris; Jonuscheit, Joachim; Moor, Michael; Denman, David; Bramble, Jamie; and Savage, Nick: "Terahertz Radome Inspection," *Photonics*, v 5, n 1, p 1, 2018.

5.7.2 Eddy Current

Eddy current testing is a well-established technique for NDE of aerospace structures, typically applied to metallic components [refs. 1 and 2]. Commonly used for non-contact conductivity measurements and the detection of surface breaking fatigue cracks in metals, the method relies upon the coupling of an inspection coil with the part under test via a time-varying magnetic field. An alternating current drives the inspection coil, thereby creating an alternating magnetic field near the coil. A conducting object within this field will develop an induced current flow to oppose the changing magnetic flux as explained by Faraday's law of electromagnetic induction [ref. 3], with the strength of the induced surface current proportional to the product of the time rate of change of the magnetic flux and the part conductivity. The shielding effect produced by the surface currents leads to an exponential decay of current density with depth into the part under test, given by the skin depth relationship as:

$$J_x = J_0 \exp(-x/\delta) \qquad \text{Equation 13}$$

$$\delta = 1/\sqrt{\pi f \mu \sigma} \qquad \text{Equation 14}$$

Where J_0 is the current density at the surface of the part in amp/(meter)^2, x is the depth into the part in meters, f is the frequency in hertz, μ is the magnetic permeability in henry/meter, and σ is the electrical conductivity in 1/(ohm*meter). Due to the strong dependence of induced current density with part conductivity, eddy current methods have historically focused on inspection of metallic parts. The high conductivity of these materials leads to typical inspection frequencies in the 10s to 100s of kilohertz (kHz) and coil diameters in range of millimeters. As an example, the operating frequency required to achieve a skin depth of 1 mm in an aluminum alloy structure would be approximately 13 kHz.

With the increased use of carbon fiber composite materials, eddy current techniques are extended to this class of structure. While still conductive, a typical carbon fiber epoxy composite has a conductivity three orders of magnitude lower than an aluminum alloy. By equations (13) and (14), an equivalent increase in operating frequency to the order of 10s of MHz are required to induce the same current density throughout the inspection area. Complications involved in eddy current operation in the 10s of MHz range include increased capacitive effects that can increase noise and limit applicability of standard predictive models. Nonetheless, application of eddy current techniques for measurements of carbon composite materials was demonstrated. Some examples include detection of oxidation induced mass loss in Space Shuttle wing leading edge [refs. 4 and 5], measurement and modeling of impact damage and fiber orientation effects in carbon fiber composites [ref. 6], and measurement of fiber orientation in compression molded carbon fiber prepreg automotive components [refs. 7 and 8].

Typically, eddy current applications for carbon fiber composites are narrowly focused, somewhat exploratory in nature, and used in conjunction to more conventional composite NDE methodologies such as thermography, ultrasonic, and radiography. In effect, most common carbon fiber composite flaws are ill posed for eddy current testing. Laminar disbonds and delaminations, for example, are unlikely to disrupt the induced eddy current flow in the structure and thus unlikely to produce a pronounced eddy current response. Likewise, detection of porosity within the part will be troublesome as the electromagnetic properties of the epoxy matrix is equivalent to potential voids at the working frequency of eddy current techniques.

5.7.2.1   References

1. McMaster, R. C.; and Udpa, S.: "Basic Concepts and Theory of Eddy Current Testing," in *Nondestructive Testing Handbook, Second Edition, Electromagnetic Testing*, P. Mcintire, Editor. American Society for Nondestructive Testing, pp. 25-51, 1986.
2. Libby, H. L.: *Introduction to Electromagnetic Nondestructive Test Methods*, New York: Wiley-Interscience, 1971.
3. Jackson, J. D.: Classical Electrodynamics. New York: John Wiley and Sons, pp. 209-213, 1962.
4. Madaras, E.; et al.: "Nondestructive Evaluation for the Space Shuttle's Wing Leading Edge," in *41st AIAA/ASME/SAE/ASEE Joint Propulsion Conference and Exhibit*, American Institute of Aeronautics and Astronautics, 2005.
5. Wincheski, B.; and Simpson, J.: "Application of Eddy Current Techniques for Orbiter Reinforced Carbon-Carbon Structural Health Monitoring," *AIP Conference Proceedings*, 820(1): 1082-1089, 2006.
6. Washabaugh, A.; et al.: *NDT and SHM of Carbon Fiber Composites using Linear Drive MWM-Arrays*, NASA Technical Report Server, 20130011668, 2013.
7. Wincheski, R. A.; Zhao, S.; and Berger, L.: "Fiber orientation assessment on laminated carbon fiber composites using eddy current probe," in *American Society for Composites: Thirty-First Technical Conference*, 2016.
8. Wincheski, R. A.; and Zhao, S.: "Development of eddy current probe for fiber orientation assessment in carbon fiber composites" *AIP Conference Proceedings*, 1949, 120004; https://doi.org/10.1063/1.5031591, 2018.

5.7.3   Microwave

NDE methods, based on microwave and millimeter (mm) wave principles, are increasingly utilized in a number of critical applications, addressing a plurality of needs in space, aerospace, transportation, utilities and civil infrastructure industries. Microwave frequency range spans ~300 MHz to 30 GHz with a corresponding wavelength (in air) range of ~1000 to10 mm, while millimeter wave frequency range occupies the frequency range of 30 GHz to 300 GHz with a corresponding wavelength range of 10 to 1 mm. Signals at these frequencies readily penetrate dielectric materials, and interact with their inner structures. This interaction is used to perform materials characterization, or flaw detection in the form of high-resolution images [refs. 1–4]. Consequently, in the past few years innovative NDE and imaging techniques capable of addressing a number of critical space and aerospace structural inspection needs were developed [refs. 5–8]. Here, several examples of these applications are illustrated.

Figure 5.7-2a shows a picture of a mockup panel of the Space Shuttle external fuel tank, covered with SOFI. Figures 5.7-2b and c show the image of this SOFI panel obtained using a lens-focused imaging system operating at 150 GHz, with the lens focused at the substrate, showing several embedded voids and inserts using perpendicular (to the stringers) and parallel polarizations, respectively. These images illustrate the utility of this technique for producing high-resolution images. Similarly, Figure 5.7-3a shows a picture of a panel with several heat tiles with surface damage and one covering several corrosion pits on the backing substrate. Figure 5.7- 3b shows a high-resolution wideband synthetic aperture radar (SAR) image of the panel at Q-band (33 to 50 GHz), showing the surface damages and the corrosion pits [ref. 5].
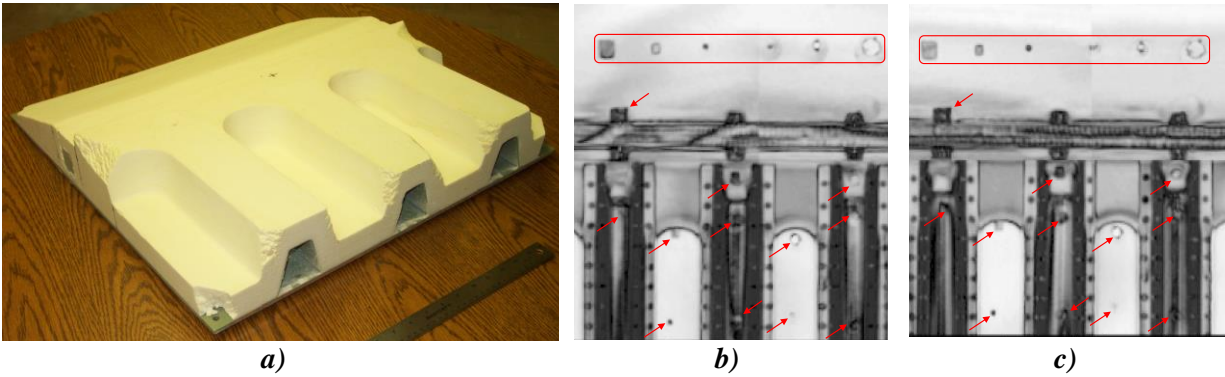
Figure 5.7-2. a) Picture of a SOFI PoD panel, image of the panel with the lens focused at the substrate at 150 GHz showing various embedded voids and inserts, b) perpendicular polarization, and c) parallel polarization.
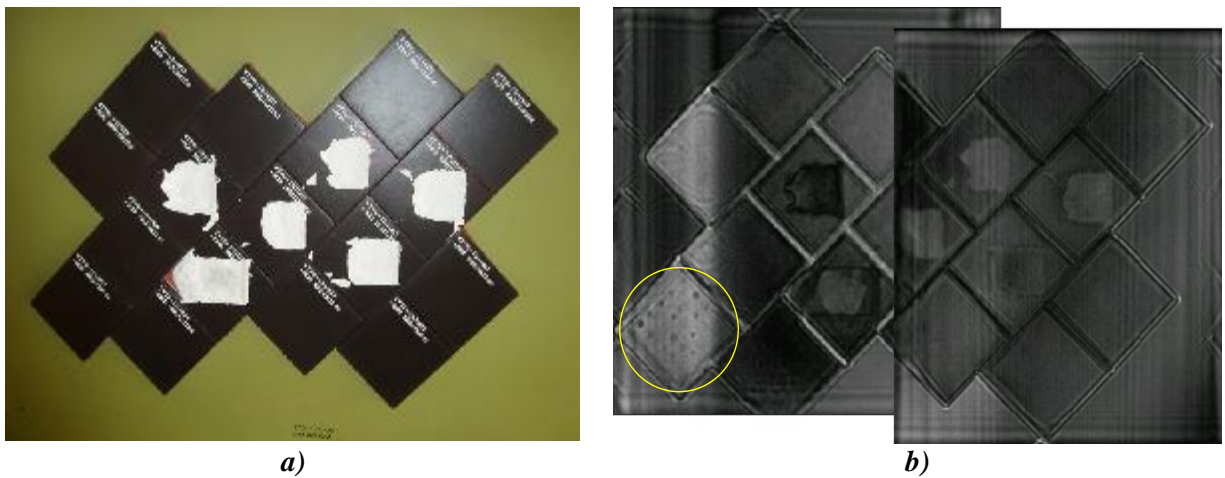
Figure 5.7-3. a) A picture of a panel with several heat tile sections, and b) wideband SAR image at Q-band (33 to 50 GHz) showing surface damage and corrosion pits at substrate within the yellow circle. Reprinted with permission from [ref. 5], ©IEEE, 2007.

Figure 5.7-4 shows a picture of a mimic of an aircraft radome with several embedded flaws with different sizes, shapes and locations (spatial and through depth). Figures 5.7-4b shows a lens-focused image of the panel at 100 GHz, and Figure 5.7-4c shows near-field images at 73 GHz using a small horn antenna [ref. 8]. Once again, these images demonstrate the utility of these different imaging techniques for high-resolution aircraft radome inspection.

a)   *b)*   *c)*
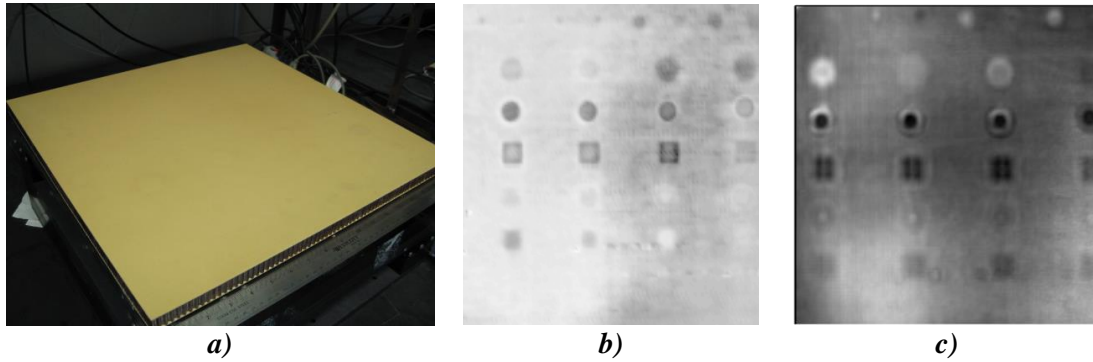
***Figure 5.7-4. a) Picture of an aircraft radome mimic with embedded flaws, b) lens-focused image at
100 GHz, and c) near-field images at 73 GHz.
Reproduced from Reference 8 with the permission of AIP Publishing.***

Due to the limitations associated with skin depth at these frequencies, these signals cannot penetrate inside of highly electrically conductive materials, such as metals. However, they are effectively used to detect and evaluate corrosion under paint and surface-breaking cracks in metallic structures. [refs. 9–11].

With respect to inspecting CFRP composites, these signals cannot penetrate inside of multi-directional CFRP composites, but can inspect their surface properties, namely; issues related to impact damage and surface fiber breakage. However, using proper signal polarization, these techniques are used effectively to inspect uni-directional CFRP composites for interior flaws such as delaminations and voids [ref. 12]. Figure 5.7-5a and b show near-field images of two embedded thin voids under a uni-directional CFRP sheet (commonly) used to strengthen a concrete bridge abutment at perpendicular (relative to the carbon fiber orientation) and parallel polarizations, at x-band (8.2 to 12.4 GHz), respectively. While the former is sensitive to the presence of *both* the voids and any liftoff variation due to the presence of the voids, the latter is only sensitive to the liftoff variation over the region of the voids. Figure 5.7-5c shows the efficacy of using the latter data to remove liftoff variations from the former data to produce an image, which is primarily due to the presence of the voids [ref. 12].

a)   *b)*   *c)*
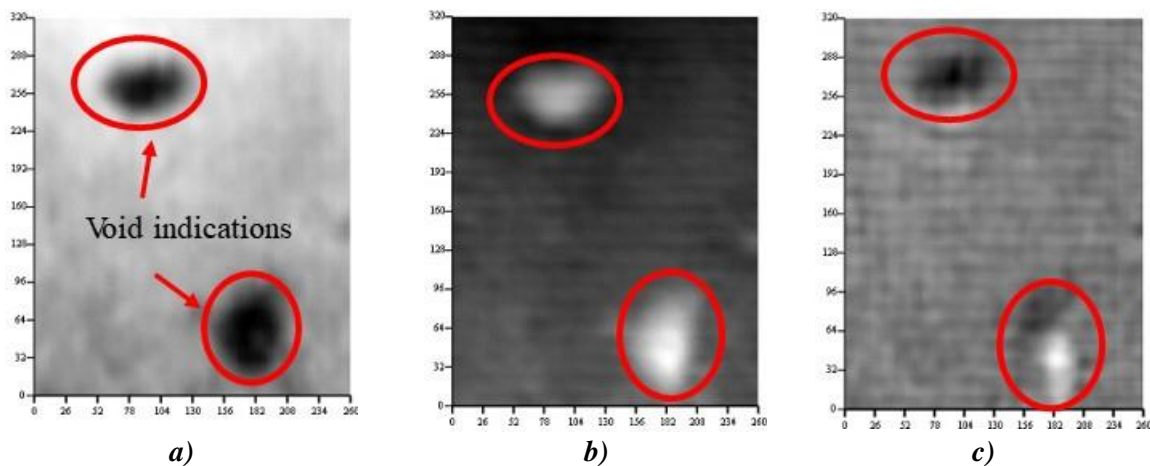
***Figure 5.7-5. Microwave images of a uni-directional CFRP patch at a bridge abutment with two
embedded thin voids.***

193

On another important front, microwave and millimeter wave techniques have been developed during that past two and a half decades for simultaneously evaluating thickness and complex dielectric properties of multi-layered dielectric composites. This is particularly the case for layered composites that are backed by conducting substrates (i.e., metals and carbon composites) used in space and aerospace structures [refs. 13 and 14]. Additionally, microwave techniques have shown great potential for accurately evaluating thickness and dielectric properties of generally lossy coatings, such as paints and primers, applied to carbon composites [ref. 15]. Figures 5.7-6a and b show schematics of two cases in which an open-ended waveguide probe, with an engineered flange [ref. 14], is shown to radiate into two layered structures with a conducting or carbon composite substrate. Table 5.7-1 shows the recalculated coating thicknesses for two different coating types when applied to a conducting and carbon composite substrate, respectively [ref. 15].
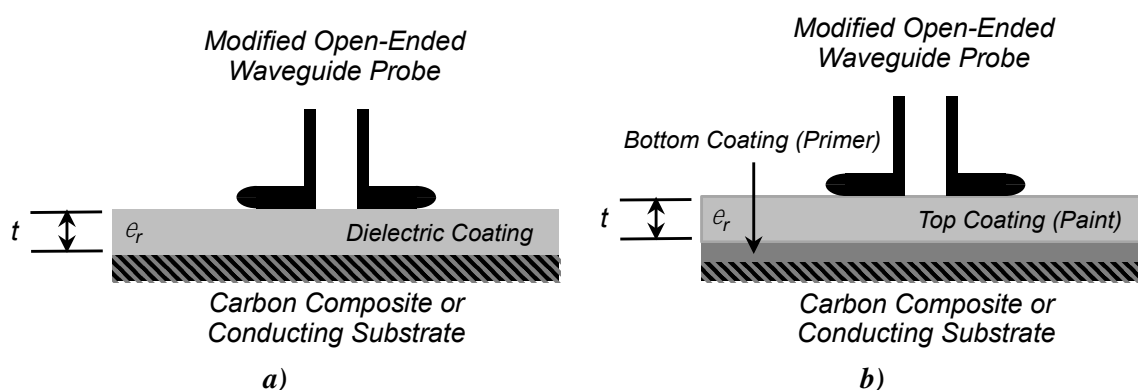
Figure 5.7-6. Schematic of modified open-ended rectangular waveguide probe radiating into carbon composite or conducting substrate.
a) Thin single-layer coating and b) thin two-layer coating (i.e., paint and primer), not-to-scale (reprinted with permission from [ref. 15], ©IEEE, 2016).

Table 5.7-1. Recalculated thickness results for low permittivity and low loss, and high permittivity and high loss coatings on conducting and carbon composite substrates.
Reprinted with permission from [ref. 15], ©IEEE, 2016.

Actual Thickness (mm)	Calculated Thickness and (% Difference)			
	Conductor $\varepsilon_r = 3.3 - j0.01$	**Graphite** $\varepsilon_r = 3.3 - j0.01$	**Conductor** $\varepsilon_r = 17.5 - j7$	**Graphite** $\varepsilon_r = 17.5 - j7$
0.25	0.259 (3.5%)	0.259 (3.6%)	0.262 (4.7%)	0.263 (5.0%)
0.50	0.518 (3.6%)	0.520 (4.0%)	0.516 (3.2%)	0.518 (3.6%)
0.75	0.777 (3.6%)	0.780 (4.0%)	0.767 (2.3%)	0.769 (2.5%)
1.00	1.026 (2.6%)	1.028 (2.8%)	1.016 (1.6%)	1.017 (1.7%)

Given the relatively small wavelengths and the large available signal bandwidths at these frequencies, portable, high-resolution, real-time, and 3D-capable "cameras" were developed in the past decade specifically with NDE applications in mind [refs. 16 and 17]. Figure 5.7-7 shows the

picture of a high-resolution, real-time, 3D (wideband) and portable microwave camera operating in the 20 to 30 GHz range [ref. 17].

Figure 5.7-7. High-resolution, real-time 3D (wideband) and portable microwave camera [ref. 17].
https://youtu.be/RE-PPXmtTeA.

5.7.3.1 References

1. Zoughi, R. "Microwave Non-Destructive Testing and Evaluation Principles," *Springer Science and Business Media*, 2000.
2. Zoughi, R., "Microwave and Millimeter Wave Nondestructive Testing Principles – Back to Basics," *Materials Evaluation*, vol. 76, no. 8, pp. 1051-1057, August 2018.
3. Case, J. T. and Kenderian, S.: "Microwave NDT: An Inspection Method," *Materials Evaluation*, vol. 75, no. 3, pp. 338-346, March 2017.
4. Kharkovsky, S.; and Zoughi, R.: "Microwave and Millimeter Wave Nondestructive Testing and Evaluation – Overview and Recent Advances," *IEEE Instrumentation and Measurement Magazine*, vol. 10, no. 2, pp. 26-38, April 2007.
5. Case, J. T.; Kharkovsky, S.; Zoughi, R.; and Hepburn, F.: "High Resolution Millimeter Wave Inspecting of the Orbiter Acreage Heat Tiles of the Space Shuttle," *Proceedings of the IEEE Instrumentation and Measurement Technology Conference*, #7694, Warsaw, Poland, 2007.
6. Kharkovsky, S., Case, J. T.; Abou-Khousa, M. A.; Zoughi, R.; and Hepburn, F.: "Millimeter Wave Detection of Localized Anomalies in the Space Shuttle External Fuel Tank Insulating Foam," *IEEE Transactions on Instrumentation and Measurement*, vol. 55, no. 4, pp. 1250-1257, August 2006.
7. Kharkovsky, S., Hepburn, F.; Walker, J.; and Zoughi, R.: "Testing of the Space Shuttle External Tank SOFI using Near-Field and Focused Millimeter Wave Nondestructive Testing Techniques," *Materials Evaluation*, vol. 63, no. 5, pp. 516-522, May 2005.
8. Ravouri, M., Abou-Khousa, M. A.; Kharkovsky, S.; Zoughi, R.; and Austin, R.: "Microwave and Millimeter Wave Near-Field Methods for Evaluation of Radome Composites," *Proceedings of the Thirty-Fourth Annual Review of the Quantitative Nondestructive Evaluation Conference*, vol. 27B, pp. 976-981, AIP Conference Proceedings 975, Golden, CO, July, 2007.
9. Zoughi, R.; and Kharkovsky, S.: "Microwave and Millimeter Wave Sensors for Crack Detection," *Fatigue and Fracture of Engineering Materials and Structures*, vol. 31, no. 8, pp. 695-713, 2008.
10. De, S.; Gupta, K.; Stanley, R. J.; Ghasr, M. T.; Zoughi, R.; Doering, K.; Van Aken, D.; Steffes, G.; O'Keefe, M.; and Palmer, D.: "A Comprehensive Structural Analysis Process for

Failure Assessment in Aircraft Lap-Joint Mimics Using Multi-Modal Fusion of NDE Data," *IEEE Transactions on Instrumentation and Measurement*, vol. 62, no. 4, pp. 814-827, April 2013.

11. Kharkovsky, S.; McClanahan, A.; Zoughi, R.; and Palmer, D.: "Microwave Dielectric-Loaded Rectangular Waveguide Resonator for Depth Evaluation of Shallow Flaws in Metals," *IEEE Transactions on Instrumentation and Measurement*, vol. 60, no. 12, pp. 3923-3930, December 2011.

12. Kharkovsky, S.; Ryley, A. C.; Stephen, V.; and Zoughi, R.: "Dual-Polarized Near-Field Microwave Reflectometer for Non-Invasive Inspection of Carbon Fiber Reinforced Polymer (CFRP)-Strengthened Structures," *IEEE Transactions on Instrumentation and Measurement*, vol. 57, no. 1, pp. 168-175, January 2008.

13. Ghasr, M.; Simms D.; and Zoughi, R.: "Multimodal Solution for a Waveguide Radiating into Multilayered Structures - Dielectric Property and Thickness Evaluation," *IEEE Transactions on Instrumentation and Measurement*, vol. 58, no. 5, pp. 1505-1513, May 2009.

14. Kempin, M.; Ghasr, M. T.; and Zoughi, R.: "Modified Waveguide Flange for Evaluation of Stratified Composites," *IEEE Transactions on Instrumentation and Measurement*, vol. 63, no. 6, pp. 1524-1534, June 2014.

15. Zoughi, R., Gallion, J. R.; and Ghasr, M. T.: "Accurate Microwave Measurement of Coating Thickness on Carbon Composite Substrates," *IEEE Transactions on Instrumentation and Measurement*, vol. 65, no. 4, pp. 951-953, April 2016.

16. Ghasr, M. T.; Abou-Khousa, M. A.; Kharkovsky, S.; Zoughi, R; and Pommerenke, D.: "Portable Real-Time Microwave Camera at 24 GHz," *IEEE Transactions on Antennas and Propagation*, vol. 60, no. 2, pp. 1114-1125, February 2012.

17. Ghasr, M. T.; Horst, M. J.; Dvorsky, M. R.; and Zoughi, R.: "Wideband Microwave Camera for Real-Time 3D Imaging," *IEEE Transactions on Antennas and Propagation*, vol. 65, no. 1, pp. 258-268, January 2017.

6.0   NASA NDE Handbook Further Reading

Qualification/Recommended Practice
- ATA Spec 105; Guidelines for Training and Qualifying Personnel in Nondestructive Testing Methods
- ASD-STAN - PREN 4179, Aerospace Series Qualification and Approval of Personnel for Non-Destructive Testing
- NAS 410; NAS CERTIFICATION & QUALIFICATION OF NONDESTRUCTIVE TEST PERSONNEL
- Recommended Practice No. SNT-TC-1A, Personnel Qualification and Certification in Nondestructive Testing
- ISO 9712:2012 Preview; Non-destructive testing -- Qualification and certification of NDT personnel

FAA Advisory Circulars
- AC 25-29 Development of a Nondestructive Inspection Program/Organization
- AC 65-31B Training, Qualification, and Certification of Nondestructive Inspection Personnel

- AC 65-33A Development of Training/Qualification and Certification Programs for Composite Maintenance Technicians
- AC 43-214A Repairs and Alterations to Composite and Bonded Aircraft Structure
- AC 20-107B Composite Aircraft Structure
- AC 21-26A Quality System for the Manufacture of Composite Structures
- AC 23-20 Acceptance Guidance on Material Procurement and Process Specifications for Polymer Matrix Composite Systems

Additional FAA Guidance
- On-Line Job Aid for Evaluating a Repair Facility Conducting Composite Repairs - 04-30-2013
- Job Aid-Composite Repair
- Inspect a Repair Facility Accomplishing Composite Maintenance and Repairs
- 8900.1,Vol.6,Ch11,Sec28
- Evaluating the Size Limits for Bonded Repairs

FAA Policy Statements
- PS-ANM-25-20: Subject: High-Energy Wide-Area Blunt Impact for Composite Structures
- PS-ACE100-2001-006: Subject: Static Strength Substantiation of Composite Airplane Structure
- PS-ACE100-2004-10030: Subject: Substantiation of Secondary Composite Structures
- PS-ANM100-1991-00049: Subject: Policy Regarding Material Strength Properties and Design Values, § 25.613.
- PS-ACE100-2005-10038: Subject: Bonded Joints and Structures - Technical Issues and Certification Considerations
- PS-ACE 100-2002-006: Subject: Material Qualification and Equivalency for Polymer Matrix Composite Material Systems
- AIR100-2010-120-003: Subject: Acceptance of Composite Specification and Design Values Developed using the NCAMP Process

Society of Automotive Engineering Documents

(Commercial Aircraft Composite Repair Committee)
- AIR5279; Composite and Bonded Structure Inspector: Training Document
- ARP5605A; Solid Composite Laminate NDI Reference Standards
- ARP5606A; Composite, Honeycomb NDI Reference Standards

DOT/FAA Sponsored Research Reports
- DOT/FAA/AR-02/121, Guidelines for analysis, testing, and nondestructive inspection of impact-damaged composite sandwich structures.
- DOT/FAA/AR-00/44, Impact damage characterization and damage tolerance of composite sandwich airframe structures

- DOT/FAA/AR-02/80, impact damage characterization and damage tolerance of composite sandwich airframe structures: phase 2
- DOT/FAA/TC-14/42, Innovative wide-area image-based nondestructive inspection techniques for modern rotorcraft composites
- DOT/FAA/TC-14/39, Literature review of weak adhesive bond fabrication and nondestructive inspection for strength measurement
- DOT/FAA/AR-10/46, Monitoring of impact damages in adhesively bonded composites
- DOT/FAA/TC-14/52, Nondestructive inspection research of composite materials used on the commercial fleet: infrared imaging for defect detection in aircraft structures using chaotic and broadband sound excitation
- DOT/FAA/TC-15/4, A quantitative assessment of advanced nondestructive inspection techniques for detecting flaws in composite laminate aircraft structures
- DOT/FAA/TC-15/63, A quantitative assessment of conventional and advanced nondestructive inspection techniques for detecting flaws in composite honeycomb aircraft structures
- DOT/FAA/TC-15/6, A quantitative assessment of conventional nondestructive inspection techniques for detecting flaws in composite laminate aircraft structures
- DOT/FAA/TC-15/51, Composite thermal damage measurement with handheld fourier transform infrared spectroscopy
- DOT/FAA/CT-93/42, Nondestructive inspection (NDI) of reduced strength bonds
- DOT/FAA/TC-14/27, Nondestructive evaluation for damage in composites and their repair

Additional Information
- Care and Repair of Advanced Composites (second addition) Keith Armstrong, L. Graham Bevan, William F. Cole II (authors)
- Essentials of Advanced Composite and Repair, Louis C. Dorworth, Ginger L. Gardiner, Greg M. Mellema (authors)

REPORT DOCUMENTATION PAGE

Form Approved
OMB No. 0704-0188

The public reporting burden for this collection of information is estimated to average 1 hour per response, including the time for reviewing instructions, searching existing data sources, gathering and maintaining the data needed, and completing and reviewing the collection of information. Send comments regarding this burden estimate or any other aspect of this collection of information, including suggestions for reducing the burden, to Department of Defense, Washington Headquarters Services, Directorate for Information Operations and Reports (0704-0188), 1215 Jefferson Davis Highway, Suite 1204, Arlington, VA 22202-4302. Respondents should be aware that notwithstanding any other provision of law, no person shall be subject to any penalty for failing to comply with a collection of information if it does not display a currently valid OMB control number.
PLEASE DO NOT RETURN YOUR FORM TO THE ABOVE ADDRESS.

1. REPORT DATE *(DD-MM-YYYY)*	2. REPORT TYPE		3. DATES COVERED *(From - To)*
02/01/2020	Technical Memorandum		

4. TITLE AND SUBTITLE	5a. CONTRACT NUMBER
Nondestructive Evaluation (NDE) Methods and Capabilities Handbook	
	5b. GRANT NUMBER
Volume I	
	5c. PROGRAM ELEMENT NUMBER

6. AUTHOR(S)	5d. PROJECT NUMBER
Howell, Patricia A. (Editor)	
	5e. TASK NUMBER
	5f. WORK UNIT NUMBER
	826611.04.07.02.02

7. PERFORMING ORGANIZATION NAME(S) AND ADDRESS(ES)	8. PERFORMING ORGANIZATION REPORT NUMBER
NASA Langley Research Center Hampton, VA 23681-2199	L-21112

9. SPONSORING/MONITORING AGENCY NAME(S) AND ADDRESS(ES)	10. SPONSOR/MONITOR'S ACRONYM(S)
National Aeronautics and Space Administration Washington, DC 20546-0001	NASA
	11. SPONSOR/MONITOR'S REPORT NUMBER(S)
	NASA/TM-2020-220568/Volume I

12. DISTRIBUTION/AVAILABILITY STATEMENT

Unclassified - Unlimited
Subject Category 37 Mechanical Engineering
Availability: NASA STI Program (757) 864-9658

13. SUPPLEMENTARY NOTES

14. ABSTRACT

This Handbook is a guidance document that facilitates the selection of appropriate Nondestructive Evaluation (NDE) techniques and provides recommended protocols for detecting and characterizing common flaw types in complex composite structures. It seeks to reduce the time required to develop qualified inspection processes for composite aircraft structures during the development, certification, and manufacturing phases by providing a reference that helps minimize trial and error and provides guidance on best practices, techniques, and settings, for specific flaw types and geometries.

15. SUBJECT TERMS

Nondestructive Evaluation; Inspection; Handbook; Composites; Carbon Fiber Reinforced Polymer; Ultrasound,; Thermography; X-ray CT

16. SECURITY CLASSIFICATION OF:			17. LIMITATION OF ABSTRACT	18. NUMBER OF PAGES	19a. NAME OF RESPONSIBLE PERSON
a. REPORT	b. ABSTRACT	c. THIS PAGE			STI Help Desk (email: help@sti.nasa.gov)
			UU	216	19b. TELEPHONE NUMBER *(Include area code)*
U	U	U			(443) 757-5802

Standard Form 298 (Rev. 8/98)
Prescribed by ANSI Std. Z39.18